

New Reliability Assessment of MEMS Components under Accumulative Testing for Space Applications

Présentée le 21 octobre 2021

Centres pour l'innovation
Centre spatial suisse
Programme doctoral en génie électrique

pour l'obtention du grade de Docteur ès Sciences

par

Maxime AUCHLIN

Acceptée sur proposition du jury

Prof. C. Enz, président du jury
Prof. V. Gass, Dr O. Sereda, directeurs de thèse
Prof. T. Ghidini, rapporteur
E. Rugi Grond, rapporteuse
Prof. Y. Bellouard, rapporteur

Acknowledgements

This adventure started during my stay in the United States, when I was working on my Master thesis' research in Houston. On Tuesday May 10th, 2016, an email from the person who would become my academic supervisor and thesis co-director appeared in my mailbox. I was proposed to apply for a research project in an intriguing yet uncharted field to me: MEMS reliability in space applications. Prof. Volker Gass, head of today's Space Innovation (formerly: Swiss Space Center) at EPFL, gave me four days to respond. Initially, I was not envisioning to pursue further academic studies, aiming at the more applied and pragmatic life of an engineer in industry. However, the opportunity to pursue a Ph.D. thesis, working as an employee of the Swiss Center of Electronics and Microtechnology (Centre Suisse d'Électronique et de Microtechnique, CSEM) in my hometown of Neuchâtel, and in collaboration with the European Space Agency (ESA) and Space Innovation, convinced me to take the leap. Both my intention to work in an environment close to industry, as well as my passion for space and interest in science were fulfilled. I would like to deeply thank Prof. Gass for his trust, guidance, and advice during my four years as his student. The funding of this work by ESA's Networking/Partnering Initiative (NPI), CSEM and Space Innovation are also gratefully acknowledged.

ST Microelectronics, by the intermediate of Ms. Chira Vinci and M. André Roessinger, is greatly thanked for the gracious procurement of 120 devices for this research. Acknowledgements are also addressed to Michele Palmieri, current vice-president of the Micro and Nano Systems division at CSEM, whose extended network in the MEMS fields allowed this to happen.

A project like this would also never have been possible without an amazing team of colleagues at CSEM, and above all the continued and enthusiast support, scientific expertise, and rigor of my co-director Dr. Olha Sereda. I never felt hindered in the pursuit of new ideas and propositions, while being provided with adequate and pertinent advice. She also encouraged me to tackle new challenges that I encountered and pushed me to explore uncharted scientific lands. Working as a Ph.D. student at CSEM comes with the task of being involved with industrial works. In this respect, I would like to further thank her for granting me with the opportunity to evolve as an engineer, while pursuing research and development as a scientist. I had the exceptional opportunity to acquire experience with cutting-edge tools such as high-resolution X-ray diffractometer (XRD), scanning electron microscope (SEM), and computer-assisted design (CAD) programs.

The Additive Manufacturing and Components Reliability (formerly the Characterization & Quality Assurance sector) at CSEM, led by Olha, is a very stimulating and pleasant work environment, comprising of many skillful and adorable people. Michele Palmieri, vice-president of the Micro & Nano Systems Division, contributed to obtaining the MEMS devices. His help is greatly acknowledged. I am furthermore very thankful to my colleagues, who allowed me to grow as a person: Prof. Massoud Dadras (for his sometimes very insistent – yet often justified – ideas and propositions), Dr. Ivan Marozau (for his constant kindness and highly valuable expertise in reliability), Silvia Biselli and Véronique Courbat (their helpfulness, skills, and good mood), my office friends and materials science peers Dr. Kaushik Vaideswaran and (future Dr.!) Gaëtan Bernard, and finally to Dr. Saba Zabihzadeh and Dr. Václav Pejchal for their support. I would like to further thank Dr. Sébastien Lani and Olivier Chandran for sparking my interest of additive manufacturing, Dr. Nicholas Hendricks for his comments on the manuscript, and my other colleagues for the good time: Samuel, Maël, and all the other awesome individuals who are not mentioned here.

Beyond my everyday working environment, I warmly thank Edo Franzi and Pierre-Alain Beuchat for their valuable help in the early stages of the project, during the elaboration of the electronic socket for characterizing the MEMS devices. Special acknowledgements go to Dr. Dara Z. Bayat and Dr. Ivar Kjelberg for their dazzling expertise and precious help for COMSOL and Finite Element Modeling. I am moreover grateful to the mechanical workshop team, managed by Laurent Beynon, for their advice and fast manufacturing of hardware that was needed, sometimes, within short deadlines. I also thank Dr. Michel Despont for the valuable insights and giving me the possibility to participate to interesting industrial projects.

Acknowledgements

This thesis would also not have been possible without the many space enthusiasts who I have met in the Netherlands. First and foremost, I am deeply grateful to Laurent Marchand, who has contributed to the initiation of this research, and who offered me the extraordinary opportunity to spend a total of six months at ESTEC, ESA's main technology development and test center for spacecraft and space technology. His considerable experience in MEMS technology, reliability and quality, his enthusiasm and valuable insights were extremely precious. During my time at ESA, I have met experts from many horizons and who allowed me to learn about various high-end characterization and test equipment, as well as the reliability requirements, quality standards and other space-related knowledge and stories. I am grateful to have been able to take advantage of the cutting-edge facilities and know-how at ESTEC. Special thanks go to my colleagues Joaquín Jiménez, Ulla Laitinen, Nicolas Saillen, Michele Brondi, Paavo Heiskanen, Léo Farhat and Liam Murphy for their valuable help, advice, and good company. I would like also to thank the space geeks crew: Xavier, Luc, my flatmates Denisa, Mattias, and George, and all the young graduates (YGT) and national trainees (NTP) who I have met in this very exciting environment.

The space community in Switzerland is also incarnated by Prof. Claude Nicollier. His contagious passion for space and communicative talent to share it is for sure what motivated generations of students – including me – to pursue research or a career in this field. I am deeply grateful for having had the opportunity to participate to his course “Space mission design and operations”: first as a student, then as a teaching assistant and examiner. Additionally, I would like to thank the Space Innovation team for their cordiality and support: Grégoire Bourban, Martine Harmel, Gilles Feusier, Yannick Delessert, and Julien Bonnaud. Dr. Tobias Bandi and his previous research done on MEMS reliability is also greatly acknowledged. I also thank Gary Perrenoud for his flexibility for the many X-ray tomography measurement performed at EPFL. I finally wish good luck to my peers Tatiana Volkova, Michael Julliard and, most importantly, to my friend, Dr. Timothée Frei, with whom were spent countless hours of videocalls during the pandemic and writing times. I wish them brilliant successes in their research and professional lives.

And of course, I would like to warmly thank my family and friends for their unconditional support through life, during my studies and when the decision came to start and work on this thesis. Finally, I thank Arina. Большое спасибо за радость и любовь, которую ты приносишь мне каждый день, и за безусловную поддержку в течение этих 4 лет и 3 месяцев аспирантуры.

This has been a formidable adventure. I am very grateful to have met these people, have worked in an exciting field, and lived these unforgettable experiences. They will always be remembered!

Résumé

Cette thèse propose une nouvelle méthode d'essais accumulatifs pour unités de mesure inertielle (IMU) du secteur automobile et basées sur les MEMS. Le besoin de clarification et d'augmentation des connaissances sur la fiabilité des MEMS pour les applications spatiales est abordé. Des procédures d'essai plus rapides et moins fastidieuses, une meilleure compréhension des modes de défaillance et de leurs effets ainsi que des modèles de prévision et simulations numériques sont développés. L'IMU a subi plusieurs campagnes de tests accumulatifs séquentiels sous différents environnements. La structure de cette recherche culmine avec un test de contrainte en sept étapes, alternant entre vibrations et chocs thermiques, suivi d'une analyse approfondie des modes de défaillance des dispositifs défaillants ou dégradés.

Le **Chapitre 1** décrit le monde des MEMS, leurs domaines d'application et leur fiabilité. Les points forts des utilisations dans les technologies spatiales, leur fiabilité et les mécanismes de défaillance sont présentés. Enfin, ce chapitre couvre les travaux scientifiques existants réalisés et questions ouvertes restantes sur le thème spécifique des tests accumulatifs.

Le **Chapitre 2** présente les parties prenantes concernées par cette recherche. Il est important de garder à l'esprit la vocation applicative et industrielle des tests de fiabilité. Les raisons du choix de l'IMU pour les différentes campagnes de tests sont décrites. Une analyse physique destructive approfondie a été effectuée pour comprendre la construction des IMUs.

Le **Chapitre 3** détaille la méthode expérimentale. Les tests fonctionnels ont été effectués avant, entre et après une étape de test sur les dispositifs seuls, sans circuit périphérique. La description de la méthodologie de test continue avec le développement d'une procédure mono-paramétrique en deux étapes. Cette procédure n'a pas permis d'évaluer correctement la fiabilité des composants MEMS robustes, même dans des environnements plus contraignants que les normes communément utilisées (MIL-STD-883). Des tests accumulatifs ont donc été effectués.

Le **Chapitre 4** présente les résultats expérimentaux des différentes campagnes accumulatives : (i) cycles de température suivis de vibrations, (ii) chocs thermiques suivis de vibrations, (iii) vibrations et chocs thermiques alternés en 7 étapes. La première campagne a donné lieu à la défaillance des dispositifs en raison de l'affaiblissement de l'adhésif conducteur, tandis que les deux autres ont montré une dégradation avancée sans défaillance. La tomographie aux rayons X a été utilisée pour identifier les modes de défaillance, ainsi que la diffraction des rayons X à haute résolution pour mesurer les contraintes résiduelles dans le silicium des MEMS. D'autres tests complémentaires ont été effectués (arrachage des puces, traction des fils de connexion).

Au **Chapitre 5**, une analyse par éléments finis de l'IMU est faite. Un modèle thermique permet de vérifier que les dispositifs sont à l'équilibre thermique pendant les tests. Ensuite, les données de contrainte et de déformation peuvent être obtenues sur un cycle thermique pour l'adhésif en appliquant un modèle viscoélastique. Les valeurs trouvées suggèrent que l'accumulation de dommages plastiques est probable en raison de l'accumulation de contraintes thermiques : un résultat corroboré par les observations expérimentales.

En proposant une nouvelle approche de la fiabilité robuste des MEMS et en plongeant dans les modes de défaillance et les effets des essais d'accumulation, cette recherche vise à contribuer à l'élaboration du prochain cadre qui aidera la communauté spatiale à favoriser une plus large utilisation des dispositifs commerciaux dans les applications spatiales.

Mots-clés : système micro-électro-mécanique, MEMS, fiabilité, essais accumulatifs, normes spatiales, rodage, essais bi-paramétriques, vibrations, chocs thermiques, cycles de température, tomographie aux rayons X, reconstruction 3D, diffraction des rayons X à haute résolution, modélisation par éléments finis, effets thermomécaniques, dégradation, adhésif isotrope conducteur, viscoélasticité

Abstract

This dissertation proposes a novel accumulative test method for MEMS-based, commercial off-the-shelves inertial measure units (IMUs) from the automotive field. The need for clarification and augmentation of the corpus of knowledge on MEMS reliability for space applications is addressed. Faster and less tedious test procedures, better understanding of the failure modes as well as the possible prediction models and numerical simulations are at the center of a pragmatic vision that shall keep the industrial end-user and applications in sight. The IMU is used in several sequential accumulative test campaigns under various environments. The device comprises notably of a X,Y-axis accelerometer. The structure of this research is elaborated following an increasing level of complexity, culminating at a seven-step stress test, alternating between thermal shocks and vibration testing, followed by thorough failure modes and effects analysis of the failed or degraded devices.

Chapter 1 describes the world of MEMS. Highlights of uses in space technologies are presented, as well as the state-of-the-art of reliability testing and corresponding failure mechanisms. Remaining open questions about accumulative testing are covered.

Chapter 2 elaborates on the stakeholders implied in this research. It is important to keep in mind the highly applicative and industrially oriented vocation of reliability testing. Choice of the IMU for the various test campaigns is done. A thorough destructive physical analysis has been performed to gain knowledge of the devices' construction.

Chapter 3 details the experimental method. Functional tests were performed before, in-between, and after a test step on the devices alone (no peripheral circuitry). Testing methodology description follows with the development of a mono-parameter, two-step stress test procedure. Such procedure fails to properly assess the reliability of the robust MEMS components, even with harsher environments than commonly used standards (MIL-STD-883). Accumulative testing was therefore performed.

Chapter 4 reports the experimental results from the different test campaigns: (i) temperature cycling followed by vibration, (ii) thermal shocks followed by vibration, (iii) vibration and thermal shocks alternated in a seven-step sequence. The first campaign yielded to the failure of the devices due to die attach weakening, while the two others showed intense degradation without failing. X-ray tomography was used to identify failure modes, as well as high-resolution X-ray diffraction for residual stress identification in the silicon dies. Other complementary tests were performed (die shear, wire bonds pull).

In **Chapter 5**, a finite element model of the MEMS device is designed. A thermal-only model allows to verify that devices are at thermal equilibrium during testing. Then, by relying on a viscoelastic, stress and strain data can be obtained over a thermal cycle for the die attach. The found values suggest that accumulation of plastic damages are very likely to occur due to the build-up of thermal stress in the adhesive: a result corroborated by the experimental observations.

By proposing a novel approach to robust MEMS reliability approach and diving deep into the failure modes and effects of accumulative testing, this research aims at contributing to the elaboration of the next framework that will help the space community to foster a wider use of COTS devices in space applications.

Keywords: microelectromechanical system, MEMS, reliability, accumulative testing, space standards, burn-in, bi-parameter testing, vibration, thermal shocks, temperature cycles, X-ray tomography, CT scan, 3D reconstruction, high resolution X-ray diffraction, finite element modelling, thermomechanical effects, degradation, die attach, viscoelasticity

Contents

Acknowledgements	i
Résumé	iii
Abstract	v
Contents	vii
List of Figures	xi
List of Tables	xvii
List of Abbreviations	xix
Chapter 1 Introduction	21
1.1 The world of MEMS and their applications.....	22
1.2 MEMS in space application.....	24
1.3 Testing for reliability: classical approach for MEMS-based devices	26
1.3.1 Failure mechanisms in MEMS	26
1.3.2 Harsh operating environments and relevant test methods	29
1.3.3 Standards for MEMS: an open question	32
1.4 Beyond the classical approach for reliability evaluation.....	34
1.5 Key findings of the literature review	36
Chapter 2 Selection and pre-evaluation of the MEMS device	37
2.1 Selection scheme	37
2.1.1 Selection of space missions and applications of MEMS.....	38
2.1.2 MEMS device attractiveness/suitability for space applications	43
2.1.3 Industrial actors for COTS MEMS	45
2.1.4 Final choice of MEMS device	46
2.1.5 Selected component	46
2.2 Pre-evaluation of the MEMS device.....	47
2.2.1 Analyses	47
2.2.2 Discussion of the observations	52
2.2.3 Conclusions from the construction analysis.....	53
Chapter 3 Experimental method	55
3.1 Test hardware and standards	55
3.1.1 Equipment repository.....	55
3.1.2 Standards	56
3.1.3 Functional characterization	57
3.1.4 Failure criteria.....	57

3.2	Experimental details	59
3.2.1	General experimental setup	59
3.2.2	Data quality and experimental error	59
3.3	Initial screening and burn-in.....	61
3.4	Testing methodology	62
3.4.1	Mono-parameter testing.....	62
3.4.2	Bi-parameter accumulative testing.....	65
3.4.3	Global view of the test plan.....	66
Chapter 4	Experimental results	69
4.1	Mono-parameter reliability campaign	69
4.1.1	Temperature cycles and thermal shocks	70
4.1.2	Vibration test.....	72
4.1.3	Intermediate conclusions on mono-parameter testing mode	72
4.2	Bi-parameter reliability testing.....	73
4.2.1	CVF-Series: accumulative temperature-vibration tests	73
4.2.2	XVX-Series: accumulative thermal shocks/vibration & extensive thermal shocks tests	76
4.2.3	VXV-Series: accumulative vibration-thermal sequential testing	78
4.2.4	Conclusion of the observations in the reliability test campaigns	82
4.3	Failure modes and effects analyses (FMEA)	82
4.3.1	X-Ray tomography and die attach study.....	82
4.3.2	High resolution X-ray diffraction (HRXRD)	89
4.3.3	Wire bonds pull tests	93
4.3.4	Post-tests die shear.....	94
Chapter 5	Finite Element Analysis	97
5.1	Thermal model	97
5.1.1	General hypotheses	98
5.1.2	Materials and geometrical considerations	99
5.1.3	Numerical results and discussion	99
5.2	Thermomechanical study.....	102
5.2.1	Materials and geometrical definitions.....	102
5.2.2	Viscoelastic model for the die attach's material	103
5.2.3	Two-dimensional partial model	105
5.2.4	3D numerical results	110
Chapter 6	Discussions and conclusions	113
6.1	General discussion.....	113
6.2	Synthesis of the research	115
6.3	Outlook	115
6.3.1	Recommended test sequence	115

Contents

6.3.2	Challenges ahead for a self-standing reliability test procedure for MEMS in space applications	116
6.4	Future works	117
6.4.1	Effect of preconditioning on lifetime.....	117
6.4.2	Accumulative simultaneous testing.....	117
6.4.3	DUTs functionality characterization	118
6.4.4	Development of a mechanical model.....	119
6.4.5	Further die shear tests analysis.....	120
6.4.6	Refined 3D finite element models.....	120
References	121
Appendix	133
A.	MEMS market overview	133
B.	Full results of the construction analysis	133
❖	Visual and radiographic inspections	133
❖	Wire bond test.....	141
❖	Cross-Sections and SEM imaging.....	142
C.	MATLAB script for functional characterization	149
D.	Initial devices screening	160
❖	Physical and electrical characterization.....	160
❖	Pin-to-pin insulation.....	161
E.	Parasitic resonance measurement and vibration sample holder	162
F.	Gyroscope readouts recording example.....	164
G.	ImageJ bandpass and constrast macro.....	164
H.	Die attach tomography and post-die shear imaging	164
❖	G21-CVF group.....	164
❖	G22-XVX group.....	165
❖	G23-XVX group.....	166
❖	Control group.....	167
I.	Details of the post-campaign bond pull test.....	168
❖	Accelerometer die and ASIC connections	168
❖	Gyroscope die and ASIC connections	168
❖	Wire bonds between the ASIC and the package	169
Curriculum Vitae	171

List of Figures

Figure 1.1: Deformable micromirror (left) and insulin miniature pump (Nanopump, courtesy to Debiotech Switzerland).....	23
Figure 1.2: (<i>left</i>) View of the 22mm x 22mm micropump, (<i>right</i>) engineering model of the space bioreactor mounted on the base of a Type II experiment container [44].	24
Figure 1.3: Selection of failure in MEMS silicon structures. (a) Surface fracture, (b) stiction in MEMS fingers, (c) Electrostatic Discharge (ESD) in an electrostatic actuator, (d) wear debris in the micro-engine, (e) particle contamination on MEMS, (f) surface wear in drive gears, micro engine gear under humidity stress at (g) 1.8%RH, (h) 24%RH, (i) 39%RH [83].	28
Figure 1.4: Overview of the main sources of failures in MEMS devices [84].	28
Figure 1.5: Pie chart of failures of MEMS under severe shocks and impact loading [107].	29
Figure 2.1: Stakeholder value network diagram of the stakeholder related to the current thesis.....	38
Figure 2.2: Top view of MRS FExp front end PCBs (<i>left</i>) and view of the MRS Exp unit on the CryoSat-2 nadir panel (<i>right</i>) [184].	39
Figure 2.3: An instrument for test of the micromirrors in the ISS with a cover removed [195].	41
Figure 2.4: SEM micrograph of the MEMS interferometer. A set of fixed and movable micromirrors enable quantification of light path difference [209].	41
Figure 2.5: CSEM's MEMS atomic vapor cells. A Rubidium gas is created in the hermetic chamber formed by the silicon ring, encased between two quartz blades. A laser excites the gas, the interactions permits measurement of quantum decay [212]	42
Figure 2.6. The microfabricated atomic clock physics package based on Cs atoms. (A) Schematic of assembly. Layers from bottom to top: a, Laser and baseplate; b, Glass (500 μm); c, ND filter (500 μm); d, Spacer (375 μm); e, Quartz (70 μm , not shown); f, ND filter (500 μm); g, Glass/ITO (125 μm /30 nm); h, Glass (200 μm); i, Si (1000 μm); j, Glass (200 μm); k, Glass/ITO (125 μm /30 nm); l, Si (375 μm); m, Glass (125 μm). Total height, 4.2 mm, width and depth, 1.5 mm. Photographs (B), photodiode assembly, (C), cell assembly, (D), optics assembly and (E), laser assembly and (F), the full atomic frequency reference physics package realized as a microchip. The black scales are 1mm. Reproduced from [214].	42
Figure 2.7: Utility functions.	44
Figure 2.8: External view of the device: (a) vent, (b) lid adhesive (glass frit), (c) gold contact pad.....	48
Figure 2.9: Radiographic views of device and uncapped MEMS dies. (A) stands for accelerometer, (G) for gyroscope. The MEMS structures are clearly visible (debris are present) and uncovers the complexity of the system, as explained in the paragraph.	49
Figure 2.10: Optical views of a device with lid removed. (A) stands for accelerometer, (G) for gyroscope. Details: wire bonds and die attach.	50
Figure 2.11: Strength distribution of the wire bonds. The connections between the ASIC and the package distribution are centered at the 85-90 mN pull force while the connections	

between the gyroscope, respectively the accelerometer and the ASIC are centered at around 105-110 mN.....51

Figure 2.12: Sections of optical microsections. (*left*) The white line on the device's image depicts the location of the cross-section. (*right*) Details of a wire bond pad (top), the accelerometer intra-die solder (middle) and the die attach (bottom) are shown.....51

Figure 3.1: Test bench with the COMBOG device in place (left) and top view (right) with the 0.8 mm pogo-pins enabling the connection. The top lid permits to clamp the sensor tightly in the housing, made of non-conductive resin. The socket is fixed into a U-shaped aluminum profile with controlled orthogonality of its sides for better (X, Y, Z) positioning.57

Figure 3.2: Example of data obtained from the devices and automatic processing.58

Figure 3.3: Plot of the deviations of the two failure criteria for the X-axis after 1000 thermal shocks.58

Figure 3.4: Schematic of the device.59

Figure 3.5: Five minutes measurement (raw signals): top is zero-g X and Y axes; bottom is gyroscope signal and temperature. Signals for stationary measurements were observed as following a normal law.....60

Figure 3.6: "Bathtub curve" hazard function.61

Figure 3.7: Burn-in bench with the four sockets for device connection. A thermocouple is fixed to the baseplate for continuous in-situ temperature recording.61

Figure 3.8: Test flow for the two-step stress reliability evaluation.62

Figure 3.9: Difference in soak times between temperature cycles (left) and thermal shocks (right). The blue and red semi-transparent strips indicate the cold and hot subranges.63

Figure 3.10: Unshielded (direct air stream) and shielded (chamber temperature) temperature plots. The position of the thermocouple inside the aluminum profile is indicated by the asterisk and corresponds to the test values indicated in this section.....64

Figure 3.11: Definition of one vibration cycle in terms of g-force as a function of time. It consists of three complete sweeps from 20 to 2000, back to 20 Hz.64

Figure 3.12: Vibration profile at 50g between 20 and 2000 Hz.....65

Figure 3.13: Sample holder and its dimensions, in millimeters. The weight of one sample holder with two M5 screws is 140g. Dimensions are in millimeters and technical drawings are reported in Appendix E.65

Figure 3.14: Bi-parameter accumulative sequential testing. View of the test flow.66

Figure 3.15: Global test flow and samples numbering. TCy: Temperature Cycles, Vibr: Vibration sweeps, ThSh: Thermal Shocks. Series naming and associated numbering are reporter on the left side. The total numbers of cycles or sweeps are reported on the right.67

Figure 4.1: Typical deviation of the failure criteria after the burn-in. Step 1: pristine device. Step 2: device after electrical characterization and pin-to-pin insulation test. Step 3: device after the burn-in procedure (260 hours at 100°C, direct bias 3.6 V).70

Figure 4.2: G21- and G22-CVF Series (step 1). Box-and-whiskers plots showing order statistics (minimum, 25% quantile, median, 75% quantile, maximum) of the deviation criteria per axis as a function of the number of temperature cycles. Notice the different scales.71

Figure 4.3: G21- and G22-XVF Series (step 1). Box-and-whiskers plots showing order statistics (minimum, 25% quantile, median, 75% quantile, maximum) of the deviation criteria per axis as a function of the number of thermal shocks. Notice the different scales.71

Figure 4.4: G21- and G22-VXV Series (step 1). Box-and-whiskers plots showing order statistics (minimum, 25% quantile, median, 75% quantile, maximum) of the deviation criteria per axis as a function of the number of vibration cycles. Notice the different scales. 72

Figure 4.5: Sequence for the 13 devices tested in accumulative temperature cycles and vibration tests. Number indicated in the bar charts refer to the cycle count for a deviation event of at least one axis, or at failure. The letters next to the numbers refer to the affected axis..... 74

Figure 4.6: Effect of the CT-scan on deviation criteria. Measurement at 90 cycles is a discrepancy. Criterion D_2 shows a nearly symmetrical behavior to D_1 . Not only the averaged gravity value shifts, but the zero-level shifts as well. 74

Figure 4.7: G21-CVF Series (step 2). Box-and-whiskers plots showing order statistics (minimum, 25% quantile, median, 75% quantile, maximum and outliers) of the deviation criteria per axis as a function of the vibration cycles. Deviations are essentially due to the CT scans, which stretched the quantiles to values beyond $\pm 2\%$ 75

Figure 4.8: G22-CVF Series (step 2). Box-and-whiskers plots of the deviation criteria per axis as a function of the vibration cycles. Data reduces to a single point when only one device is left. The large deviation observed was essential due to device G22-CVF-04, observed under CT scan. D_1 remains however stable. 75

Figure 4.9: X-ray tomography view of a severely damaged die attach. Weaking of the adhesive ultimately led to complete delamination. 76

Figure 4.10: Weibull probability plot for the G22-CVF Series. Seven failed devices are used (one is censored at 45 sweeps) under accumulative testing (220 temperature cycles followed by vibration). Shape parameter $\gamma=133.78$. The scale parameter $\alpha=1.38$ meaning that the failure rates increase. 76

Figure 4.11: Reliability test for series for devices under accumulative thermal shocks followed by vibration. All devices belonging to series G22-VXV displayed a greater than 2% deviation of one of the two axes at 1000 cycles of step 4. Subgroups of devices in G23-VXV were taken out at regular steps of the campaign for FMEA comparison. Overall, only one device lost functionality. 77

Figure 4.12: Results for the global deviation of parameters for the G22-VXV sequence. The devices have seen a total of 1720 thermal shocks. 78

Figure 4.13: Results for the global deviation of parameters for the G23-VXV sequence. 78

Figure 4.14: Accumulative alternative thermal and vibration loads. The “Out” tags indicate that the device is taken out from the set for further analyses. The X and Y-axes letters show for which axis one of the two criterion failed. Device 219 lost functionality due to a manipulation mistake which disrupted the ASIC-accelerometer wire bonds during lid regluing. 79

Figure 4.15: G21-and G22-VXV Series (steps 1 to 7). Box and whisker plots showing order statistics (minimum, 25% quantile, median, 75% quantile, maximum and outliers) of the deviation criteria per axis as a function of the vibration cycles. While the thermal steps have an obvious detrimental effect on criteria’s deviations, the vibration steps effects were smaller. 79

Figure 4.16: From left to right – from step tests with increasing stress levels V_i leading to failure over time, the concatenation of the cumulative distribution functions (CDF) segments $F_i(t)$ lead to an aggregated equivalent distribution function $F_0(t)$ 80

Figure 4.17: Weibull plots for the G21-VXV and G22-VXV Series. The number of cycles is aggregated into a single count value: $N_C = N_{\text{thermal}} + N_{\text{vibration}}$ with the number of thermal shocks and vibration sweeps respectively. The failure event is either define by both axes failing (left column) or when only one axis fails (right column). 81

Figure 4.18: Radiographic (tomographic) close-up view of the device (pristine) and contrast view of the ASIC-to-package die attach layer (G21-CVF series after 110 temperature cycles and 40 vibration cycles).83

Figure 4.19: Degradation of the die attach at successive vibration cycles (step 2) after a 220 temperature cycles preconditioning. Brighter areas are delaminated areas of die attach.84

Figure 4.20: CT-Scan cross-section at the level of the die attach and strategies for adhesive surface loss quantification. 3D reconstruction of the die attach (device G22-CVF-04). The scale delamination on the lower left of the gyroscope die is visible.85

Figure 4.21: X-ray tomography views of the devices at various thermal shocks counts. The white circle pinpoints the location of the first observed cracking (in two different devices at 220 shocks, as well as the reported location of the first crack in a device after 500 additional thermal cycles). Degradation of the die attach beneath the gyroscope is obvious starting already at 500 thermal shocks, while it develops later underneath the ASIC/accelerometer dies.87

Figure 4.22: (*left*) X-ray tomography view of device G22-VXV-02 with visible globular delamination (brighter spots), (*center*) post-die shear optical view of the die attach with debris of the fillet, (*right*) bottom side (mirror) view of the gyroscope die with residues of the adhesive.87

Figure 4.23: General tomography pictures of full 7-step test flow, showing the progression of damages in the IMUs. The first and the third steps, consisting of vibration, have been removed for clarity due to minor evidence of change. Needle-shaped cracks start to appear in step 2, while generalized tessellation in the die attach takes place starting the fourth step. Severe delamination progresses in the case of the ASIC's die up to step 7.88

Figure 4.24: Illustration of a fulfilled Bragg condition: the path difference of the incident beam is equivalent to a integer multiple of the wavelength. Source: <https://www.microscopy.ethz.ch/bragg.html>90

Figure 4.25: (*top*) direction of illumination on a pristine and a failed device, (*bottom*) depiction of asymmetrical and symmetrical reflections used in high-resolution XRD configuration. The first measurement of the Si(004) and Si(115) reflections take place on the top cover of the die, while the Si(220) reflection is found with a lateral illumination.90

Figure 4.26: Space map (real space) of the intensity peaks for sample number 52 (G22-XVX-08) after an accumulative 1720 thermal shocks and 60 vibration cycles. The two halves of the gyroscope's package are resolved and show a misalignment of 0.03204°. HRXRD epi-biaxial stress calculated at the $\pm 10\%$ shoulders of the intensity peaks for the selected planes by use of the Reciprocal Space Maps (RSM).91

Figure 4.27: RSM maps for the Si(220) reflection between a pristine gyroscope die and the one of device n°252 (1720 thermal shocks and 180 vibration sweeps). Asymmetry of the reflection intensity is visible for the aged MEMS, as well as the major and minor peaks of the gyroscopes bonded parts.92

Figure 4.28: Lattice stress in the gyroscope die. Si(004) and Si(115) intensity peaks correspond to the top of the MEMS. The Si(220) intensity peaks correspond to the lateral side of the gyroscope, shown for the minor and major reflections. Measurement uncertainty is ± 10 MPa.92

Figure 4.29: Strength distribution of the wire bonds in the test space after accumulative testing for the three different localizations in the MEMS device. Averaged experimental standard deviations are: 32 MPa (gyroscope-ASIC), 8 MPa (accelerometer-ASIC) and 20 MPa (ASIC-package). This variation is due to the variable arch geometries, lengths and heights of the wire bonds.93

Figure 4.30: Illustration of a die shear test. The tool pushes the die by applying a force on its side, shearing the die attach until detachment thereof, or until catastrophic failure of the silicon. ICA: Isotropic Conductive Adhesive.	94
Figure 4.31: Die shear results as a function of (upper left) the thermal shocks, (upper right) the vibration, (lower left) 3D dispersion of the experimental points and (iv) 3D surface plot from the experimental points and heat map of the shear force.	95
Figure 5.1: CAD reconstitution of the MEMS device (top view and cross-section views).	98
Figure 5.2: Die attach CAD model and cross-section, extracted from the numerical clone.	98
Figure 5.3: From real sample to CAD model, and finally 2D COMSOL model in the shielded configuration.	99
Figure 5.4: Temperature profile used as input in the FEA study. The first progression and long soak time at 460K corresponding to the initial warm-up and temperature stabilization of the apparatus. Such smooth transition also helps with convergence.	100
Figure 5.5: (top) Meshing of the 2D model. (bottom) Behavior of the aluminum profile in the air flux. Input airstream velocity has been set to 1 m/s.	100
Figure 5.6: Graphical comparison shows the experimental data of temperature recordings in the chamber (solid lines) versus the simulated values (dashed lines).	101
Figure 5.7: (top) Sub-model used for the thermomechanical simulation, (middle) cross-section in the X-Z plane, middle section of the device, (bottom) view of the sub-millimeter fine mesh used. This work plane is set as the starting point of a sweeping mesh with a minimum element size of 0.3 μm	102
Figure 5.8: Spring-dash pots representation of a viscoelastic material in the Generalized Maxwell Model.	104
Figure 5.9: (top) Two-dimensional model of the package-die attach-die stack with locations of boundary conditions. (bottom) Temperature profile used in the 2D model and the analysis points. The horizontal line at 90°C corresponds to T_g	106
Figure 5.10: Cauchy-Green strain tensor element τ_{xy} , depicting shear at four locations in the die attach (neutral line).	107
Figure 5.11: 2D heat maps representing the von Mises stress and volumetric strain in the package-die attach-die stack for several time-temperature values over one thermal shock. Minimum strain and maximum strain and von Mises stress are shown.	108
Figure 5.12: Close-up view of the die attach region to identify the displacement field at regions' boundaries and volumetric strain represented with a symmetrical color range. The time range corresponds to a single thermal shock.	109
Figure 5.13: (left) von Mises stress heat map of the die attach domain. (right) strain plots with exaggerated deformation factor.	110
Figure 5.14: Relaxation of the thermally induced stress past T_g . Compressive shear stress – of similar amplitude – is not displayed for clarity.	111
Figure 6.1: Tentative test program with an accumulative thermal and vibration test step.	116
Figure 6.2: Depiction of the hypothesis to be confirmed by experiment of the effect of "preconditioning" (that is: number of thermal cycles prior to vibrations testing for example) to the lifetime of a set of devices.	117
Figure 6.3: Accumulative simultaneous temperature and vibration testing.	118
Figure 6.4: Accumulative concurrent testing.	118

List of Figures

Figure 6.5: Illustration of a degradation-based data treatment from the accelerometers' signals. Computed from real experimental measurements.....118

Figure 6.6: Mechanical model used for representing the die / die attach / package sandwich, used in FEM. Cross-section of a device used in the present study, with a similar sandwich indicated.119

Figure 6.7: Force-displacement curve for a die shear test.....120

Figure 6.8: FEM stress heat map of the die attach. The square indicated a region of the volume where symmetrical boundary conditions could be applied and still constitute it a representative model.....120

Figure 1.1: Pin-to-pin insulation.....162

Figure 1.2: Pull test for the wire bonds connecting the accelerometer to the ASIC.168

Figure 1.3: Pull test for the wire bonds connecting the gyroscope to the ASIC.168

Figure 1.4: Pull test for the wire bonds connecting the ASIC to the package.....169

List of Tables

Table 1.1: Examples of harsh environment requirements for MEMS.....	23
Table 1.2: Typical values for stresses occurring in near-Earth space [50].	25
Table 1.3: Three models for the prediction of the influence of acceleration factors on the time to failure, or number of temperature cycles to failure. The zero-index indicates the nominal operation conditions while “test” indicates the stress applied during an accelerated test.	27
Table 1.4: Typical launch vehicle environments [111].	29
Table 1.5: Summary table of selected reliability testing performed on MEMS devices and outcomes.	30
Table 1.6: Summary of well-known standards applied for reliability of MEMS.	33
Table 1.7: MEMS ADXL50 accelerometer qualification plan. MEMS accelerometers, such as ADXL335, 3-axis accelerometer, typically have shock survival ratings of 10,000 g in any axis, both when powered and unpowered.	34
Table 2.1: MRS (MEMS Rate Sensor) key requirements and 2008 status.	39
Table 2.2: Datasheet of PRESENS' MEMS pressure sensor.	40
Table 2.3: Criteria for the MUAA.	43
Table 2.4: Comparative matrix for weighing criteria with respect to each other.	44
Table 2.5: Final ranking of the MEMS candidates.	45
Table 2.6: Characteristics of the chosen IMU.	47
Table 2.7: List of tests performed in the frame of the construction analysis and corresponding ESA standards.	47
Table 2.8: Deviation of measured dimensions compared to the datasheet values.	48
Table 2.9: Materials analysis of the devices.	52
Table 3.1: List of equipment.	55
Table 3.2: Non-destructive measurement equipment.	56
Table 3.3: U.S. Department of Defense standards used in MEMS reliability assessment for space application.	56
Table 3.4: European Space Component Coordination (ESCC) standards.	57
Table 3.5: Standard deviation as a percentage of the measured value of gravity (arbitrary unit). Sample size: 30 devices.	60
Table 3.6: Soak times at high and low temperature.	63
Table 3.7: Progression of the thermal load (ranks) in temperature cycles.	64
Table 3.8: Vibration levels and acceleration progression.	65
Table 4.1: Two steps stress test under single parameter loads.	70
Table 4.2: Weibull parameters and goodness-of-fit tests for six variants of data selections.	81
Table 4.3: Tomography tools and main parameters, all with sub-micron resolution.	83

List of Tables

Table 4.4: Fraction of remaining (not delaminated) die attach (CVF-Series) depending on the method used.	85
Table 5.1: Thermal physical characteristics of the materials (from COMSOL's database).	99
Table 5.2: Mechanical properties of the linear elastic materials (from COMSOL's database).	103
Table 5.3: Assumptions in the FEA.	103
Table 5.4: Viscoelastic properties of the die attach isotropic conductive adhesive.	105

List of Abbreviations

AOCS	Attitude and Orbit Control Systems	EU	European Union
ASIC	Application-Specific Integrated Circuits	FEM	Finite Element Modeling
BGA	Ball Grid Array	FMEA	Failure Modes and Effects Analysis
BI	Burn-in	GOF	Goodness-of-fit
CA	Construction Analysis	HALT	Highly Accelerated Life Test
CAD	Computed Assisted Design	HAST	Highly Accelerated Stress Test
CNES	Centre National de Recherche Spatiale (National Center for Space Research)	HRXRD	High Resolution X-ray Diffraction
CNRS	Centre National de Recherche Spatiale	HTOL	High Temperature Operating Life
COTS	Commercial Off The Shelves	HTS	High Temperature Storage
CSEM	Centre Suisse d'Électronique et de Microtechnique (Swiss Center for Electronics and Microtechnology)	IMU	Inertial Measurement Unit
CTE	Coefficient of Thermal Expansion	JPL	Jet Propulsion Laboratory
CVF	Temperature cycles followed by vibra- tion.	MEMS	Micro-Electro-Mechanical Systems
DARPA	Defense Advanced Research Projects Agency	MUAA	Multi Utilities Attribute Analysis
DMD	Digital Micromirror Device	NASA	National Aeronautics and Space Administration
DPA	Destructive Physical Analysis	PCB	Printed Circuit Board
DUT	Device Under Test	RF	Radio Frequencies
EADS	European Aeronautic Defence and Space company	RH	Relative Humidity
ECSS	European Cooperation for Space Standardization	RSM	Reciprocal Space Map
EDS	Energy Dispersive Spectroscopy	SEM	Scanning Electron Microscopy
EPFL	École Polytechnique Fédérale de Lausanne (Swiss Institute of Technology in Lausanne)	ThCy	Thermal cycles
ESA	European Space Agency	ThSh	Thermal shocks
ESCC	European Space Components Coordina- tion	TRL	Technology Readiness Level
ESD	Electrostatic Discharge	Vibr	Vibration
ESP	Electronic Stability Program	VXV	Vibration-thermal shocks-vibration se- quence.
ESTEC	European Space Research and Technology Center	XRD	X-Ray Diffraction
		XVX	Thermal shocks followed by vibration followed by thermal shocks

Chapter 1 Introduction

Micro Electro Mechanical Systems, or MEMS, designate a vast variety of devices capable of sensing and/or actuation. They are complete systems consisting of one or several micro-scale transducers featuring moving parts, interconnects, bonds, and joints as well as packaging elements that are assembled following rigorous cleanliness and/or hermeticity requirements. Generally based on silicon and micromanufacturing technologies, their functioning is relying on various types of physics and complex assembly techniques, which give rise to reliability issues. Reliability in MEMS is a multi-faceted discipline, since degradation or failure can take place not only at the sensing/actuating or packaging levels, but also at the surrounding sub-systems (PCB and electronics elements, interfaces, etc.) enabling the exploitation of the electrical signals by the end-user.

This thesis has been initiated with aim to investigate a new reliability assessment method dedicated to MEMS devices for space applications. There is a strong impulse coming from the scientific and technical community to speak the same language when dealing with reliability. Also, there is an increasing demand for robust and affordable COTS elements from industrial actors as well as institutional structures such as space agencies, with aim to streamline satellite manufacturing and tend to mass production.

Several aspects motivate this research. Firstly, the generation of widely acknowledged standards dedicated to MEMS for space applications is missing. Secondly, currently used methodologies often require lengthy and costly testing campaigns, both in terms of time and resources, hence the need to make reliability testing more efficient. Finally, there is a scientific interest to understand the effects of the accumulation of different environmental loads on devices that are nowadays mostly tested following “one factor at a time” procedures. In this respect, the European Space Agency (ESA) emitted the call for a Ph.D. project with strong industrial ties in the form of the Networking/Partnership Initiative (NPI). This framework has been overseen by ESA and encompasses the Swiss Institute of Technology in Lausanne (EPFL) and the Swiss Center for Electronics and Microtechnology (CSEM). The main aim of this work can be summarized as following:

Investigation of the effects of accumulative thermal shocks and vibration tests on automotive commercial MEMS inertial measurement units. Understanding of the failure mechanisms and the root causes thereof is aimed. A novel reliability assessment method is developed and is followed by in-depth destructive and non-destructive, as well as statistical characterizations of the healthy, damaged, and failed devices, showing the progressive impact of accumulative testing.

This research stands therefore at the crossroads between a fundamental research on materials, microtechnology and statistical analyses, development of novel testing methods for reliability, and the need of standardized methods applied to MEMS for space application – hence an industrial need as main drive. Those aspects are incarnated by the organizations sponsoring the NPI.

Should that be the means of measuring physical quantities or issues arising from assembly techniques, studying reliability of MEMS requires to get a grasp of the world of MEMS and their applications. Section 1.1 starts with a general overview of the world of MEMS, their applications and related environment, with a focus on the community’s definition of “harsh operational conditions”. The scope is considerable and can apply to various levels, should that be at the microscale, package, or system-level. Analytic methodologies also greatly vary depending on the application fields (defense, space, automotive, consumer electronics, etc.) and on the chosen strategy (laboratory testing or numerical methods). The teeming interest in MEMS technology emerges from their qualities: wide range of applications and functionalities as well as their inherent advantages such as small footprint, low power consumption, and robustness for the most mature ones. These advantages are attractive in the case of the space field, but their use is still posing challenges [1]:

- Uniqueness and complexity of MEMS devices.
- Lengthy and costly qualification for space applications.

- Questioning regarding the qualification of a new and unique device (or a very small sample size).
- Methodology for re-qualifying (de-rating) COTS devices for space are being developed.
- Tolerance to risk: if a reliable but lower-performing non-MEMS component with a greater background of reliability data is available, it will be preferred.

Section 1.2 covers the use of MEMS in space applications and the key-factors and challenges arising from the space environment. Despite the large amount of research and investigations performed on MEMS, and regardless of their proven or potential long-term performances (typically such as the commercial components used on Swisscube [2]), the international landscape of standards lacks tools and methods to evaluate the reliability of highly robust devices in a conclusive manner, since single parameter testing often does not yield more than a “pass” as outcome.

Space agencies and space-hardware manufacturers constitute a rather conservative field for which “old but proven” systems are preferred over newer and sometimes more performant technologies. Requirements on weight and volume in the budgets of a space mission can certainly benefit from a larger implementation of MEMS technologies, especially in systems that nowadays rely on bulkier instruments. MEMS can, such as NASA’s James Webb Space Telescope and its micro-shutter array, become mission enablers. This lack of trusted and established knowledge on MEMS reliability partially comes from the absence of methods acknowledged by the space community. These aspects are presented in a literature review in Section 1.3, which develops the classical approaches to testing for reliability, the subsequent failure mechanisms in MEMS and ultimately the reason why traditional testing methods miss to properly assess highly robust devices.

Finally, Section 1.4 covers the state-of-the-art of non-classical approaches to reliability testing. “Non-classical” designates testing procedures that go beyond the traditional *one parameter at a time*, single-stress level conditions that are typically used in reliability procedures. The focus is on accumulative testing: parameters of different natures, such as thermal and mechanical loads, are combined either in a sequential or in a simultaneous fashion, aiming at better representing operational conditions. The scarcity of the research performed in this field, and a preponderance of works with qualitative results and observations demonstrate the need of a synthetic, more comprehensive approach to accumulative testing on MEMS. Key findings from this literature review are summarized in Section 1.5.

1.1 The world of MEMS and their applications

Micro Electro Mechanical Systems (MEMS) have been increasingly studied over the last 30 years, with success stories like the DMD (Digital Micromirror Device) [3],[4], gyroscopes [5] or accelerometers [6],[7] that are widely used nowadays. Such devices feature compactness and energy efficiency, enabling countless fields of applications in today’s everyday life. They especially shine in domains such as automotive, defense, medical or consumer electronics, thanks to their mass production capabilities insuring low cost applications [8]. The continuous developments in these fields pushed the boundaries of technology for integrating *more on less*, with higher sensitivity, signal-to-noise ratio, reliability, and variability thanks to progresses achieved in microfabrication techniques and characterization methods. Historically, the invention of the first bulk-etched silicon technologies performed at Bell Lab in the late 1950s [9] – beginning of the 1960s [10], enabled silicon (and other semiconductor materials) microfabrication that is widely used nowadays. The first occurrence of a MEMS device began in 1965 with a resonant gate field effect transistor designed at Westinghouse Research Labs in Pittsburgh (USA) by Nathanson and Wickstrom [11]. It then took 25 years for MEMS to evolve from technical curiosities to the commercial world [12]. Supported by further advancements in bulk micromachining, the development of the first MEMS pressure sensors or inkjet nozzles appeared in the 1970s [13] and generated billion-dollar market in 2007 [14]. Accelerometers are nowadays commonly adopted sensors: in cars, smartphones, airplanes, drones, machinery, etc. They opened new fields in demanding applications [15], [16] thanks to their high-performance/high-reliability characteristics [17]. MEMS gyroscope [18] and oscillators (in particular in high relative humidity and high-g environments [19]) are other families of devices that demonstrated good performances, especially in harsh environments. Spectacular examples of MEMS technologies are existing nowadays, such as deformable mirrors [20] or insulin micropumps (Figure 1.1).

A market overview of the MEMS landscape in 2016-2017 is provided in Appendix A.

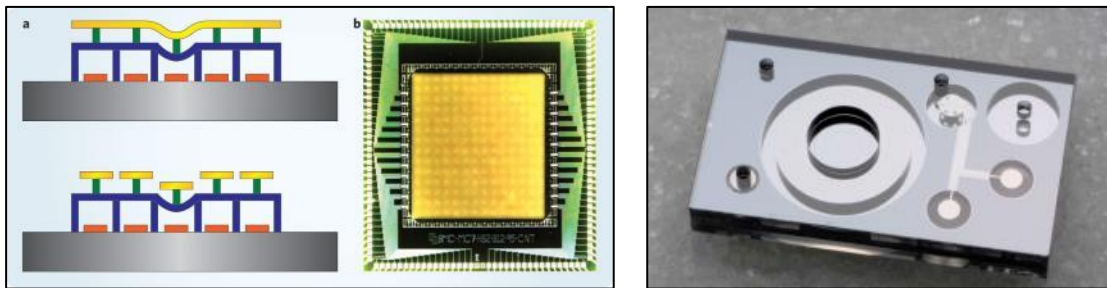


Figure 1.1: Deformable micromirror (left) and insulin miniature pump (Nanopump, courtesy to Debiotech Switzerland).

MEMS cannot be operated or controlled alone. They are constituents of a functioning device's many subsystems, fulfilling different types of roles that together provide clear benefits such as a high compacity in overall footprint for a fully integrated sensing system, while relying on a low power consumption and low mass [14], [21]–[24]. General properties of MEMS are listed:

- Sensing of physical signals such as temperature, accelerations, rotations, pressure, etc.
- Actuation of active element as in micromirrors, gyroscopes, RF MEMS, resonators, etc.
- Application-Specific Integrated Circuit (ASIC): enables electronic (analogic) signal processing from the MEMS to digital information exploitable by a data-acquisition system or a computer.
- Electrical connections: wire bonds, ball-grid arrays.
- Structural joints: metallic solders, conductive or non-conductive adhesives, glass-frit.
- Packaging: silicon casing of MEMS structures and subsystems. Can contain electrical tracks, gel (covering subsystems for damping or corrosion resistance), overall protecting constituents of the device from the external environment, permitting safe handling.
- Materials: silicon dies for the MEMS; thermoset, glass, or metallic joint materials; gold wire bond; silicone gel; ceramic, polymeric or metallic package.

Historically, defense applications have led to thrusts in technologies, where high performance for best possible efficiency and reliability are aimed while cost considerations are deemed less prominent during tradeoff processes. Typically, artillery projectiles and rockets require draconian reliability figures in operational requirements, such as temperature exposure, thermal cycles, pressure, humidity, acceleration and vibration [25], [26]. Orders of magnitude are given in Table 1.1 as an example of “harsh conditions” for reliability testing in MEMS technologies [15]. In the 90s, the U.S. Government and state agencies (such as DARPA) started to envision use of MEMS in air force and defense, in addition to NIST which started to support foundries in their evolution. Demonstrators were built in aerospace with examples such as Mighty Sat 1, Shuttle Orbiter STS-93, the DARPA-led consortium of the flight of OPAL (Orbiting Picosatellite Automatic Launcher), and the suborbital flight on Scorpius 1 (Microcosm). In less than a 10-year time frame, MEMS advanced to a full, regimented, space-grade technology [22].

Table 1.1: Examples of harsh environment requirements for MEMS.

Vibration	40g RMS
Shock	40'000g
Temperature	-40°C...200°C, sometimes >500°C
Environment	Radiation, ESD, chemical, biological hazards, vacuum...
Security	Reliability, safety (communication)

Several ground-based applications that are constrained by harsh environmental conditions and mission profiles are well-studied, such as shock impacts in handheld devices [27]–[29]. Analyses in these works demonstrated the great variety of failure modes that can occur in MEMS, and the difficulty to adequately predict them: sensor structural damage, ball grid array (BGA) solder or wire bonds fractures, MEMS detachment from the substrate. The automotive industry is also, for nearly 30 years, widely using MEMS in their products with hundreds or more devices embarked on a modern car, for applications such as tire or engine pressure monitoring [7]. They need to endure various heavy-duty conditions [30] such as salt, technical fluids, humidity, fuels – added to the aforementioned operational requirements. Usages in automobile range from pressure sensor to accelerometer [31], gyroscopes [32], [33], power electronics [34], telecommunication [35], RF-MEMS [36] or microphones [37], [38]. Several literature references cover

concrete examples of security systems in automotive, such as the Electrical Stability Program (ESP) and Anti-lock Brake System (ABS). Reliability and environmental aspects for these systems feature among the most demanding earth-bound applications [39]–[41]. Others examples of applications can be cited, such as a capacitive pressure sensor for high vacuum and biomedical application [42].

Overall, it is visible that MEMS are extremely versatile systems that can operate in various kinds of environments and operational conditions. Most papers are highlighting their robustness in dedicated applications such as defense, automotive or handheld devices. Reliability is either tested for a given use case, or following widely accepted or legacy standards, some of them becoming obsolete as newer technologies develop and outperform the previous generations both in terms of performance and robustness. This is mostly due to the slow renewal cycles of standards and thrusts in technology. Also, standards nearly exclusively consider single parameters (or one factor at a time testing) or similar testing at a higher temperature (for example, the 85°C/85%RH temperature/humidity test) to assess reliability. While being good reference points, these benchmarks miss to represent real-life operation, where several natures of stresses are taking place and can lead to combined effects. One can typically think of thermally activated phenomena: how are vibrations acting on a device experiencing or having experienced thermal loads? This kind of questioning becomes especially stringent when dealing with the most inhospitable environment an engineer can think of: space. Future missions relying on reusable hardware will need to be designed taking these considerations into account.

1.2 MEMS in space application

Space is one of the most challenging environments a device can operate in. Early on, the attractiveness of MEMS in this field arose due to their compact footprint, low mass, and low power consumption. Price can also be lower for space missions due to the high price-per-kilo tag for space launchers. For example, in 2018, the estimation for the European Ariane 5 rocket is 8,900 USD per kilo for a Low Earth Orbit launch (based on the maximum payload capacity and rocket unit cost) [43]. Already in 1994, a micromachined miniature bioreactor (Figure 1.2) has been flown on the Space Shuttle, in the frame of the International Microgravity Laboratory (IML-2) mission [44]. In 1998, Janson *et al.* covered the possible applications of MEMS inertial sensors in micro-propulsion, guidance, navigation and control (GN&C) [45]. A famous application of a commercial MEMS accelerometer is the Mars Microprobes mission, a piggy-back experiment on the Mars Polar Lander [46]. Moreover, a pressure sensor has been evaluated at NASA Glenn Research Center for measuring airflow of inlet compressor of a turbofan propulsion system [47]. The variety of application cases of MEMS in space typically benefit from the miniaturization of scientific equipment, in highly focused space missions, or for pico- to micro-satellites [48], [49], which demonstrate the capabilities of MEMS as cost reducers or mission enablers.

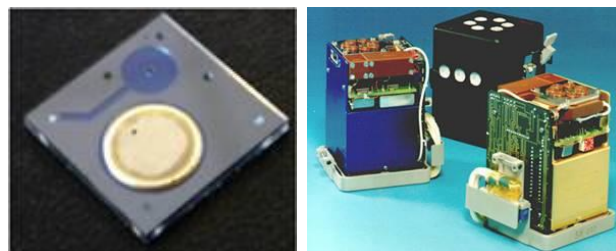


Figure 1.2: (left) View of the 22mm x 22mm micropump, (right) engineering model of the space bioreactor mounted on the base of a Type II experiment container [44].

Putting aside the question of accuracy and sensitivity, the greatest concern relies in their reliability during a spacecraft pre-launch (especially humidity¹), launch (shocks and vibrations) and commissioning phases in the inhospitable environment of space (thermal loads and radiations) which can lead to catastrophic effects on hardware. Table 1.2

¹ For context, European Space Agency's spaceport is based in Kourou, French Guiana. It features a tropical climate, hence high humidity. In principle, spacecraft and its components are safely stored in controlled environments throughout production, transit, and assembly.

summarizes typical values present in the space environments, which dictate the type of requirements defining reliability testing [50].

Table 1.2: Typical values for stresses occurring in near-Earth space [50].

Stress source in space	Typical value
High vacuum	10^{-7} mbar
Large temperature deltas when exposed to the sun or obscured from it	$\pm 100^\circ\text{C}$
Ionizing radiation	425 $\mu\text{Sv/d}$ ionizing
Ionospheric plasma in Earth's vicinity	Charging down to -140 V

This combination of harsh environmental conditions in space restricts the panel of devices that can be used in such applications. The dual-axis accelerometer ADXL250 from Analog Devices is an example of a well-studied, space-flown commercial MEMS device [51], [52]. In these papers, distinct sets of 10 devices were tested: 1,000 thermal cycles between -65°C and 150°C were performed on one set, 30,000 mechanical shocks at 2,000 g (out-of-plane direction) on a second set, and a third set experienced 10,000 shocks in one in-plane direction. A single failure, likely caused by a defect in the sealing glass, was observed in one device after 10,000 shocks in the out-of-plane direction. Otherwise, only minor parametric changes were observed, demonstrating their robustness. The sample size was however little.

Space agencies' interest for MEMS technologies has been documented, with establishments of guidelines by NASA already in 1999 [52], or by CNES with several works about the wide panel of characterization techniques dedicated to failure analysis of microsystems and reliability methods [53]–[55]. The European Space Agency (ESA) has manifested its interest for MEMS gyroscopes and their potential use in space missions, and more generally for using COTS components in ESA Space programs [56]. While the need of commercial components in space is nowadays undisputed, the remaining question relies in their appropriate usage for given space mission profiles in terms of safety, reliability, and availability [57] as well as suitability [58], [59], since robust MEMS designed for earthbound applications would face other risks in space such as mentioned in Table 1.2.

Most of the space hardware flying on missions is generally not reused, to the notable exceptions of the Space Shuttle and SpaceX's rockets and spacecrafts in more recent times. MEMS that have been used for redundancy, for instance, on launch vehicles, cannot be studied on the long term and after their end-of-life, since they are disposed of or burn down in the atmosphere during reentry. Case studies exist nonetheless, in particular in the world of cubesats, where low mission costs and draconian requirements on weight and footprint apply. MEMS are typically used in universities-built cubesats where a higher risk is still tolerable, and missions precisely enabled thanks to MEMS. There are already a few examples of missions designed as MEMS test beds *e.g.*, Delfi 3C (TU Delft, 2008), PRISMA (ASI, 2010), or OPAL (Stanford, 2000). For example, the high reliability of commercial MEMS has been demonstrated by the long term mission of SwissCube (flying since 2009), insuring their suitability for small scale space missions thanks to a hard selection and redundancy [2].

MEMS for space application face a wide range of challenges for succeeding at passing screening and qualification steps imposed by agencies and regulatory institutes. In the case of COTS components, the procedures were initially developed for ground-based applications, which cause several challenges in terms of reliability due to the non-uniqueness of failure modes that can take place [60]–[64]. A recent work done by Osiander *et al.* (2018), treating of MEMS and microstructure in aerospace applications, features a synoptical review of the best current and past practices for reliability [12]. Recent developments have been done in the frame of an industrial cooperation including ESA which serves as the starting point for the present research. A two-step load stress methodology has been compiled in technical memorandum, dedicated for the harsh space environment mainly focused on thermal shocks, vibrations or mechanical shocks [65].

However, these works do not divert from the traditional single parameter testing, while the space environment and operations can feature several stress loads in conjunction. The lack of widely accepted standard applying to MEMS for space application has also an influence on how the research is performed. Researchers are building their own test plans based on launch models, physics-of-failure or standards applied from the microelectronics field. Results cannot always be compared beyond the observational fact that commercial MEMS are robust or display similar failure modes, as equivalent comparison points and thorough understanding on large groups of samples are often lacking.

1.3 Testing for reliability: classical approach for MEMS-based devices

Reliability testing aims at accelerating failure in devices by overstressing them beyond their nominal operating domain. Moreover, it aims at creating failures, under a replicable environment that is designed to represent at best conditions in which the device will operate. And thus, the goal is to reveal design weaknesses before they arise while in operation. In other terms: testing aims at accelerating a failure that would otherwise take place in experimentally unmanageable time scales and generate insights that can be fed back to the designer for improvements on the device. The concept of accelerated testing is therefore to compress time and trigger the failure mechanisms so that a device lifetime can be assessed in a timely fashion by the engineer [66].

It is clear from the plethora of materials and assembly techniques exploited in MEMS technology that devices will experience various physics of failure and root causes. MEMS reliability attracted a lot of attention since the years 2000s and earlier with various general works [67]–[69] and comprehensive reviews giving general scopes of MEMS reliability [70]–[72], and also more recently such as contribution of Skogström *et al.* [38] Su *et al.* [74]. Overall, it is no less than three decades of testing and elaboration of procedures that were studied and reported in the literature.

Space, due to its inhospitable environments, required definition of specific strenuous tests for components. In 1999, Stark at NASA [75] elaborated the *MEMS Reliability Assurance Guidelines dedicated to space applications*. Test sequencing is designed to accurately simulate the environment sequence that flight hardware must endure. The sequence corresponding to a rocket launch compiles vibration, shocks due to pyrotechnics, acoustic stress – followed by thermal vacuum. During spaceflight typically, the hardware can be exposed to intense radiations and temperature extremes, which can irremediably damage the electronic materials necessary for a well-functioning of a system.

In 2000, testing infrastructures and methods dedicated to the field of MEMS were elaborated by Tanner *et al.* in the case of defense applications [76]. This report features a thorough reliability analysis on temperature cycles, mechanical shocks, vibration, humidity, and storage life. Even though most of the experiments were performed on MEMS micro engines, Tanner suggested that the discovered failures modes can be generalized to any MEMS device. This report features a comprehensive approach that represented a major milestone in the developments linked to single parameter testing and failure modes and effects analysis. It is widely cited in the world of MEMS reliability still nowadays, and recurrently constitutes the starting point of the developments made in reliability testing.

1.3.1 Failure mechanisms in MEMS

A widely referred phenomenon that can provide a physical explanation to failure is the Arrhenius thermal activation laws. A vast amount of situations have proven to be empirically described by an Arrhenius equation: failures modes in integrated circuits, LEDs, adhesive bonds, or lubricants typically [77]. Those thermodynamical relations between failure modes and external factors are reported in Table 1.3 and can apply to several conditions. As for an exemplification, one can imagine that a MEMS device’s Achilles’ heel is the adhesive insuring hermeticity of the package of an initially controlled sensing environment. This adhesive is sensitive to high temperature, so that its failure rate will be accelerated as temperature increases.

For the demonstration, an activation energy of 0.5 eV is assumed [78]. Two temperatures are defined as $T_0 < T_{stress}$, with T_{use} the nominal operational temperature is 25°C (298.15 K). Instead of assessing the adhesive’s lifetime at room temperature (which might require experimentally unpractical time scales), a test is performed at a high temperature, say $T_{stress} = 190^\circ\text{C}$ (463.15 K). Failure rate is expected to be higher – or *accelerated* – at higher temperatures. Therefore, the equation in Table 1.3, for a simple thermally activated phenomenon, yields:

$$AF(T_{test}, T_{use}, E_a) = \exp\left[\frac{0.5}{8.617 \cdot 10^{-5}} \left(\frac{1}{298.15} - \frac{1}{463.15}\right)\right] = 1026$$

Table 1.3: Three models for the prediction of the influence of acceleration factors on the time to failure, or number of temperature cycles to failure. The zero-index indicates the nominal operation conditions while “test” indicates the stress applied during an accelerated test.

Mechanism (model name)	Failure rate dependance	Acceleration factor	Comments
	$R(T)$	$AF(T_{test}, T_{use}, E_a) = \frac{R(T_{test})}{R(T_{use})}$	
Temperature (Arrhenius)	$A_0 \exp\left(\frac{-E_a}{k_B T}\right)$	$\exp\left[\frac{E_a}{k_B}\left(\frac{1}{T_{use}} - \frac{1}{T_{test}}\right)\right]$	A_0 : arbitrary scale (frequency) factor [-] E_a : activation enthalpy [eV] $k_B = 8.6175 \cdot 10^{-5} \text{ eV} \cdot \text{K}^{-1}$ (Boltzmann constant)
Temperature and humidity (Peck)	$A_0 RH^{-N} \exp\left(\frac{-E_a}{k_B T}\right)$	$\left(\frac{RH_{test}}{RH_0}\right)^{-N} \exp\left[\frac{E_a}{k_B}\left(\frac{1}{T_{use}} - \frac{1}{T_{test}}\right)\right]$	RH : Relative Humidity [%] $N \sim 2.7$ (humidity coefficient) [-]
Thermal cycling (Coffin-Manson)	$C_0 \Delta T^{-n}$	$\left(\frac{\Delta T_{test}}{\Delta T_0}\right)^n$	C_0 : material dependent constant $\Delta T = T_{max} - T_{min}$ [K] (temperature range) $n \sim 2.5$: empirically determined constant [76]

An equivalent way of understanding this value: if a failure phenomenon occurs at 190°C after 1 hours, in real operating life the equivalent failure rate would be a little more than 42 days. As it can be seen the equation strongly depends on the value of E_a : if the activation energy were 0.7 eV, AF would be 16 times greater.

More sources report the use of accelerated aging models in the case of MEMS. Caruso and Dasgupta [79] presented an overview of accelerated aging analytical models. Fung [80] reported the an industrial application of an accelerated aging study with very applicative examples and acceleration factors for specific failure modes. Oppositely, the study of Łuczak *et al* [81] considered a fully natural aging under bias at normal laboratory conditions for the evaluation of a true reliability of COTS accelerometers with failure taking place after 4.5 years of continuous operation. Humidity is often combined with high temperature (such as the well-known 85°C/85%RH standard) for accelerating aging, leading to surface phenomena such as adhesion in MEMS devices [82].

The variety of testing combined with multiple types of materials, assembly techniques, and involved physics in MEMS leads to inasmuch failure mechanisms. They can be categorized as follows: (i) silicon related, (ii) packaging related, and (iii) supporting electronics related. The first category focuses on the sensing or active element of the MEMS, often movable and prone to specific types of failure mechanisms as displayed in Figure 1.3 [83]. Packaging and electrical failure on the other hand can happen while the MEMS' silicon organs remain untouched. Loss of hermeticity, bonding failure of a thermally and/or electrically conductive adhesive, wire bond rupture, or package breakage are different ways a component can fail (Figure 1.4) [84].

Failures in MEMS in their various forms are well-studied topics of research and are often hardly generalizable to all kinds of MEMS technologies. Failure mechanisms were notably studied for categorizations of processes and in-use physics occurring at different systemic levels or processes implicated in the manufacturing and life of devices (micromachining, CMOS processes, in-use faults) and various superposed natures of intrinsic faults, such as: short-circuits or stiction, diffusional or electrostatic issues, structural, or material failures [83], [85]–[90]. Hartzell *et al.* [91] comprehensively covered the science and best practices relative to MEMS reliability: the chapter “Lifetime Prediction” focuses on important concepts used in the present work, such as: Weibull probability of failure, bathtub curve (infant mortality), cyclic fatigue, fracture due to shocks and vibration and the related root causes, and failure analyses. Another comprehensive book on the matter has been published by van Spengen *et al.* [92], inspired from an earlier work on reliability of MEMS from a failure mechanisms perspective [87]. Ramesham [47] made a review of key failure mechanisms: wear and stiction of MEMS microstructures. Stiction is an electrostatic fault where, for example, the fingers of a capacitive accelerometer's comb drive sticks to a nearby surface due to electrostatic adhesion (due to a mechanical shock for instance) and are not able to measure capacitive signals anymore. Delamination of bonding layers is another major problem covered in this paper, with packaging being also a source of failure. Such events can lead to the loss of protection or integrity of devices. In vacuum operated sensors – such as the resonating structure of a gyroscope, damping linked to loss of hermeticity or sealing, will negatively affect device performances. Man [93] provided a thorough review of failures modes in MEMS and the underlying physical phenomena in the case of space applications. In this paper, the author also proposed a path to elaborate a finite element model and numerical

simplifications that are exploitable to render MEMS reducible for modelling. Kayali *et al.* completed this hardware-oriented work by an article on common reliability and qualification practices and methods related to the utilization of COTS microelectronics for qualification in critical space applications, with an exemplification of common environmental challenges [58].

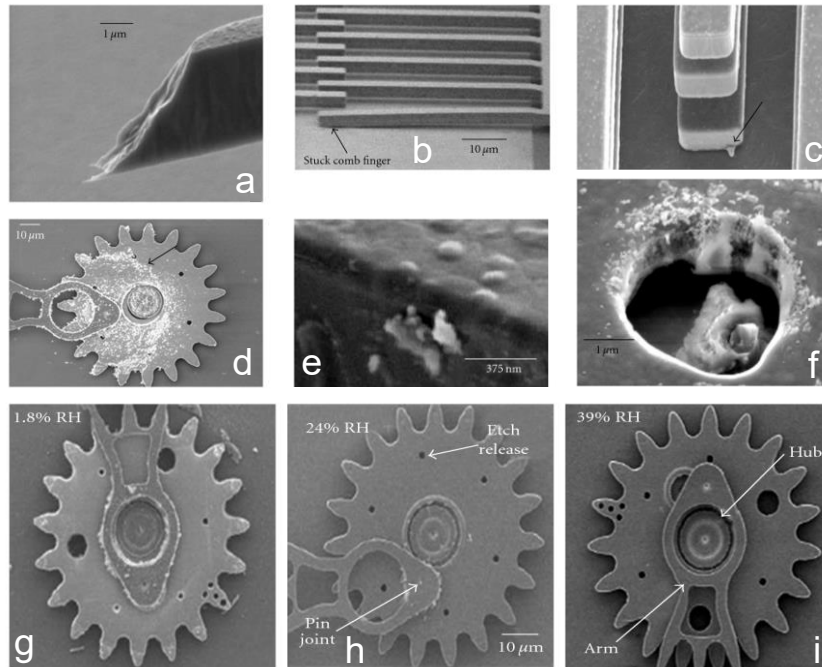


Figure 1.3: Selection of failure in MEMS silicon structures. (a) Surface fracture, (b) stiction in MEMS fingers, (c) Electrostatic Discharge (ESD) in an electrostatic actuator, (d) wear debris in the micro-engine, (e) particle contamination on MEMS, (f) surface wear in drive gears, micro engine gear under humidity stress at (g) 1.8%RH, (h) 24%RH, (i) 39%RH [83].

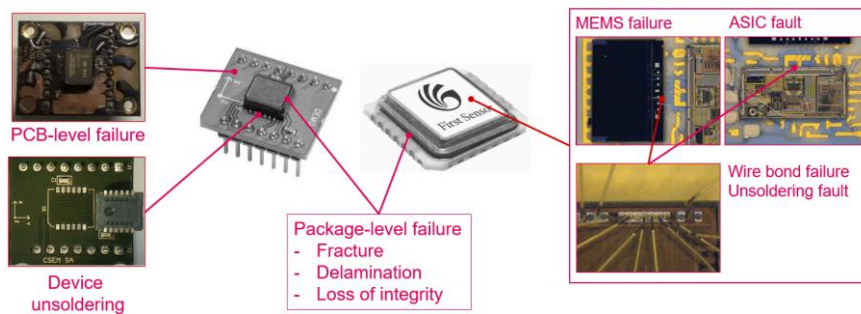


Figure 1.4: Overview of the main sources of failures in MEMS devices [84].

Numerical simulations are useful in thermally variable environments and are also widely used in application to MEMS. A handful of examples are given here. For example, it can help to predict thermal stress occurring in devices due to the mismatch between the numerous materials being joined together in a MEMS-based system. Such typical interfacial failures under thermal fatigue loads in multi-layered structures were studied by Maligno *et al.* in [94], further refined to investigate delamination by mean of FEM [95]. Multilayered materials are typical for MEMS technologies, where dissimilar materials are joined to create functionality or protection against the environment. Such complex structures need to be thermally modeled in order to guide designs toward thermally resilient systems, for example in the case of the porous alumina-based thin film package for MEMS developed by Zekry *et al.* [96]. Thermal fatigue is also a concern for MEMS gas sensors, as showed in the work of Puigcorb  *et al.* [97]: a hysteretic behavior with strain amplitude of 0.8% and stress amplitude of up to 700 MPa can be observed in thin metal films. The die attach, for example in the pressure sensor studied by Meyyapan *et al.* [98], is subjected to intense stress levels due to coefficient mismatch on the two sides of the adhesive's layer, also studied in the case of a pressure sensor by Krondorfer and Kim [99]. Several works focus on accelerometers and countermeasures to cope with temperature effects [100], [101], FEM helping to design and optimize thermally robust devices [102]–[105] and analyze thermal drift [106]. From these

numerous examples, FEM and MEMS are closely linked and benefit from the understanding of the multiphysics that are taking place.

A synoptic view of a selection of literature references treating of the testing and failure analysis of common or specific MEMS devices is reported in Table 1.5. They are often multidisciplinary and focus on several stress loads and natures of tests. While the previous paragraphs show that MEMS structures alone are well studied subject on both the theoretical and experimental fronts, package reliability is often designated as the culprit in MEMS reliability. MEMS packaging accounts for 79% of the failures under shocks and impact loading, as depicted in Figure 1.5 [107]. This is corroborated in Marozau's work [65].

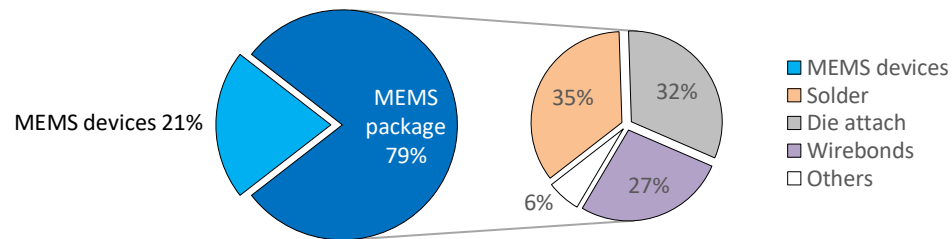


Figure 1.5: Pie chart of failures of MEMS under severe shocks and impact loading [107].

1.3.2 Harsh operating environments and relevant test methods

Out of the various harsh environments that a MEMS device can experience, mechanical shocks and impacts, as well as exposure to high operational temperatures, induce stresses that impact their lifetime and reliability. In the following paragraphs, the literature review continues with the most relevant tests that are performed for studying reliability: mechanical shocks and vibration, and thermal cycles and shocks, and key numbers.

Mechanical shocks testing is a well-studied area in microelectronics and MEMS, with common fields of application in consumer electronics [27], automotive [108], military, and space [25]. Patel *et al.* [18] summed up the variety of failure causes from the MEMS perspective: fracture of microstructures due to excessive stress, stictions of comb drives, particles blocking movable elements, short-circuits between contact parts, or package failure (interfacial debonding or hermeticity failure) can be mentioned. High-g shock levels or sudden drops can induce cracks in sub-systems, possibly breaking off small pieces from the suspended silicon structures that may cause either short-circuits or block the movement of vibrating masses, such as in gyroscopes [109], [110].

Military developments drove a very intensive research on the effects of shocks on MEMS: typical relevant values for mechanical shocks are above 2000 g's and thermal cycles from -65°C to 150°C. Such thermo-mechanical loads are also met in the case of space applications, as covered by the works of Sharma [51] or Ghaffarian [52]. A study case is the challenging dynamical environment that takes place during a rocket launch sequence (Table 1.4) [62], [111], [112].

Table 1.4: Typical launch vehicle environments [111].

	Acoustics	Random vibration	Sine vibration	Shocks
Lift-off	x	x		
Aerodynamics / Buffet	x	x		
Separation (stage, fairing, spacecraft) / pyrotechnic bolts				x
Motor burn / Combustion / Pogo		x	x	

Experimentally, shocks can be performed on a pendulum, or a tower equipped with an impactor, on which a device under test (DUT) is fixed. The impactor is elevated at a given angle or height, from which it is released to hit a target made of various materials: composite, hard or soft polymers, or a metallic bumper with optional mitigating (cushioning) materials. The shock pulse shall be a half sine waveform, as mentioned for instance in MIL-STD-883 Test Method 2020. Several papers have investigated techniques and equipment used to perform shock tests on MEMS devices, either on methods themselves [33], [113] or on study cases, such as handheld devices [28].

Table 1.5: Summary table of selected reliability testing performed on MEMS devices and outcomes.

Legend		Acoustic = acoustic test, HTOL = High Temperature Operating Life, HTS = High Temperature Storage, Life = Life Test, LTS = Low Temperature Storage, MShocks = Mechanical Shock, NAg = Natural Aging, Rad = Radiations, RH = Humidity, TShocks = Thermal Shocks, TC = Temperature Cycling, Vibr = Vibration, TVac = Thermal Vacuum			
Ref.	MEMS type	Nature	Tests	Standard	Comment
[76] [109]	Micro engine	Custom	Life, MShocks, RH, TShocks, Vibr	Not mentioned.	No detrimental effect of thermal tests. Mechanical shocks: majority functioning, wire bond damage at 4 Kg, structural damage at 20 Kg and package failure at 40,000g. Vibration: 3/4 th of devices survived with no apparent damage. Only humidity lead to wear intensification and failure.
[114]	Micro engine	Custom	Vibr	Not mentioned.	Test under white noise condition over the range 20-2000 Hz with RMS acceleration of 40g (peak 120g). 2/19 micro engine failures after movement of slivers of debris were observed without consequence on the functionality of the device.
[51]	Accelerometer (capacitive)	COTS	MShocks, TC	Not mentioned.	No failure, minor parametric drift after 1000 temperature cycles from -65°C to +150°C and to 30,000 mechanical shocks of 2000g in the Z-direction and 10,000 in the X-direction of the component.
[52]	Accelerometer (capacitive) & thermometers	COTS	TC, MShocks	Not mentioned.	TC: up to 1000 cycles on the maximum range -65°C to +150°C. No significant change was observed on the devices. MShocks: over 34 devices, one only failed at 10,000g while all others sustained 30,000g with only minor change in electrical parameters. In the failed device: presence of free particles inside the cavity due to a damage found in the sealing glass of the device. Additionally, a particle was found jammed in the comb drive of the Y-accelerometer MEMS.
[65]	Accelerometer (capacitive)	COTS	MShocks, Pressure, Rad, RH, TShocks, Vibr	MIL-STD-883	No silicon failure. Only package-linked failure occurred (interconnects and ASIC). Three commercial devices were tested. Maximum ΔT for the thermal part is -65°C to 250°C. Mechanical shocks up to 5000g. Vibration are performed over the range 20-2000 Hz up to 41.6g. Pressure cycling up to a delta of 6.75 bar. Humidity resistance tested at 85°C/85%RH. Radiation: up to 110 krad under gamma exposure, 100 krad under proton exposure.
[81]	Accelerometer (capacitive)	COTS	NAg	Not mentioned.	4.5 years of testing, natural aging led to a decrease of accuracy, ultimately to failure. Root-cause is unknown, rendering the study inconclusive.
[115]	Accelerometer (capacitive)	Custom	HTOL, HTS, MShocks, TShocks, TC, Vibr	MIL-STD-883	7 failures over more than 4700 samples. Mostly due to shocks and one only due to thermal (HTOL) condition.
[113]	Accelerometer (capacitive & piezoresistive)	COTS	MShocks	Not mentioned.	Capacitive accelerometer tested in comparison to a piezoresistive reference. Deviations in the measured accelerations are superimposed for the comparison. A series of accelerometers displayed delamination which directly led to fracture of the silicon elements at 70,000g. Another series displayed failure at 30,000g with failure of the seismic mass of the MEMS and catastrophic lid detachment.
[116]	Accelerometer (unknown type)	COTS	HTS+Vibr (combined), HTS+Tilting (combined)	Not mentioned.	36 accelerometers tested: (i) vibration at 85°C and 145°C for 200 hours, (ii) tilting under bias at 25°C, 100°C and 125°C for 1000 hours. For test (i), no visible degradation at 85°C, very small performance degradation at 145°C. For test (ii), no failure occurred. Assumption of a "worst case" failure right after the interruption of testing, the failure rate is calculated at $6 \cdot 10^{-8}$ hours ⁻¹ .
[18]	Gyroscope	Review paper	MShocks, Vibr, Acoustic, TC, RH	JESD22-B111 (shock/drop)	Shock test at 35,000g with variable outcome. Failure occurred at bonding interfaces. Vibration at 9G from 15-55Hz without failure. Acoustic environment: 130 dB at 20 kHz caused signal failure (proof mass resonance frequency). Thermal cycling caused rate drift or signal failure for the range: 25-150°C. Humidity caused package (glass frit) failure and performance degradation.
[33]	Gyroscope	Unknown	RH, MShocks	JESD22-A101-B (humidity)	Humidity: 85°C / 90%RH for 167 days. 11/27 transient device failures with 10 occurring below 50 days. Short circuits caused by moisture, desorbed after the test. Shock test: cracking at the borosilicate glass layer (70%), silicon cracking (16%). Electrical failures occur between 3900-4200g and package failure above 8 kg.
[117]	Gyroscope	COTS	Life, MShocks, RH, TC, TShocks, TVac, Vibr	Not mentioned.	Failure observed for thermal shocks, important impact of life test on performance. Good survivability under mechanical tests (shocks and vibration).
[118]	IMU	COTS	Vibr	MIL-STD-810	Based on Allan variance calculation and observation of physical failure. The main reliability problems are related to the electrical component connections, circuitry anchoring, and external frame flexibility. Vibration was operated between 15 and 2000 Hz with maximum PSD of 0.266 g ² /Hz.
[41]	Microphone & gyroscope	COTS	MShocks (microphone) TC (gyroscope)	Not mentioned.	Shock impacts are performed up to 70,000g. The microphones were functionally tested acoustically. Gyroscope were powered periodically while testing for characterization. This paper covers only the reliability testing method.
[37]	Microphone	Unknown	MShocks	Not mentioned.	The microphone's diaphragm cracked or detached following 65,000g shock pulses in the out-of-plane axis of the MEMS.
[119]	Microphone	COTS	HTOL, LTS, RH	Not mentioned.	HTOL: 125°C at 3.3V bias for 600 hours. LTS: -35°C for 300 hours, no effect. Humidity: 85°C and 85%RH at 3.3V bias for 400 hours, outcome is significant signal deviation due to electrochemical corrosion. Overall, the impact of high temperature and humidity is important on the IC connected to the MEMS
[120]	Resonator	Custom	MShocks	Not mentioned.	Two series of experimental devices were designed for high-g applications: a tuning fork resonator and a stiction test structure. The resonator device survived to 20,000g, despite repetitive shock pulses. The stiction device detected a slight increase in the stiction force following high-g impacts, while the non-contact behavior remained stable.
[121]	Pressure sensor	COTS	HTOL, LTS	Not mentioned.	Low temperature storage at -35°C for 120 days. High Temperature Operating Life at 125°C for 120 days under a 3.3V bias. Incremental damage leading to a drift of the signal with respect to ideal values in both cases. LTS samples appeared to have much severe damage after prolonged storage at sub-zero temperatures than at high temperature. Measure output done in low vacuum at 640 mmHg and at atmospheric pressure. Damaged also recorded on the test boards. ASIC related damage in the device: burn sites and crack sites.

A paper of interest from Hokka *et al.* addressed the shortcomings of standard shock testing in microelectronics. They performed shocks with a travelling table equipped with a pneumatic device, to fit at best the shock pulses waveform defined in the JESD22-B110A and JESD22-B111 standards at accelerations up to 2900g. This paper also demonstrated the effect of mechanical shocks in commercial portable electronic products, showing that forces generated by drop impacts make component boards inside of products bend and vibrate rapidly, which may induce failure unrelated to the MEMS component itself [122].

Reliability with respect to mechanical shocks is often accompanied by Finite Element Modeling (FEM), which provides insights on resonant phenomena and other stress concentration sites. Li *et al.* used a pneumatic impactor for generating a shock impact up to 80,000g on a MEMS microphone [37] as well as for a gyroscope [110]. In those cases, FEM is used to predict and understand the concentration of stress in MEMS structures. FEM, used for simulating the MEMS structures (not the system), is backed up with experimental testing. The model predicted stiction, particulate-induced blocking, or fracture of silicon structures as failure root-causes, observing that functional failure occurred at lower g-loads than the package counterpart. Several other studies applied FEM to the case of MEMS gyroscopes [33], [88], [89], microphones [37], [124] or microscale pad structures [125]. Physical-based approaches were also explored, with analytical development being fed to a numerical model in the unique case of mechanical shocks [126]–[132], in specific use cases such as in automotive [108], taking into account vibration [128], [133] or more than one environmental constraint [134]. A multiphysics modelling has also been done by Lall [135], taking as reference the standard MIL-STD-883, Test Method 2002: a relevant approach to numerical prediction for space-related studies. Yang *et al.* in [136] developed a multiscale analysis of the MEMS/package system. Considering the system as a whole permits to take into account interactions between sub-systems, ultimately increasing the representativeness of the numerical model.

As corollary to mechanical shocks, vibration also constitutes a challenge in MEMS devices. Moving or oscillating silicon structures are designed with mechanical end-stops to mitigate any exaggerate motion or bending modes due to resonance phenomena and that could lead to failure. A common test method consists in placing a set of devices on a laboratory shaker and excite over a selected frequency range – from 20 to 2000 Hz in the case of standard MIL-STD-883, Method 2007. Works in this field aim at understanding if, over a given frequency range of vibration, the sensory organ of a MEMS but also the supporting electronics and structural elements are prone to failure if resonance occur. For example, Tanner evaluated the MEMS micro engine susceptibility to a white noise vibration between 20 to 2000 Hz with peak acceleration of 120g along three orientations [114]. High robustness IMUs, due to the small scale of their constituents, are generally proven to have excellent immunity to vibrations [137], [138]. Capriglione *et al.* proposed a reliability- and metrological-oriented test dedicated to MEMS-based IMUs under vibration, as a first trial to propose a possible international standard [139]. FEM is also exploited in the case of vibration, for example, in order to derive a modal analysis of an accelerometer’s supporting PCB for automotive applications [31], [128], [140], [141].

Thermal reliability testing aims at promoting possible failure modes in devices by accelerating aging of its constituents, which would naturally require extended durations of time to be observed. In the space field, ultra-high reliability must be assured already before the mission. Spacecrafts’ life can require years spanning over several successive phases before operations: procurement, assembly, storage, launch, and hibernation periods. As an example, it is worth mentioning that ESA’s comet exploration mission Rosetta [142], approved in 1993 and launched in 2004, has been dormant for most of its mission (12 years in space). Another example is the long awaited James Webb Space Telescope [143], which is for more than a decade in gestation, still as of today. While in orbit or in interplanetary space, thermal loads experienced by embarked components are challenging in terms of long-term reliability. This constitutes a compelling reason for thorough thermal reliability assessments and qualifications, as thermally activated aging phenomena can be promoted during testing (Table 1.3). Thermal management is a major issue in microelectronics in general, especially in layers bonding the silicon chips to the protective package or heat sink. Works on the reliability of Ball Grid Arrays (BGA) [144]–[147], solders [148], or conductive adhesives [149]–[152] have been well covered.

A distinction is made between thermal cycles (temperature cycles) and thermal shocks. While the first category follows slow thermal gradients between temperature extrema, the second one supposes abrupt changes from the hot-to-cold (respectively cold-to-hot) temperatures. The difference between thermal cycling and shocks is in the definition of transfer time (*dwelling time*) between the hot and cold chamber, specified in the case of shocks: 10 seconds in the case of the standard MIL-STD-750-1A, Method 1051.9. This detail differs with the procedure mentioned in MIL-STD-883, Method 1010. A distinction between air-air test and liquid-liquid test is presented by Moreau *et al.* [153] with the degradation of the solder joint of 40 test components at a maximum range -55 to +150°C with variable dwell

times. Another study by de Vries *et al.* explored the same issue with experiments on BGA and following the standard JESD22-A104-B and the maximum temperature range -55 to +125°C [154]. Lellouchi *et al.* developed a new equipment designed specifically for environmental testing of MEMS, which permits a large temperature scale and different pressure testing. This system has been used to characterize the environmental behavior of two types of RF MEMS from -20 to 200°C [155]. Duong *et al.* studied the effect of a harsh temperature environment on the deflection of various designs for RF MEMS for space application with a thermal FEM simulation. FEM is also exploited for studying the impact of the temperature on MEMS structures, component subsystems such as adhesives, interconnects, and packaging elements.

1.3.3 Standards for MEMS: an open question

Most of the sources, engineers, researchers, and institutional actors, rely on historical U.S. military norms in the absence of dedicated standards for MEMS in general. Space agencies have elaborated methodologies, such as in the case of ESA, developed for individual types of MEMS devices for space application. For instance, a methodology for RF MEMS has been exposed at the ESA round table on micro- and nanotechnologies [156], [157]. International authorities like IEC started to streamline procedures for testing in 2011, with a first step dedicated to RF-MEMS switches in 2011 [158].

Table 1.6 below presents a selection of the most used standards, which can be further completed by Hartzell's developments [159]. In the absence of proper dedicated methods, MEMS are often tested as per guidelines applying to testing microelectronic circuits, first with digital circuits, and later with analog and mixed-signal devices, should that be for the military/aerospace or automotive domains. Additionally, an essential distinction between qualification and testing must be made. Qualification is a pass/fail procedure for components preceding their further integration, say, on a spacecraft. On the other hand, testing aims at pushing the component to its limits by overstressing several of their capabilities and thoroughly study their reliability figures and lifetime. The qualification methods nevertheless constitute a good starting point to assess stresses a device shall sustain.

While these standards have the advantage of setting points of comparison through a uniformization of testing procedure among researchers and industries, they are not uniquely applicable to the full spectrum of MEMS devices. Legacy standards can even be outdated and inappropriate nowadays for modern technologies, such as for example MIL-HDBK-217 [160]–[162]. Hokka [38] pointed out the necessity of thinking MEMS reliability assessments beyond the context of circuit boards and ICs. An excellent overview of the underlying challenges of interconnection and packaging in MEMS as well as the fields of application is proposed by Ramesham and Ghaffarian: they concluded by mentioning that testing MEMS packages using the same methodologies as those for electronics packages with standard procedures might not always be possible, especially when quality and reliability need to be assessed [163]. Dhennin *et al.* referred to the physics of failure for evaluating MEMS reliability in the absence of proper standardized procedures, since it constitutes a physics-based set of criteria [158].

Though devices are exposed to the same conditions as the electronic assembly, health monitoring requires special care since their intrinsic reliability is not necessarily the same as the surrounding electronics. MEMS, by their complex design bringing in common several materials, functions and joining techniques, require specific definitions of testing procedures to truly evaluate their high reliability figures. Reliability behavior and failure causes in MEMS can therefore take multiple forms, as also driven by the application fields such as automotive [40] or defense in the case of the U.S. Department of Defense's case [164]. The latter mentions that not only should MEMS devices and components be considered for testing but also the impact of transportation, storage environments, operating environments, packaging and interconnection issues, and other issues that directly and indirectly affect lifetime.

Comparative studies have been done on commercial components, highlighting differences between manufacturers for diverse applications and operating environments. Delak *et al.* also performed testing largely based on MIL-STD-883 standards on three different accelerometer designs and a large sampling of up to 4700 units, with little failure [115]. Olney [165] made a very comprehensive summary of qualification plans for four categories of commercial MEMS products: an ADXL50 accelerometer (reported in Table 1.7), ADMP421 microphone, an ADXRS610 gyroscope in ceramic BGA package and a RF MEMS switch. All mentioned MEMS devices passed qualifications at the selected values. Marozau *et al.* [65] set up a reliability assessment program for several COTS accelerometers that led to little to no failure, even though conditions were following the prescribed stresses as per MIL-STD-883. The global results

Table 1.6: Summary of well-known standards applied for reliability of MEMS.

Standard denomination	Concerns	Comment
MIL-STD-883K	Monolithic ICs and hybrid devices	Temperature cycling, mechanical shocks, vibration, etc. Widely used standard adopted for MEMS reliability testing.
MIL-STD-750-1A	Discrete semiconductors	Alternative option to MIL-STD-883.
MIL-HDBK-217	Military Handbook: Reliability Prediction of Electronic Equipment	Outdated standard developed in the 60s and not updated since the late 90s. A contemporary more realistic approach is the FIDES approach.
ISO/IEC 60068-Series	Environmental testing	Widely used standard, describe all classical environmental tests used for accelerated aging: high temperature operating lifetime, low temperature, thermal cycling, vibrations, moisture cycling [84]
JEDEC JESD22-Series	Solid state devices, component and solder interconnection, board-level...	Temperature cycling, storage life. Common alternative to the IEC 60068.
JESD91A	Method for Developing Acceleration Models for Electronic Component Failure Mechanisms	The method described in this document applies to all reliability mechanisms associated with electronic components. Arrhenius law is notably reported and explained.
ESCC Basic Specification No. 2265000	Evaluation test programme for discrete non-microwave semiconductors	From the European Space Agency. Often refers to MIL-STD-883.
ESCC Basic Specification No. 2269000	Evaluation test programme for integrated circuits	From the European Space Agency. Often refers to MIL-STD-883.
ESCC Generic Specification No. 9000	Evaluation test programme for integrated circuits	Parent standard to ESCC 2269000.
ECSS-Q-ST-30-11C	Space product assurance: Derating - EEE components	Derating is a means of extending component life, increasing reliability and enhancing the end-of-life performance of equipment. Derating participates in the protection of components from unexpected application anomalies and board design variations.
NASA-HDBK-7005	Dynamic Environmental Criteria	This handbook reviews Dynamic Environmental Criteria.
ASTM E2244-06 ASTM E2245-06 ASTM E2246-06	Standard on in-plane length, residual strain and strain gradient measurements of thin films using optical interferometer	Task group E08.05.03 working on Structural Films and electronic Materials developing standards for electronics and micromechanical applications [49].
SAE J1211 SAE J575G	Sensors for Automotive Applications	Standardized testing of MEMS components is partially covered in the Society of Automotive Engineers and the military via SAE J1221, SAE J575G [18], [45]
IEC SC 47F Work programme (IEC 62047-Series)	Semiconductor devices - Micro-electromechanical devices	Still at various stages of development [85]
IEEE 2700-2017	IEEE Standard for Sensor Performance Parameter Definitions	A common framework for sensor performance specification terminology, units, conditions, and limits is provided. Specifically, the accelerometer, magnetometer, gyrometer / gyroscope, accelerometer / magnetometer / gyroscope combination sensors, barometer / pressure sensors, hygrometer / humidity sensors, temperature sensors, light sensors (ambient and RGB), and proximity sensors are discussed.
Telcordia GR-468-CORE	Generic Reliability Assurance Requirements for Optoelectronic Devices Used in Telecommunications Equipment	Provides a large panel of test procedure criteria, characterization procedures (among which: physical characteristic of the devices like internal moisture and hermeticity, ESD test, die shear, wire bond strength) as well as stress test procedures (mechanical and thermal shocks, vibration, damp heat, high temperature accelerated aging).
SEMI MS-Series	Test Method for Step Height Measurements of Thin Films; Terminology for MEMS Technology; Standard Test Method for Young's Modulus Measurements of Thin, Reflecting Films Based on the Frequency of Beams in Resonance; Guide to Evaluating Hermeticity of MEMS Packages; Test Method to Measure Fluid Permeation Through MEMS Packaging Materials.	Metrology-related standards in four areas: microfluidics, materials characterization, wafer bonding, and terminology. The best contender to be a true reliability standard [85]

of the performed failure modes and effects analysis (FMEA) reported that the MEMS structures do not themselves constitute the failure root causes. Other device components, *e.g.*, interconnects, ASIC or packaging, exhibit lower reliability limits to the specific stresses of space harsh conditions. Sharma and Teverovsky proposed one of the first test plan that took a step back from the MEMS structures (micromachined movable elements) only and produced a comprehensive evaluation of commercial MEMS accelerometers (ADXL250). Mechanical shocks and temperature cycles were performed with only minor parametric changes, which demonstrated that thermomechanical robustness of the chosen devices is adequate for most space applications, provided a proper control and qualification of packaging materials and processes [51].

Overall, the previous references systematically report single parameter testing methods yielding little to no conclusive results for predicting MEMS devices' reliability. That is: there is a lack of valuable statistical or physical information

that can be obtained through these methods, which in turn does not translate into interpretable data that can be used for lifetime prediction.

Table 1.7: MEMS ADXL50 accelerometer qualification plan. MEMS accelerometers, such as ADXL335, 3-axis accelerometer, typically have shock survival ratings of 10,000 g in any axis, both when powered and unpowered.

Stress test	Conditions
Mechanical shocks	0.5 ms pulsed shocks at 500 g to 1500 g conducted at -40°C, +25°C, and +105°C in 3 package spatial axes.
Variable frequency vibration	50 g pulses applied from 20 Hz to 2000 Hz (logarithmically swept) at +25 °C
Mechanical drop	4000 g minimum shocks from 1.0 m drops onto concrete in 3 package spatial axes.
Thermal shock	1000 cycles -65 °C to +150 °C (liquid-to-liquid) per MIL-STD-883 Method 1011 Cond. C
Temperature cycle plus constant acceleration	1000 cycles -65 °C to +150 °C (air-to-air) per MIL-STD-883 Method 1010 Cond. C followed by 30,000 g acceleration in the +z axis (perpendicular to the die surface)
High temperature operating life	2000 hours at +125°C T _A with V _S = 6.0 V per MIL-STD-883 Method 1005
Low temperature operating life	1000 hours at -55°C T _A with V _S = 6.0 V
High temperature storage	1000 hours at +150°C T _A per MIL-STD-883 Method 1008
Low temperature storage	1000 hours at -40°C T _A

1.4 Beyond the classical approach for reliability evaluation

As seen previously, various reasons explain challenges ahead of MEMS reliability evaluation for space applications. Apart from the lack of well-established and broadly accepted test procedures, the diversity of micromanufacturing and assembly techniques as well as the various physical principles exploited for sensing and actuation contribute to this situation [24]. A consequence is the difficulty to establish unique or trivial categorizations among devices and component types. This called for definitions of dedicated reliability assessment programs [164].

Regardless of existing guidelines and standards, a MEMS-specific standardized method that is uniquely applicable to all types of MEMS-based components is still missing. While they are good points of comparison in the many references that have been presented, they often focus on silicon (MEMS structures) instead of considering the full device as an integrated system that needs all its constituents to perform flawlessly through time. In the reported studies that have considered both components and the supporting electronics, the observed tendency has been to report inconclusive outcomes (due to the lack of obvious failures), especially in the case of robust devices. In several cases, it is the supporting electronics (PCB, external solders) that fails and is reported as failure (while the device might still function). These conclusions hence do not permit to predict the lifetime of a given test vehicle. As mentioned in a presentation made by an industrial actor at ESA's roundtable on micro and nano technologies [166], there is still a need for the international and European Space community of MEMS-specific reliability assessment and qualification standards, in particular when it comes to COTS components [57]. In a tentative answer to this challenge, an international consortium, the Heterogeneous Technology Alliance (HTA) Reliability Platform, has been created with an aim to merge key reliability labs integrated in different R&D environments. Its mission is to communalize expertise in simulation, reliability assessment, testing, standardization [167]. But how to effectively define a universal testing plan for highly reliable devices?

Nowadays reliability qualification tests for space applications are elaborated based on MIL, NASA, or ESA standards (which are often themselves referring to MIL standards). Their purpose is to ensure that a device will perform nominally in a specified lifetime and based on a single-parameter test. While being good references, they nevertheless miss to accurately represent real operation conditions, where loads of different natures can simultaneously put devices under stress. For example, a satellite during the first phase of launch goes through high acceleration, vibration, and temperature variations at the same time. In orbit, radiations have effects on the device's circuits due to electronic effects, which can also be annealed thanks to exposure to high temperature. Several stresses accumulate, either sequentially or simultaneously in their chronology. A combination of different parameters during testing may lead to unexpected failure modes due to synergies between failure mechanisms, typically because of thermally activated or degradation phenomena. Overall, multi-parameter accumulative reliability testing is much less prominent in the literature compared to mono-parameter studies.

An approach consists in considerably increase the test conditions difficulty, typically with the combination of heat and humidity or an applied voltage. Acronyms defining such harsh, normalized tests are encountered in the literature [168]:

- HAST (Highly Accelerated Temperature and Humidity Stress Test: 130°C, 85% humidity, bias voltage +10%, 96 hours),
- HTOL (High Temperature Operating Life: 125°C, bias voltage +10%, 1000 hours),
- HTS (High Temperature Storage 125°C, unbiased, 1000 hours).

The HAST method has been initially developed by Sinnadurai to demonstrate better hermeticity of polymer-based packaging for ICs [169]. Those three procedures are nowadays typically referred to in the JEDEC standards². In such test, humidity control is achieved at temperatures higher than 100°C, which yields a greater accelerating factor as per the Peck equation reported in Table 1.3. Several papers mention HAST as constituent of test protocols: Bazu *et al.* in [171], Olney in his synthesis of the evolution of MEMS qualification requirements [165], Margomenos and Katehi for RF MEMS package hermeticity [172], and several other works in packaging solutions [173]–[176]. In most cases, tested devices passed the intense tests. In the book of Valldorf [168], a MEMS oscillator did not display any failure, even to HAST. As pointed out by Bensoussan [177], the common approach for assessing device reliability in the recent times (2016) is the High Temperature Operating Life (HTOL) testing. It assumes that just one dominant failure mechanism is taking place in the device, while multiple failure mechanisms act simultaneously.

Several papers treating of combined parameters can be found in the literature but only few incorporate tests of mechanical nature (shocks or vibration). Bazu *et al.* [171] depicts a set of methodologies considering various combined load cases such as temperature, humidity, and electrical or temperature and mechanical stresses. Numerous examples are reported in this paper: combined high temperature and electrical bias on piezoelectric accelerometer, a humidity sensor under high temperature, humidity, and electrical bias as well as an IMU under combined thermal and mechanical loads (vibration). Highly Accelerated Stress Test (HAST) is also mentioned: the combination of high temperature, humidity, pressure, and electrical bias, aiming at reducing testing time. The same author developed in [116] a form of accumulative testing, performed on 36 accelerometers by tilting and varying the temperature. This did not lead to any conclusive impact on the devices' performances. Lall *et al.* [178] proposed later more advanced work by combining high temperature and vibration on a dual axis gyroscope. The devices' output voltage was thoroughly investigated, ultimately showing that combined testing had greater deteriorating effects on the gyroscope than a single thermal stress environment. FMEA was however not performed since no catastrophic failure took place. In another study [179], Lall proposed a study on the exposure of a dual-axis accelerometer to temperature shocks, followed by high-g mechanical shock in an accumulative, sequential way. The devices have been soldered on boards (which the present research aims at avoiding) and have been subjected to mechanical shocks following test condition G in MIL-STD-883, Method 2002. Shock pulse amplitudes have been ramped from 500 to 30,000g. Failure mostly occurred at solders: the MEMS devices did not fail themselves. In Szűcs' work [180], thermal shocks are combined to vibration. The latter has been obtained by exciting the component intrinsically through application of an excitation signal, which is predicted to reach 70 g. This did not lead to failure of the chosen capacitive accelerometers at the selected test parameters: up to 100 cycles between 50°C to 150°C. This method differs from traditional testing method relying on extrinsic vibration produced by the testing apparatus. Moreover, the devices were tested on their supporting electronics (PCB) and the statistical analysis was performed on a limited number of five devices.

The closest paper to the present study has been published by Duesterhaus *et al.* [127], who studied devices mounted on a penetrator propelled into a hard target. Three temperatures (converted from the Fahrenheit scale) were selected for the test campaign: -59.9°C, 23.9°C, 73.9°C. The DUTs, constituted of a patchwork of custom-made MEMS structures manufactured by Deep Reactive Ion Etching (DRIE) and surface micromachining processes, were checked for survivability under mechanical shocks ranging from 25, 50, 125 and 250 thousand of g's. This work drew qualitative conclusions of the combined effect of temperature/mechanical shocks following a pass/fail method (no FMEA): high temperatures favored higher resilience of the MEMS structures', hence a better reliability. On the other hand, Lall *et*

² JESD22-A110-B High accelerated stress testing (HAST), JESD22-A108C High-temperature operating life (HTOL), JESD22-A103B High-temperature storage (HTS) (from [170])

al. [181] determined the main failure root cause in MEMS accelerometers to be stiction under the application of sequential thermal and high-g shocks environments.

These references overall summarize the landscape of accumulative testing in the literature. Seldom sources exist on this matter, on a field that has otherwise been widely studied in the single parameter testing.

1.5 Key findings of the literature review

The previous sections have shown that reliability assessment of MEMS devices still lacks proper methodologies to tackle high levels of robustness. Moreover, the standardization framework cannot yet rely on universally accepted procedures dedicated to MEMS – specifically since they exhibit a wide variety of constructions and relevant physics for sensing/actuation. While the thesis does not aim at developing a universal solution to this challenge, new developments are investigated in terms of methodologies of testing, notably the combination of thermal and mechanical stresses. The findings will be building blocks of a greater objective: assuring that MEMS technology can, by its numerous advantages and qualities in terms of performance, be confidently exploited in space applications thanks to a better knowledge of their reliability under the combination of harsh environments.

In the reviewed papers, MEMS devices are often tested with supporting electronics, solders, and connections. The present research aims at by-passing this issue by testing the MEMS and observing their behavior in a standalone fashion, thanks to a specific hardware and test sequence developments. That is: the MEMS devices selected for this research are not tested with soldered on a PCB. Only the MEMS systems (comprising of the packaged MEMS structures, ASIC and wire bonds) are exposed to the environmental loads. Deep understanding of the parameters influencing devices' lifetime can thus be obtained thanks to statistical analyses of the failed devices, chronological non-destructive and punctual/conclusive destructive testing, and materials analyses at progressive steps of the test campaigns. Damage evolution and propagation are therefore closely tracked. Finally, the selected DUT will also be represented in a FEM, highlighting the role of the die attach adhesive, with aims to correlate the failure modes to the simulation. This will allow a comprehensive representation of the effect of accumulative testing on the reliability behavior of MEMS devices.

To conclude, the following key points can be drawn from this chapter:

- MEMS designate a family of technologies and processes that burgeoned in the 1980s to become a fully matured technology nowadays, having diverse scopes of applications (consumer electronics, automotive, defense and space).
- Space, however, is a conservative field that requires time and extensive and convincing work to adopt newer technologies, if it means replacing an already excellent performing technology. Besides in mission-enabling cases, the tradeoff still tilts toward proven technologies. Despite their low footprint, low mass and low energy consumption, and demonstrated robustness under space-like conditions, end-users can still be reluctant to rely on MEMS devices to replace proven technologies.
- This situation is partly due to a lack of standardized framework acknowledged by the community, which would provide a common point of comparison when testing reliability of MEMS in the case of space applications.
- Testing following legacy standards such as the MIL-STD fail to properly assess reliability of highly robust devices due to the lack of conclusive results, hindering proper lifetime prediction. Additionally, numerous studies are using small sample sizes that do not permit to be statistically relevant or yield enough data.
- Accumulative testing is not the norm and has been less studied. Space being a multi-faceted environment, combination of loads of different natures are expected to lead to synergies and specific failure cases (such as thermally activated phenomena).
- This research aims at developing novel methods of accumulative testing for highly robust devices for space application. Results are envisioned to help the establishment of new standards that would permit a wider use of MEMS in space.

Chapter 2 Selection and pre-evaluation of the MEMS device

The present research aims at tackling three of the most common situations found in the literature:

- Reliability works relying on a limited number of samples, which fall short of providing enough statistical data for robust devices.
- Studies considering the supporting electronics, necessary to the MEMS devices functioning but unrelated to it when it comes to failure modes, as part of the defined failure modes.
- Test programs constituted of single parameter, one factor at a time procedure featuring a lesser representativeness than accumulative testing for depicting the space operational environment.

The first preparation step of this work consisted in selecting a unique set of devices (from a unique production lot) to be used for the test campaign. It is also upon selecting the best candidate to be tested: its inherent complexity and the existing body of literature available (as point of comparison for the new developments) are also weighed. This chapter aims at presenting the selection scheme that led to choosing a commercial Inertial Measurement Unit (IMU) from ST Microelectronics as test vehicle for the accumulative testing campaigns. Additionally, the results of this research are envisioned to be as useful information about the robustness of such devices (construction, MEMS sensors, assembly techniques) that could steer design plans and manufacturing procedures. It could finally help the end-user in the space field to orientate tradeoffs during the build-up of a space mission or service.

Provided the strong industrial implications of the present work, a systematic method for selecting the type of devices to be investigated is presented in this section. The idea of this preliminary study has also been to determine if a given “device candidate” has enough industrial and scientific background to be suited for the coming investigations. It is also framed by the needs and interests for a standardization portfolio, as well as of the academic/private stakeholders active in the MEMS field. It is therefore important, at first, to identify who are the stakeholders having a role since the thesis features an industry-oriented facet. To help this process, a stakeholder value network diagram, as shown in Figure 2.1, has been done at the early stages of the investigation and depicts the value chain for a given industrial partner. This basis sets the ground for the systematic selection scheme presented hereafter.

2.1 Selection scheme

A new technology is used for a space mission when it has achieved the maximum technology readiness level. A TRL depicts the maturity level of a given technology [182]. At TRL 9 (highest), technology has proven success in real-life operations, while TRL 1 (lowest) relates to a technology of which only basic principles have been observed and reported. A TRL 5 means that a component has been validated in the relevant environment. Along this scale of progression, various actors developing MEMS dedicated to space applications are identified:

- Universities (with increasing NASA, ESA, DARPA, EU funding...) and research centers such as CSEM.
- MEMS foundries (ST Microelectronics, Bosch, Texas Instrument, etc.), though the market size for space applications is orders of magnitude smaller than their primary playground.
- Internal R&D departments at major space companies like EADS Astrium, as well as at some national agencies (e.g. CNES and JPL).
- Small companies and startups, e.g. NanoSpace (Sweden)

The issue is therefore to select a MEMS candidate that can not only demonstrate a high TRL, since it would be more relevant as COTS component for space application, but also because proven technology benefits from a greater body of knowledge on its reliability. This is however not restricted to the type and purpose of MEMS, but also linked to

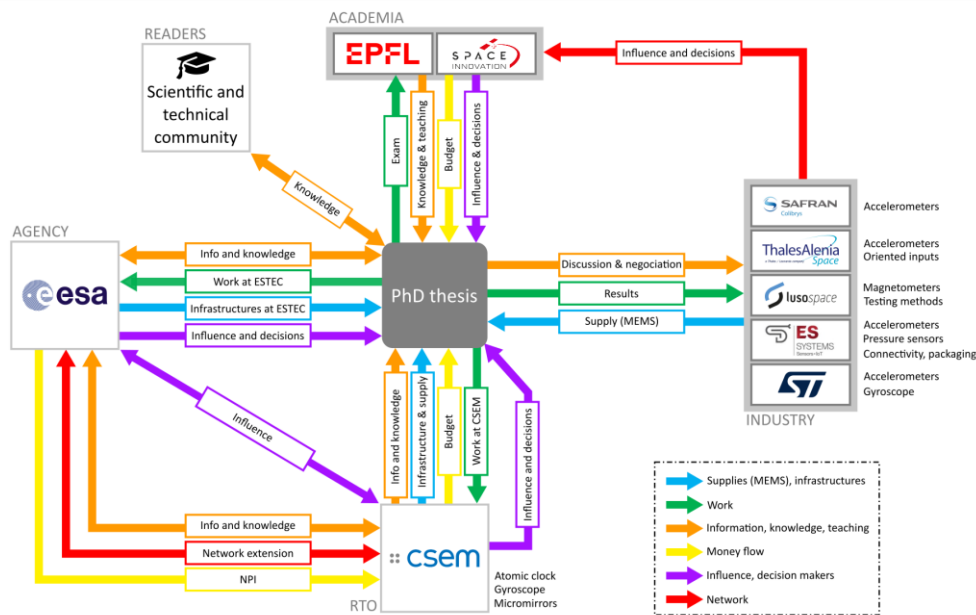


Figure 2.1: Stakeholder value network diagram of the stakeholder related to the current thesis.

manufacturing and assembly techniques that are transversally present in this technology. This section starts with a listing of MEMS that have been used or can potentially be used in space missions, followed by the development of the selection process based on a selected set of criteria. Finally, the European landscape of MEMS producers is presented, and the final candidate choice explained.

2.1.1 Selection of space missions and applications of MEMS

This section reports examples of space missions by MEMS devices' types. This review aims at helping the selection process: well-known devices are more suitable for the development of a novel reliability assessment method, since the accumulation of previous knowledge and experimental details are expected to be referred to when performing the study. The greater part of the content reported in the following sections refers to the very insightful eoPortal Directory³ for the related missions.

2.1.1.1 Accelerometer

Several NASA/DOD missions featuring MEMS accelerometers have flown in the past, such as PSSCT and PSSCT-2 (Space Shuttle mission which used COST IMUs from Analog Devices). Communications satellite of the Iridium NEXT constellation will also use such technology with the MASS (MEMS Accelerometer for Space Science) instrument. The variety of such sensors is shown by the various technologies that can be used, such as capacitive-based displacement accelerometers (in- and out-of-plane), piezoelectric-based featuring high robustness and resonance-based (vibrating beam accelerometers or VBA), protected in polymeric, metallic, or ceramic packaging. Reliability studies on COTS sensors were made as well [52]. Potential industrial partners have also published information regarding rugged accelerometers for harsh environment, with radiation tolerances with the goal of having components at TRL 5, with full specs for space (environment and performance) qualified [17], [183]. Substantial information is potentially at hand. The general trend is that the complementary sub-systems to the MEMS, such as the ASIC and the connection wiring, are more likely to be sensitive to the environment in space-like conditions.

To the author's knowledge, few major European missions used MEMS accelerometers. The first ExoMars mission⁴ can be mentioned as an example: the IMU used on Schiaparelli incorporated solid-state fiber-optic gyros and MEMS accelerometers operated at 200 measurements per second. Additionally, the Finnish student nanosatellite Aalto-1 features a MEMS sensors suite (gyro, accelerometer, magnetometer) and was launched in June 2017.

³ Website: <https://directory.eoportal.org/web/eoportal/satellite-missions>

⁴ Website: <http://spaceflight101.com/exomars/esa-narrows-schiaparelli-failure-to-imu-and-software/>

2.1.1.2 Gyroscopes

Gyroscopes are undeniably one of the most mature MEMS technologies that has been flown to space. Widely used on picosatellites (such as Swisscube) but also a couple of full-size European mission, they offer a compromise of compactness and decent performances for this range of applications. The GIOVE program, that launched first in December 2005, used two sets of 3 QRS11 MEMS gyros from Systron Donner Inertial (Walnut Creek, CA, USA) for attitude rate sensing. The QRS11 is a technology based solid-state "gyro on a chip."

CryoSat-2 (launched 2010) was designed with an experimental rate sensor as technological demonstrator. Three orthogonal MEMS gyroscopes are mounted in the experiment, to measure 3-axis attitude rates (Figure 2.2). The unit is called MRS (MEMS Rate Sensor) in the CryoSat context and its goal is to provide a low-cost rate-sensor or gyro [184].



Figure 2.2: Top view of MRS FExp front end PCBs (left) and view of the MRS Exp unit on the CryoSat-2 nadir panel (right) [184].

Following the CryoSat demonstrator, ESA launched Sentinel-3 (February 2016) with an AOCS featuring MEMS 3-axis gyroscopic sensors under the name of SiREUS. The gyros are used for identifying satellite motion and to place it into a preset attitude in association with optical sensors after its separation from the launcher, for Sun and Earth acquisition. Each unit measures 11 cm x 11 cm x 7 cm, with an overall mass of 750 grams [185]. The SiREUS device is of SiRRS-01 heritage, a single-axis rate sensor built by AIS (Atlantic Inertial Systems Ltd., UK), which is based on a Vibrating Structure Gyroscopes. The SiRRS-01 MEMS gyro has been used in the automobile industry. More reference documents about lessons learned for SiREUS and the qualification process are reported in [186] and [187] respectively.

Another project has then been developed in the context of ESA's sequel technology program named SiREUS-FExp, for European Silicon Rate Sensor Flight Experiment. The UK-based development team consisted of AIS (Atlantic Inertial Systems - formerly BAE Systems of Plymouth), SEA (Systems Engineering & Assessment Ltd. of Bristol), and SELEX-GALILEO a Finmeccanica owned company (formerly BAE Systems of Edinburgh). The technology is based on the established BAE SYSTEMS automotive MEMS detector. However significant developments were required to meet the performance requirements while achieving compatibility of the electronics to the space environment, while ensuring low recurring price [188]–[190]. Key requirements of the MEMS Rate Sensor (MRS) are provided in Table 2.1.

Table 2.1: MRS (MEMS Rate Sensor) key requirements and 2008 status.

Parameter	Requirement	MRS status
Configuration	3-axis, rate or integration mode (an optimized mechanical and electronics configuration)	Ok
Instrument mass	< 0.75 kg (electronics and mechanical architecture commensurate with MEMS detector)	0.745 kg
Power consumption (nominal)	< 3.5 W	5.4 W
Bias stability (3σ), $\Delta T < \pm 10^\circ$	5 to $10^\circ/\text{h}$ over 24 hours (this represents a factor 10 improvement on the best existing MEMS devices)	10-20°h
Angular random walk	$< 0.2^\circ/\sqrt{h}$	$0.04^\circ/\sqrt{h}$
Range	Up to $20^\circ/\text{s}$	Ok
Interface	RS-422, SpaceWire, analog	RS-422, analog
Mission	18 years in GEO (this required radiation hardened implementation and ITAR free electronics)	Ok

Source: <https://directory.eoportal.org/web/eoportal/satellite-missions/c-missions/cryosat-2#footback16%29>

2.1.1.3 Pressure sensor

One of the challenges with MEMS pressures sensors is to manufacture a thin membrane with rigorously controlled thickness. Due to the variety of thermomechanical and chemical environments of the micromanufacturing processes, such membranes can be prone to residual stress. Such issue is of utter importance when dealing with reliability testing, especially if several stress conditions are applied simultaneously, and could lead to the activation of subsequent phenomena dependent on temperature within the material, ultimately leading to catastrophic failure. Pressure sensors being of a simple build, robustness to harsh conditions is expected due to a lower overall complexity. As for accelerometers or gyroscopes, the supporting electronics (ASIC and connections) are more likely to be affected by the environment.

Some European example of space applications are found. Delfi-n3Xt of TU Delft, the Netherland, has tested in condition MEMS pressure sensors on its 3U-CubeSat (mentioned in introduction). It also used 3 MEMS gyros and 3 magnetometers (COTS). The Norwegian supplier PRESENS has previously developed a microsystem for space in a collaboration with ESA and launched in 2010 on the PRISMA⁵ satellite, a technology demonstration satellite developed by Swedish Space Corporation, which is spun-out of a development performed for oil-drilling applications⁶. Its characteristics are provided in Table 2.2. There are moreover industrial benchmarks on the reliability of such devices, as there are automotive manufacturers which massively use pressure sensors for tires, engine feed, etc. On more academic aspects, there has been studies of new designs dedicated for space [191], [192].

Table 2.2: Datasheet of PRESENS' MEMS pressure sensor.

Max. operational pressure	320 bar
Burst pressure	1280 bar
Total error band	< $\pm 0.2\%$ FS
Long-term drift at 25°C	< $\pm 0.02\%$ FS/year
Operating temperature	-40°C to +75°C
Lifetime in GEO	15 years
Miscellaneous	Chemical resistance to hydrazine, low power consumption

Source: <https://spacecomponents.org/download/webDocumentFile?id=52357>

2.1.1.4 Micromirrors

Micromirrors' application have applications in space in optical and detection instruments, where compacity is needed to diverge a light beam or induce changes in light's flight path. Sangameswaran [193] studied the effect of reliability issues under electrostatic discharges. Proton radiation testing of DMD for space application has been carried on by Fourspring *et al.* in [194]. An important study was the *in-situ* characterization by Yoo *et al.* [195], who based their work on a device which was flown on two missions: at first in 2008, a dedicated test bed (Figure 2.3) was used for a one-week test on board of the ISS. Before the flight on the space station, mechanical shocks, and vibration testing, stiction prevention and electrostatic charging tests were carried out. In 2009, the DMD was then integrated in the MTEL⁷ space telescope, embarked on the Russian microsatellite Tatiana-II. Its mission was to observe transient luminous events in Earth's atmosphere from space. The main conclusion was that micromirrors were hardly influence by the launch environment and their time in space.

On the European side, in 2010, Hernandez *et al.* covered the potential of Micro-Opto-Electro-Mechanical Systems (MOEMS) and the available European sources for applications in space [196]. Zamkotsian (CNRS) together with industrial and institutional partners demonstrated a successful evaluation of DMD [197], [198] and MOEMS [199] for space applications. A However, there has not been any full-fledged European mission with such devices so far. In other commercial options, one must look for the industrially DMDs produced by Texas Instrument for consumer electronics. Scientific work done on the matter since their first release in the 70s has been covered in the literature review [3].

⁵ Homonym of the ASI mission mentioned in introduction.

⁶ <https://directory.eoportal.org/web/eoportal/satellite-missions/p/prisma-prototype>

⁷ MTEL stands for "MEMS Telescope for Extreme Lightning".

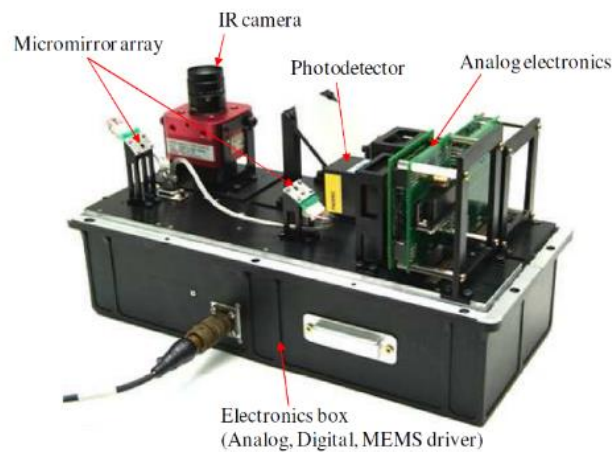


Figure 2.3: An instrument for test of the micromirrors in the ISS with a cover removed [195].

2.1.1.5 RF MEMS

Only a couple of American missions from the 2000s have been found to use (or demonstrate the use of) RF MEMS switches. Yao *et al.* in [200] worked on such actuator on a picosatellite mission. The same author did also a review of the progresses done at that time from a device perspective [201]. Stanford University also launched the OPAL satellite⁸ in 2000, which embarked RF MEMS switches.

One of the application of RF MEMS was for Phased Array Antennas as illustrated by Ponckah *et al.* [202], and by Zaghoul *et al.* [203]. Rebeiz *et al.* proposed a comprehensive review of MEMS phase shifters [204] and switches with an emphasis on reliability and packaging [205], [206].

2.1.1.6 Interferometer

There is a sustained interest of the community to qualify MEMS-based interferometry in space, since compact and accurate devices could help space exploration for atmospheric studies and exoplanets discoveries, as highlighted in Saari *et al.*'s article on a Fabry-Perot interferometer for hyperspectral imaging [207]. It is to be noted that a world first for MEMS FTIR spectrometer⁹ was done by Hamamatsu in 2013 [208]. Another study mentions both Fabry-Perot and Michelson interferometers (Figure 2.4) [209].

The only European mission which features a MEMS interferometer is Aalto-1, a yet-to-be-launched student 3U CubeSat from the University of Aalto [210]. It embarks a COTS Fabry-Perot interferometer from VTT [211], Finland, used as a gas sensor (spectrum selectivity coupled with a photodiode).

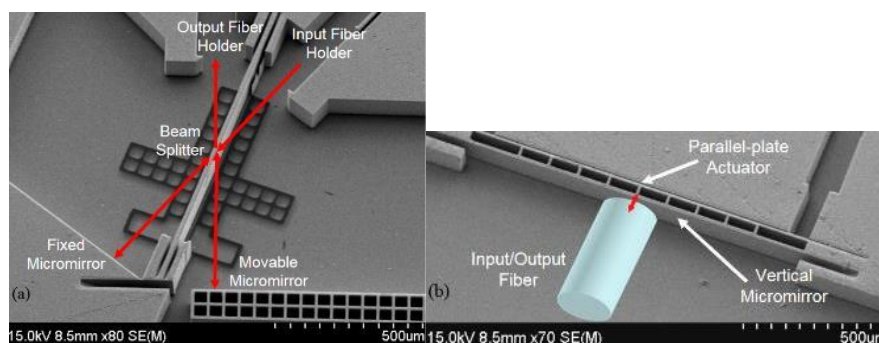


Figure 2.4: SEM micrograph of the MEMS interferometer. A set of fixed and movable micromirrors enable quantification of light path difference [209].

⁸ Source: <https://directory.eoportal.org/web/eoportal/satellite-missions/o/opal>

⁹ Source: <http://www.hamamatsu.com/eu/en/news/development/20130129160000.html>

2.1.1.7 Atomic clocks

Last ten years, CSEM focused on developing its own miniature MEMS atomic vapor cell (Figure 2.5) which could potentially be used in space [212]. However, the development is still in its early stages and industrial production (with the researched constancy in characteristics) is yet to be achieved [213]. Chip-scale atomic clocks are also being developed, such as at the National Institute for Standardization and Technology, NIST (Figure 2.6 reproduced from [214]).



Figure 2.5: CSEM's MEMS atomic vapor cells. A Rubidium gas is created in the hermetic chamber formed by the silicon ring, encased between two quartz blades. A laser excites the gas, the interactions permits measurement of quantum decay [212]

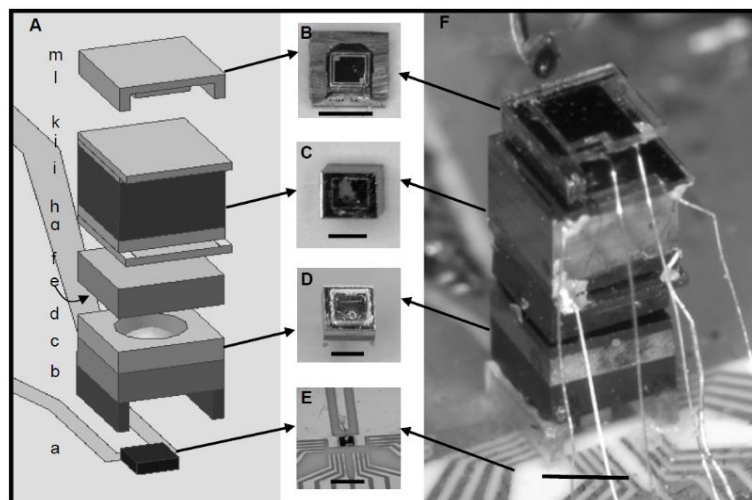


Figure 2.6. The microfabricated atomic clock physics package based on Cs atoms. (A) Schematic of assembly. Layers from bottom to top: a, Laser and baseplate; b, Glass (500 μm); c, ND filter (500 μm); d, Spacer (375 μm); e, Quartz (70 μm , not shown); f, ND filter (500 μm); g, Glass/ITO (125 $\mu\text{m}/30\text{ nm}$); h, Glass (200 μm); i, Si (1000 μm); j, Glass (200 μm); k, Glass/ITO (125 $\mu\text{m}/30\text{ nm}$); l, Si (375 μm); m, Glass (125 μm). Total height, 4.2 mm, width and depth, 1.5 mm. Photographs (B), photo-diode assembly, (C), cell assembly, (D), optics assembly and (E), laser assembly and (F), the full atomic frequency reference physics package realized as a microchip. The black scales are 1mm. Reproduced from [214].

2.1.1.8 Magnetometer

A few micro- and pico-satellites have already flown MEMS magnetometers, such as IMS (Indian Microsatellite-1) in 2008 and YouthSat / IMS-1A, an Indian-Russian joint work (launched 2011), the Japanese SpriteSat (Rising) in 2009 or MinXSS (Miniature X-ray Solar Spectrometer) in 2015. This kind of use of MEMS magnetometers are therefore recent and tells that the degree of development remains low for major space mission.

An industrial process-bases magnetometer is proposed by Langfelder *et al.* in [215], which comes along what is proposed to be done during this thesis. A couple of articles relates to MEMS magnetometer, without specifying any space applications. A resonant MEMS magnetometer with capacitive read-out is proposed in the article of Thompson and Horsley [216], who are fairly productive on this topic. Díaz-Michelena produced a review of the small magnetic sensors for space applications, which engulfs MEMS [217]. Nevertheless, there is still scarce references treating of MEMS magnetometers.

2.1.2 MEMS device attractiveness/suitability for space applications

Space applications describe a wide range of fields: telecommunications, Earth observation, defense and remote sensing or space exploration, designed today with either COTS or application-specific devices. Due to the variety of engineering and technical disciplines that are necessary to achieve a mission, various actors, technical considerations, and tradeoffs as well as financial, maturity levels or geopolitical interests are to be included in this research. Systems engineering is one of the disciplines that provides the tools to manage such complex, multi-faceted projects. The present chapter aims at using systems engineering tools for initial screening and establishing tradeoffs.

The previously covered MEMS types are evaluated with respect to a selection of criteria that are reported in Table 2.3. The approach takes as reference literature and academic references [218], [219], aiming at going along a systematic path mixing quantitative and qualitative developments. The method consists of two steps: first, a definition of certain key criteria must be made. Upon these definitions, a weighing of every criterion with respect to the others is made. This is called a Multi Utilities Attribute Analysis (MUAA) [219]. This method enables concepts screening and selection thanks to a procedural method based on user-defined criteria and respective weighing. A ranking of the competitive alternatives is then obtained and guide the final choice with respect to a datum or, in the present case, from a relative point of view between MEMS candidates. The procedure starts with the definitions of the criteria (Table 2.3).

Table 2.3: Criteria for the MUAA.

Code	Design	Definition
MissEn	<i>Mission Enabler</i>	Technological breakthrough that enables new mission designs based on the advantages of MEMS.
Cost	<i>Cost</i>	How much costs a given MEMS (absolute estimated cost).
TRL	<i>TRL</i>	To which extent is the technology mature enough for extending a given MEMS' application to space.
Cmpx	<i>Complexity</i>	How complex is the MEMS, hence how complex the definition of a reliability model can be.
CH	<i>Interest of CH</i>	Which repercussions can scientific and industrial actors in Switzerland (CH) get from the thesis
ESA	<i>Interest for ESA</i>	Which scientific and industrial repercussions can ESA and the European Space community get from the thesis.
Knwldg	<i>Knowledge</i>	How advanced is the science behind the understanding of the effect of MONO-parameters (temperature, pressure, vibration, shocks, humidity) on the relevant aspects touching MEMS reliability.

Criteria can be attributed to any physical or abstract aspect related to either the thesis itself or the MEMS devices that have to be evaluated. In the case of the scientific repercussions, a distinction is made between the Swiss arena and the more global European arena. This is linked to the functioning of the European Space Agency and the concept of "georeturn"¹⁰: funding from the member states is collected and is expected to be distributed back in research and development contracts to the member states. There is therefore two overlapping interests: on one hand the member state which, in the present case Switzerland, expects to have the Agency attribute projects and missions based on the magnitude of its contribution. On the other hand, the Agency's interest is to realize space projects in the best interest of the European's space program, for example in response to the U.S. International Traffic in Arms Regulations (ITAR) limitation imposed on sensitive fringes of technologies used in defense and space applications.

Each criterion is then evaluated with each other in a matrix form, using a simple ± 1 or 0 weight, based on a simple "more important than", "less important than" and "equally important as" comparison. A given criterion accumulates or loses points, and its importance is quantified, as done in Table 2.4.

The next step consists in attributing to each MEMS candidates a score on a utility function, which is linked to each criterion mentioned above. A utility function evaluates the selected MEMS candidates in a hierarchical fashion with

¹⁰ More detail on: http://www.esa.int/About_Us/Business_with_ESA/How_to_do/Industrial_policy_and_geographical_distribution

respect to qualitative or quantitative, user-defined scales. This is done arbitrarily based on consultations between stakeholders in the present research: CSEM, ESA and EPFL. Figure 2.7 reports all the functions applied on the selected devices.

Table 2.4: Comparative matrix for weighing criteria with respect to each other.

Evaluation X		Evaluation Y						
		MissEn	Cost	TRL	Cmpx	CH	ESA	Knwldg
MissEn		0	0	0	1	0	1	
Cost		0	1	1	1	1	1	
TRL		0	-1	0	0	1	-1	1
Cmpx		0	-1	0	0	1	1	0
CH		-1	-1	-1	-1	0	-1	0
ESA		0	-1	1	-1	1	0	1
Knwldg		-1	-1	-1	0	0	-1	0
$\Sigma+$		0	0	2	1	5	2	4
$\Sigma 0$		4	1	2	3	1	1	2
$\Sigma-$		2	5	2	2	0	3	0
General sum		-2	-5	0	-1	5	-1	4
Weight		2	1	5	3	8	3	7
Ponderated Σ		0.069	0.034	0.172	0.103	0.276	0.103	0.241
Importance [%]		6.9	3.4	17.2	10.3	27.6	10.3	24.1

Σ
 0
 29
 1

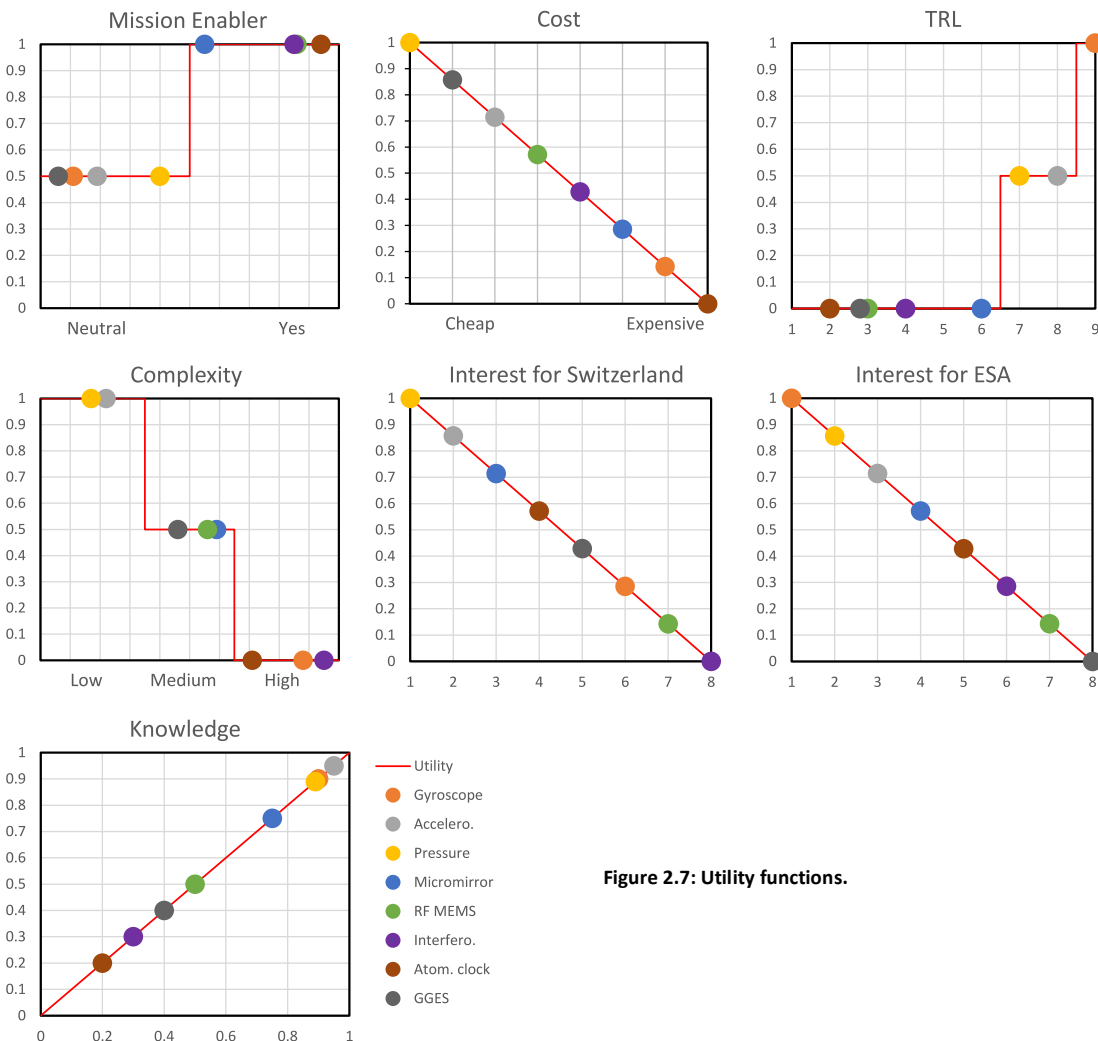


Figure 2.7: Utility functions.

The results of the multi-attribute utility analysis follow the equation summing each partial utility function with their respective weight:

$$U(J_1, \dots, J_n) = \sum_{i=1}^n k_i U_{i(J_i)}$$

$U(J_i)$ is the score for a given MEMS candidate J_i , k_i the weighing of a given criterion from Table 2.4 and $U_{i(J_i)}$ the utility score from the graphs given in Figure 2.7. The results are reported in Table 2.5. The podium is therefore 1st pressure sensor, 2nd accelerometer and 3rd gyroscope. This ranking is straightforward to understand, since a great importance has been given to the estimated scientific body of literature available for a given MEMS (especially considering reliability questions), which is corollary to TRL in a certain way. Finally, the scientific and industrial interest of the criterion "Switzerland", *i.e.*, the stakeholders who will have an obvious/potential interest in developing reliability questions on a given MEMS leads to this score (*cf.* Figure 2.1).

Table 2.5: Final ranking of the MEMS candidates.

MUAA	U _i (J _i)							Score	Ranks
	MissEn	Cost	TRL	Cmpx	CH	ESA	Knwldg		
Gyroscope	0.50	0.14	1.00	0.00	0.29	1.00	0.90	61.13	3
Accelerometer	0.50	0.71	0.50	1.00	0.86	1.00	0.95	81.80	2
Pressure sensor	0.50	1.00	0.50	1.00	1.00	0.86	0.89	83.80	1
Micromirror	1.00	0.29	0.00	0.50	0.71	0.57	0.75	56.77	4
RF MEMS	1.00	0.57	0.00	0.50	0.14	0.14	0.50	31.53	7
Interferometer	1.00	0.43	0.00	0.00	0.00	0.29	0.30	18.57	8
Atomic clock	1.00	0.00	0.00	0.00	0.57	0.43	0.20	31.92	6
Magnetometer	0.50	0.86	0.00	0.00	0.43	0.00	0.40	33.05	5
Weighing	6.9	3.4	17.2	10.3	27.6	10.3	24.1		

2.1.3 Industrial actors for COTS MEMS

The discussion around the selection of MEMS also considered the availability of commercial devices. To define a reliability test plan, it is necessary to have at hand enough test devices (tens to a hundred) with tightly contained variability. A typical failure rate for automotive part lower than 10 FIT (Failure-In-Time, defined as 1 failure per billion hours) [83] or in the sub-part-per-million range [32]. That is why, along with the criteria weighing, it has been considered within the criterion "Interest for CH" the potential Swiss partner (CSEM included) which could have interest in financing, helping or even supplying test vehicles for this project. The market field is limited to European actors.

Gyroscope – Links with ST Microelectronics, France/Italy, permitted to establish a cooperation for a reliability study. ESA has also funded a UK consortium with AIS (Plymouth), SEA (Bristol) and SELEX Galileo (Edinburgh) in the past for the SIREUS instrument. It is a common COTS element, the acquisition of which is not an issue.

Accelerometer – A preliminary selection process for another internal project at CSEM has already identified a manufacturer for MEMS accelerometer applications, namely First Sensors. There are nevertheless many others which could potentially have an interest in taking part in this study, such as Colibrys with their VS1000 series, already known by the author of this report. STMicroelectronics, ThalesAlenia Space or VTT are also possible manufacturers. It is also a common COTS element. Theon sensors (Greece) are also stating to be working on MEMS accelerometers for future launchers [220].

Pressure sensor – It is a common COTS element for the automotive industry. One of the reference industrial partner, ESS European Sensor Systems, is producing such sensors. The Norwegian manufacturer, Sensoron, and PreSens from Germany. In the US, Motorola is notably producing pressure sensors for the automotive industry, such as tires pressure sensors.

Micromirrors – An internal project at CSEM focused on the production of a steerable MEMS micromirror. This technology is however different than the micromirrors arrays commercially produced by Texas Instrument, typically for consumer electronics video projectors. Its full-scale production goes back to as early as 1992.

RF MEMS – An article from 2005 by Bouchaud and Wicht [221] reviews the industrial actors in the RF MEMS business in Europe: Thales (France), Airbus Group with Tronics¹¹ (France), Infineon (Germany), MEMSCAP (France) or even STMicroelectronics (France). More information about RF MEMS activities in Europe can be found in [222].

Interferometer – Hamamatsu (Japan) is alleged to have been the first company to produce a commercial Fabry-Perot Interferometer. Otherwise, only few information has been found on this topic.

Atomic clock – CSEM is currently working on its own rubidium gas cell, though still facing challenges in terms of variability. Besides a couple of other groups working on miniaturized atomic clocks, such as the NIST.

Magnetometer – The Japanese CubeSat SpriteSat from the late 2000 had a Swedish MEMS magnetometer unit named TAMU (for Tohoku-ÅAC MEMS Unit), an advanced magnetometer subsystem developed at Ångström Aerospace Corporation (ÅAC).

2.1.4 Final choice of MEMS device

There is a necessity to focus the thesis on MEMS devices featuring the lowest possible variability over their manufacturing, so that the full reliability study can rely on a set of test samples as homogeneous as possible. Doing so, statistical phenomena taking place during testing can therefore safely be assumed to arise preponderantly from the testing itself, and not from the sampling. COTS components from the automotive industry are therefore optimal candidates: they are designed and manufactured to achieve a part-per-million reliability figures. Synergies with the space field seem therefore possible and desirable. This aspect restricts the choice freedom to the three MEMS devices evaluated previously: pressure sensors, accelerometers, and gyroscopes, which are ranked among the three best choices from the analysis. These devices are already embedded in modern cars: MEMS accelerometers trigger airbags; MEMS pressure sensors check tires' pressure and MEMS gyroscopes help to prevent brakes locking and maintain traction during skids (ESP).

Pressure sensors are well-known and previously mission-enabling components that has come a long way already in the MEMS environment. It is therefore not surprising to such device in the top of the ranking. Nevertheless, to the author's opinion, a MEMS pressure sensor does not have any moving mechanical parts being worth of investigation for the context of a thesis. Due to the challenge of having a controlled membrane thickness devoid of internal stress and the complexity this implies, it is decided to focus on another candidate.

Gyroscopes are candidates of choice, since the thesis would take advantage of relations between CSEM and industrial partners such as ST Microelectronics. It is a technology, such as the SiRRS-01 MEMS gyroscope, that has been also used in the automobile industry. Nevertheless, the inherent complexity of a MEMS gyroscope makes the study a lot more challenging than a simpler accelerometer.

To conclude, the final choice for a test vehicle was validated following the arguments:

- Solid existing scientific background,
- Availability and maturity aspects of COTS component,
- Interest of industrial partners,
- Comparison to the classical single-parameter reliability evaluation for out-of-the shell MEMS accelerometers (and EEE provider). Those results were carried out under ESA "MEMS REAL"¹² project.

2.1.5 Selected component

Following, 120 COTS MEMS inertial measurement units were obtained from the partner manufacturer ST Microelectronics and will be henceforth defined as Devices Under Test (DUTs). The DUTs feature a dual axis in-plane accelerometer with an out-of-plane gyroscope. Its characteristics are reported in Table 2.6. From an experimental standpoint,

¹¹ Source: <http://www.tronicsgroup.com/Airbus-Group-and-Tronics-partner-on-RF-MEMS-switches>

¹² Selection process for an ESA project where were put in competition First Sensor, Murata and ST Microelectronics. First Sensor has been demonstrated as the most suitable test vehicle. Based on the obtained evaluation, the presented results shown good reliability outcome. ESA-ESTEC Contract No: 4000109903/13/NL/PA.

measurements of accelerations and rates require distinct procedure: gravity can simply be used as ubiquitous benchmark while rate must be generated using an apparatus. Therefore, using gravity for the functional characterization of the devices appears more practical and more constant: only the accelerometers' signals will therefore be used for characterization of the state of the devices throughout the thesis. The signals of the gyroscope are however recorded for their qualitative informative values.

Table 2.6: Characteristics of the chosen IMU.

Manufacturer	ST Microelectronics
Series code	COMBOGZAXY
Component Type	MEMS (pre-commercial)
Applications	Automotive field
Functions	1D gyroscope 2D accelerometers Temperature compensation
Design	Ceramic package, non-hermetic
Interface	SPI (Serial Peripheral Interface) with wettable flanks

2.2 Pre-evaluation of the MEMS device

This chapter section documents the typical workflow for a construction analysis (CA) of electronic components as commonly followed at ESTEC. This section therefore references the pristine condition in all subsystems of the device for future comparison. Five "COMBOGZAXY" IMU MEMS components were picked for the CA. Under the term of "construction analysis" are encompassed the tests:

- External Visual Inspection (Section 2.2.1.1), which aims at revealing any external anomaly if present.
- Physical dimensions (Section 2.2.1.2), to be compared to the datasheet value.
- Radiographic Inspection (Section 2.2.1.3), non-destructive technique for detecting any internal anomaly before package opening.
- Internal Visual Inspection (Section 2.2.1.4), which helps at understanding the architecture of the device and the underlying manufacturing technique – detecting particle contamination, anomaly, or feature of interest not visible by radiographic inspection.
- Bond strength (Section 2.2.1.5) evaluates the strength of wire bonds by mean of a pull test, compared to the standard.
- Die shear (Section 2.2.1.6) tests the resistance to shear loads of the dies' adhesive to the ceramic package with respect to the relevant standard.
- Microsections (Section 2.2.1.7) give insights of the internal architectures of the whole device by uncovering interfaces and bonding techniques.
- Materials analysis (Section 2.2.1.8) use the microsections to identify, by mean of SEM and X-ray techniques, materials used in the device and those of potential particle contamination.

As part of the series of tests to be performed during this thesis program, results of this CA will serve as a basis for Failure Mode and Effects Analysis to be carried out following the reliability test campaigns. It also provides the reader the opportunity to discover the IMUs used in this thesis.

2.2.1 Analyses

This paragraph summarizes the analysis flow as per ESA's guidelines, and its most important results. The list of tests in Table 2.7 represents the typical workflow used for the characterization and qualification of MEMS components.

Table 2.7: List of tests performed in the frame of the construction analysis and corresponding ESA standards.

Test Description	Test Method	Results
1. External Visual Inspection	ESCC 2059000 Iss.3	Passed
2. Physical dimensions	MFR datasheet	Passed
3. Radiographic Inspection	ESCC 2099000 Iss.2	Passed
4. De-capping	Laboratory techniques	Passed
5. Internal Visual Inspection	ESCC 2049000 Iss.3	Passed

6. Bond strength	MIL-STD-883K/Change2, TM 2011.9, test condition D (wire pull, double bond)	Passed
7. Die shear	MIL-STD-883K/Change2, TM 2019.9	Passed
8. Microsections	Laboratory techniques	Passed
9. SEM & Material analysis	Laboratory techniques, ESCC 23500	Passed

The device is not hermetically packaged. Therefore, the usual guideline's tests such as PIND (Particles Impacts Noise Detection), seal and RGA (Residual Gas Analysis) tests were not performed.

2.2.1.1 External Visual Inspection

The images were taken with the ZEISS STEREO DISCOVER V8 microscope. The external visual inspection test was carried out according to ESCC Basic Specification No. 2059000 Iss.3. This inspection did not reveal any anomaly affecting the sample. Higher resolutions pictures with more thorough descriptions are available in Appendix B. The presence of a vent on the package (Figure 2.8) indicated that the device is non-hermetic. The lid adhesive, a glass frit, is loaded with metallic particle, making it conductive.

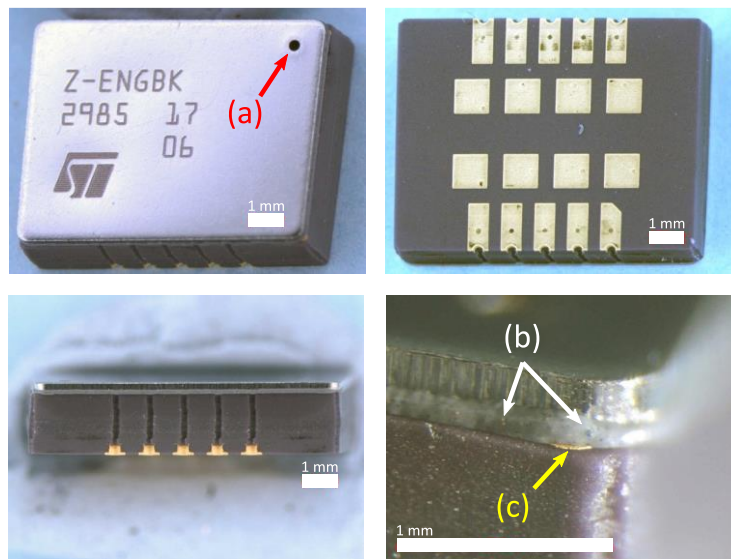


Figure 2.8: External view of the device: (a) vent, (b) lid adhesive (glass frit), (c) gold contact pad.

2.2.1.2 Physical dimensions

Dimensions have been measured on the 5 samples used for the construction analysis and have been compared to the datasheet values (Table 2.8). The measurement has been performed with a MITUTOYO digital caliper, model CD-15PMXR. Measurements show no significant deviation from the datasheet values. Weight has been measured using the Sartorius LP4200 Master Pro balance.

Table 2.8: Deviation of measured dimensions compared to the datasheet values.

	Width	Length	Height
Dimensions [mm]	7.49	9.61	2.27
Std. Dev.	0.02	<0.01	<0.01
Std. Dev. with respect to average	<0.3%	<0.1%	<0.4%
Weight			
Value [g]	0.453		
Std. Dev.	0.0010		
Std. Dev. with respect to average	0.2%		

2.2.1.3 Radiographic inspection

Radiographic inspection was performed with the YXLON Y.Cheetah radiographic system in accordance with ESCC Basic Specification No. 2099000 Iss.2. This inspection did not reveal any anomaly affecting the sample. Radiographic and internal views of a device are provided in Figure 2.9.

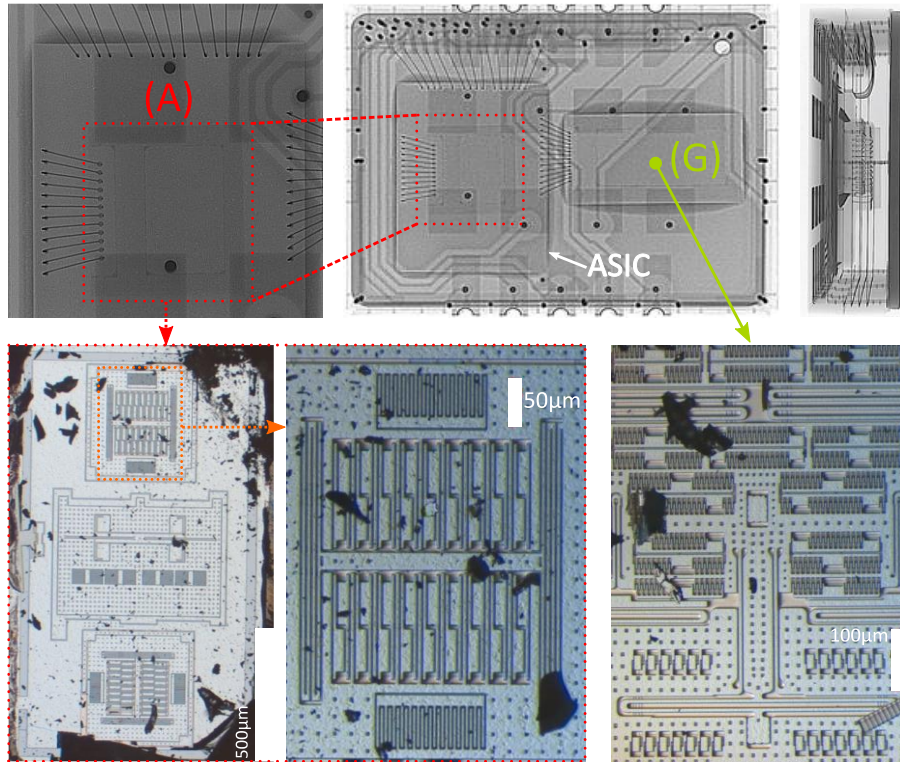


Figure 2.9: Radiographic views of device and uncapped MEMS dies. (A) stands for accelerometer, (G) for gyroscope. The MEMS structures are clearly visible (debris are present) and uncovers the complexity of the system, as explained in the paragraph.

2.2.1.4 Internal visual inspection

The 5 parts were de-capped by use of a surgical scalpel. The Internal Visual Inspection (IVI) was performed according to ESCC Basic Specification No. 2049000 Iss.3. The instrument used was the STEREO DISCOVER V8 ZEISS microscope. Figure 2.10 presents details of the interior of the device. The dies are joint with high precision and reproducibility, such as expected from an industrial process.

Notable observations are the presence of a conformal gel coating the dies. It is applied to protect against oxidation, and possibly to dampen vibrations and shocks, and insure electrical insulation. The gel also covers the wire bonds, leaving droplets attached to the suspended element in several devices. Apparent weight of the wire is therefore increased (this observation has not however been quantified), which could cause a bigger amplitude of the wire's movement during shock or vibration test. Holes at the menisci of gel formed at the corner, for instance between the ASIC's surface and the accelerometer die, are present. Finally, a detail of the silver die attach adhesive displays a phase separation between the metallic flakes (silver) suspended in the matrix (epoxy). The importance of this separation is unknown on the thermal properties of the adhesive. Anticipating the results, post-thermal tests investigations demonstrate that cracking can be initiated at those regions, between the two dies. Separation is also visible at the dies' corners: in this case, no crack initiation has been observed.

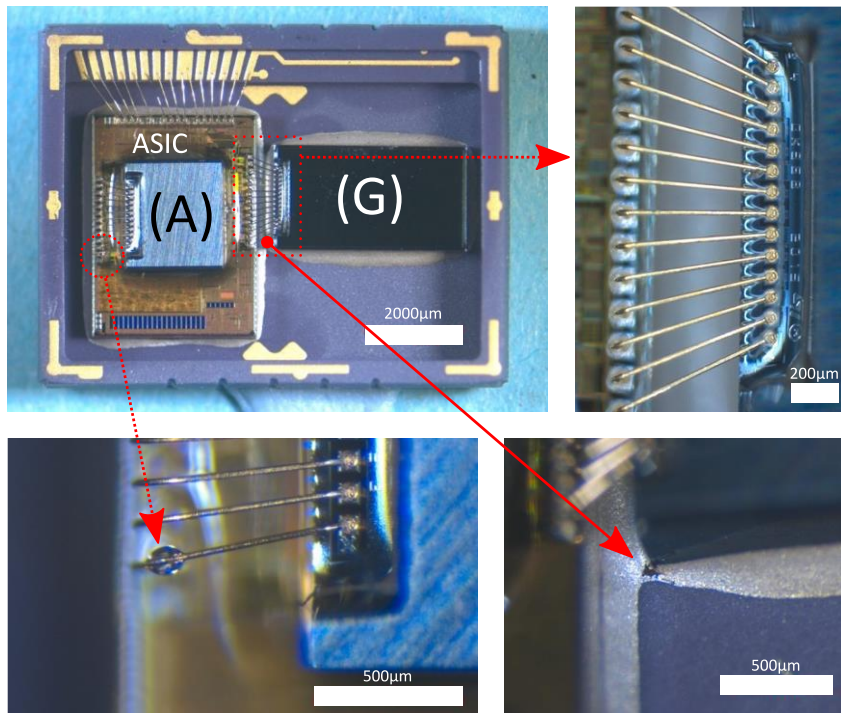


Figure 2.10: Optical views of a device with lid removed. (A) stands for accelerometer, (G) for gyroscope. Details: wire bonds and die attach.

2.2.1.5 Bond strength test

The bond strength test was performed in accordance with MIL-STD-883K (w/CHANGE2), TM 2011.9, test condition D – wire pull (double bond), using a Nordson Dage 4000PLUS bond pull tester. The coating gel, present on all samples, was not removed. Samples had not been submitted to heat storage before bond strength testing.

Each device features a total number of 41 wires.

- 12 wires from the accelerometer to the ASIC.
- 15 wires from the ASIC to contact pads on the ceramic package.
- 14 wires from the gyroscope to the ASIC.

Bond pull started at the first wire at the gyroscope die, at the vent's side. It continued clockwise until the last wire on the ASIC as depicted in Figure 2.11. It was observed that wires from the ASIC to the ceramic package were the weakest, in general. Force distributions for the ASIC-package, ASIC-gyroscope, ASIC-accelerometer bonds are shown in said figure. All of them broke at a greater force than the 25 mN (500 μ m/s rate) required by the specification (see MIL-STD-883K w/CHANGE2¹³, TM 2011.9, TABLE I, test condition D, Au 0.0010 in, post seal). Therefore, the 5 MEMS samples satisfactorily passed the bond strength.

- Most of the wires broke with failure category a-1: at the neckdown point on the accelerometer, gyroscope, or package side, that is, the opposite of the ASIC side.
- 6 wires broke on the ASIC side (failure category a-9).
- 2 wires broke approximately at the middle of the wire arc (failure category a-2).
- 1 bond broke at the interface between wire and metallization (a-3) with a value of 88 mN, which is higher than the 25 mN limit specified by the standard.

The detailed results for each of the 5 samples are given in Appendix B.

¹³ Forces in the standard are expressed in [gf] units. They are converted to S.I. units, here [mN].

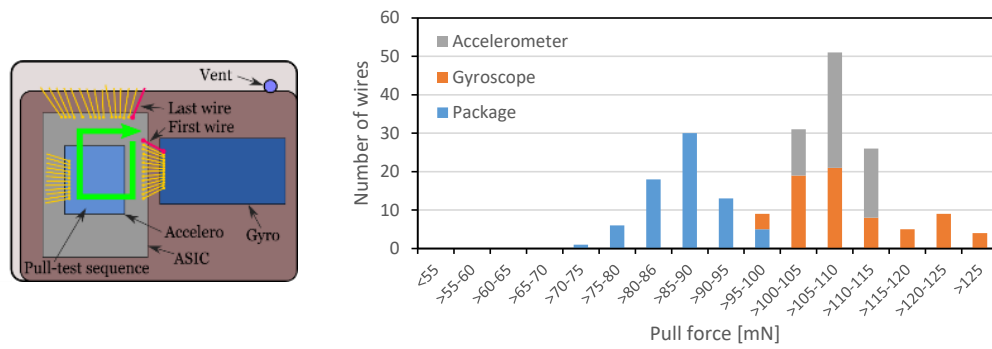


Figure 2.11: Strength distribution of the wire bonds. The connections between the ASIC and the package distribution are centered at the 85-90 mN pull force while the connections between the gyroscope, respectively the accelerometer and the ASIC are centered at around 105-110 mN.

2.2.1.6 Die shear test

The bond strength test was performed in accordance with MIL-STD-883K (w/CHANGE2), TM 2019.9, using a DAGE 4000PLUS die shear tester. The coating gel remained in place during testing.

Neither the accelerometer nor the gyroscope nor the ASIC die could be detached, as the DAGE 4000 PLUS instrument reached the maximum force of 50 N specified in the MIL-STD-883K (w/CHANGE2), TM 2019.9. The MEMS device therefore passed satisfactorily the die shear test.

2.2.1.7 Microsections

Sample G11-FFF-05 was potted in resin after bond strength test, to perform three cross-sections visible in Figure 2.12. The gel was not removed for this operation. A zoomed-in view of the accelerometer solder and solder reflow is shown. The aforementioned phase separation of the die attach silver-loaded epoxy is also highlighted here. For more details, the reader is invited to refer to Appendix B.

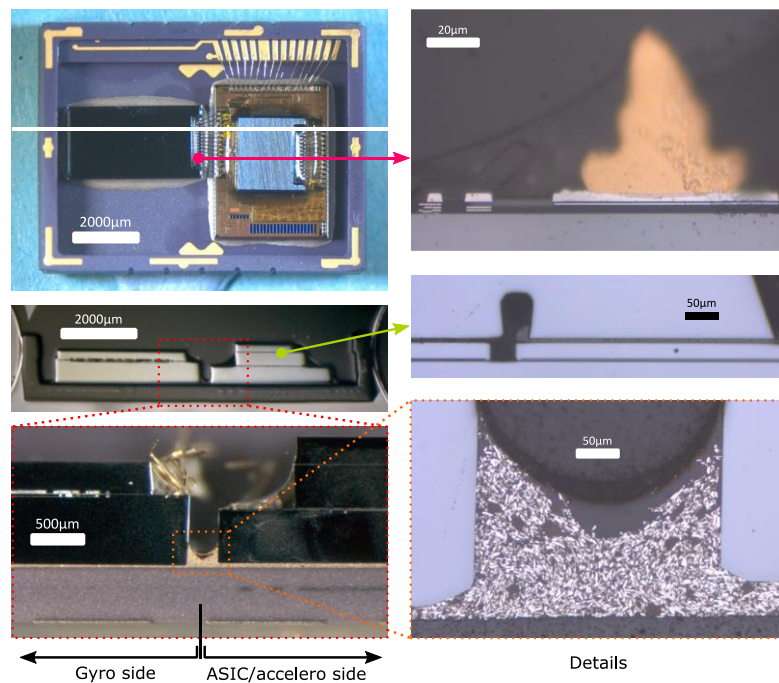


Figure 2.12: Sections of optical microsections. (left) The white line on the device’s image depicts the location of the cross-section. (right) Details of a wire bond pad (top), the accelerometer intra-die solder (middle) and the die attach (bottom) are shown.

2.2.1.8 SEM and materials analyses

The material analysis was carried using FEI QUANTA FEG 650 SEM and Oxford X-Max 50mm² EDS at ESTEC. Complementary analyses were performed on CSEM's FEI Scios 2 LoVac Dual Beam with FIB capabilities. It is equipped with an EDS Octane Elite Super from EDAX METEK.

No information regarding the composition of the materials was supplied by the manufacturer. Therefore, their identification has been compiled in list of materials presented in Table 2.9.

Table 2.9: Materials analysis of the devices.

Part	Identified material
0-level package (gyroscope)	Si (100%)
0-level package (accelerometer)	Si (100%)
0-level package adhesive to 1-level package	Resin with Ag filler
0-level package solder	Pb O with Si Mg and Al fillers, probably lead silicate glass frit.
Bond wires	Au (100%)
Conformal gel	Si O (C) silicone
Ceramic package	Al O
Ceramic package internal tracks	SiO ₂ , W
Ceramic package outer contact pads	Al ₂ O ₃ , W, Ni, Au
Top layer of the bond pads (gyroscope)	Al (100%)
Lid base material	Stainless steel Fe-Cr
Lid adhesive	Zn, Na and O glass frit

SEM micrographs of a selection of previous optical cross-section are reported in Appendix B.

2.2.2 Discussion of the observations

All five non-hermetic MEMS-based COMBOGZAXY inertial measurement units, picked randomly among the 120 devices provided by STMicroelectronics in the frame of the thesis, passed the constructional analysis successfully. Overall, the evaluation showed mastered design and manufacturing processes.

The external visual inspection (Section 2.2.1.1) did not call for any notice besides the wear traces on the electrical contacts, which indicated that a read-out is performed on the devices before shipment. Physical dimensions (Section 2.2.1.2) and weight of the devices stand within narrow ranges. Standard deviation has been measured to be no greater than 0.3% of the datasheet's values (dimensions and mass included). Nothing stands out from the radiographic inspection (Section 2.2.1.3) either. The inspection also identified a phase separation of the silver-filled adhesive the dies and the package. This was observed in observed in 4 of the 5 parts submitted to this CA (see Section 2.2.1.7).

De-capping was performed using a surgical blade, free of damage for the internal part of the device. The absence of large-scale damage permitted to analyze the composition of the pristine lid material and adhesive in Section 2.2.1.8.

The dies are conformally coated with a protective and isolating silicone gel, as revealed by the internal visual inspection (Section 2.2.1.4). Bubble trapped in the menisci formed by the gel at the edges of the ASIC-accelerometer dies have been detected. Additionally, droplets of various sizes have been observed to be attached on the wire bonds (typical case in Figure 2.10).

Bond strength (Section 2.2.1.5) showed excellent resistance, as compared with the reference value of 25 mN for 25 μm diameter wire bonds in MIL-STD-883K/Change2, TM 2011.9, test condition D (wire pull, double bond). Values for the package only are centered on 865 mN with standard deviation of 5.2 mN, while the accelerometer only

features a force distribution centered at 108 mN with standard deviation of 3.4 mN. The gyroscope-ASIC bonds are centered at 110 mN with standard deviation being 8.4 mN. Higher values found for the gyroscope and accelerometer are explained by the shorter length and lower apex of the wire bonds. All devices passed die shear testing (Section 2.2.1.6) as no detachment has occurred for the maximum force of 5 N specified in MIL-STD-883K/Change2, TM 2019.9, stating a high resistance of the compound used for 0-level bonding regardless of the previous observation. Further analyses on those two points, taking this information as a reference, will be covered in Chapter 4.

The microsections (Section 2.2.1.7) reveal minor porosity in the adhesive found at the interface between the ASIC and the accelerometer (see Appendix B). Morphology of the solder within the 0-level package of the accelerometer and the gyroscope showed fine control of the process. The most notable observation from the materials analysis (Section 2.2.1.8) was the presence of lead in the 0-level package frit. However, no noteworthy discrepancies nor forbidden materials or compounds as per space applications were found.

In general, more investigation analysis will be conducted during FMEA in the thesis and will enable better understanding of the role of found non-critical observations. As for potential use of COMBOGZAXY devices for space application, additional indispensable analyses would be necessary, namely due to the lack of hermeticity of the package or the presence of the conformal gel (due to its unknown behavior under vacuum).

2.2.3 Conclusions from the construction analysis

The tested parts all successfully passed the tests and inspections carried out in this CA. The devices demonstrated well-controlled manufacturing capabilities and quality assurance. Results were excellent, with the following noteworthy observations:

- 1) Conductive adhesive between package and dies:
 - a. A separation of the two compounds of the silver-filled adhesive, between the ASIC and the gyroscope at the interface with the ceramic package, was observed in 4 of the 5 parts submitted to this CA.
 - b. Criticality of this separation is yet to be evaluated in light of reliability test campaign.
 - c. All devices passed however the die shear test by a large margin, indicating that it does not impede on mechanical resistance.
- 2) Conformal gel coating the subsystems in the device:
 - a. Bubbles are present in the gel being used as coating of the subsystems (dies, wire bonds and contact pads). Expansion of the gas trapped inside could lead to dispersion of said gel into the package.
 - b. Droplets of gel of various sizes have been observed to be attached to the wire bonds of all 5 devices, which could be problematic in case of high-g loads: due to droplets' inertia. Alternatively, detachment of said droplets could occur.

Chapter 3 Experimental method

This research considers a MEMS device to be a complete functional unit that includes an ASIC (Application Specific Integrated Circuit) chip, sensing dies (accelerometer and gyroscope) as well as various package-related elements: wire bonds, adhesives, ceramic enclosure with electrical leads and cover lid. The test procedures aim at overstressing the devices beyond their nominal operational conditions, in order to assess their robustness and reliability. This chapter is structured around three sections:

- Section 3.1 covers the experimental framework for the test campaigns to come. The used equipment, the standards from which are inspired the developed procedures as well as software and hardware aspects related to devices' functional characterization.
- Section 3.2 details the experimental conditions, data quality and the possible experimental errors.
- Section 3.3 presents the first steps leading to the test campaigns: the namely the initial screening procedure and the burn-in step that aims at eliminating cases of infant mortality.
- Section 3.4 finally develops the testing methodology. It starts with mono-parameter procedures, aiming at probing the extrema for environmental loads. In a second step, the novel bi-parameter, accumulative flows are presented. The section concludes with a global view of the test plan.

The test conditions were selected and gauged to lead to failure of one or several of the enumerated subsystems and elements constituting the MEMS device. Namely, the following points are in focus: packaging, mechanical integrity of the device, electronic functionalities of the MEMS sensors, the ASIC and dependencies (electrical connections).

3.1 Test hardware and standards

This section details all used hardware, test methods and standards that have served in the many tests performed in the frame of this multifaceted reliability study. A "campaign" defines here one specific type or sequence of test(s) applied to a given set of devices. The campaigns have been performed in most of the cases at CSEM in Switzerland, while some sections have been performed at ESTEC in The Netherlands. By default, any description will assume the use of hardware at CSEM and will be specified otherwise.

3.1.1 Equipment repository

Hereafter are compiled the various equipment that has been used for reliability testing. It mostly concerns types of tests that have been carried out following the flows presented later in Section 3.4.3. The list, reported in Table 3.1, is sorted out by test type (or nature, should it be thermal or mechanical).

Table 3.1: List of equipment.

Test type	Hardware	Technical specifications
Temperature cycling	ESPEC SH-662 single humidity chamber	Temperature -60 to 190°C (extended) Humidity control 30-95% RH Ave. change rate 2.5°C/min heating and 0.8°C/min cooling
Temperature shocks	ESPEC TSE-11-A dual chamber	Temperature -60 to 200°C Worst case recovery time 15 min
Vibration testing Location: CSEM	<ul style="list-style-type: none"> • Bruël&Kjaer LDS-V555 low force shaker • LPA1000 Linear Power Amplifier 	Sine force 0.94 kN, velocity (sine peak) 1.5 m/s, 100 g acceleration (unloaded), 25.4 mm displacement (half range peak-to-peak), 25 kg payload capacity. Rated power output 951 VA @4.0Ω, max. power output 1294 VA @4.0Ω, frequency range 40 Hz to 10 kHz with distortion <0.2% up to 5 kHz, maximum output current 17.75 A rms, SNR > 95 dB

	<ul style="list-style-type: none"> LDS Field Power Supply 	Field voltage at nominal supply 70 VDC @5.5Ω, low-field voltage 44 VDC 5.5Ω, full field current 12.7 A and low field current 8 A.
Location: ESTEC	<ul style="list-style-type: none"> Vibration Research VR4600 shaker Vibration Research VR9500 power amplifier 	Sine force 0.82 kN, velocity (sine peak 1.5 m/s, 95g acceleration (unloaded), 45 mm peak-to-peak displacement). Output voltage 105 V rms, output current 40 A rms, maximum continuous dissipation 4200 VA rsm.

Other equipment used repetitively for non-destructive (radiographic) testing during test campaigns are reported in Table 3.2 below.

Table 3.2: Non-destructive measurement equipment.

Test type	Hardware	Technical specifications
Radiographic inspection	YXLON Cheetah	X-ray voltage 25-160 kV, sub-μm resolution.
Computerized Tomography Scans (CT)	General Electrics v tome x s240 RX-SOLUTIONS Utratom micro CT	Up to 180 kV, 200 nm resolution. Equipped with DXR250RT Real Time Detector, amorphous silicon, 4000x4000 pixels imaging. Dual X-ray source, Hamamatsu 230 kV (reflection mode) and 160 kV (transmission mode). A high-resolution plane sensor (2176 x 1792 px) with micro positioning stage

3.1.2 Standards

One of the aims of the present research consists in demonstrating that currently used standards fail to yield conclusive results from the assessment of highly robust devices. The main concern relates to the fact that, as they can pass a given test without displaying any significant degradation or failure, little to no exploitable information of their lifetime can be drawn. The proposed test campaigns are therefore taking as a baseline the existing standards. Stress conditions will then be increased to harsher levels.

Reliability requirements for space are typically stricter than those for non-space applications and are strongly related to those from the military domain. This proximity is shown by the widespread use of U.S. military standards (MIL-STD) in various tests procedures, even within the European community and the European Space Components Coordination (ESCC). The chronology of a space mission dictates these strict guidelines: conditions of manufacturing, assembly and transport to the launch site (implicating vibration, shocks, thermal and humidity considerations), installation of the payload on the launch vehicle, the launch itself with severe vibration and pyrotechnic-sourced shocks and finally the space mission itself with the inhospitable environment of space (thermal and radiation). The testing methodology and test plan must address the variety of conditions mentioned above with the highest fidelity and quality to prevent failure in orbit.

The chosen test methods will be detailed in the following sections. Table 3.3 hereafter is reporting the used standards (see Table 1.6 for more details). While being good starting points, they were recurrently adapted in this thesis to better fit to the high robustness of the DUTs described in Section 2.1.4.

Table 3.3: U.S. Department of Defense standards used in MEMS reliability assessment for space application.

Standard designation	Title
MIL-STD-883K	Test method standard microcircuits
MIL-STD-750-1A	Environmental test methods for semiconductor devices

The standards mentioned above are often referred to in the ESCC standards applicable to MEMS and reported in Table 3.4.

Table 3.4: European Space Component Coordination (ESCC) standards.

Standard designation	Title
ESCC Generic Specification No. 9000	Integrated circuits: monolithic and multichip microcircuits, wire-bonded, hermetically sealed & flip-chip monolithic microcircuits, solder ball bonded, hermetically and non-hermetically sealed & die.
ESCC 2269000 Basic Specification No. 2269000	Evaluation test program applicable to ESCC No. 9000.

It is to be noted that none of the reported standards are mentioning “MEMS” in their titles and descriptions, but rather refer to “microcircuits” in general. The historical reason lies in the epoch of their definition. As covered in Chapter 1, MEMS debuted in the 60s but reached maturity for commercialization only in the 80s. During the space race, the burgeoning era of microelectronics and microcircuits called for efforts towards standardization. This reaffirms the need to overhaul the framework within which the MEMS community is working.

3.1.3 Functional characterization

To assure the functionality of the DUTs, a pre-evaluation before and after the test cycle was performed. The readouts from the temperature sensors, in-plane (X and Y) accelerations and out-of-plane (Z) rate measurements are recorded. A custom-made read-out bench has been designed for retrieving the analogic signal from the devices (Figure 3.1).

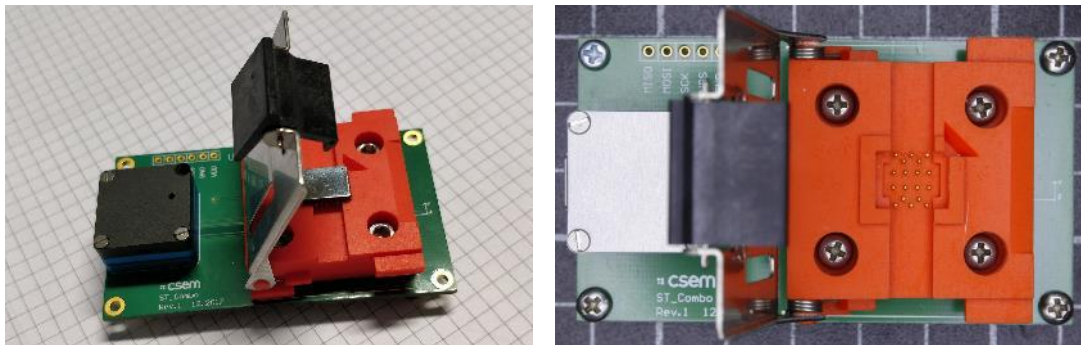


Figure 3.1: Test bench with the COMBOG device in place (left) and top view (right) with the 0.8 mm pogo-pins enabling the connection. The top lid permits to clamp the sensor tightly in the housing, made of non-conductive resin. The socket is fixed into a U-shaped aluminum profile with controlled orthogonality of its sides for better (X, Y, Z) positioning.

Read-out is made at 200 Hz through an in-house operating system and processing platform from CSEM, connected by USB to an Apple Macbook computer. The implementation is made possible thanks to a computer running a Unix distribution (compatible with either macOS or Linux), the serial port terminal CoolTerm and Sysquake, a proprietary numerical computation environment (used for live display). The outputs are 6-columns *.txt files (time, temperature, acc X, acc Y, rate X (unused), rate Z) text files that are treated with a MATLAB script, permitting extraction of the data from the sensors. The functional test only considers the readouts of the accelerometers, while the signals of the temperature sensor and the out-of-plane gyroscope are only recorded. The procedure uses gravity ($\pm g$) as reference and lasts 60 seconds – divided into sequences of 10 seconds following the order: neutral, -X, -Y, +X, +Y, neutral. The test is done on a flat, levelled ESD-safe surface. The text file is then fed to the MATLAB script which extracts the data and plateaus of gravity (Figure 3.2).

3.1.4 Failure criteria

A dedicated, finite differences-based algorithm permits to identify the acceleration plateaus and extract the values for $0g$, $+1g$ and $-1g$ in terms of the device’s own arbitrary units, which are then normalized to the value of gravity based on the value at $t=0$. Mathematically:

$$K_{0,i} = \frac{a_{+g,i} + a_{-g,i}}{2} \quad K_{1,i} = \frac{a_{+g,i} - a_{-g,i}}{2}$$

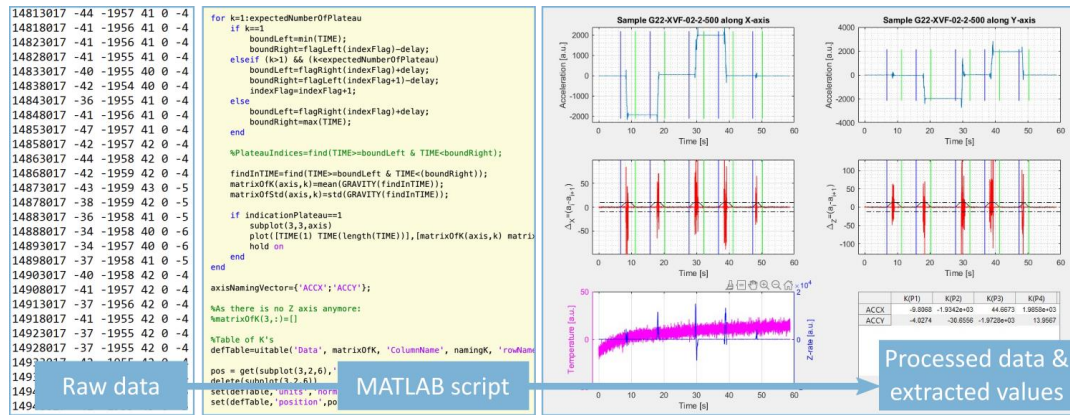


Figure 3.2: Example of data obtained from the devices and automatic processing.

With $K_{0,i}$ the computed zero-value, $K_{1,i}$ the computed average value of +1g in arbitrary units. The raw signal $a_{\pm g,i}$ [a.u.] is given by the accelerometer when subjected to an acceleration of $\pm g$ in the primary direction i . A device is declared failed when no signal can be obtained, or when signal noise overcomes a threshold equivalent to 1.5 times the standard deviation of the plateau, or when one of the following acceptance criteria is not met:

- Deviation of the value of the current $K_{1,i}$ with respect to $K_{1,i}^o$, the value before testing.

$$D_1 = \frac{K_{1,i} - K_{1,i}^o}{K_{1,i}^o};$$

- Deviation of the value of the current $K_{0,i}$ with respect to $K_{0,i}^o$, the value before testing, with respect to the reference $K_{1,i}^o$.

$$D_2 = \frac{K_{0,i} - K_{0,i}^o}{K_{1,i}^o}$$

The full MATLAB script is available in Appendix C. For each step, the deviation of the acceleration measurement is compared with the value at time-zero, allowing for plotting the graphs of the evolutions of D_0 and D_1 as the number of cycles increases. The outputs, for a test step, are two plots for the deviation of the accelerometers' readouts along the X and Y axes, as shown in Figure 3.3.

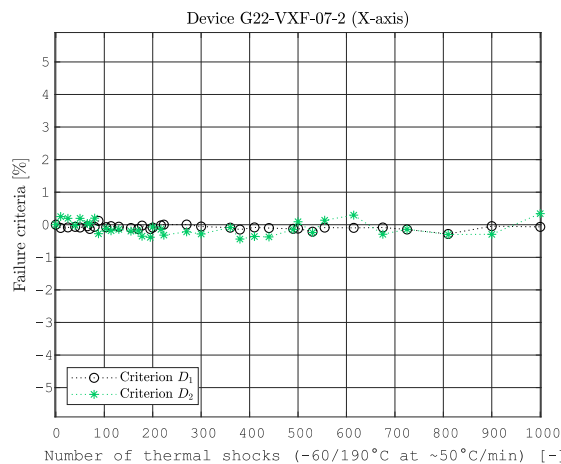


Figure 3.3: Plot of the deviations of the two failure criteria for the X-axis after 1000 thermal shocks.

3.2 Experimental details

3.2.1 General experimental setup

The following testing conditions are met:

- Room temperature: $(22 \pm 3) ^\circ\text{C}$
- Relative humidity: $(55 +10/-20) \%$
- Atmospheric pressure

Although the DUT features both an accelerometer as well as a gyroscope, the latter's readouts are only used sporadically. In most cases, when speaking of devices' signals, the accelerometer's readout is meant. Gravity in Neuchâtel, Switzerland, 443 meters above sea level, is used as a benchmark. Hereafter is a schematic of the device and the placement of the sensor. Its features in (Figure 3.4) are to scale.

The bench presented in Section 3.1.3 enables the recording of the readouts of the temperature sensor, the Ω_z gyroscope and the X and Y accelerometers at a frequency of 200 Hz. Raw values are saved and treated thanks to the MATLAB script enabling automatic extractions of the values of the acceleration in terms of gravity constant g . Measurements from the temperature sensor and gyroscope are not used in the present work, though remain of interest for a purely informational purpose. For the functional characterization, it takes 60 seconds to test all main directions of the accelerometers' axis (neutral, -X, -Y, +X, +Y, neutral). Gravity is extracted using this data and compared to the zero-time initial values.

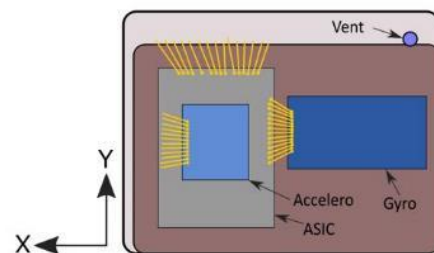


Figure 3.4: Schematic of the device.

3.2.2 Data quality and experimental error

Since functional testing remains a manual operation with various possible sources of deviations, several types of indicators have been observed throughout the test campaigns. Namely:

- Effects of time (variability on the socket's or device's side due to intrinsic heating).
- Effects of the hardware (non-identical positioning of devices in the socket due to geometrical tolerances).
- Repeatability of the measurement's condition: table levelling, ESD safe measures.

An indication of the device's stability is the measurement over time for a single static test. The sensors are temperature-compensated, and it has been observed that devices generate heat, as detected by the integrated temperature sensor. Therefore, several five-minutes long recording of the raw signals have been performed. The intrinsic noise of a typical 5-minutes measurement is shown in Figure 3.5.

Readouts follows to a normal distribution for a fixed acceleration, which would suggest that its distribution parameters could also be used as characteristic values for evaluating reliability (refer to Section 6.4.3 for further development). The device's internal temperature requires close to a minute to stabilize. The accelerometers feature standard deviations that are respectively 3.4 and 3.7 (arbitrary units), which in terms of percentage correspond to 12-13% with respect to the maximum envelope of the noisy signal for the zero-g configuration (26 and 31 in arbitrary units, respectively). These values must be compared to the amplitude of the gravity measurement, which is about 2000 (arbitrary device units). Therefore, the effect of intrinsic heating is not determinant.

Another verification has been performed by repetitive measurements (30 iterations) on an identical device, for an identical gravity check (same as for the standard functional testing) and on a same table. The measurements, reported in Table 3.5, did not show a significant manipulation error that could produce unwanted deviations. The arbitrary raw signal from the accelerometers reaches values of about $\pm 1900-2000$ when measuring gravity. In this case, the standard deviation over the 30 samples when measuring gravity is 3.4 for -g and 3.6 for +g. Overall, the manipulation error

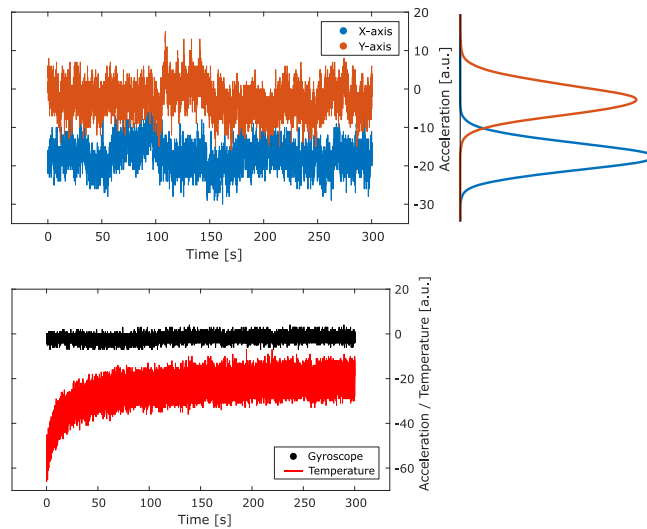


Figure 3.5: Five minutes measurement (raw signals): top is zero-g X and Y axes; bottom is gyroscope signal and temperature. Signals for stationary measurements were observed as following a normal law.

Table 3.5: Standard deviation as a percentage of the measured value of gravity (arbitrary unit). Sample size: 30 devices.

[%]	X-axis	Y-axis
+g	0.20	0.18
-g	0.15	-0.18
2g	0.07	0.07

does not have a significant effect on the measurement since the magnitude is the same between the 5-minutes static test and the 30 identical manual functional tests.

Another factor of influence could be the geographic location of the test bench during functional testing. During the present research, experiments have been carried out in different locations: at CSEM in Switzerland (430 m above sea level) and at ESTEC in The Netherland, sea level. From the development of the gravitational field equation (Newton) [223], one gets for a distance $R = R_0 + h$ from Earth's center:

$$g = \left(\frac{R_0}{R_0 + h} \right)^2 g_0$$

With $g_0 = 9.8145 \text{ m/s}^2$ the Earth's gravity at sea level and R_0 Earth's average radius. Since the altitude $h \ll R_0$, one can assume that gravity does not change significantly regardless of the location of testing.

Over testing, the devices' package lid commonly became undone and had to be reglued. This is not considered as a failure in this work: the DUTs being not hermetic, a loss of integrity does not lead to a deviation or loss of signal, as long as the MEMS device, the ASIC and the interconnects are still intact. 12 devices in total have experienced this issue, mostly in advanced phases of the test campaigns including vibration. This is due to the application of a pressure (not quantified) on the top of the package due to the sample holder used in vibration. A protrusion, smaller in size than the top surface of the package's lid, has been designed in the holder's counter piece clamping the device in place¹⁴. Shear stress builds up at the adhesive (glass frit) interface between the ceramic package and the lid, causing its detachment for several devices throughout the campaigns. In all cases, the regluing operation did not lead to any significant deviation of the failure criteria (that is: less than 0.5%). Lid failure is therefore not critical to this campaign. This operation was done with a cyanoacrylate adhesive. It is therefore acknowledged as being an adequate fix.

Finally, natural aging would need to be investigated in further detail. The campaign being spread over several months, four back-up samples were put aside for episodic check of any discrepancy at the socket level. For each check, three

¹⁴ Geometrical details are reported in Appendix D.

iterations were performed over the course of 8 months. No significant variation of the measurement induced by location was observed throughout the entire experimental part of this research.

3.3 Initial screening and burn-in

An important step in reliability testing is to make sure that infant mortality is avoided by the experimental design. Infant mortality, as its name suggests, postulates that devices might experience early failures due to design flaws, particular contamination in the sensitive subsystems or manufacturing inconsistencies [224]. Graphically, it is often referred as the “bathtub” curve shown in Figure 3.6, which plots the theoretical failure rate of a given device with respect to its lifetime [225]. The curve is a superimposition of the three “ages” of a device’s lifetime: early failure (or infant mortality, as explained herein), random failure (constant failure rate) and finally: wear out failures.

Before this step, pristine devices have their dimensional and electrical characteristics measured. This information is stored in a database for use in the FMEA. The results are displayed in Appendix D.

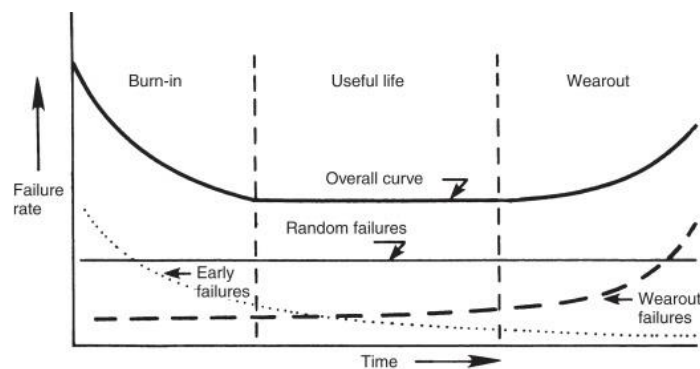


Figure 3.6: "Bathtub curve" hazard function.

Infant mortality can be avoided by mean of a burn-in procedure, which consists in performing a limited high temperature operating life test (HTOL) on the set of devices to be tested for reliability. This acts as an accelerator and position the devices’ lifetime in the “useful life” section of the aggregated curve in Figure 3.7.

In the present study, a burn-in procedure is introduced as a first step on the selected IMUs. The method follows the standard MIL-STD-883 with a test time of 260 hours at 110°C, which corresponds to the maximum nominal rating temperature for the devices. As applied bias, the maximum nominal voltage is applied during the burn-in: 3.6 VDC (forward). For doing so, as specific hardware has been developed by mean of stereolithography of high temperature resin. Four devices can be connected in parallel and powered. Devices are characterized for gravity measurement with the test bench at pristine state, after electrical inspection.

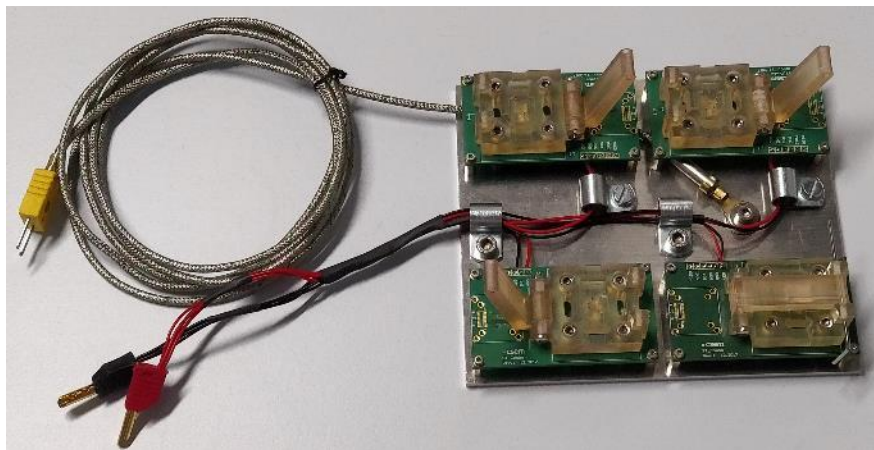


Figure 3.7: Burn-in bench with the four sockets for device connection. A thermocouple is fixed to the baseplate for continuous in-situ temperature recording.

3.4 Testing methodology

Below are reports all testing procedures that have been followed to assess the reliability and failure root-causes of the COMBOG accelerometers. The first section covers the initial testing, following the traditional one-parameter (or mono-parameter) testing procedure such as the ones that can be found in standards or qualification test plans. The following section covers the transition to multi-step, bi-parameter testing which is at the core of the present investigation of tests accumulation. Finally, the global test plan of all DUTs that have been tested throughout this research is presented.

3.4.1 Mono-parameter testing

The first series of tests that have been carried are dubbed « step-stress tests » as per the work previously reported by Marozau [65]. By step-stress, it is understood that the sequence decomposes into two steps fulfilling two different objectives:

- Step 1: Analysis of the failure sensitivity to load to identify the device reliability limit(s) and define the load parameter to be applied accordingly in Step 2. Practically: the cycles count per step is kept constant, while the stress level is increasing.
- Step 2: Device reliability test applying the load parameter defined in Step 1. This step involves repetitive (cycling) tests at a fixed load to acquire failure statistics over cycles, determine failure rate, device lifetime and failure probability at a fixed load value close to the reliability limit. Practically: the cycles count is increasing while the stress level remains constant.

The emphasis was dedicated to the following environmental and mechanical stress tests, that are particularly important for space application: temperature cycling, thermal shocks, and mechanical vibration. These conditions are met during all the steps of a spacecraft's lifetime until launch. In space, a variable thermal environment is then only left, besides the specific cases of a spacecraft's atmospheric reentry or planetary/satellite landing. Radiations have not been covered in the present study. The interested reader is invited to refer to the Bandi's dissertation [226] or Marozau's paper [65] for further developments on radiation testing.

The two-step test procedure is graphically shown in Figure 3.8. The definitions of the two natures of testing are developed hereafter.

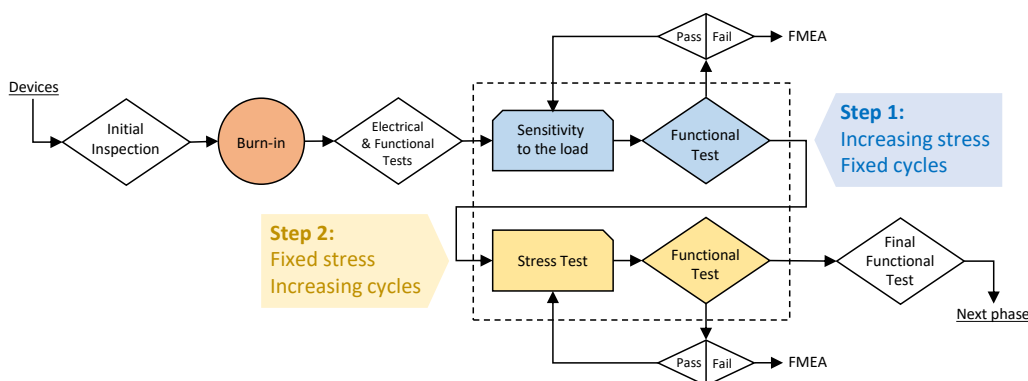


Figure 3.8: Test flow for the two-step stress reliability evaluation.

3.4.1.1 Thermal

Temperature cycles and thermal shocks are distinguished between their respective thermal gradients. Both notions are respectively described in the standard MIL-STD-883, Test Method 1010 and MIL-STD-750-1A, Test Method 1051. In the present work, the different effects resulting from these two tests are highlighted. Graphically, the differences become obvious when a fixed time frame is observed, as illustrated in Figure 3.9 with the example of a temperature range of 250°C between -60°C and +190°C, with a 10-minute soak time.

The difference notably lies at the total cumulative time spent at the highest and lowest temperatures, also name *soak time*. Another notion is often used in thermal testing, with the *dwel time*: it corresponds to the time between the change of apparatus' set point, to when the measured temperature has reached it. For comparing those two thermal tests, one considers the high and low soak times contained within the 10% temperature bounds of the full range. In other words, taking the range $T_{min} = -60^{\circ}C$ and $T_{max} = 190^{\circ}C$, this means the cumulative time spent above $165^{\circ}C$ or below $-35^{\circ}C$. In mathematical terms, the two subranges can be expressed as a function of the total range $\Delta T = T_{max} - T_{min}$.

$$\begin{cases} [T_{min}, T_{10}] \text{ with } T_{10} = T_{min} + (0.1 \cdot \Delta T) = -35^{\circ}C \text{ (cold range)} \\ [T_{90}, T_{max}] \text{ with } T_{90} = T_{max} - (0.1 \cdot \Delta T) = 165^{\circ}C \text{ (hot range)} \end{cases}$$

The average soak time at one or the other bound is then computed from experimental data. Table 3.6 summarizes the count. The soak time in the cold subrange is dubbed t_{10} and t_{90} in the hot subrange.

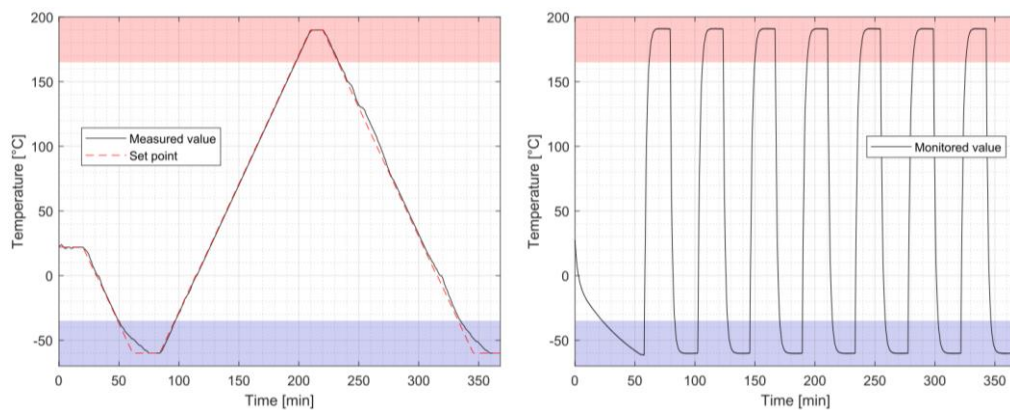


Figure 3.9: Difference in soak times between temperature cycles (left) and thermal shocks (right). The blue and red semi-transparent strips indicate the cold and hot subranges.

Table 3.6: Soak times at high and low temperature.

Test type	t_{cold} (1 cycle) [min]	t_{hot} (1 cycle) [min]	t_{cold} (220 cycles) [hr]	t_{hot} (220 cycles) [hr]
Temperature cycle	45.6	35.2	167	129
Thermal shocks	19.5	19.9	71	73

On the long term, temperature cycling implies a more extended cumulative soak time at the high and low temperatures, comparatively to thermal shocks. The difference will also be related to the thermal gradient when switching from the two extrema. As for the hot, respectively cold soak times in the temperature cycle case, this comes from the definition in the machine set points: the lowest temperature has been observed to be reached at a slower pace, as it is limited by the refrigerating capability of the used equipment. To cope with this disparity, soak time at $T = -60^{\circ}C$ has been, by design, increased to 15 minutes, instead of the 10 minutes initially defined for the high temperature set point.

Step 1 of the step-stress test in Figure 3.8 has been applied on two series of samples. Progression of the thermal load in the case of the thermal shocks is given in Table 3.7. It is to be noted that the thermocouple has been shielded in an aluminum profile. The shielded configuration permits to mitigate the strong disparity between the positive and negative thermal gradient at thermocouple level, when exposed to direct air stream in the chamber, as temperature increases and decreases, respectively. This behavior is highlighted in the figure and displays moreover a temperature overshoot in the high temperature range. The values of thermal gradients in Figure 3.10 are therefore the shielded experimentally measured values.

As for the temperature cycles, the progression does not induce any change in the thermal gradient since it is set by the user to the machine's set points. To have two equivalent points of comparison during reliability testing, the minimum and maximum temperatures have been fixed to the same values for both temperature cycling and thermal shocks.

Table 3.7: Progression of the thermal load (ranks) in temperature cycles.

THERMAL SHOCKS	Rank	T_{min}	T_{max}	ΔT	∇T_{up}	∇T_{down}
		[°C]	[°C]	[°C]	[°C/min]	
	1	-40	110	150	32	-38
	2	-55	125	180	37	-45
	3	-60	135	195	39	-51
	4	-65	145	210	41	-55
	5	-65	160	225	43	-54
	6	-65	175	240	45	-60
	7	-65	190	255	46	-59
	8	-65	200	265	47	-51

TEMPERATURE CYCLES	Rank	T_{min}	T_{max}	ΔT	$\nabla T_{up} = \nabla T_{down}$
		[°C]	[°C]	[°C]	[°C/min]
	1	-40	110	150	2
	2	-55	125	180	2
	3	-60	135	195	2
	4	-60	150	210	2
	5	-60	165	225	2
	6	-60	180	240	2
	7	-60	190	250	2

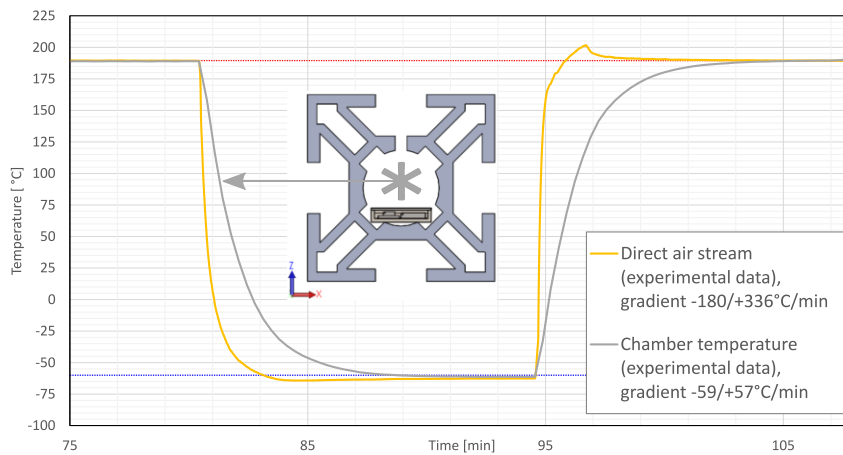


Figure 3.10: Unshielded (direct air stream) and shielded (chamber temperature) temperature plots. The position of the thermocouple inside the aluminum profile is indicated by the asterisk and corresponds to the test values indicated in this section.

3.4.1.2 Vibration

In the following chapter, by definition, a single cycle as shown in the experimental data will be understood as being three full sweeps. During vibration testing, frequency is swept between 20 to 2000 Hz with a progressive increase of the acceleration load to 50 g. Graphically, one vibration cycle in the time domain, following this definition, is represented as in Figure 3.11. The backward (mirror, as illustrated by a dot) procedure follows then immediately to go back down to the minimum measured g-value. The vibration tests are henceforth expressed in terms of full sweeps (20-2000-20 Hz).

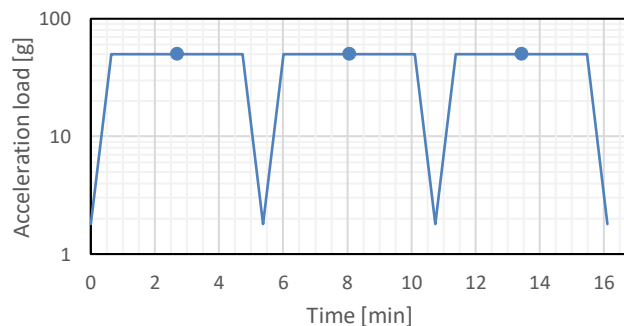


Figure 3.11: Definition of one vibration cycle in terms of g-force as a function of time. It consists of three complete sweeps from 20 to 2000, back to 20 Hz.

The vibration test applied at first in the step-stress procedures starts with the values indicated in the DUTs' datasheet. The progression (Table 3.8) follows as similar trend as for thermal testing, starting from the experimental considerations from standard MIL-STD-883K, Test Method 2007.

Graphically, a vibration sweep is visualized in log-log scale in Figure 3.12. The devices, instead of being soldered or cemented on a PCB or flat samples holder, are tested in a standalone fashion by inserting them in precision-machines aluminum sample holders (Figure 3.13, full blueprint in Appendix E). Due to slight dimensional variability, compensation is obtained by wrapping the DUTs' side and bottom faces in Parafilm (waxes and polyolefins semi-transparent films from Bemis Company, Inc.). Waxes are known materials to display low damping ratios, which makes them suitable for vibration testing. An example of this kind of application is the use of beeswax for joining the control accelerometer on the shaker's baseplate [227].

Once the sample are tightly contained in the holder, it needs to be fixed on the shaker's jig with a torque of at least 15 N·m to avoid any significant parasitic resonances modes. Only minor parasitic vibration occurred over the range 20-2000 Hz on the used equipment. An example of a full sweep (two-ways) curve is displayed in Appendix E to demonstrate the limited presence of parasitic vibration modes, despite the peculiar geometries of the sample holders.

Table 3.8: Vibration levels and acceleration progression.

Range $[v_{min}, v_{max}] = [20 \leq v \leq 2000] \text{ Hz}$			
Rate $\dot{v} = 3 \text{ octave/min}$			
Rank	Acc. [g]	Rank	Acc. [g]
1	6	6	35
2	15	7	40
3	20	8	45
4	25	9	50
5	30	10	55

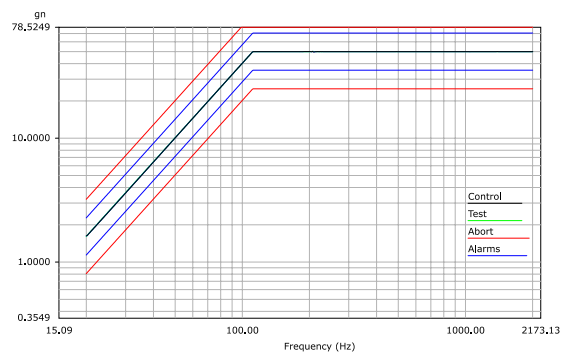


Figure 3.12: Vibration profile at 50g between 20 and 2000 Hz.

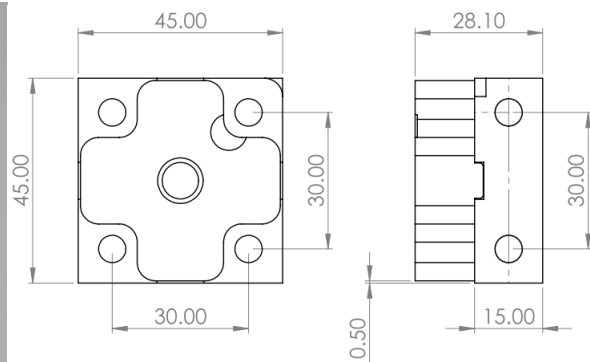


Figure 3.13: Sample holder and its dimensions, in millimeters. The weight of one sample holder with two M5 screws is 140g. Dimensions are in millimeters and technical drawings are reported in Appendix E.

3.4.2 Bi-parameter accumulative testing

Following the single parameter procedures developed previously, the campaign transits into bi-parameter testing as the primary objective of this thesis. The accumulative reliability evaluation was based on a sequential approach: testing follows a linear timeline, with tests of different natures being applied alternatively. The fundamental aim of testing two parameters sequentially, in a single test flow, is to assess testing factors and environmental conditions/effects that impact the performances of the MEMS devices. Another option is the simultaneous timing: the tests of different natures are applied at the same time during testing, combining their effects onto the devices. This was not covered hereby but features promising further investigations.

Accumulative sequential testing aimed at first to reuse devices which have survived the mono-parameter test campaign, and test them in another stress condition, namely another nature (thermal or mechanical). Graphically, the sequence can be decomposed, for a unique two-parameters cell, as displayed in Figure 3.14.

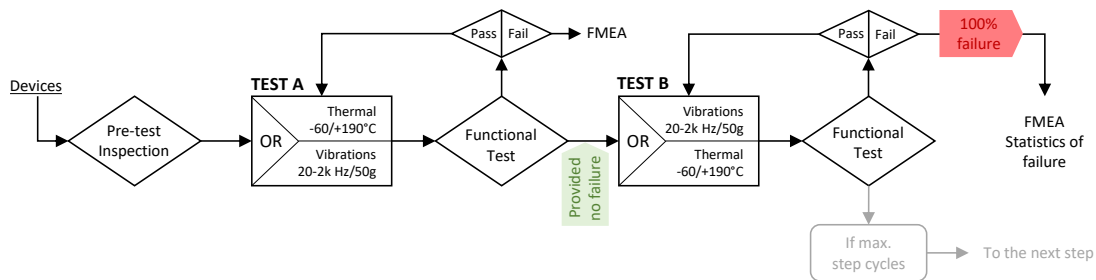


Figure 3.14: Bi-parameter accumulative sequential testing. View of the test flow.

Practically, the first loop named “TEST A” can be the mono-parameter test of Section 3.4.1, or simply a newly defined test flow. “TEST B” shall be of a stress of different nature: if A is thermal, then B is mechanical. The general view in Figure 3.15 relies mostly on this kind of progression. In “Pre-test inspection”, a burn-in procedure is implemented in the cases of newly defined test flows. The mention of “Functional Test” refers to the functional characterization described in Section 3.1.3. FMEA refers to “Failure Mode and Effects Analysis” and will be thoroughly covered in Section 4.3.

3.4.3 Global view of the test plan

Relying on accumulative testing, test series have been elaborated as the progression was taking place. In the figures below, the test flows are described on the left side by the input devices (with codenames, number in parentheses and ID numbers below), and the sequence of testing they have undergone. As the devices, in most of the sequences, experienced several successive tests without displaying failure, more steps have been progressively added. The global view of the tests flows is provided in Figure 3.15 (next page) and the results thereof will be covered in the dedicated section in Chapter 4.

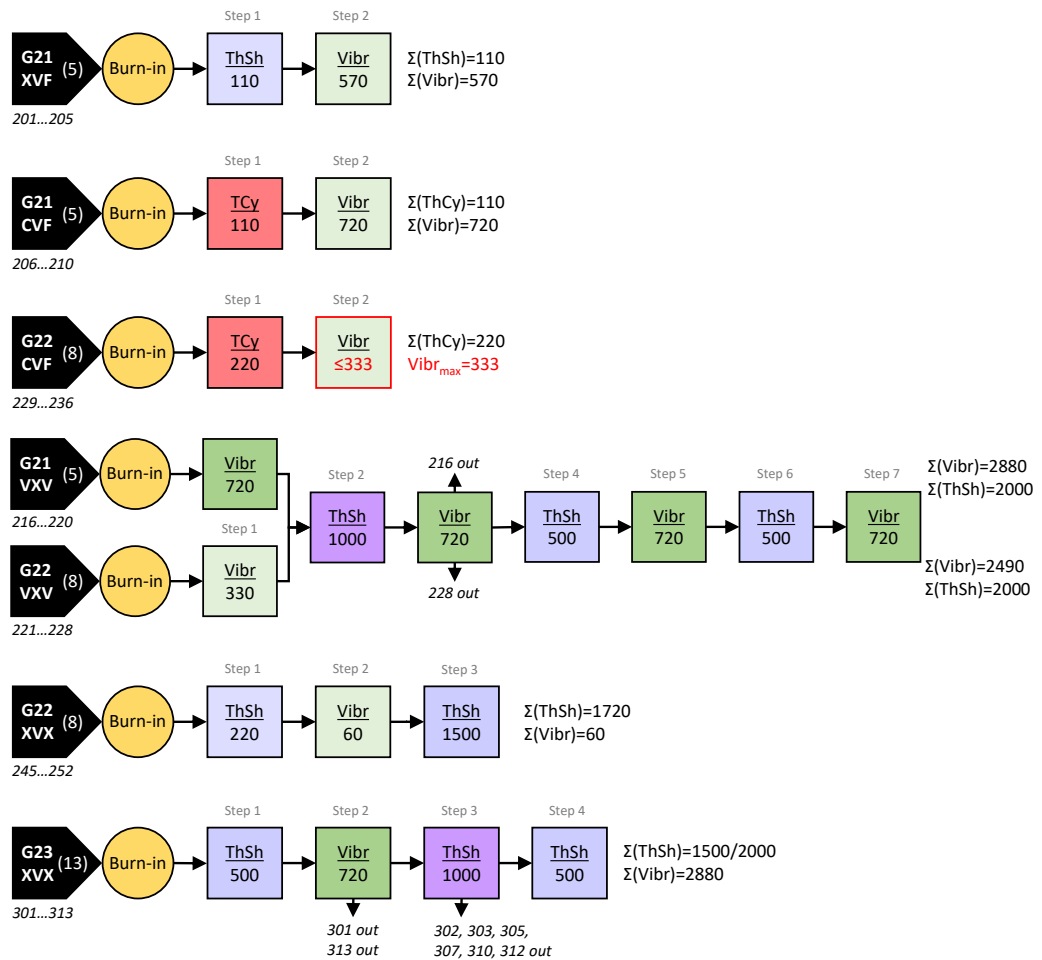


Figure 3.15: Global test flow and samples numbering. TCy: Temperature Cycles, Vibr: Vibration sweeps, ThSh: Thermal Shocks. Series naming and associated numbering are reporter on the left side. The total numbers of cycles or sweeps are reported on the right.

Chapter 4 Experimental results

The present chapter reports the experimental results of the six test flows presented in the previous section. The DUTs were all systematically numbered according to the system reported in Figure 3.15 (Section 3.4.2). An additional, more direct way of naming the samples is codified with 3-digits numbers. This information is useful for identifying the results and analyses that will be developed hereafter. Presentation of results will follow the progression of complexity during testing:

- In Section 4.1, observations from single-parameter testing are developed and first conclusions are drawn. Temperature cycles, thermal shocks and vibration are covered. Results are presented in the form of box-and-whisker plots.
- In Section 4.2, results from accumulative sequential test campaigns are reported. Three main groups of samples were constituted:
 - Accumulative temperature-vibration tests,
 - Accumulative thermal shocks/vibration and extensive thermal shocks tests,
 - Accumulative vibration-thermal shocks sequences (7-steps).
- Section 4.3 finally presents the failure mode and effects analysis, as well as complementary analyses. A radiographic study details how damages propagate in the MEMS devices' die attach adhesive. X-ray diffraction is also performed on the silicon dies, revealing the presence of residual stress and its evolution with testing. Finally, wire bonds pull and die shear test results provide information of the integrity of the device over testing.

A general discussion about the results is then compiled in Section 6.1 with the additional knowledge obtained from the Finite Element Modeling study in Chapter 5.

4.1 Mono-parameter reliability campaign

Three categories of tests have been carried out applying the two-steps stress test procedure for mono-parameter testing:

- Temperature cycles
- Thermal shocks
- Vibration

All samples have already survived the burn-in procedure without noticeable deviation of the sensors' signals. A typical example of results is provided in Figure 4.1. Overall, in the following Sections, the appreciation of the significance of the deviation of one of the two failure criteria is compared to the experimental, manipulation error.

This section presents the overall results and observations. In general, neither failure nor significant degradation (as per the failure criterion developed in the previous chapter) has been seen. A recapitulative summary of the test that have been carried out is recalled in Table 4.1. It refers to the progression detailed in Section 3.4.1.

In case of vibration (step 1), only 12 devices can be tested simultaneously for the X and Y axes. Along the Z-axis, the number reduces to only 8, due to the geometrical constraints of the shaker's baseplate. At maximum, three sample holders can be fitted on the apparatus due to the weight limitation imposed by its power output for reaching 50g.

In the temperature-based tests (step 2), the devices are grouped by batch. Three batches of 13 devices each were tested under a single parameter mode, to provide a baseline for accumulative testing. In general, the tests take for reference the U.S. military standard (which are also referred to in the European Space ESCC standards).

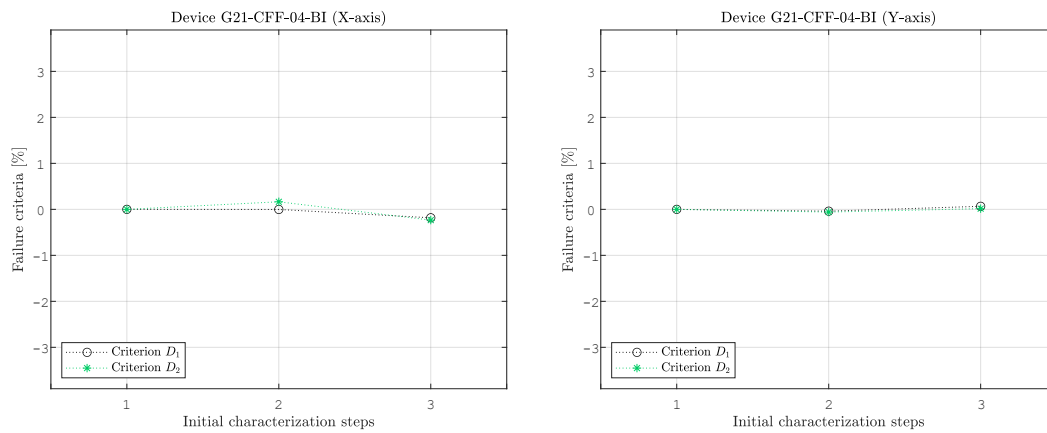


Figure 4.1: Typical deviation of the failure criteria after the burn-in. **Step 1:** pristine device. **Step 2:** device after electrical characterization and pin-to-pin insulation test. **Step 3:** device after the burn-in procedure (260 hours at 100°C, direct bias 3.6 V).

Table 4.1: Two steps stress test under single parameter loads.

Test type	Step 1	Step 2
TEMPERATURE CYCLES $\frac{\partial T}{\partial t} = 2^\circ\text{C}/\text{min}$	G21-CFF (5 devices) ● 7 ranks -40/+110°C to -60/+190°C	G21-CFF (5 devices) 110 cycles at -60/+190°C G22-CFF (8 devices) 220 cycles at -60/+190°C
THERMAL SHOCKS $\begin{cases} 32 \leq \frac{\partial T_{up}}{\partial t} \leq 47 \\ -60 \leq \frac{\partial T_{down}}{\partial t} \leq -38 \end{cases} \text{ [}^\circ\text{C}/\text{min}]$	G21-XFF (5 devices) ● 8 ranks -40/+110°C to -65/+200°C	G21-XFF (5 devices) 110 cycles at -60/+190°C G22-XFF (8 devices) 220 cycles at -60/+190°C
VIBRATIONS $20 \leq \nu \leq 2000 \text{ Hz}$	G21-VFF (5 devices) ● 10 ranks from 6g to 55g	G21-CFF (5 devices) 240 cycles at 50g G22-CFF (8 devices) 110 cycles at 50g

The choice for representing the evolution of the deviation of groups of samples is the box-and-whiskers plot. It shows order statistics (minimum, 25% quantile, median, 75% quantile, maximum and outliers) of the data. This adequately covers the large variability of measurements between devices, due to the naturally random physical phenomena of the responses measured as reliability indicators. It is more informative than a single error-bar system which only depicts the mean and standard deviation of a distribution.

4.1.1 Temperature cycles and thermal shocks

The distinction between temperature cycles and thermal shocks becomes evident when comparing the total time spent in the apparatus, as developed in Section 3.4.1. Where, in temperature cycles, DUTs have spent about 45 days for 220 cycles, in thermal shocks the duration is reduced to about 22 days (equivalent 220 cycles).

When the first step did not lead to any failure or significant deviations for all three tests of the G21 series, devices were reused for the second step. Another series of 8 samples, in each of the tests, is added to create two groups of devices with distinct cycles counts. Values of D_1 and D_2 are computed using a MATLAB script for all available samples at a given cycle count. Those values are plotted in a form of box-and-whiskers plot, and for a restricted selection of cycle count in Figure 4.2. For $D_{2,y}$, one device momentarily passed the 2% threshold but then produced signals within bounds again. This result being observed only once, it is not considered in the overall statistics.

The difference in amplitude of the box-and-whiskers plots between values below and above 110 cycles is due to the greater number of devices counted (G21 and G22 series). The main observation is the rather limited deviation for all devices, even up to 220 temperature cycles. All values stayed within the failure criterion bounds. The variability of the D_1 criterion (0g evaluation) is especially narrow (in the 0.1% range). This indicates that sensors remain accurate in detecting an acceleration along the X or Y axis (neutral position). Criterion D_2 (g-value averaging from the raw

signal) demonstrates a higher variability, reaching about +1.5% for the extrema outliers of the data set. The shift is mostly observed for positive values of the g-averaging. This overall indicates a very good robustness for tests that are vastly harsher than the datasheet values (-60/+190°C instead of -40/+100°C) and higher than the ESCC Generic Specification No. 9000. Since the 5 devices from Step 1 were still perfectly functional, their cycle count was increased to 110. Results for the thermal shocks were treated in a similar manner as before (Figure 4.3)

The distinction between temperature cycles and thermal shocks is most visible on the variability of criterion D_2 (averaged gravity). It seems moreover that the Y-axis sensor is more sensitive to thermal aging than the X-axis. This phenomenon will be observed again at a later stage during the accumulative thermal-vibration sequences. Overall thermal shocks cause less of an effect on the accelerometers, keeping the values of D_1 and D_2 below the $\pm 1\%$ range.

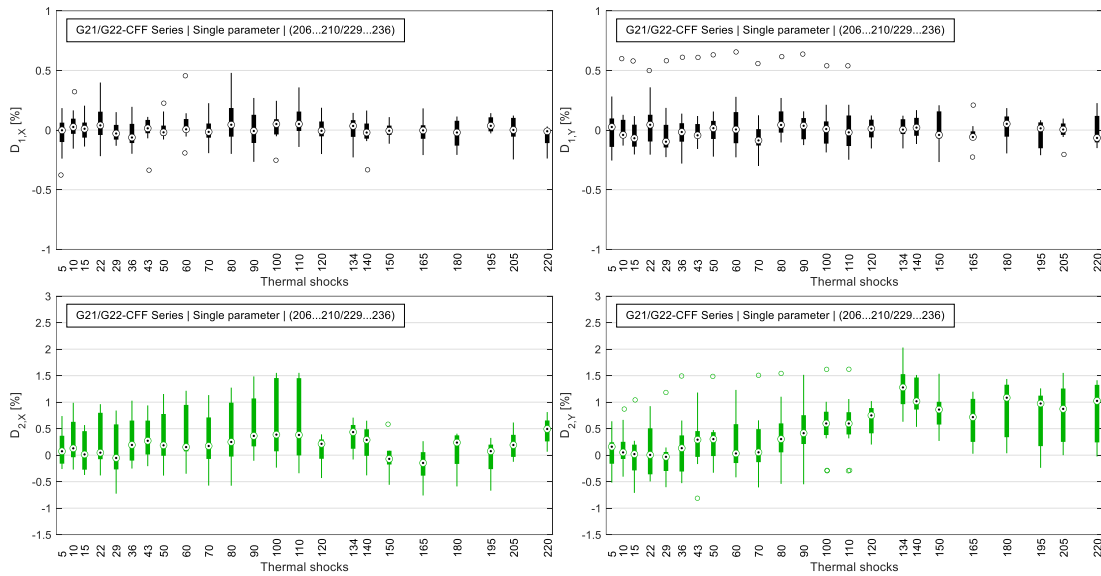


Figure 4.2: G21- and G22-CVF Series (step 1). Box-and-whiskers plots showing order statistics (minimum, 25% quantile, median, 75% quantile, maximum) of the deviation criteria per axis as a function of the number of temperature cycles. Notice the different scales.

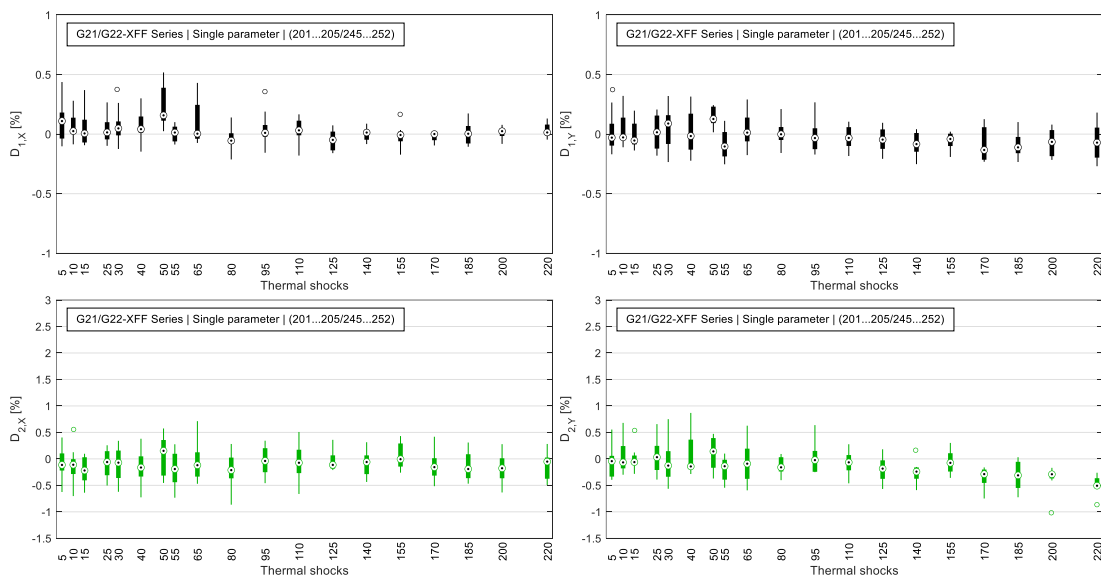


Figure 4.3: G21- and G22-XVF Series (step 1). Box-and-whiskers plots showing order statistics (minimum, 25% quantile, median, 75% quantile, maximum) of the deviation criteria per axis as a function of the number of thermal shocks. Notice the different scales.

4.1.2 Vibration test

As previously, Step 1 of the two-steps stress test starts at peak acceleration value of 6g taken from the datasheet. Five samples, inserted in the holder shown in Figure 3.13 (page 65), undergo five cycles at each stress level. One cycle is defined as 3x3 to-and-fro sweeps along the X, Y and Z axes. The maximum apparatus value of 50g was reached with no failure occurring. The eight samples used for Step 2 underwent 110 cycles (total sweeps count: 330 per axis, 990 total) and did not show any failure as per the selected criteria. The batch of five samples from Step 1 were brought to 240 cycles (720 sweeps), without displaying any deviation in their accelerometers' metrics.

The effect of the test is negligible on the accelerometers (Figure 4.4), but also on the gyroscope as reported in the Appendix F. In both criteria, the deviation is contained within 0.5%, which makes it comparable to the experimental error. In a sense, the devices are exhibiting immunity to vibrations. It is also to be noted that the typical standard ESCC No. 9000 mentions an acceleration load of 20g over the range 20 to 2000 Hz, which makes the current test condition much harsher.

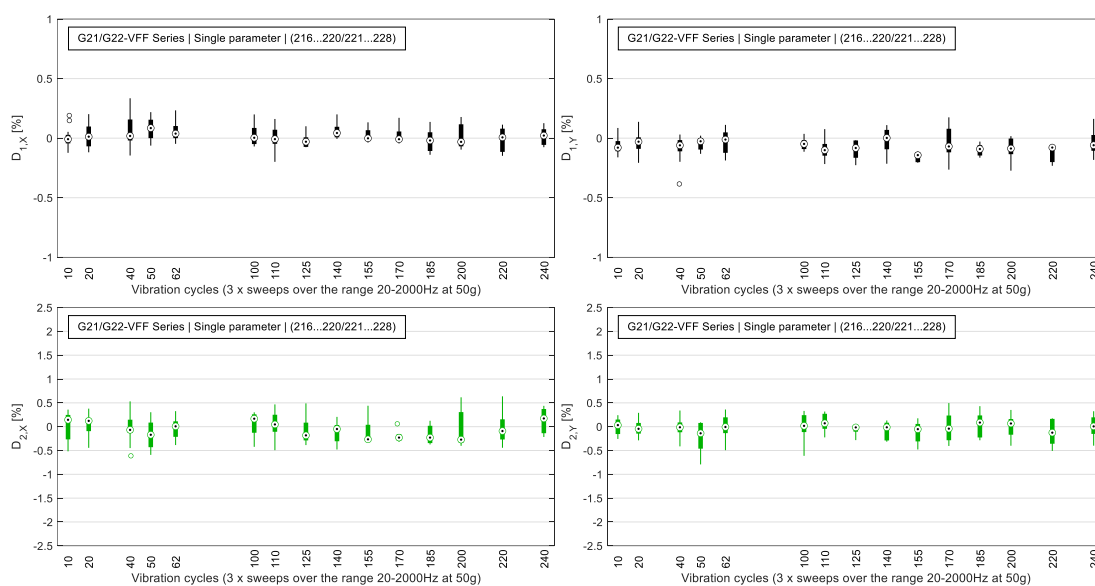


Figure 4.4: G21- and G22-VXV Series (step 1). Box-and-whiskers plots showing order statistics (minimum, 25% quantile, median, 75% quantile, maximum) of the deviation criteria per axis as a function of the number of vibration cycles. Notice the different scales.

4.1.3 Intermediate conclusions on mono-parameter testing mode

In the present case, under the defined criteria, the mentioned standards that served for experimental design are not adequate for the selected type of devices. No failure, as defined by the failure criteria, was observed on the three sets of 13 devices which have been tested under three load cases: thermal cycling, thermal shocks and vibrations. Cycles count beyond the number specified in ESCC No. 9000 for qualification (up to 220 cycles here compared to 100 cycles) did not yield any significant deviation. Under vibration testing, four sweeps per axis are mentioned in MIL-STD-883K, Test method 2007 while DUTs have undergone up to 3·240 full sweeps per axis. Even at numbers of cycles beyond the values provided in the MIL or ESCC standards, or the number of cycles defined in the previous methodology [65], no significant deviation in the measurement of accelerometers readouts has been detected. A noteworthy observation is also that the defined environmental conditions are significantly higher than the maximum datasheet values (Section 2.1.4).

As a conclusion, the currently used standards show their limits for an accurate reliability assessment, since highly reliable components in ceramic packaging withstand the defined loads. No insight on their lifetime is achievable in this fashion, even with conditions vastly more severe than the engineering datasheet values. Therefore, the investigations and impact of accumulative testing have the potential of more precise life-time evaluation and behavior in the failure mode mechanisms.

Following these first observations and conclusions, the same three batch of samples were reused for continuing reliability testing with application of two parameters, henceforth named “bi-parameter”. As second step, a load of different nature is applied, that is: if a devices batch has seen a thermal load, it undergoes vibration – and vice-versa.

4.2 Bi-parameter reliability testing

While sequential testing can be used in qualification standards, its role is not to study reliability rather than “passing an exam” to the device under test. In this Section, the main aim is focused on the observations and understanding of the effects of bi-parameter testing and DUTs failure root causes. Using as references the knowledge of the mono-parameter testing, evolutive test plans were progressively designed as tests steps were performed.

To represent the full variation of the DUTs’ readouts over its lifetime, one considers the evolution of the degradation at each step’s last measurement. In sequential testing, the latest state of the device will drive its behavior in the next step of testing. The global history of damage is a valuable information, since it records faults that may disappear again over time, such as for example: stiction, comb drive fingers overlap restored due to a violent shock, or an ASIC bit error erased by a high temperature bake of the silicon chip. Stiction depicts the adhesion of micromachined structures featuring large aspect ratios, when restoring forces are not able to overcome interfacial forces such as capillary, electrostatic, van der Waals, and residual stress [228]. Comb drives are a type of micromachined structures that permit acceleration or rate sensing, typically displaying such large aspect ratio.

The following developments also use the box-and-whiskers plots for representing testing time-related degradation. In this Section, the box-and-whiskers is fed with the deviation of the failure criteria at the very last step measured: (i) either the last functional test at the cycle count before catastrophic device failure, or (ii) at the last cycle of the current test step.

Over the course of the testing, several devices have seen the adhesive (glass-frit) of the package’s lid fail. Several operations of re-gluing have therefore been performed to continue the testing. Samples were not considered as failed if the gravity measurement was functioning or within the pre-defined bounds. Even though the progressive depletion of samples causes the statistical relevance of the results to diminish, it remains of interest to carry on testing and characterizing the devices up to the very last one.

4.2.1 CVF-Series: accumulative temperature-vibration tests

The 13 devices that have undergone temperature cycling in single parameter testing were reused for vibration testing. The two series of devices dubbed G21- and G22-CVF, with a history of 110 and 220 temperature cycles respectively, demonstrated either a progressive degradation of one or the two axes, or a complete loss of signal due to catastrophic failure of the die attach. Graphically, the testing sequence and results are represented (Figure 4.5) in a horizontal bar chart. The number of cycles is reported in abscissa. Note the change of test nature (thermal or mechanical).

The Y-axis has been observed to be more sensitive to degradation than the X-axis, even though both combs (refer to Figure 2.9 of Section 2.2.1.3, page 49) were manufactured during the same process steps. In terms of MEMS design, the two accelerometers are built in the same silicon die – only the orientation of the comb drives is changing. There is yet no satisfying explanation to this phenomenon. Sensors’ integrity seems compromised after vibration testing, potentially due to unidentified resonance mode along this direction, within the die or in the dependencies which transmit the amplitude of the mode to the accelerometer. Nevertheless, such hypothesis could not be verified with the shaker’s feedback loop system. Another noteworthy observation is the effect of CT-scans performed on several samples, which induces a large shift (up to 4% in magnitude) of the failure criteria. A full CT scan is equivalent to nearly 6 hours of radiation exposition. While radiation testing is not part of this study, this shift is considered as having no consequence on the functionality of the device: gravity was still recorded without additional deviation as long as radiation exposure was not repeated. An illustration of this effect, after two CT scans performed at 44 and 60 cycles, is presented in Figure 4.6. The shift occurs twice for criterion D_2 while it is only visible for the first CT scan in the case of D_1 .

Overall, this behavior may come from a radiation impact on the ASIC, which artificially and permanently (at least in this vibration step) amplifies or diminishes the analogic signal coming from the MEMS. No further investigation was performed on this effect and the degradation phenomenon was focused on thermal or vibration effects. A similar

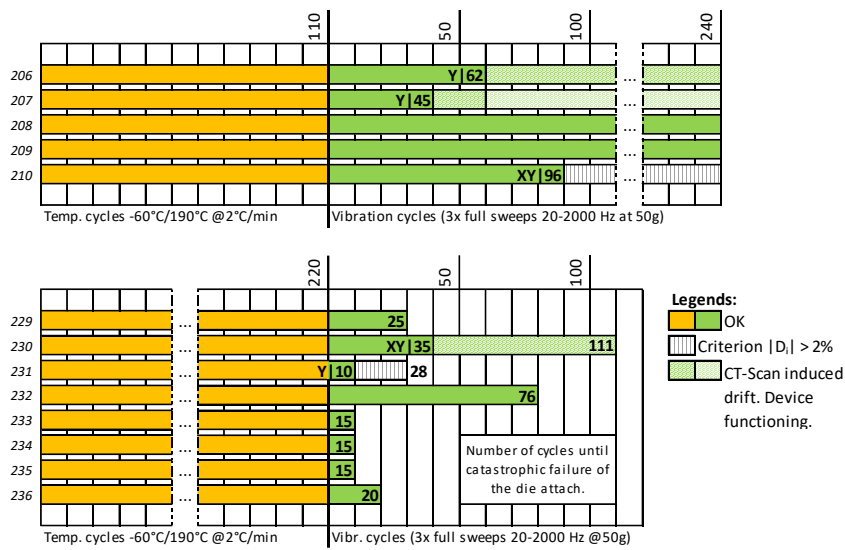


Figure 4.5: Sequence for the 13 devices tested in accumulative temperature cycles and vibration tests. Number indicated in the bar charts refer to the cycle count for a deviation event of at least one axis, or at failure. The letters next to the numbers refer to the affected axis.

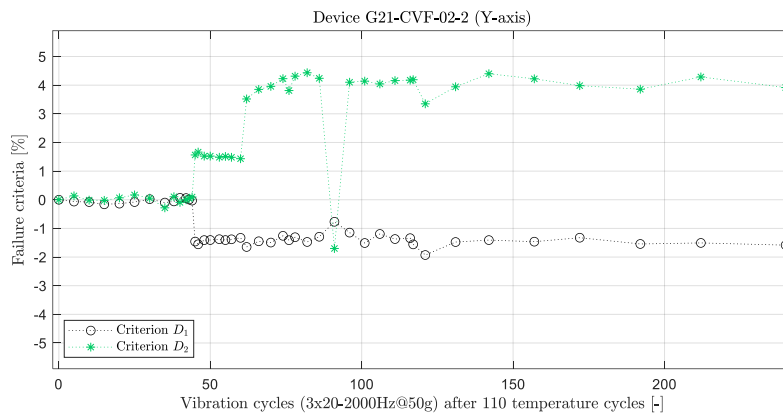


Figure 4.6: Effect of the CT-scan on deviation criteria. Measurement at 90 cycles is a discrepancy. Criterion D₂ shows a nearly symmetrical behavior to D₁. Not only the averaged gravity value shifts, but the zero-level shifts as well.

tendency is observed in the other bi-parameter testing sections. In the box-and-whiskers in Figure 4.7, the shift induces an enlargement of the boxes while the median remains below the ±2% deviation threshold.

Devices group G22-CVF, which experienced 220 temperature cycles before undergoing vibration, displayed a more interesting phenomenon. Six of the eight devices failed catastrophically before 30 vibration cycles (90 full sweeps) and the two remaining devices failed after 76 and 111 cycles, respectively. The box-and-whiskers plot is showing the combined effect of degraded devices due to testing and the effect of the CT-scan on the dispersion of the box (Figure 4.8). Weakening of the die attach adhesive, as shown in Figure 4.9, caused dies to delaminate from the package, ripping off electrical connections and causing a total loss of signal. This behavior was identified using the tomography tool. More thorough developments are presented in Section 4.3.1.

A Weibull plot is common statistical tool used to assess the degradation effect going on. The generalized Weibull distribution is given by the probability density function [229]:

$$f(x) = \frac{\gamma}{\alpha} \left(\frac{x - \mu}{\alpha} \right)^{\gamma-1} \exp \left[- \left(\frac{x - \mu}{\alpha} \right)^\gamma \right]$$

With γ the shape parameter, μ the location parameter and α the scale parameter. The conditions are: $f(x) \geq 0$, $x \geq 0$ or $\gamma, \beta > 0, \alpha > 0$ and $-\infty < \gamma < \infty$. In the specific case where $\mu = 0$, it is called a two-parameter Weibull distribution. Such a plot, for the G22-CVF Series failure numbers, is plotted in Figure 4.10. Three devices failed at 45

vibration sweeps. The regression was done on seven samples instead of eight, with one of the early failures being censored. This fit gives for the shape parameter $\gamma = 133.78$ and for the scale parameter $\alpha = 1.38$. A parameter α greater than unity means that failure rate goes increasing with time. There is a wear-out of the die attach if it has seen the thermal preconditioning (step 1). This has not been seen in the vibration-then-thermal two-step sequence, where no device failure was observed under the same test loads, showing vibration immunity. Figure 4.8 moreover completes this analysis.

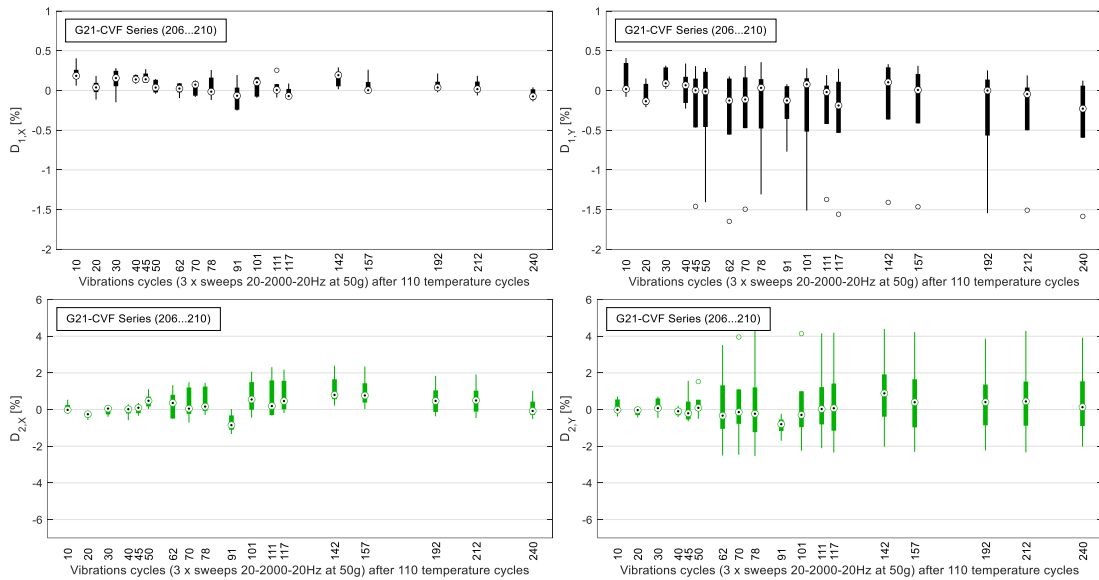


Figure 4.7: G21-CVF Series (step 2). Box-and-whiskers plots showing order statistics (minimum, 25% quantile, median, 75% quantile, maximum and outliers) of the deviation criteria per axis as a function of the vibration cycles. Deviations are essentially due to the CT scans, which stretched the quantiles to values beyond $\pm 2\%$.

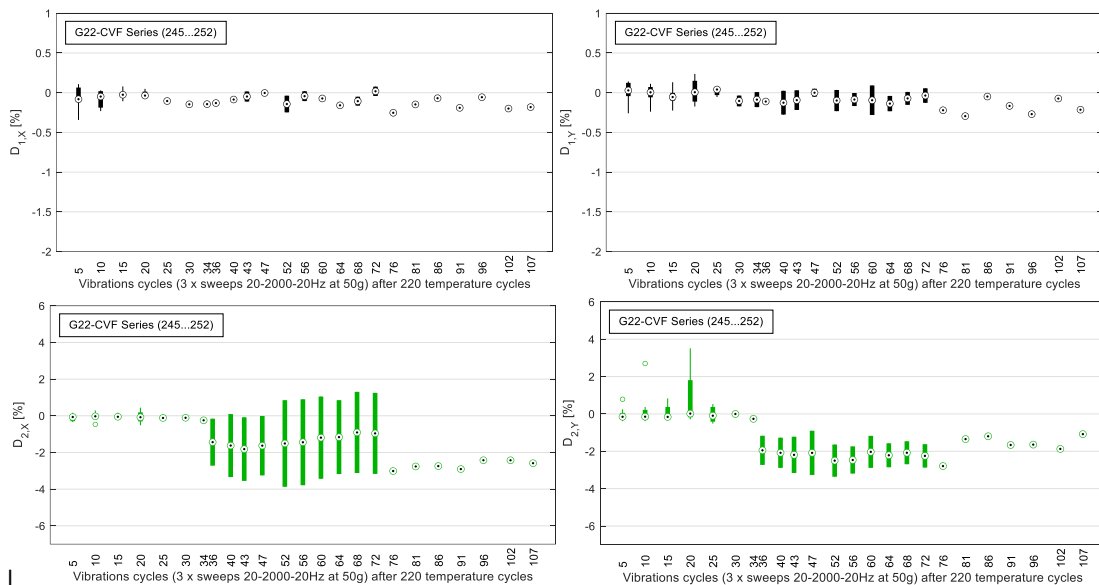


Figure 4.8: G22-CVF Series (step 2). Box-and-whiskers plots of the deviation criteria per axis as a function of the vibration cycles. Data reduces to a single point when only one device is left. The large deviation observed was essential due to device G22-CVF-04, observed under CT scan. D_1 remains however stable.

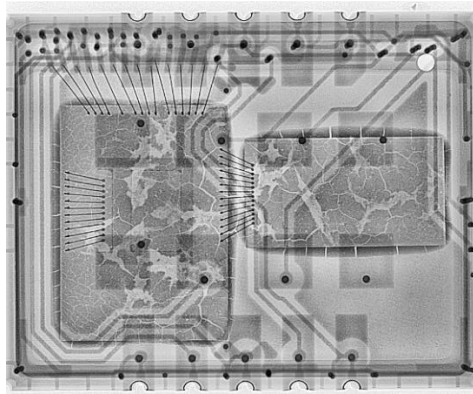


Figure 4.9: X-ray tomography view of a severely damaged die attach. Weakening of the adhesive ultimately led to complete delamination.

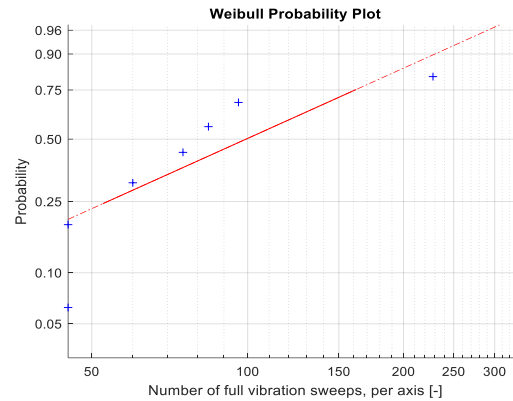


Figure 4.10: Weibull probability plot for the G22-CVF Series. Seven failed devices are used (one is censored at 45 sweeps) under accumulative testing (220 temperature cycles followed by vibration). Shape parameter $\gamma=133.78$. The scale parameter $\alpha=1.38$ meaning that the failure rates increase.

4.2.2 XVX-Series: accumulative thermal shocks/vibration & extensive thermal shocks tests

After observing that the single parameter testing (XFF-Series) did not yield to failure, the devices were submitted to a second phase: accumulative testing of vibrations following the initial thermal shocks tests (Figure 4.11). The G21-XVF series was interrupted after a early lid failure on all samples. DUTs were discarded from the campaign after 190 vibration cycles which did not cause any detectable deviation of the failure criteria. The other series, which had undergone 220 thermal cycles followed by 60 vibration cycles, did not display significant deviation either. Thus, vibration is assumed to have no significant effect on healthy samples. Provided the knowledge that thermal shocks, for a same number of cycles, are much less harsh than temperature cycles, the devices a tested only under thermal shocks up to a total of 1720 repetitions. The experimental results, shown in Figure 4.12 in the form of box-and-whiskers, clearly demonstrates that the extended thermal step has led to significant deviation with $D_{2,Y} > 2\%$.

A third group of devices was used for a test aiming at evaluating the effect of 500 thermal shocks in step 1, followed by vibration in step 2. Nevertheless, no failure was observed at this stage. The MEMS were submitted again to thermal shocks, attempting to produce devices failure. Deviation of the values of the failure criteria for one or two axes were observed, which highlights their sensitivity to extended thermal tests. While devices remained functional, deviations were in some cases considerable, such as DUT n°309 (-6.4% at 1000 shocks in step 3 and -8.7% at +500 cycles in step 4). Box-and-whiskers plots for the G23-XVX series are reported in Figure 4.13.

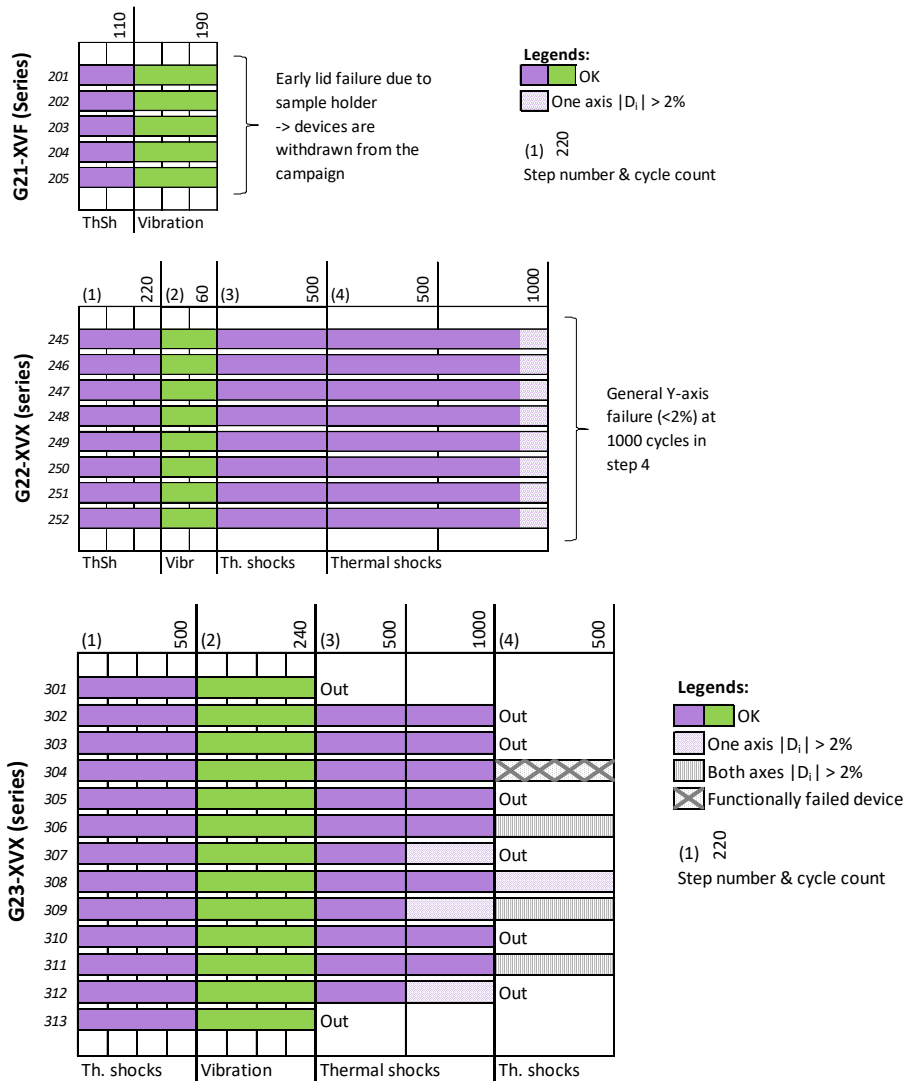


Figure 4.11: Reliability test for series for devices under accumulative thermal shocks followed by vibration. All devices belonging to series G22-VXV displayed a greater than 2% deviation of one of the two axes at 1000 cycles of step 4. Subgroups of devices in G23-VXV were taken out at regular steps of the campaign for FMEA comparison. Overall, only one device lost functionality.

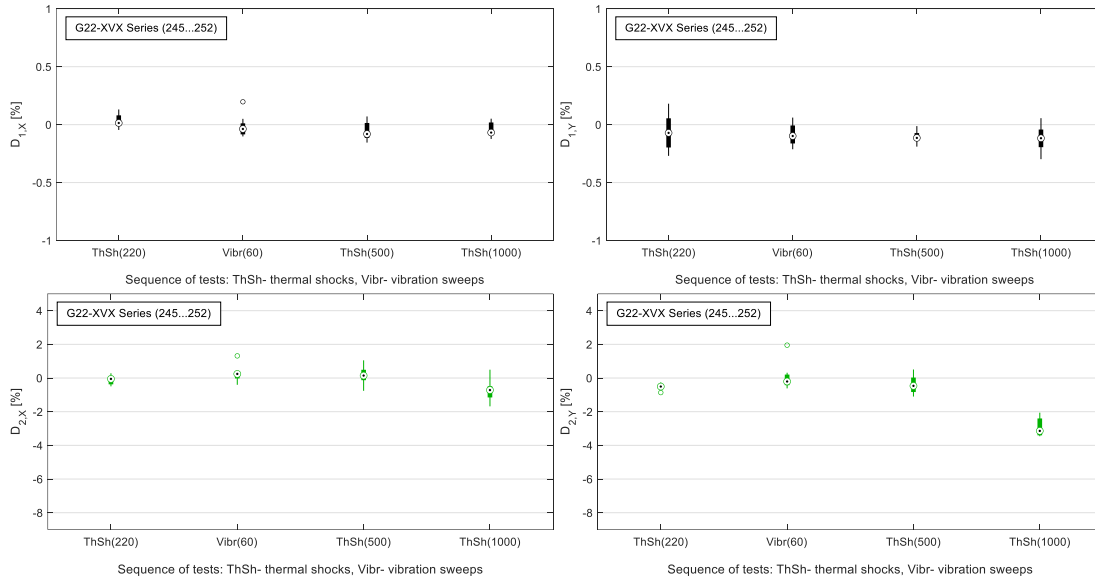


Figure 4.12: Results for the global deviation of parameters for the G22-XVX sequence. The devices have seen a total of 1720 thermal shocks.

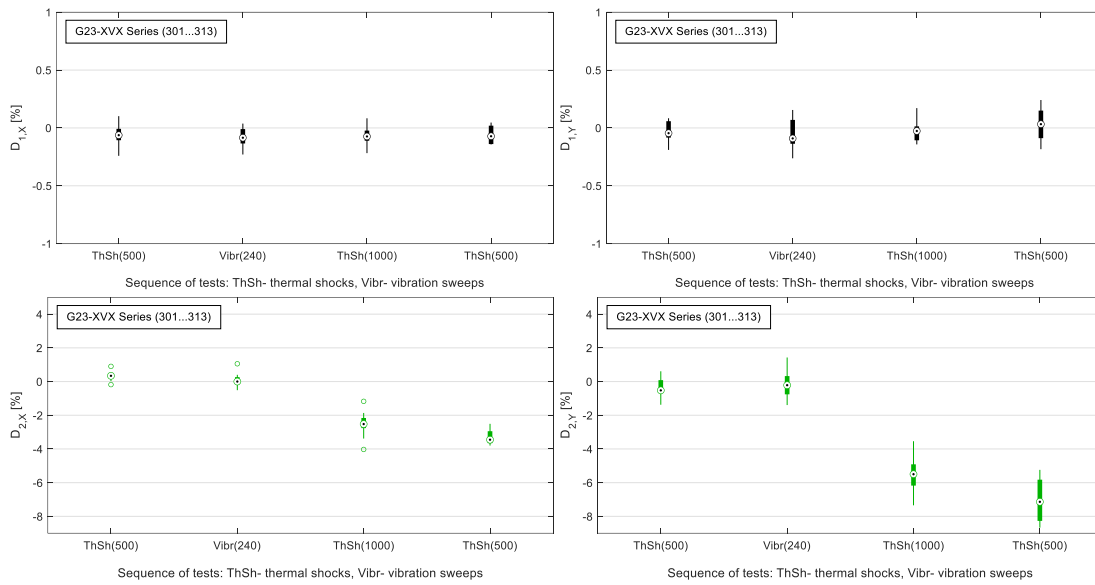


Figure 4.13: Results for the global deviation of parameters for the G23-XVX sequence.

4.2.3 VXV-Series: accumulative vibration-thermal sequential testing

This series of devices were submitted to the most extended campaign in this research, with the goal to push them over their reliability limit by alternating between vibration (uneven step number) and thermal shocks (even step numbers). The sequence comprises of 7 steps in total. Since no failure occurred in the single parameter testing phase, the samples were reused in the second phase: accumulative testing was performed on all 13 devices. A bar chart representation of the sequences as well as the timing of removal of devices from the set, for further post-test die shear analyses, is presented in Figure 4.14.

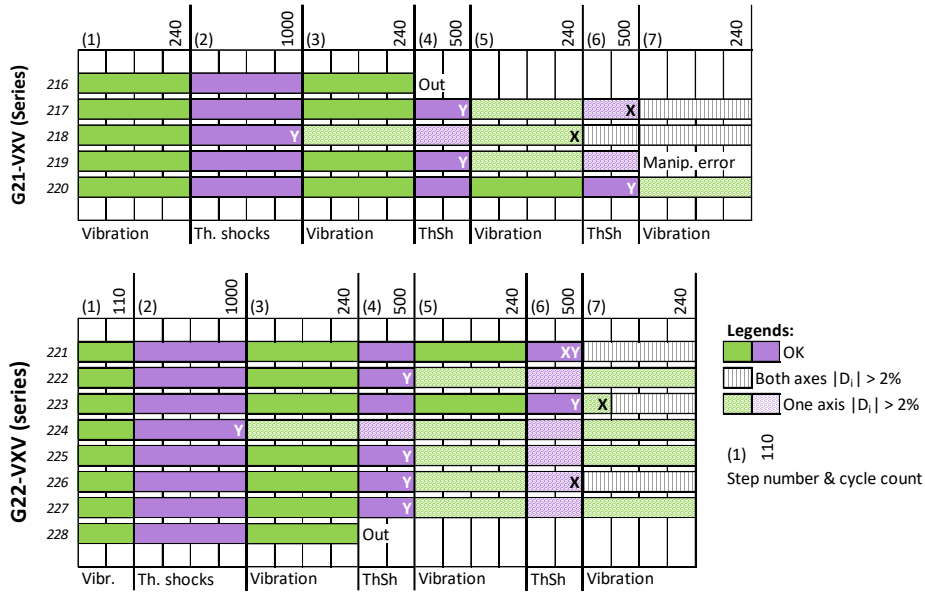


Figure 4.14: Accumulative alternative thermal and vibration loads. The “Out” tags indicate that the device is taken out from the set for further analyses. The X and Y-axes letters show for which axis one of the two criterion failed. Device 219 lost functionality due to a manipulation mistake which disrupted the ASIC-accelerometer wire bonds during lid regluing.

This extended campaign demonstrated the overall fragility of the Y-axis compared to the X axis, for the potential reasons probably caused by unidentified resonance at the die level as mentioned in Section 4.2.1. Alternatively, it could come from a non-anisotropic behavior of the silicon material which behaves differently along the Y direction than the X direction. This hypothesis has not been verified and no residual has been detected on the MEMS (see Section 4.3.2 for the details). Nevertheless, only 5 over 11 devices showed deviations greater than 2% for both axis, and none of them remained healthy. This indicated that an extended campaign of thermal shocks combined with vibration has a detrimental effect on reliability. Details, shown in the box-and-whiskers plots in Figure 4.15, showed a tendency of the degradation to be essentially influenced by the thermal step. The successive vibration step, to a thermal shocks step, does not cause the value of the median to shift significantly. The data is represented grouped for both series (G21 and G22).

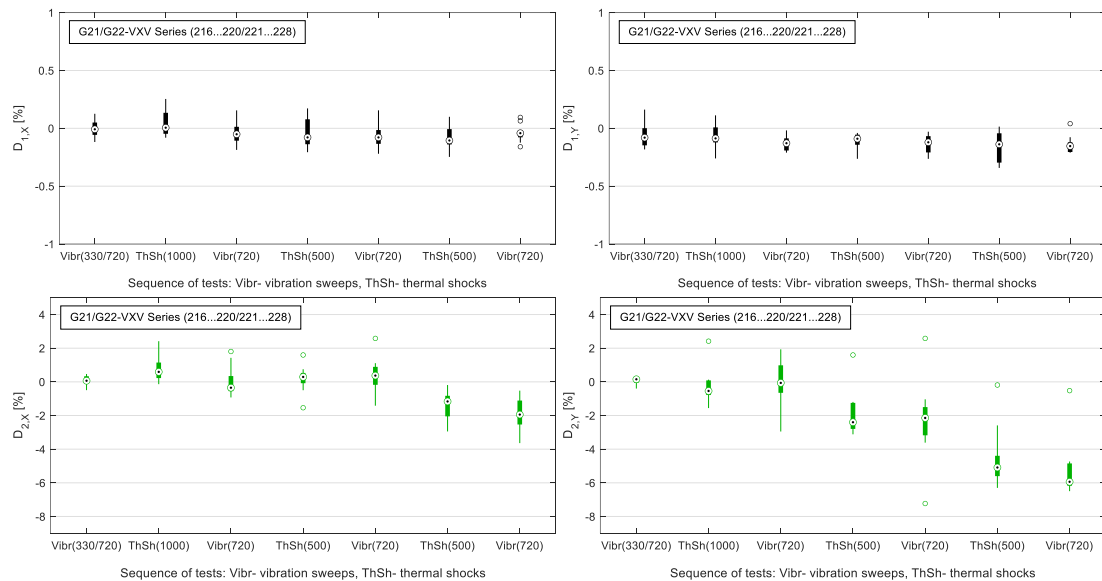


Figure 4.15: G21- and G22-VXV Series (steps 1 to 7). Box and whisker plots showing order statistics (minimum, 25% quantile, median, 75% quantile, maximum and outliers) of the deviation criteria per axis as a function of the vibration cycles. While the thermal steps have an obvious detrimental effect on criteria’s deviations, the vibration steps effects were smaller.

The vibration immunity of the healthy devices is therefore propagated also when thermal degradation, typically of the die attach, is already advanced (see Section 4.3.1.3 for tomography details). This contradicts the findings of the CVF series when catastrophic failure under vibration occurred within 111 cycles. The reason lies allegedly in the cumulative soak time at temperature extremes, as developed in Section 3.4.1.1. The failure root cause is comparably greater in the temperature cycles test. In terms of failure mechanism, this implies that for a similar cracking state, delamination is not as critical in the case of thermal shocks (VXV) as it can be for temperature cycles (CVF). The remaining contact surface for the adhesive in the CVF devices group is smaller (hence weaker) than the VXV series. More developments about this observation are provided in Section 4.3.1. A possible explanation is the quick change of temperature in the thermal shocks test may not give enough time for the physical phenomena governing the adhesive's degradation leading to a catastrophic weakening of the bond. It is however interesting to note that no sample completely failed at the end of the 7 steps, even with deviations being down to -6, even -8% for criterion $D_{2,Y}$ in the case of device number 224 and centered around -2% for any $D_{X,i}$ criterion in all cases.

Representing lifetime in accumulative testing is challenging due to the various physical phenomena taking place under the different loads. Theories of step-stress testing claim that a sample is using its lifetime ("health points") – that cannot be recovered – independently from the testing history. Therefore, a lifetime curve can be found at any step of an accumulative test and constitutes a segment of the total lifetime of the DUTs. Such models are notably proposed by Nelson [230]–[232] and later by Benavides [233]. Graphically, a test plan with 4 increasing stress levels is represented in Figure 4.16.

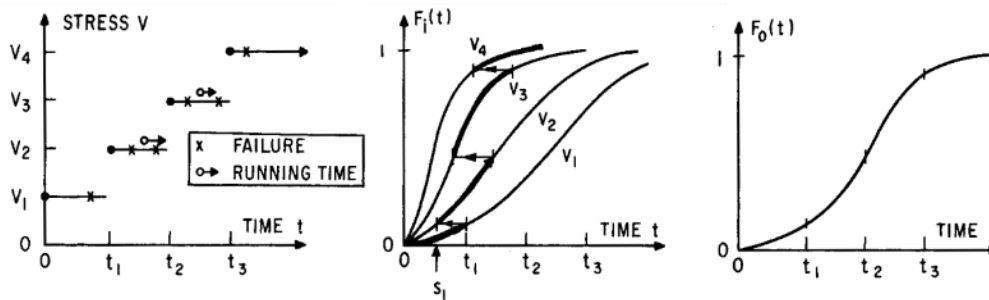


Figure 4.16: From left to right – from step tests with increasing stress levels V_i leading to failure over time, the concatenation of the cumulative distribution functions (CDF) segments $F_i(t)$ lead to an aggregated equivalent distribution function $F_0(t)$.

This concept is tested using Weibull probability plots on the global data, in order to estimate the parameters and goodness-of-fit of an equivalent aggregated curve fit on the VXV-Series dataset, shown in Figure 4.17. Such curve would be, in the present case, corresponding to the last bit of the CDF at $V = V_4$.

The representation, summarized in Table 4.2, was made choosing two logical considerations for failure criteria: either a failure event is recorded when both axes fail (that is: if X and Y have at least one failed criterion D_i), either when only one axis (X or Y) fills the same condition. Moreover, the plot were made for three different sets, based on the failure events of Figure 4.14: (i) all the cycles, regardless of their nature, are cumulated in terms of thermal shocks numbers and vibration sweeps numbers, (ii) only thermal shocks are considered (if the assumption is that the preponderant degradation occurring is due to thermal shocks), or (iii) only the vibration steps are counted. All shape parameters are greater than 1 (increasing failure rate), which agrees with the observations.

A verification is additionally made on the Weibull fits regarding their meaningfulness: a goodness-of-fit (GOF) is performed on each fit. It relies on the Lilliefors test: a normality test on the represented data, based on the Kolmogorov-Smirnov test [234] which evaluates the null hypothesis on a dataset which, in the present case, corresponds to a Weibull distribution. For the accumulative testing data, the corresponding *lillietest* MATLAB function is used, which returns 0 if *lillietest* fails to reject the null hypothesis at the 5% significance level. It returns 1 if the test succeeds at rejecting the null hypothesis, indicating a bad goodness-of-fit. All cases besides the thermal-only plots returned 0, indicating that a Weibull plot can possibly describe the accumulative test performed here.

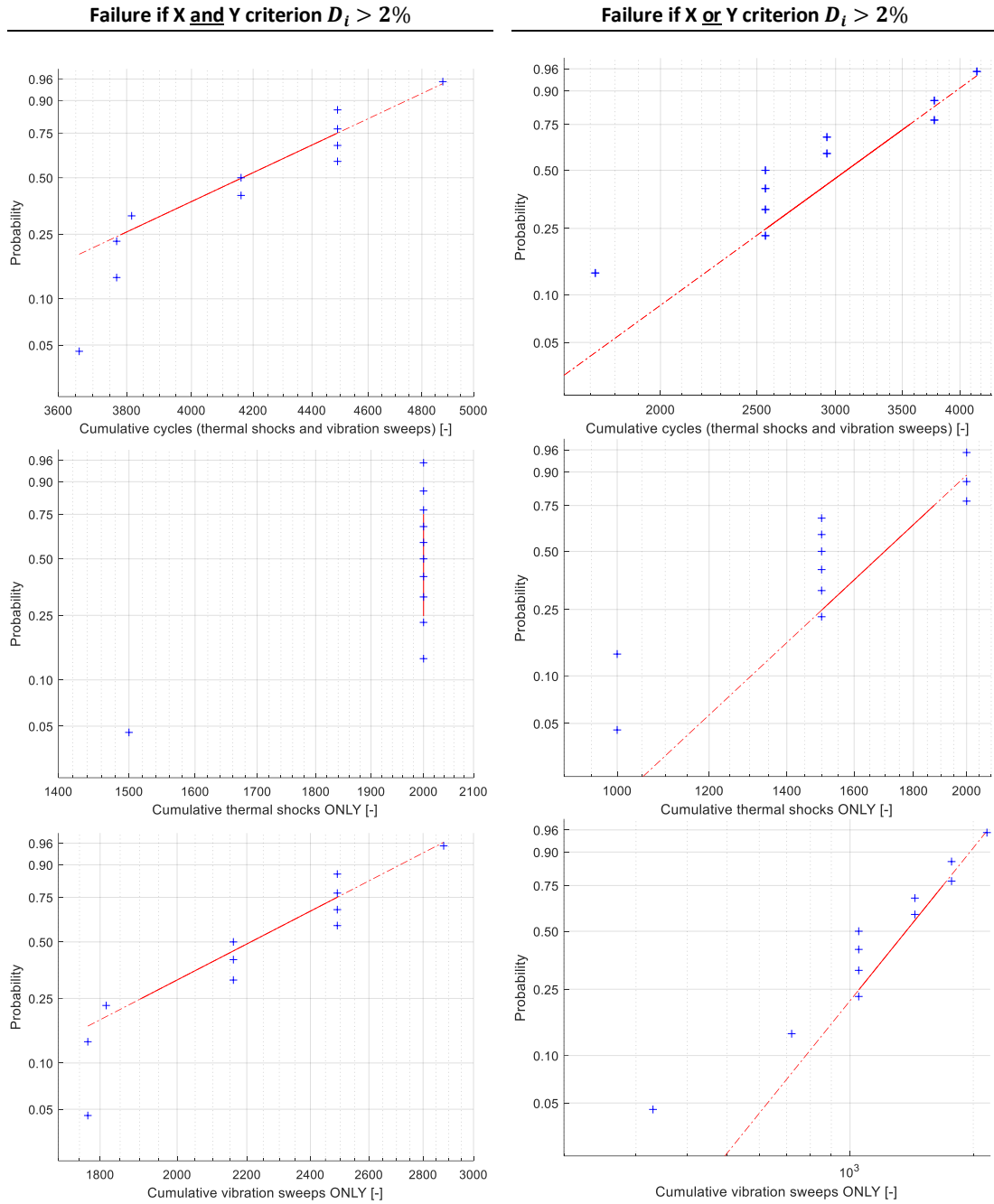


Figure 4.17: Weibull plots for the G21-VXV and G22-VXV Series. The number of cycles is aggregated into a single count value: $N_c = N_{thermal} + N_{vibration}$ with the number of thermal shocks and vibration sweeps respectively. The failure event is either define by both axes failing (left column) or when only one axis fails (right column).

Table 4.2: Weibull parameters and goodness-of-fit tests for six variants of data selections.

	Failure if X and Y criterion $D_i > 2\%$		Failure if X or Y criterion $D_i > 2\%$	
γ : scale parameter				
α : shape parameter				
GOF: goodness-of-fit test				
Cumulative cycles (thermal shocks and vibration sweeps)	$\left\{ \begin{array}{l} \gamma = 4374 \\ \alpha = 12.1 \end{array} \right.$	GOF = 0	$\left\{ \begin{array}{l} \gamma = 3126 \\ \alpha = 3.90 \end{array} \right.$	GOF = 0
Cumulative thermal shocks ONLY	N/A	GOF = 1	N/A	GOF = 1
Cumulative vibration sweeps ONLY	$\left\{ \begin{array}{l} \gamma = 2382 \\ \alpha = 7.3 \end{array} \right.$	GOF = 0	$\left\{ \begin{array}{l} \gamma = 1412 \\ \alpha = 2.8 \end{array} \right.$	GOF = 0

4.2.4 Conclusion of the observations in the reliability test campaigns

The main motivation for this thesis is the understanding of failure mechanisms in MEMS devices due to the application of three accumulative test procedures. The test campaigns that have been proposed combined thermal stress steps and vibration. They highlighted degradation phenomena and the required intensiveness of testing to damage highly robust devices featuring a non-hermetic ceramic package. Classical reliability approaches, based on single-parameter test procedures, showed their limits for efficiently evaluating their lifetime performances.

The general observation is the extreme robustness of the COTS IMUs used in the campaigns, which remained functional (though inaccurate) even after seven alternating steps in the worst case. Moreover, the sequence of testing demonstrated its importance: while temperature cycling followed by vibration (A then B) caused the total failure of a series of devices, vibration testing followed by thermal loads (B then A) did not lead to failure. Thermal effects are therefore responsible of a degradation phenomenon that render the devices less resilient to vibration due to the degraded die attach (studied in detail in the next sections). The opposite is however not true: the immunity to vibration that has been observed during the mono-parameter test is confirmed here, and temperature cycles alone are not enough to generate failures at the selected stress levels and cycle counts.

The multiple series of devices demonstrated that combined effects could take place. Vibration, even at stress levels much greater than the maximum datasheet values, does not have any significant impact on the functional response of the accelerometer. If applied on DUTs of which the die attach adhesive has been severely weakened by repetitive temperature cycles, vibration can lead to catastrophic failure and the loss of a full device series. A Weibull probability plot was drawn on the results of the vibration cycling performed at 50g between 20 to 2000 Hz with a preconditioning consisting of 220 temperature cycles. Weibull parameters concluded on an aggravating failure rate, with a scale parameter greater than one ($\alpha=1.38$). The interpolated shape parameter was $\gamma=133.78$ on the vibration sweeping scale.

On the other hand, thermal shocks have comparatively a smaller impact. With up to 500 thermal shocks, vibration did not lead to failure. This observation might lead to a clarification in the procedures used in, where the distinction is not always well established and calls for special care when performing life cycle tests. For an identical number of temperature cycles or shocks, a device seeing in operations longer soak times would not demonstrate the same behavior as one experiencing short soak times. As seen here, the long-term impact appeared very different between series. The Y-axis was seen to be more sensitive to the loads, as demonstrated by the frequent deviation beyond $\pm 2\%$ of at least one of the failure criteria.

Finally, an extended accumulative test campaign has permitted to determine the ultimate resistance of the IMUs to alternating thermal shocks and vibration steps. The main contribution to degradation of devices' readouts has been observed as being the thermal parts. Vibration only brought a minor contribution to the deviation of the electrical signals. In most of the cases and as before, the Y-axis failed before the X-axis, in some cases measurement an averaged value for gravity beyond -8% of its initial, pristine value. A statistical characterization, using the Weibull distribution function with successful goodness-of-fit tests, was proposed. This first use would yet need to be further confirmed with more comprehensive testing and a greater variety of stress levels.

4.3 Failure modes and effects analyses (FMEA)

While the previous section essentially covered the functional behavior of the devices, the present one aims at covering the physical non-destructive and destructive analyses of the failure modes that took place in the failed devices from the three accumulative campaigns. During the testing phase, the devices were regularly inspected by X-ray tomography method, which provided with non-destructive and 3D information on the aging of the determined sensitive element of the MEMS devices: the die attach which displays visible cracking and delamination. High-resolution X-ray diffraction was used to investigate residual internal stress building up due to the accumulative testing within the silicon dies, which could explain the observed drifts. Finally, all tested devices were destructively tested for die shear resistance and wire bonds pull resistance.

4.3.1 X-Ray tomography and die attach study

X-ray tomography was widely used for observing in a non-destructive way the evolutions of subsystems in the devices' packages. It is a convenient method that permits to identify die attach degradation, wire bond breakage, dies

delamination, etc. without the need to detach the lid. X-ray are diffused and scattered elastically or inelastically, which enables the identifications of subsystems of different sizes and geometries. X-rays being energetic radiation, they can interact with electronic silicon. Mechanical silicon, used in MEMS typically, is considered not to display any significant sensitivity [226]. The ASIC's behavior can however be influenced under a given radiation dose [235], [236], [194]. This phenomenon has been observed for several samples during the analysis as previously mentioned in Section 4.2. In practice, a drift of the accelerometer's failure criteria values is measured.

Regardless of these electronic effects, tomography here was intensively used to characterize the degradation of the die attach in the MEMS devices. With the increasing number of temperature cycles or thermal shocks, the adhesive (epoxy with 85%wt of silver flakes) degrades over time and loses its physical integrity. While the devices often remained functional, drifts in failure criteria values have been seen in the previous chapter. The characterization of the delamination is a focus of the present chapter, with discussion of the phenomena taking place as well as their effects on the resistance of the die attach over the device's lifetime.

Dies' assembly techniques shall rely on bonding materials compiling good mechanical properties, fatigue resistance and process temperatures [237], [238]. Polymer-based adhesives, as opposed to metallic solders, are used in the highly robust devices since they offer easier handling and processes in cleanroom, lower excess stresses, low curing temperature is used, comparative lower cost.

In introduction, the state of a pristine die attach is presented in Figure 4.18. A zoomed-in 2D tomography image shows the MEMS dies and the ASIC, as well as the wire bonds and package-embedded circuitry. The die attach is clearly visible as a darker area surrounding the dies. An overflow of adhesive – called fillet – can be identified around the dies and is present on all observed samples. Finally, a debris due to manual detachment of the lid is visible next to the accelerometer's die. The die attach shows an inhomogeneous structure due to silver flakes and porosity of the material. This porosity is visible in a qualitative CT-scan reconstruction shown in the same figure. Notice the crack on the inter-dies fillet on top of the image, for an already stressed device. Similar porosity, in the tens of micrometer range, appears on pristine samples. The commercial, mass production devices used for the different campaigns of the present study feature negligible variability, as their primary field of application (automotive) feature tightly control processes and high reliability. Three main tools were used for the following analyses with equivalent parameters (Table 4.3).

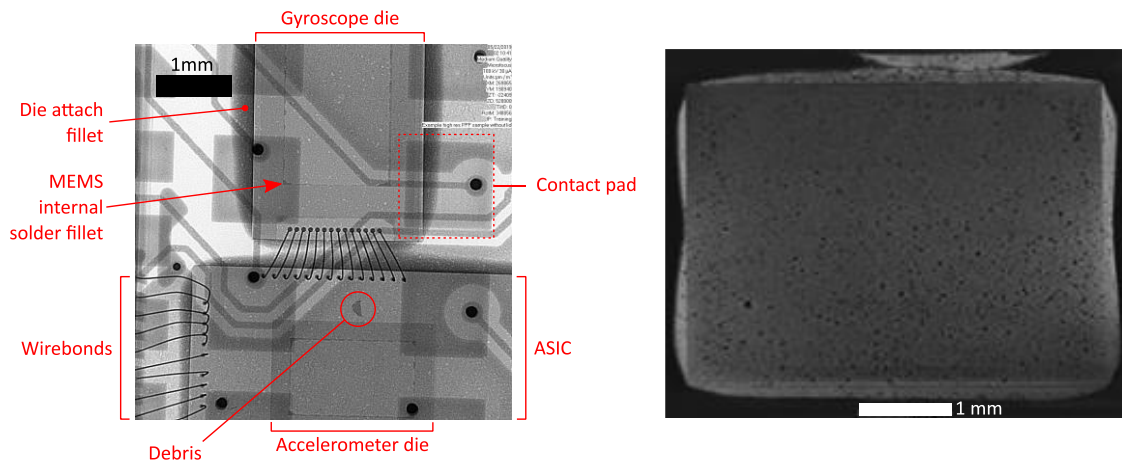


Figure 4.18: Radiographic (tomographic) close-up view of the device (pristine) and contrast view of the ASIC-to-package die attach layer (G21-CVF series after 110 temperature cycles and 40 vibration cycles).

Table 4.3: Tomography tools and main parameters, all with sub-micron resolution.

Equipment	Parameters
General Electrics v tome x s240	U = 120 kV, I = 30 μ A
RX-SOLUTIONS Ultratom micro CT	U = 100 kV, I = 36 μ A
YXLON Cheetah	U = 100 kV, I = 30 μ A

4.3.1.1 CVF Series

Devices group G22-CVF (8 devices) was the first series to display catastrophic failure for the die attach and loss of signal. This occurred not only because of the signals' drift, but also because of the thermally degraded adhesive (after 220 temperature cycles) that withstood vibration cycles only up to 333 sweeps. For comparison, other series remained sound, even when degraded. The detrimental effect of temperature cycling, particularly when compared to thermal shocks, is significantly amplified due to the longer soak times (refer to Section 3.4.1).

The analysis will focus on devices n°230 and 232, out of the batch shown in Figure 4.5, which have undergone only 72, respectively 111 vibration cycles before total delamination. Figure 4.19 depicts a sequence of images at consecutive vibration levels. The absence of notable evolution between the 34th and 50th cycle suggests that the degradation is initially present before vibration testing. This yields that most of the degradation and weakening of the die attach is due to the thermal part (220 temperature cycles).

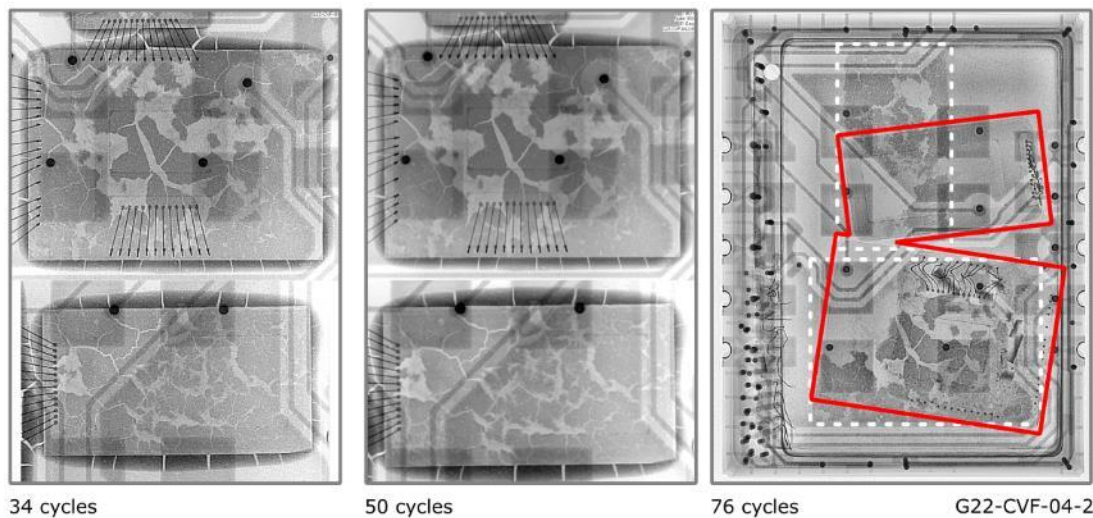


Figure 4.19: Degradation of the die attach at successive vibration cycles (step 2) after a 220 temperature cycles preconditioning. Brighter areas are delaminated areas of die attach.

The analysis of surface leads to the following observations: die attach weakening occurs to contact surface reduction due to shrinkage and delamination, and cracking. Three phenomena can be identified: (i) the adhesive chemically degrades (molecular-level destruction of the thermoset's crosslinking), (ii) difference in CTE between the package, the silicon constrains the adhesive, which weakens, or (iii) outgassing of volatiles due to soak times at high temperature (volume change). For quantitative evaluation of the die attach's degradation, analysis of the tomography images is made to measure and observe the variation of the adhesive's contact surfaces. The variation is indicated in terms of percentage of the initial footprint of the die attach, including the fillets (which are also mechanically participating to the package-adhesive-die system). ImageJ software with dedicated software routine (macro) is used for treating this image. The macro script is provided in Appendix G. The procedure is applied in two slightly different fashions, as illustrated in Figure 4.20. It can be summarized as following:

- 1) image negative generation (inversion),
- 2) conversion to 32-bit grayscale,
- 3) application of a bandpass and contrast correction to enhance shapes and features discrimination,
- 4) application of Li's threshold algorithm and creation of a binary black and white picture [239]–[241],
- 5) delimitation of the zone of interest on the original picture,
- 6) relative surface area computation.

This method, flexible and adaptable to various image brightness and contrast, has some limitations: even when using the bandpass filter combined with the contrast enhancement step, the procedure hardly compensates for the lack of contrast in the corners of the adhesive, as highlighted with dashed boxes in Figure 4.20. This lack of contrast leads to a slight underestimation of the fraction of remaining adhesive in the die attach region. Trade-offs between image parameters and algorithm parameters permit to attain the optimal settings as shown. An additional caveat is related to scale delamination: a block of die attach that delaminated over a larger area that also encompass shrinkage and

cracking. Such an area must be considered as being entirely delaminated – therefore not participating in the mechanical role of the adhesive. Such a phenomenon is highlighted in yellow in Figure 4.20 and is further visible in a 3D reconstruction of the same die attach, using a batch of 2000 CT-scans along several orientations. This area is manually selected using the automatic grayscale fuzzy selector tool with a selectivity threshold adapted following the image under treatment. This method is then compared to the macro use in ImageJ. Results for the studied device yield the fractions of remaining die attach reported in Table 4.4. Following, a $\pm 3\%$ measurement error is counted in the present and following sections.

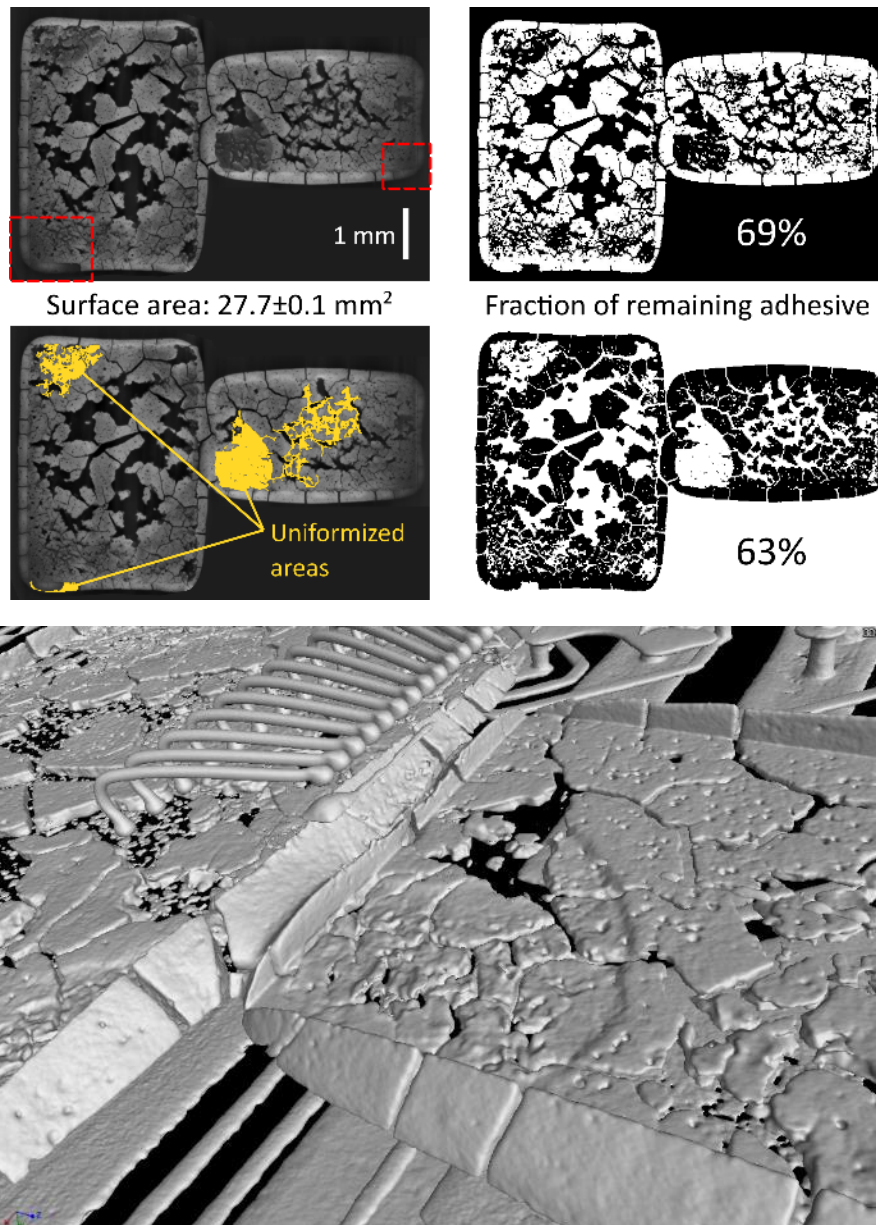


Figure 4.20: CT-Scan cross-section at the level of the die attach and strategies for adhesive surface loss quantification. 3D reconstruction of the die attach (device G22-CVF-04). The scale delamination on the lower left of the gyroscope die is visible.

Table 4.4: Fraction of remaining (not delaminated) die attach (CVF-Series) depending on the method used.

Device (vibration cycles)	ImageJ macro	Scale delamination exclusion
G22-CVF-04 (72)	69%	63%

4.3.1.2 *XVX Series*

The XVX device set sustained thermal shocks testing with a limited amount of vibration. They displayed vibration immunity, the die attach being structurally sound and the deviation of the accelerometer's readouts only appearing for an extensive number of thermal shocks (≥ 1500 repetitions). The G21 samples group did not show any effect of the sequence neither on the signals of the MEMS nor on the die attach: the appearance of the die attach is as new on the tomography images (not shown here).

First traces of cracking were observed after 220 thermal shocks on the G22 device group, with the initiation of a needle-shaped crack at the level of the gyroscope's fillet. A noteworthy observation is the location of the first crack was nearly identical in several samples, of which a small sample is shown in Figure 4.21. Anticipating the results of the finite element analysis that is covered in Chapter 5, stress concentration in the vicinity of the die's edge at the die attach's fillet level is predicted from the model. It could also be a consequence of the aspect ratio of the gyroscope's die (compared to the ASIC) that generates out-of-plane load cases, leading to stress concentration and cracking at this location.

This first trace of bond aging did not affect the performance of the MEMS in a measurable way, which is an interesting observation in terms of acceptance of reliability test results. Such an IMU can perform without significant impact on its accuracy even with light cracking of the die attach, a demonstration of robustness to initial failure of its subsystems. The intermediate vibration test in step 2 is assumed to have no significant impact on the acceleration measurement (confirmed by the data following screening of the DUTs). After an additional set of 500 cycles (step 3), delamination progressively appears in the bulk of the adhesive, between the package and the gyroscope die at first. The ASIC die displays large chunks of unbonded/cracked adhesive after 1000 cycles, still in step 3. The underlying reason of a centrally located delamination is non-trivial: the 2D numerical model (see developments in Section 5.2.3) exhibits a build-up of stress and displacement gradient across the package-die attach-die stack, which may explain the apparition of this globular delamination. An example of optical view of the detached gyroscope is provided in Figure 4.22. Assumption is made that that warping occurs due to progressive weight loss of the adhesive. The reflow of die attach the edges, identified by the fillet, helps it to cope with the progressive shrinkage. From a material's resistance point of view, a mechanical explanation could be the build-up of a greater in-plane strain than the out-of-plane component, thus maximizing the out-of-plane stress due to the geometrical constrain of the 20 μm -thick die attach, which would which could favor delamination in the central section.

Other examples of tomography of degraded die attach are provided in Appendix H.

4.3.1.3 *VXV Series*

After completion of the 7-step aging campaign (Section 4.2.3), a failure analysis was performed to evaluate the device-related degradations. As developed in the previous Sections, the devices' degradation was strongly driven by thermal shocks. In order to get an understanding of the root cause of the deterioration during the accumulative approach, inspection by non-destructive high-resolution X-ray CT analysis has also been carried out on all the VXV devices.

Vibration was not the main factor in the strong divergence of the failure criteria from the pre-defined bounds of 2%. While vibration caused catastrophic failure in the cases of the CVF group due to delamination of the severely weakened die attach adhesive, devices under test in the VXV series were still functioning – though with deviation – at the end of the campaign. It follows that tomography imaging also demonstrated that new cracking was essentially observed after thermal steps rather than following vibration. Figure 4.23 presents the progression of damage in the die attach for the most significant steps of the accumulative testing.

The first three step in the series did not cause any major deviation of the failure criteria, as demonstrated by the box-and-whiskers in Section 4.2.3, as well as structurally. For clarity, the choice has been made not to represent the first and third steps (vibration). The first 1000 thermal shocks in step 2 initiated the needle-shaped cracks, mentioned in the previous section. They originated at the fillet of the die attach and at the inter-dies space, both transversally and longitudinally (not visible here). This clear cracking is the first step to the die attach degradation.

It is only after step 4, with an additional 500 thermal shocks, that two phenomena have been observed: the initially peripheral cracking propagates in the adhesive's bulk, leading to a tessellated pattern of cracks, and a much more severe central delamination. The generalized cracking is visible in all devices of the VXV set. This internal delamination, more pronounced on the inside of the adhesive's layer where stress may be relieved less easily than on the outskirts, can find a similar explanation to its existence as the one developed for the XVX series. Greater delamination

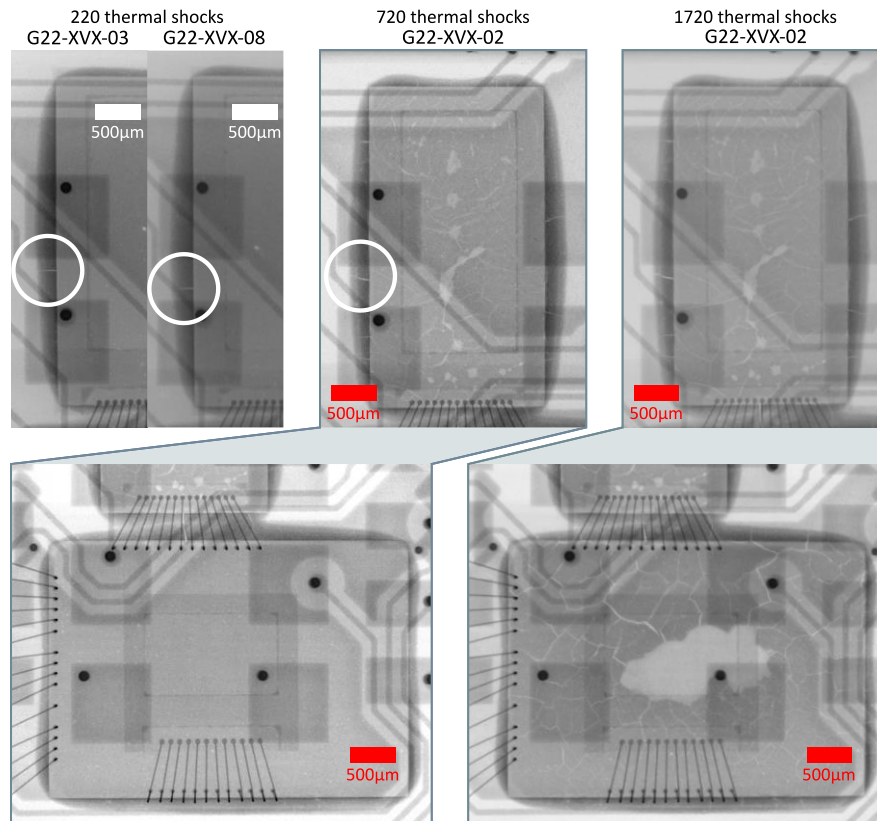


Figure 4.21: X-ray tomography views of the devices at various thermal shocks counts. The white circle pinpoints the location of the first observed cracking (in two different devices at 220 shocks, as well as the reported location of the first crack in a device after 500 additional thermal cycles). Degradation of the die attach beneath the gyroscope is obvious starting already at 500 thermal shocks, while it develops later underneath the ASIC/accelerometer dies.

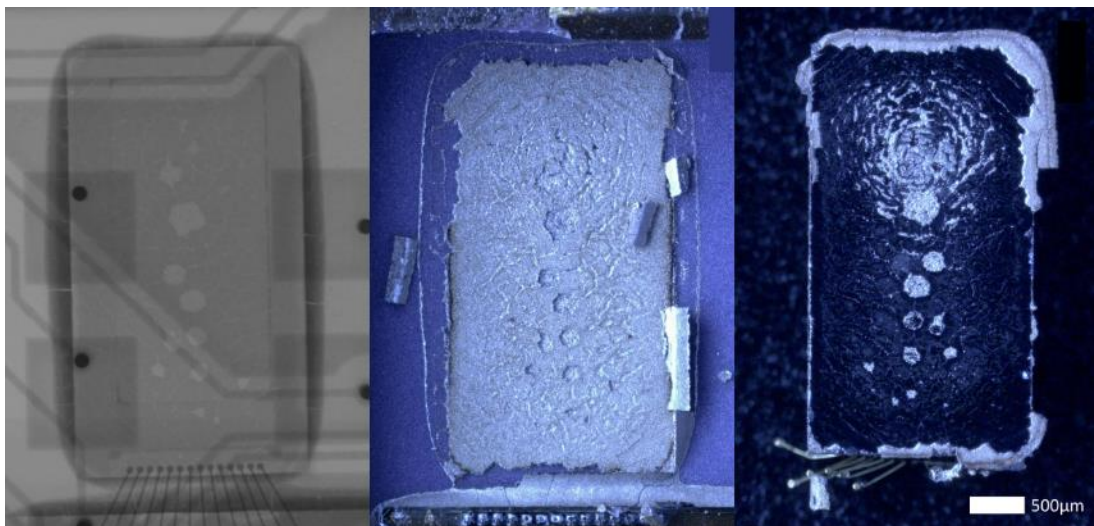


Figure 4.22: (left) X-ray tomography view of device G22-VXV-02 with visible globular delamination (brighter spots), (center) post-die shear optical view of the die attach with debris of the fillet, (right) bottom side (mirror) view of the gyroscope die with residues of the adhesive.

and cracking do not progress further during the 5th step, as vibration has a lesser detrimental effect in the present case. This fact is also corroborated by the box-and-whiskers plot for the VXV device set. Delamination, in the case of the ASIC/accelerometer dies, worsen again as the 500 thermal shocks in step 6 are applied. This indicates a role of the aspect ratio and total surface, since the elongated, smaller gyroscope die does not exhibit greater deterioration at higher steps counts. Also, the ASIC/accelerometer element consists of stacked die, which could further explain the difference geometrically speaking.

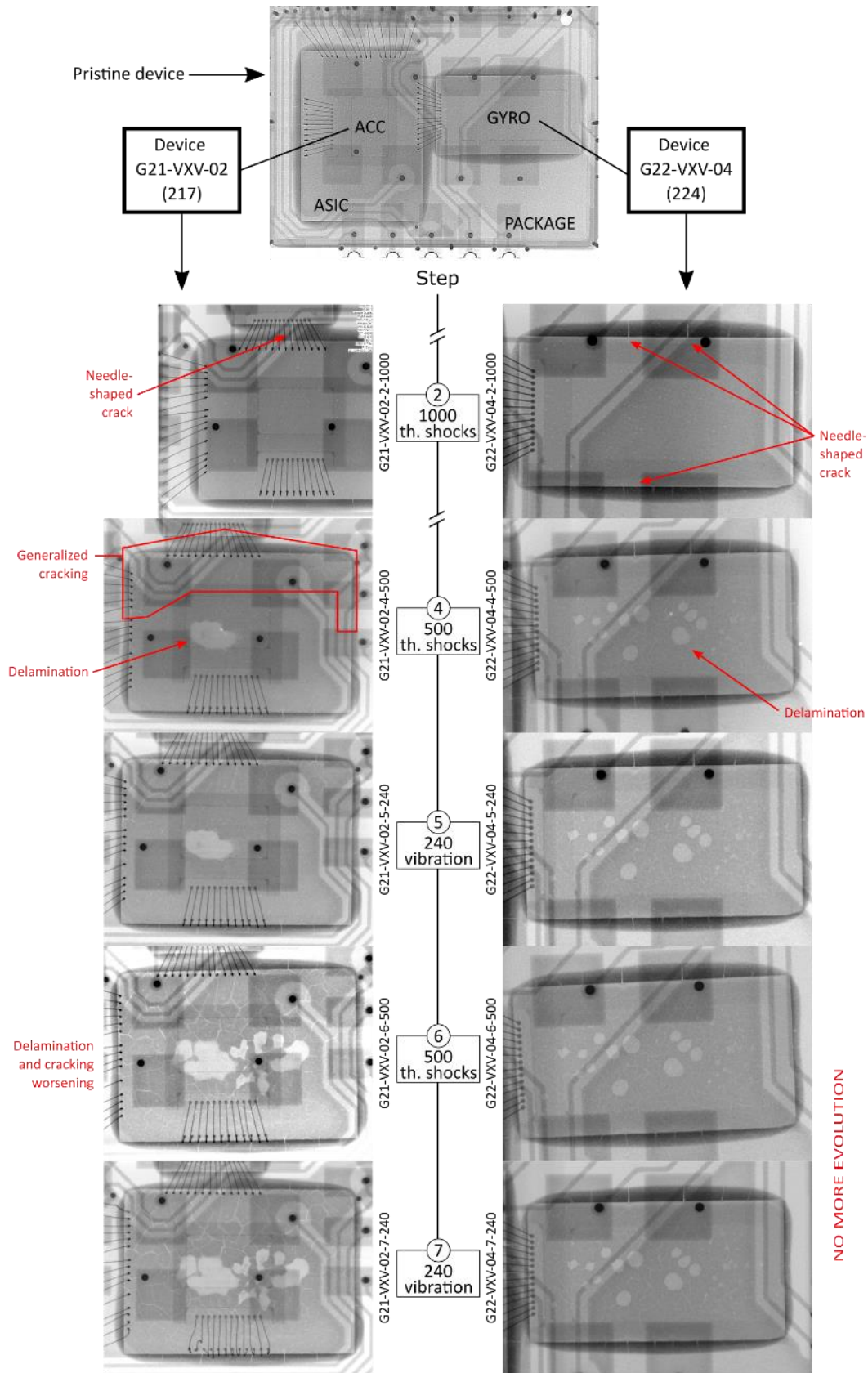


Figure 4.23: General tomography pictures of full 7-step test flow, showing the progression of damages in the IMUs. The first and the third steps, consisting of vibration, have been removed for clarity due to minor evidence of change. Needle-shaped cracks start to appear in step 2, while generalized tessellation in the die attach takes place starting the fourth step. Severe delamination progresses in the case of the ASIC's die up to step 7.

As the last vibration step was performed after a 2000 thermal shocks, one would expect the adhesive's weakening to be enough to cause catastrophic delamination – such as seen in the CVF series. However, the last (and 7th) step of vibration did not lead to any physical failure. Only the accelerometer's data deviate significantly (down to -6%) from their initial values. This last observation consolidates the knowledge that the most impactful events in the alternation of loads, up to the levels defined by this accumulative test plan, are the thermal steps.

Figure 4.23 also shows that last step of device G21-VXV-02 (left column) displayed disrupted wire bonds due to a manipulation mistake during regluing of the package's lid. This did not affect the functional measurements, as verified by functional testing performed subsequently.

4.3.2 High resolution X-ray diffraction (HRXRD)

While it is certain that detachment of the MEMS dies is the cause of the catastrophic failure of the devices, signal drifts of the accelerometers' readout have been observed during the experiments. High resolution X-ray diffraction (HRXRD) was used to non-destructively identify and analyze the origin and amplitude of internal stresses in the crystal lattice. Bandi *et al.* in [226], [242], has shown the importance of HRXRD analysis for determining the possible sources of stress-related failure and degradations in silicon devices for space applications.

This method applies to periodical crystallographic structure, such as the silicon monocrystals used in microsystems engineering, almost perfect epitaxial layers, and textured epitaxial layers. Micromachined silicon single crystal constitutes a typical material for MEMS devices, as determined in the present case during construction analysis (Section 2.2.1). A thorough study on crystalline silicon stress analysis has been proposed by Schifferle [243].

HRXRD relies on the principles governing the interaction of matter with an incident X-ray beam with wavelength closing to the crystal's atomic spacing. A crystalline structure is constituted of periodically ordered atoms that will absorb the incident radiation and emit coherent and incoherent scattering. This phenomenon can be represented by families of parallel crystalline planes that reflects the X-ray, thus creating an intensity peak under the constructive interference condition known *Bragg condition*, described by the eponymous law.

$$2d_{hkl}\sin\theta = n\lambda$$

With θ the diffraction angle for the given d_{hkl} , n an integer depicting the reflection order and λ the wavelength. The interplanar distance d_{hkl} is given for the set of Miller indices (hkl) corresponding to a given crystalline plane. The Miller indices derive from the face centered cubic crystalline structure representation (of silicon in the present case) with a set of three orthonormal unit vectors describing any point in space. Any direction in direct space can be characterized by the set of basis vectors from the unit cell length $a = 5.43 \text{ \AA}$ (silicon):

$$\begin{cases} a_x = a \cdot e_x \\ a_y = a \cdot e_y \\ a_z = a \cdot e_z \end{cases}$$

The Miller indices describe vectors in the reciprocal space, normal to the crystal planes under investigation and are inverse of the intercept of the plane at the axis in real space [224]. For example: the silicon plane Si(220) intercepts the unit cell axis at $a_x = a_y = \frac{1}{2}a$ and never crosses the out-of-plane axis a_z (it is parallel to it). On the other hand, Si(111) is the diagonal plane crossing all three axis at 1 in the cubic cell. With this understanding, an incident X-ray beam will produce reflection, for a given family of plane $\{hkl\}$, only when the Bragg condition is met (Figure 4.24).

Reflections were found on the package of the gyroscope's die: due to its positioning in the package and size, it was removed chemically by use of concentrated nitric acid (69.5%, 48 hours at room temperature) which dissolved the die attach. In the case of the failed G22-CVF dies, the detachment occurred by failure of the die attach (visible on Figure 4.25).

Finding the angle of maximum reflection intensity for a given lattice parameter enables to compare it to the theoretical value. Consequently, one can extract the residual stress that has built up in silicon during manufacturing or after reliability stress. This method has therefore been used to characterize any stress induced by the reliability testing.

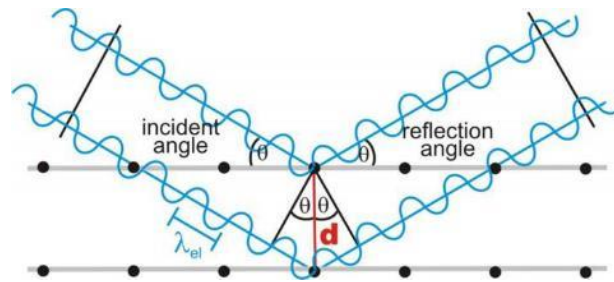


Figure 4.24: Illustration of a fulfilled Bragg condition: the path difference of the incident beam is equivalent to an integer multiple of the wavelength. Source: <https://www.microscopy.ethz.ch/bragg.html>

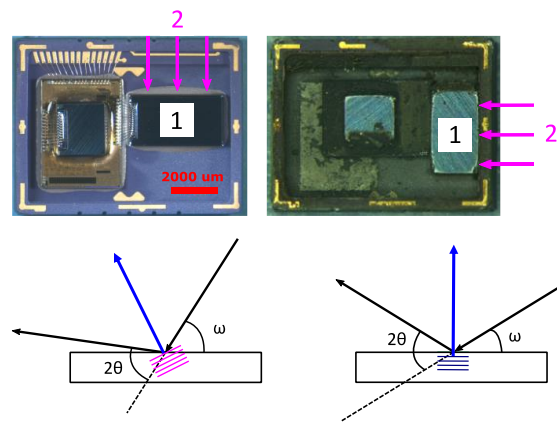


Figure 4.25: (top) direction of illumination on a pristine and a failed device, (bottom) depiction of asymmetrical and symmetrical reflections used in high-resolution XRD configuration. The first measurement of the Si(004) and Si(115) reflections take place on the top cover of the die, while the Si(220) reflection is found with a lateral illumination.

The gyroscope's die is constituted of sensing microstructures (comb drives) encapsulated in two silicon shells. The wafer used for manufacturing has been determined to be Si(001). The reflection for this symmetrical planes family is situated on the top of the gyroscope's die for both Si(004) and Si(115). By measuring the unit cell parameter, dubbed c , the out-of-plane direction can be calculated. The in-plane unit cell a can be extracted from the data obtained from the asymmetrical Si(115) reflection [244]. A graphical depiction of the a-/symmetrical modes is provided also in Figure 4.25. To obtain stress levels from the lateral sides, the asymmetrical Si(220) reflection is used.

The crystal lattice deformations/defects are analyzed using Reciprocal Space Maps (RSM) in High Resolution configuration of the XRD apparatus. The RSMs are built by measuring sequential $\omega/2\theta$ -scans ($\delta\omega$ is continuously incremented around a reference value) providing a 2D view of the distortion in the crystal lattice and allowing to determine the strain from the resulting heat map, such as on Figure 4.26. For doing so, the $\pm 10\%$ intensity isolevels cut-offs around a major and, if any, a minor intensity peak are defined by convention. This permits a graphical identification and comparison the intensity peak spread in the reciprocal space, leading to the relevant lattice parameters.

The high precision in HRXRD setup is due to the two main elements such as a curved multilayer X-ray mirrors (Göbel mirror) which is placed just after the $\text{CuK}\alpha$ X-ray tube, as well as a Bartels Ge(220) monochromator ensuring collimation and wavelength selectivity of the X-ray beam. This allows to achieve a high level of precision (1/1000th of a degree), thus, it is possible to resolve the two halves of the gyroscope, bonded together and enclosing the MEMS sensing elements (Figure 4.26).

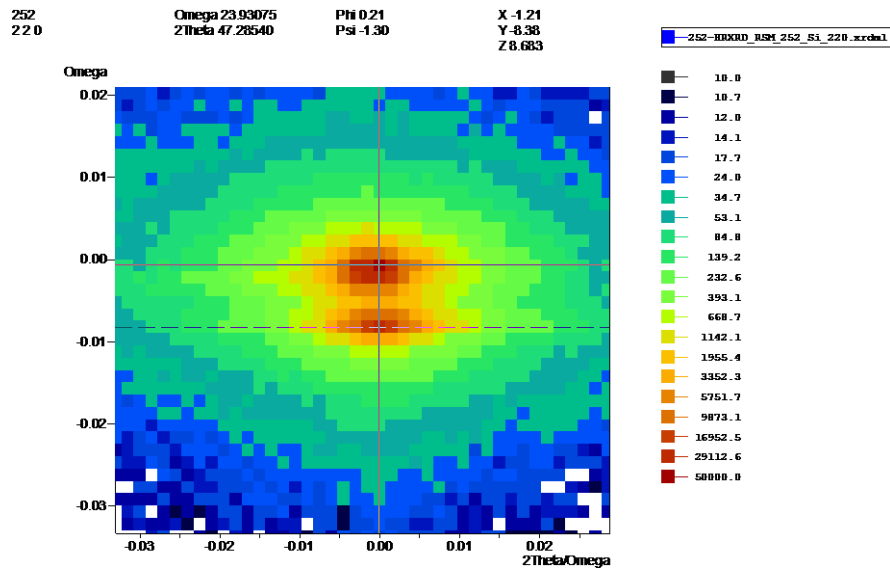


Figure 4.26: Space map (real space) of the intensity peaks for sample number 52 (G22-XVX-08) after an accumulative 1720 thermal shocks and 60 vibration cycles. The two halves of the gyroscope's package are resolved and show a misalignment of 0.03204° . HRXRD epi-biaxial stress calculated at the $\pm 10\%$ shoulders of the intensity peaks for the selected planes by use of the Reciprocal Space Maps (RSM).

The gyroscope dies were extracted from the failed G22-CVF devices with the highest vibration cycles counts (25, 76 and 111 cycles), from the G21- and G22-VXV post-campaign lot (devices number 219 and 224) as well as device number 252 from the G22-XVX group. One pristine sample was also extracted using the aforementioned method based on nitric acid. The XRD investigation aims at measuring the presence of internal stress in silicon after the campaigns. The data is grouped by vibration cycle count with indication of the thermal history. The used apparatus is a PANalytical X'Pert PRO MRD (source wavelength: 1.5406 \AA , operational conditions 45 kV, 40 mA). The first set of measurements was performed on the top of the die (Si(004) and Si(115) planes families). The lateral side is reported in a second set of measurement, for the Si(220) reflection. Strain values from the silicon lattice are extracted graphically and fed to an epi-biaxial stress model:

$$\sigma_x = -\frac{E\varepsilon_z}{2\nu} = \frac{E\varepsilon_x}{1-\nu}$$

The searched stress value is σ_x in [MPa], with ε_z is the measured strain by Reciprocal Space Mapping (RSM), $E = 130 \text{ GPa}$ for silicon and Poisson's ratio $\nu = 0.28$ [245]. The analysis (Figure 4.28) shows that the internal stress on the top cover (n^1 of Figure 4.25) of the gyroscope, observed in the in-plane direction, reveals a tensile stress of $60 \pm 10 \text{ MPa}$. Moreover, for one of the devices, an in-plane Si(115) stress level of $96 \pm 10 \text{ MPa}$ (tensile) and $-75 \pm 10 \text{ MPa}$ in compression has been measured. The gyroscope is then placed on its side to illuminate the interface of the MEMS package's joint line, where reflection is found for the Si(220) plane family and where stress can be present [226], [242]. For the lateral side (n^2), the thermally damaged samples exhibit the highest absolute stress levels between 25 and $35 \pm 10 \text{ MPa}$ (tensile and compressive irrespectively).

As the RSM measurements allows to separate lattice strain and lattice tilt features, further analyses show the apparition of an asymmetry in the RSM measured on the degraded gyroscope, as compared to the pristine gyroscope (Figure 4.27). This tends to indicate an unbalance between tensile (lower tail of the heat map) and compressive stress (upper tail) on the die's surface. This is also visible in Figure 4.28 for the a-axis Si(115) value at 60 vibration sweeps (1720 thermal shocks).

Measurement from asymmetrical reflections such Si(115) allow calculations of the perpendicular and parallel lattice constant, thus are the only indicator for the direct in-plane strain quantification, with respect to the illuminated surface. These measurements permit to detect introduced defect in the lattice and how they propagated. The obtained results showed that low stress levels (of maximum magnitude of a few tens of MPa) were introduced in the surface of silicon after accelerated aging and showed more pronounced strain values at a large number of thermal shocks. This must be compared to stress levels mesoscale silicon can sustain, in the order to the gigapascal. The observed residual strains do not contribute to an instantaneous failure, nevertheless the impact of it on the device

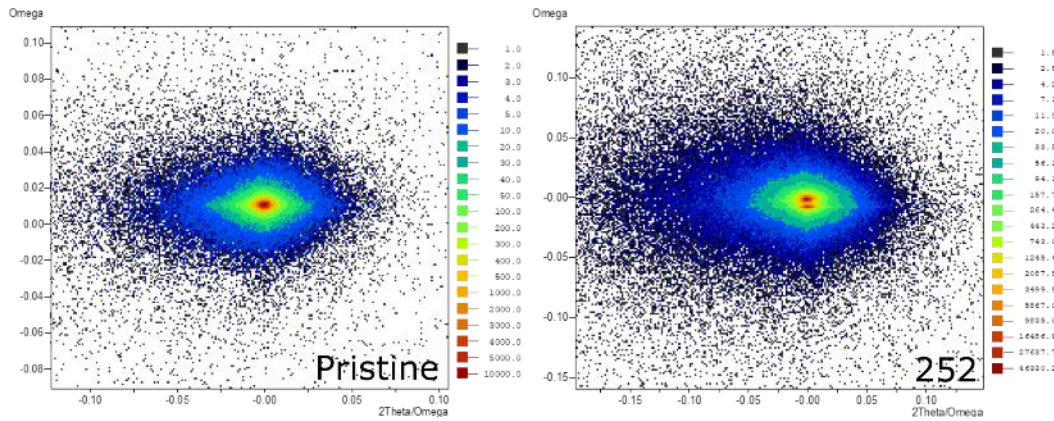


Figure 4.27: RSM maps for the Si(220) reflection between a pristine gyroscope die and the one of device n°252 (1720 thermal shocks and 180 vibration sweeps). Asymmetry of the reflection intensity is visible for the aged MEMS, as well as the major and minor peaks of the gyroscopes bonded parts.

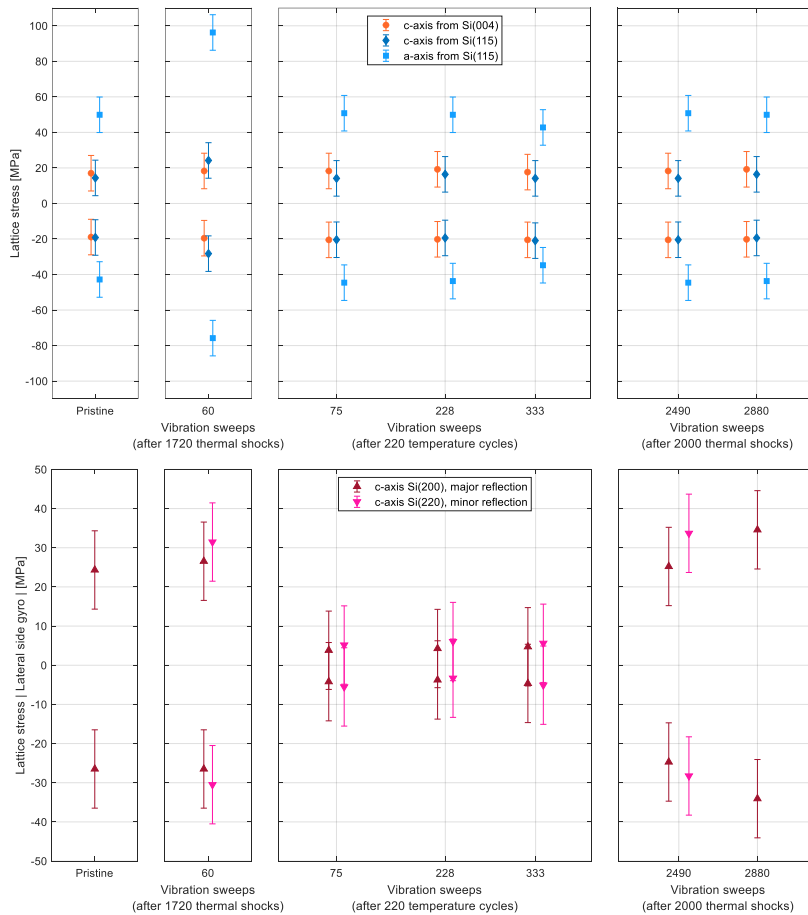


Figure 4.28: Lattice stress in the gyroscope die. Si(004) and Si(115) intensity peaks correspond to the top of the MEMS. The Si(220) intensity peaks correspond to the lateral side of the gyroscope, shown for the minor and major reflections. Measurement uncertainty is ± 10 MPa.

lifetime may cause a gradual degradation of its functionality, if the defect density continues to increase in such a small-volume structures. The gained knowledge of the residual strain in MEMS structures help in overall understanding of aging mechanisms: stress present at the movable silicon structures level can alter their geometry [224], and also at the package level [226], [242]. However a recent work by Tahir *et al.* [246] suggests an accelerometer design for which the effect of a residual stresses (in the range of ± 100 MPa) is negligible. This gets to the importance in analysis of mesoscale samples (from tens of micrometers to few millimeters), to which silicon MEMS structures, such as comb drives, are belonging. As the physical models of failures used for microscopic (atomistic) and for macroscopic (bulk) scales are fundamentally different, HRXRD helps in comprehension of the lattice defect and strain/stress concentration and its relation to aging mechanism.

4.3.3 Wire bonds pull tests

All devices that, at this stage, still retained structural integrity were submitted to wire bond pull followed by shear testing. The aim of wire bonds pull test is to evaluate the strength of the gold wire bonds by pulling thanks to a specific tooling consisting of a hook, establishing force distribution. The same machine as for die shear is adapted using dedicated cartridges. As reference, test method 2019.9 of MIL-STD-883K provided the guidelines for this test. In Section 2.2.1.5, wire bonds pull test on pristine devices showed pull forces between the ASIC and the package centered at 85-90 mN while the connections between the gyroscope, respectively the accelerometer and the ASIC are centered at around 105-110 mN. Such test has been performed on an identical equipment as previously.

The representation is summarized here in terms of a 2D projection of a piecewise fit of the experimental points. Details of pull tests (projections on axes for thermal and vibration dependencies) are given in Appendix I. Overall, poor fits are found due to a large scattering that do not permit to draw clear tendencies. Projection on the thermal shocks or vibration axes fail to prove any trend, even in the case of the accelerometer-ASIC bonds as a function of the number of thermal shocks. Degradation is expected to take place, as shown by the slightly decreasing trends in the two other cases: the gyroscope-ASIC bonds. In general, the weak slope of the regression line sits within the experimental data range, confirming that no evident generality can be drawn.

Instead, it is proposed to represent the data in the form of heat maps, as depicted in Figure 4.29. An absence of clear trend is again highlighted, though a weakening effect of the accumulative testing can be observed in the cases of the gyroscope-ASIC and ASIC-package bonds sets. The slight increasing trend of the surface plot in the accelerometer-ASIC case, though being contained within the experimental variability range, may find an explanation in the gel covering the bonds. A metallurgical hardening of the gold wires seeming improbable, an artificial hardening due to an unwanted reinforcement of a baked silicone gel may cause the slight increase in pull resistance. This has however not been observed in the other cases. Finally, this analysis did not lead to a conclusive outcome. Accumulative testing on the wire bonds' resistance demonstrated their high robustness and insensitivity to these harsh conditions.

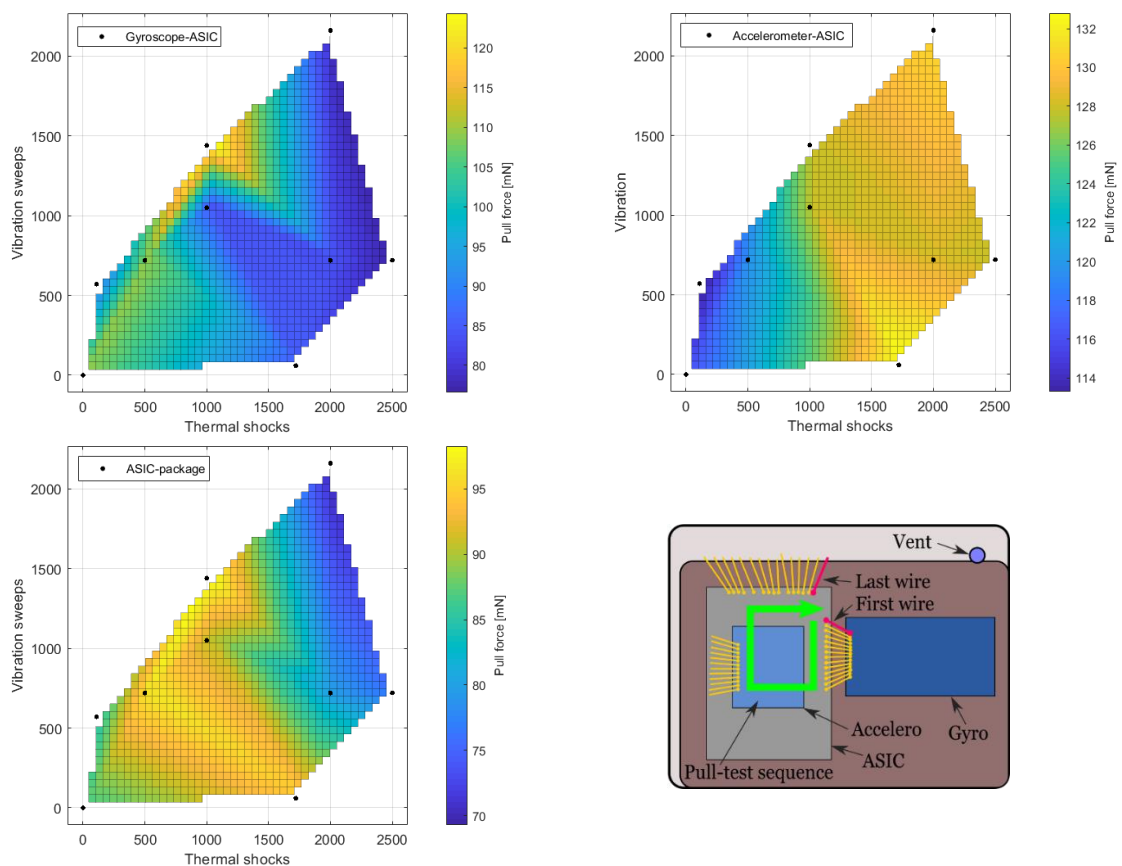


Figure 4.29: Strength distribution of the wire bonds in the test space after accumulative testing for the three different localizations in the MEMS device. Averaged experimental standard deviations are: 32 MPa (gyroscope-ASIC), 8 MPa (accelerometer-ASIC) and 20 MPa (ASIC-package). This variation is due to the variable arch geometries, lengths and heights of the wire bonds.

4.3.4 Post-tests die shear

The same set of devices as in the previous chapter were used for die shear, after the wire bonds have been tested. Referring to the well-known standard MIL-STD-883K, Test method 2019.9, the purpose of this test is to determine the integrity of materials and procedures used to attach a semiconductor material to a substrate. The die shear force is obtained thanks to a dedicated apparatus, permitting the application of a tool on the side of a given die and detach it by mean of a movement parallel to the substrate (package). An illustration of the setup is reproduced in Figure 4.30 from the work of Nguyen *et al.* [247]. The tests are performed on an identical equipment as in Section 2.2.1.6.

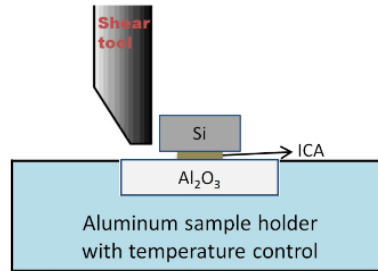


Figure 4.30: Illustration of a die shear test. The tool pushes the die by applying a force on its side, shearing the die attach until detachment thereof, or until catastrophic failure of the silicon. ICA: Isotropic Conductive Adhesive.

The procedure puts in contact a rigid tooling with the gyroscope die – the most accessible element in the package. Tooling is of an equivalent dimension (2.5 mm) as the largest side of the gyroscope’s base surface area (3.90 x 2.17 mm²). During shear testing it is essential to apply a pure shear force to the bond between the silicon chip and the substrate. After careful alignment, the tooling calibrates itself with respect to the ceramic substrate and progresses a vertical offset of 100 μm at a rate of 50 μm/s. Forty-six devices were tested in total, including the series from the CVF, VXV and VVX series as well as pristine, control samples.

The results can be presented according four different manner: (i) the shear force as a function of the cumulative number of thermal shocks (which demonstrates the effect of the thermal steps solely), (ii) the shear force as a function of the vibrations sweeps (translating the mechanical degradation of the die attach over testing), (iii) a 3D plot representing the data in the test space and (iv) a heat map derived by projecting the 3D plot. These representations are displayed in Figure 4.31. From the exponential fit computed on the shear force F versus thermal cycles (N_T) plot, one gets:

$$F = F(N_T) = 435.9 \cdot \exp [(-1.301 \cdot 10^{-3})N_T]$$

An estimation of the stress at the die attach level after a given number of thermal cycles can be done as following. It has been observed in Section 4.3.1 that tomography pictures displayed a similar appearance of the die’s cracking in the G22-CVF series due to the 220 temperature cycles, as compared to devices having been submitted to 2000 thermal shocks (regardless of the employed sequence). Therefore, one can proceed to a rough estimation of the force necessary to shear the gyroscope die based on the above formula. Inserting $N_T = 2000$ one yield:

$$\hat{F} = 263 \text{ N}$$

The footprint surface area of the gyroscope’s die is $S = 8.46 \cdot 10^{-6} \text{ m}^2$. Considering a similar adhesion’s surface loss as determined in Section 4.3.1.1 for the cracked and partially delaminated die attach of the CVF device, the remaining adhesion surface is 31% smaller. If one translates the surface loss as a parameter $\lambda = 0.31$, the equivalent shear stress yields:

$$\hat{t} = \frac{\hat{F}}{(1 - \lambda)S} = 5.5 \text{ MPa}$$

This order of magnitude is comparatively 8 times lower that values found for example in the work of Nguyen [247], [248] where die shear was also performed on a Nordson DAGE 4000. For example, a well-spread die attach silver-loaded epoxy (EPO-TEK H20E) displayed a shear stress of about 40±8 MPa in pristine condition. On the other hand, inserting $N_T = 0$ in the model yields, for a $\lambda = 0$, to a shear stress of 52 MPa. The model therefore is in reasonable agreement with this other work, provided that the slight overestimation is compensated by the uncertainty prediction bounds. It is to be noted that the standard only specified forces ranked by surface areas. It is mentioned that “*all die*

area larger than $64 \cdot 10^{-4} \text{ in}^2$ shall withstand a minimum force of 2.5 kg or a multiple thereof^p. With a die larger than this threshold since $S = 1.31 \cdot 10^{-2} \text{ in}^2$ (25.4 mm), the equivalent shear stress is here greater than the minimum specification.

It is however impossible to extract a prediction model for the shear force as a function of vibration. The graph shows a cloud of points without any obvious trend. While the upper half (above the 10^2 N shear force line) displays a decreasing trend, the lower half shows a slightly increasing one. This observation confirms the much greater influence of the thermal steps in testing compared to vibration: the $F > 10^2 \text{ N}$ values correspond to devices having undergone less than 1000 thermal cycles, while the lower half points correspond to the series with more than 1720 thermal cycles. Overall, the heat map suggests the preponderant detrimental effect of thermal shocks and to a lesser extent, of vibration. R^2 for the 3D surface is 0.9693.

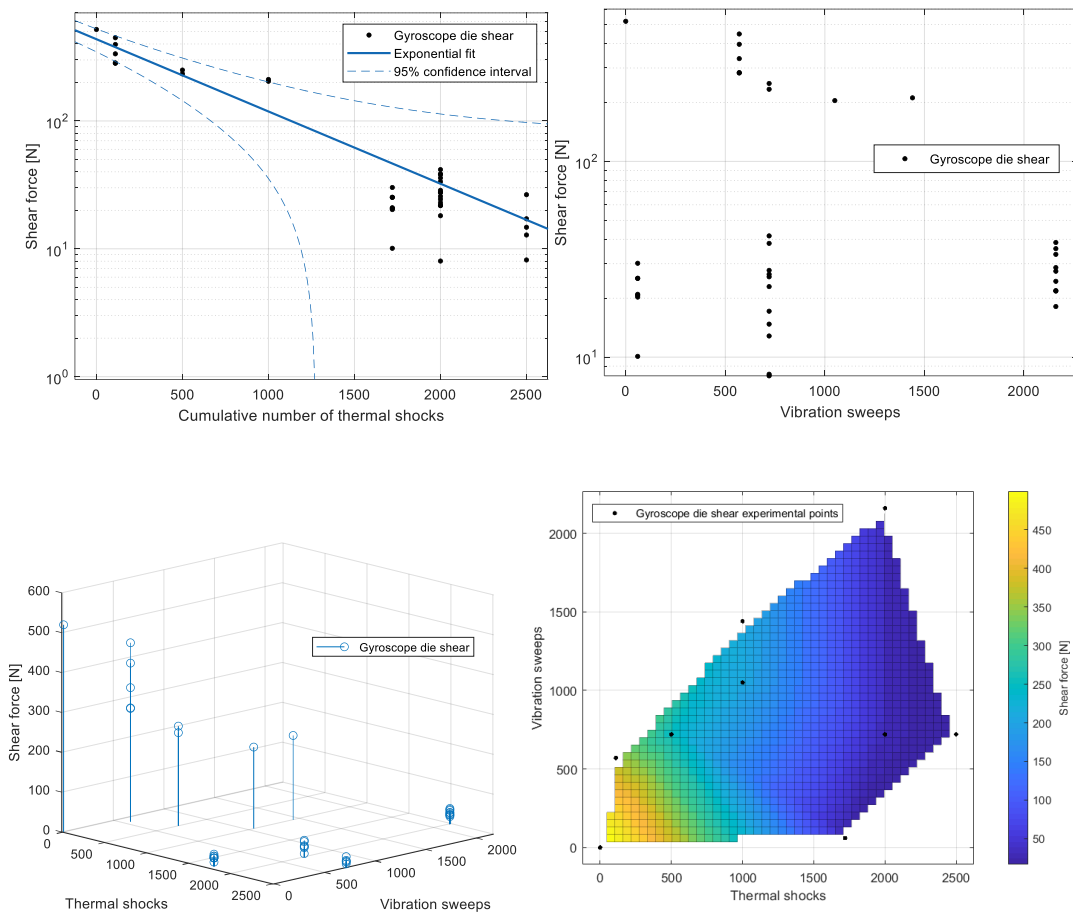


Figure 4.31: Die shear results as a function of (upper left) the thermal shocks, (upper right) the vibration, (lower left) 3D dispersion of the experimental points and (iv) 3D surface plot from the experimental points and heat map of the shear force.

Chapter 5 Finite Element Analysis

In this chapter, thermal and thermo-mechanical stresses and strains in the die-attach are investigated through Finite Element Modelling. FEM is the most used tool to simulate and predict the behavior of physical phenomena. It can also permit to obtain *a posteriori* complementary information from a given environment or in situations where experimental testing does not yield enough data. The nature of degradation phenomena occurring during this thesis' test campaigns was identified thanks to the FMEA performed in the previous chapter. The only sequence that showed catastrophic failure of the die attach was identified by performing vibration testing on pre-conditioned devices that have undergone temperature cycling. Cracking and delamination were observed for device sets that have seen extensive thermal shocks. In general, and besides the case of the CVF-Series, reliability testing was not entirely conclusive, in the sense that complete failure of DUTs could not be obtained. Hypotheses were mentioned and related to competing phenomena such as material' thermal degradation or CTE mismatch that led to different stress states in the adhesive. This chapter proposes to focus on the latter assumption.

To better understand of the thermomechanical phenomena taking place in the device, a Finite Element Analysis is performed on a numerical, representative clone of the device. COMSOL Multiphysics 5.5 has been used in this respect. Physical modules have been activated when necessary for the representation of the phenomena taking place in the simulations. The hypothesis will be detailed for each of the developed models hereafter, while results will be discussed over the course of the sections. This chapter divides the investigation in two parts:

- In Section 5.1, a thermal model of the device is constructed. This step helps identify that the die attach is thermalized at almost the same rate as the device's external environment.
- In Section 5.2, a thermomechanical model is elaborated. Numerous considerations will be made, namely on the materials side with a die attach featuring viscoelastic properties. The development is constructed of two parts:
 - A 2D model of a central section of the package-die attach-die stack to predict the stress and displacement field across the interface.
 - A global 3D model of the entire die attach to study the effect of the inter-die adhesive fillet and applicability of the 2D results to the 3D counterpart.

This section is partly based on the paper published in the journal of Microelectronics Reliability [249]. The global discussion, encompassing the results and learnings from Chapter 4, is compiled together in Section 6.1.

5.1 Thermal model

This section aims at demonstrating that the weakest element failing in devices – the die attach adhesive – is indeed thermalized and in constant equilibrium (first approximation) with the thermal chamber. This will permit to assume that the measured experiment temperature corresponds reasonably to the temperature at the die attach level, where thermally induced degradation occurs. Modelling starts with a CAD of the device, built with Solidworks 2020 and displayed in Figure 5.1. The construction of a full device replica is key to understanding the device's subsystems' thermal profiles since the system is composed of several heterogeneous materials. The dimensions are obtained from the averaged values of in Section 2.2.1.

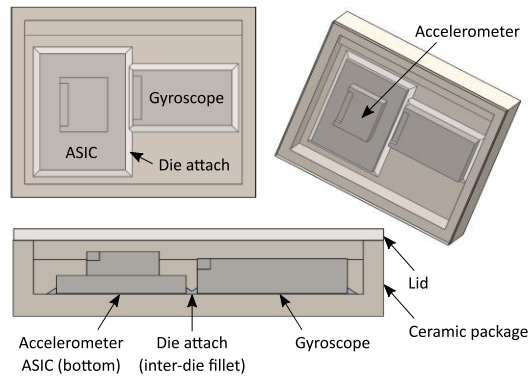


Figure 5.1: CAD reconstitution of the MEMS device (top view and cross-section views).

5.1.1 General hypotheses

While being a good representation of reality, this model is simplified as per the following points:

- The lid is constituted of a monolithic sheet of steel without the vent, since pressure is not considered in the relevant physics. The interface between the steel and the material of the package (alumina) is considered as being ideal, without the presence of any adhesive. In reality, this is not the case since a glass-frit adhesive is present at this interface (Section 2.2.1.1). As the focus of the modelling is the die attach, it is ignored: the far-field stresses are considered negligible with respect to the stresses that build up at the interfaces of interest (package-die attach-silicon die) – a reasonable assumption.
- The adhesion between silicon dies (for example: at the ASIC-accelerometer interfaces) is assumed as ideal. To recall, no thermomechanical testing procedure led to delamination at the inter-die or intra-dies interfaces.
- The package is considered as a monolithic alumina part. The embedded electrical leads (Section 2.2.1.7) are assumed to have a negligible influence on the material's thermal and mechanical behavior. While the package is made of successive sintered powdered ceramic and filling layers, it is modelled as a homogeneous bulk alumina part.
- The gas in the cavity is dry air with conduction-only mode for the heat transfer.
- The gold wire bonds and the conformal gel (see Section 2.2.1.4) are not represented in this model since it is believed to have negligible effect on the die attach's strength.
- Finally, the die attach is represented by a simplified, angular shape instead of the complex structure of menisci and overflow fillets, as visible in the observations in Sections 2.2.1.7. While the thickness of the die attach is not uniform beneath the ASIC or the gyroscope dies, it is considered as constant to the averaged value of $20\ \mu\text{m}$. The whole die attach is aggregated in the monolithic angular shape displayed in Figure 5.2. Considerations regarding the material is given in Section 5.2.1.

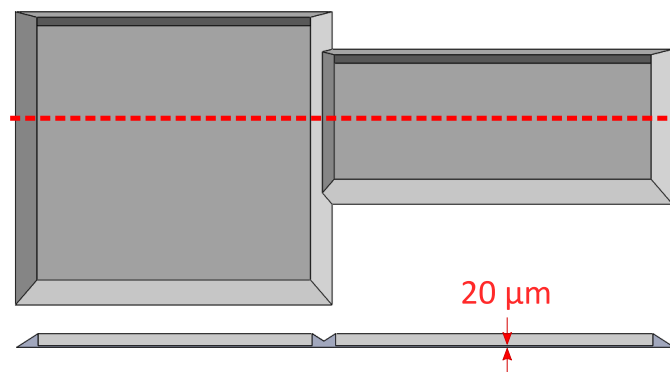


Figure 5.2: Die attach CAD model and cross-section, extracted from the numerical clone.

5.1.2 Materials and geometrical considerations

The CAD model is imported into COMSOL. Volumes attributions and materials selections with relevant metrics for the present thermal study are reported in Table 5.1. For the thermal study, no other parameters are necessary since they do not participate in the physics selected in the software. As primary environmental input, the temperature is measured in the thermal shocks chamber by means of a thermocouple directly placed next to the devices under test. Two situations are considered:

- A direct exposition to the thermal flux coming from the chamber's fan (estimated: -180 to $+336^{\circ}\text{C}/\text{min}$)
- The shielded configuration), with use of an aluminum profile, was used for the experimental thermal tests (refer to Section 3.4.1.1) to mitigate the difference between the positive (heating) and negative (cooling) thermal gradients (estimated -57 to $+59^{\circ}\text{C}/\text{min}$).

Table 5.1: Thermal physical characteristics of the materials (from COMSOL's database).

	Package Alumina (Al_2O_3)			Dies Single crystal silicon		
Heat capacity	C_p	$[\text{J}\cdot\text{kg}^{-1}\cdot\text{K}^{-1}]$	900	C_p	$[\text{J}\cdot\text{kg}^{-1}\cdot\text{K}^{-1}]$	700
Density	ρ	$[\text{kg}\cdot\text{m}^{-3}]$	3900	ρ	$[\text{kg}\cdot\text{m}^{-3}]$	2329
Thermal coefficient	k_{iso}	$[\text{W}\cdot\text{m}^{-1}\cdot\text{K}^{-1}]$	27	k_{iso}	$[\text{W}\cdot\text{m}^{-1}\cdot\text{K}^{-1}]$	130
	Cavity Dry air			Die attach Ag-filled epoxy (85%wt)		
Heat capacity	C_p	$[\text{J}\cdot\text{kg}^{-1}\cdot\text{K}^{-1}]$	1004-1023 [†]	C_p	$[\text{J}\cdot\text{kg}^{-1}\cdot\text{K}^{-1}]$	350
Density	ρ	$[\text{kg}\cdot\text{m}^{-3}]$	0.75-0.65 [*]	ρ	$[\text{kg}\cdot\text{m}^{-3}]$	2410
Thermal coefficient	k_{iso}	$[\text{W}\cdot\text{m}^{-1}\cdot\text{K}^{-1}]$	0.018-0.038 [*]	k_{iso}	$[\text{W}\cdot\text{m}^{-1}\cdot\text{K}^{-1}]$	3.3
	Lid 316 stainless steel					
Heat capacity	C_p	$[\text{J}\cdot\text{kg}^{-1}\cdot\text{K}^{-1}]$	430-550 [*]			
Density	ρ	$[\text{kg}\cdot\text{m}^{-3}]$	8005-7900 [*]			
Thermal coefficient	k_{iso}	$[\text{W}\cdot\text{m}^{-1}\cdot\text{K}^{-1}]$	12-16.5 [*]			

([†]) As per COMSOL's non-linear temperature-dependent model for C_p
 (^{*}) Pseudo-linear part (third-degree temperature dependence) over the experimental range $213 < T < 463$ [K]

To verify that the die attach is thermalized before the chamber switches from one temperature extremum to the other, the aluminum profile in which the devices are positioned is modelled as well (Figure 5.3). Therefore, devices are shielded from the stream of air coming from the chamber's fan, which dampens heat transfer between devices' external surfaces and the air flux. The profile has been sliced on the top gutter to permit air to equalize between the internal channel and the outside environment. An insertion hole for the atmospheric thermocouple has been made, which measures the temperature at the middle section of the profile. By doing so, the measured temperature profile represents the worst-case scenario in the chamber.

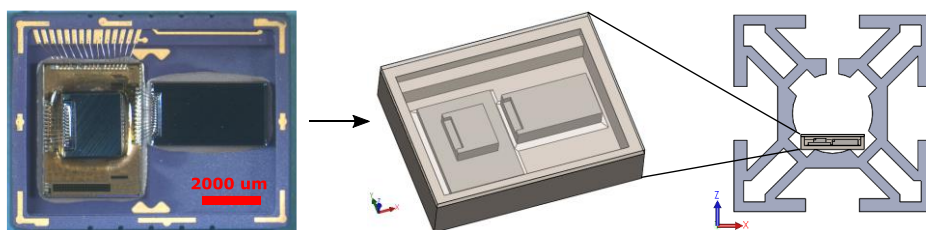


Figure 5.3: From real sample to CAD model, and finally 2D COMSOL model in the shielded configuration.

5.1.3 Numerical results and discussion

The first step of the thermal study is to represent temperature evolution at the profile's inner space, where devices are placed. This constitutes a worst-case scenario since it would correspond to the ideal, orthogonal positioning of the profile with respect to incoming thermal flux. In real experimental situations, turbulent airflow, and non-ideal positioning lead to differentiated airflow in the inner space, promoting heat transfer. However, in the simulation, this aspect was not considered in the physical inputs of the model as first approximation.

A simplified model of the median cross-section of the aluminum profile is constructed. A horizontal airflow of 1 m/s is defined as the input, from left to right. The temperature input (Figure 5.4) is obtained from an experimental measurement from an atmospheric thermocouple placed in the direct airstream at the middle of the chamber's test volume. The first longer plateau at high temperature aims at assuring the complete thermalization of the model. The model runs over a full thermal shock picked in the bulk of data from a multicycles campaign, starting from the hot bound. The thermal study synthesis is provided in Figure 5.5, which took 26.5 hours to converge to the full solution. The figure shows the air flux velocity distribution for a 1 m/s stream flowing from left to right, as well as the temperature distribution in the considered volume. The air flux's behavior is visible, and the difference in temperature between the colder profile and the warmer air is highlighted.

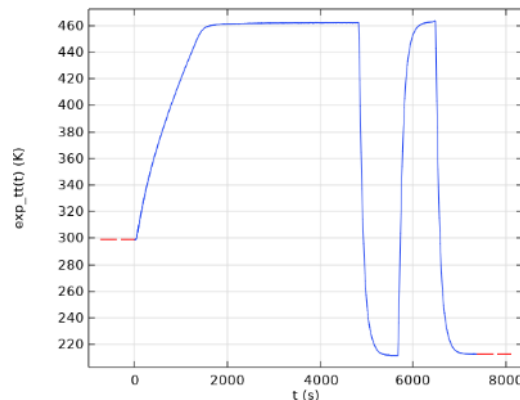


Figure 5.4: Temperature profile used as input in the FEA study. The first progression and long soak time at 460K corresponding to the initial warm-up and temperature stabilization of the apparatus. Such smooth transition also helps with convergence.

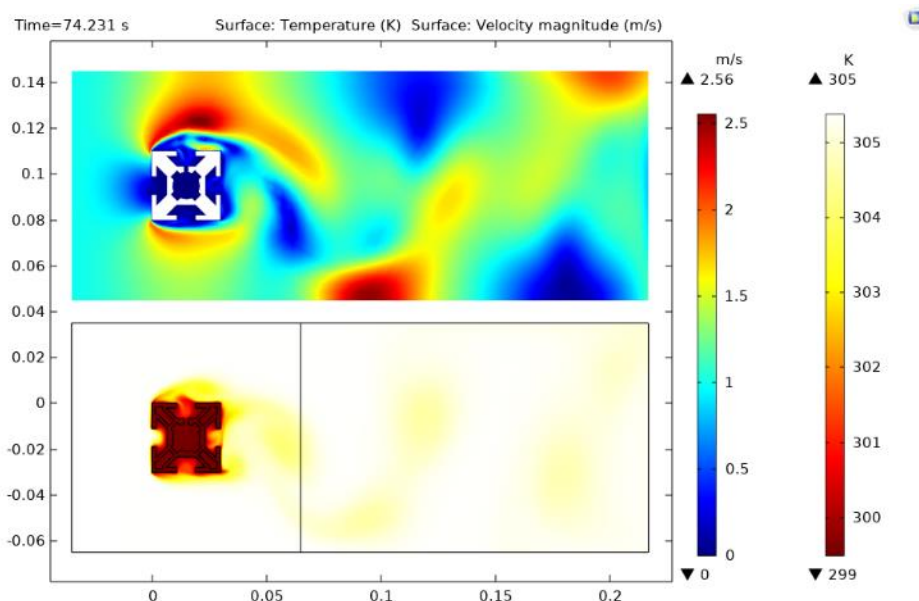


Figure 5.5: (top) Meshing of the 2D model. (bottom) Behavior of the aluminum profile in the air flux. Input airstream velocity has been set to 1 m/s.

The simulation produces as output the temperature at device's location, such as shown in Figure 5.3. This temperature, which refers to a worst-case scenario, is coherent with the experimentally measured temperature at the core of the profile. In terms of fluid flux, the air velocity in the cavity is zero in this specific case, while it would be non-zero in any other configuration of the profile with respect to the incident flux. With these observations, it is possible to coherently simulate the device in an environment that does not feature the aluminum profile, hence reducing the complexity of the analysis.

A full-scale thermal model of the device is therefore constructed using the CAD model shown in Figure 5.3. At the edge of the ASIC die embedded in the die attach, a temperature probe is defined in contact with the package. Figure

5.6 presents a cross-section view with the location of the probe point. This probe is used for the measure of the temperature variation in the numerical model. It is compared to the input (experimental) temperature.

The measured die attach temperature is characterized by two variants of the same principle used for representing the configuration. The device being contained inside the aluminum profile (worst case scenario) is surrounded by air, hence dictating heat transfer from the environment to the package, and in turn, to the inside of the package (assuming pure conduction mode in the cavity). Hence, two thermal studies run for an airbox offset from the device's surfaces by 5 and 10 mm, respectively (order of magnitude of the inside space of the aluminum profile). Obviously, any situation where the air flux would not be zero (misaligned profile in the air stream) or a direct exposition to the chamber's hot/cold air would force the heat transfer to higher magnitudes. Overall, these two conditions are compared to the chamber's experimental values in the unshielded and shielded (with aluminum profile) data.

The graphs in Figure 5.6 displays thermal gradients that can be observed when a device is inserted in the aluminum profile. It strongly contributes to control the discrepancy between positive (heating) and negative (cooling) gradients, as highlighted by the two solid lines. Undercooling and overcooling are observed in the unshielded situation. In the smaller air sheath (5 mm), the thermal gradient is nearly identical to the environments. With the 10 mm (which corresponds to the size of the profile's cavity), the die attach temperature still manages to reach the set point. Recalling the worst scenario condition, the simulation tells that the device is fully thermalized when temperature changes occur – in both the hot and cold situations. A similar plot made for pulsed air and showed no lag. Simulations further showed that the minimal dwell time indicated in the standard MIL-STD-883, Test method 1010, would not be long enough to allow the internal temperature to stabilize in the case of a more voluminous and massive device. This is an important point to take into consideration when designing a thermal experiment.

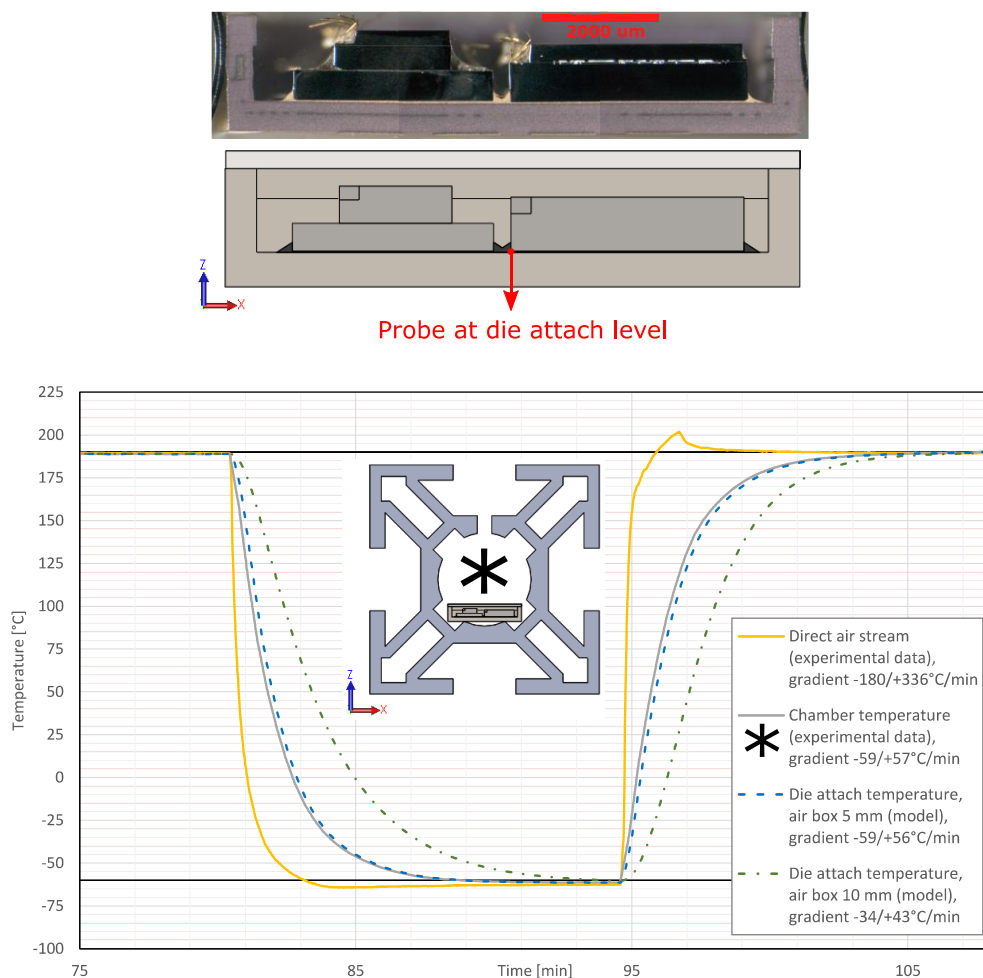


Figure 5.6: Graphical comparison shows the experimental data of temperature recordings in the chamber (solid lines) versus the simulated values (dashed lines).

5.2 Thermomechanical study

From the previous section, it has been predicted that devices are properly thermalized during thermal shocks testing. This sets good bases for elaborating a more complex model permitting simulation of the thermomechanical stresses building up at the die attach level. For doing so, the numerical clone is reduced to the relevant parts, removing the elements of volume that are not believed to participate mechanically at the die attach level, namely: the sides of the ceramic package and the lid.

5.2.1 Materials and geometrical definitions

Several volumes attributions and operations of compartmentalizing are done in order to ease discretization and reduce computing time. The 3D model shown Figure 5.7 is adapted in this respect. An additional partition is implemented at the die attach level to better delimitate the meshing at this reduced thickness of material ($20\ \mu\text{m}$), where a finer element size is used. Several locations in the model feature right angles, which would in turns be stress concentration sites. This critical observation must be considered when the thermomechanical study will yield minimum and maximum mechanical stress values.

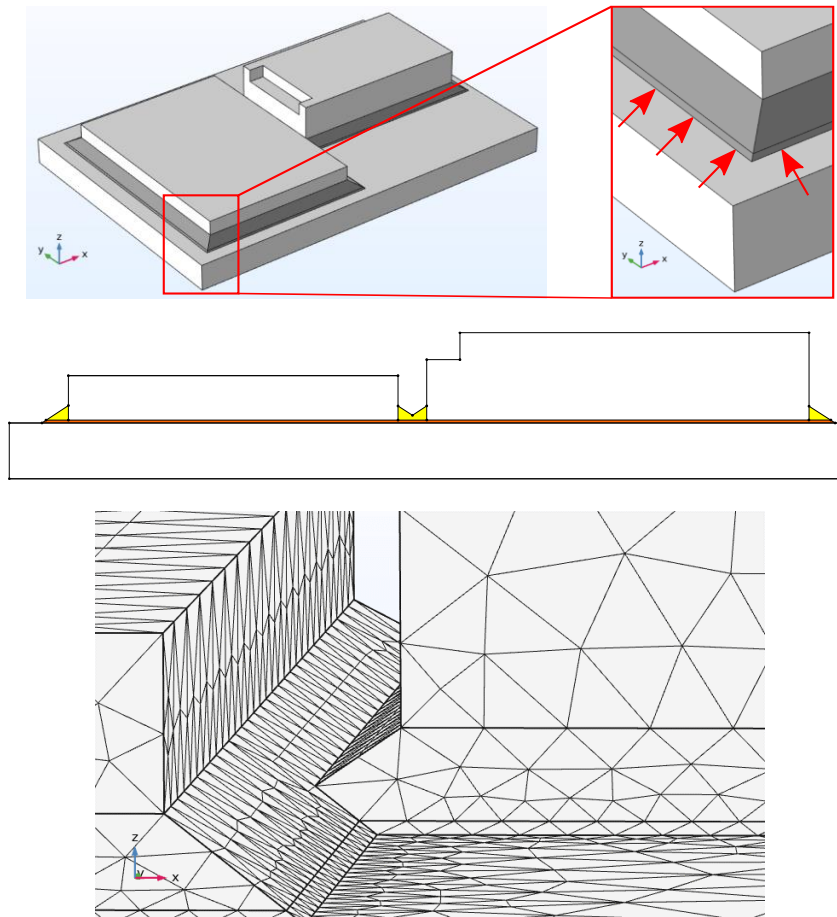


Figure 5.7: (*top*) Sub-model used for the thermomechanical simulation, (*middle*) cross-section in the X-Z plane, middle section of the device, (*bottom*) view of the sub-millimeter fine mesh used. This work plane is set as the starting point of a sweeping mesh with a minimum element size of $0.3\ \mu\text{m}$

In addition to the materials' thermal characteristics mentioned in Table 5.1, one must consider the elastic and viscoelastic properties (Table 5.2). The die attach material poses a challenge in terms of thermomechanical behavior: it is a thermoset polymer-based composite containing 85%wt of silver particles, as shown in Section 2.2.1.8. While the mechanical properties of other solid materials are considered to be elastic (linear), the die attach adhesive is developed with a viscoelastic model that will be developed in Section 5.2.2. Air is assumed to have no mechanical effects.

Also, the presence of the vent on the lid of the device's package permits pressure equilibrium between the inside of the IMU's cavity and the environment.

Table 5.2: Mechanical properties of the linear elastic materials (from COMSOL's database).

	Package	Alumina (Al_2O_3)	Dies	Single crystal silicon
CTE	α_{iso}	[K ⁻¹] $8 \cdot 10^{-6}$	α_{iso}	[K ⁻¹] $2.6 \cdot 10^{-6}$
Young's modulus	E	[Pa] $300 \cdot 10^9$	E	[Pa] $170 \cdot 10^9$
Thermal coefficient	ν	[-] 0.22	ν	[-] 0.28

5.2.2 Viscoelastic model for the die attach's material

There is a well-developed body of literature on the thermomechanical laws and failure mechanisms that affect the die attach, particularly metal-based solders. For example, an approach consists of applying the metallurgical theory of crack propagation in continuous solids, such as Coffin-Manson-based fatigue [250], [251]. However, little literature exists on FEA performed on silver-filled epoxy adhesives. While the Coffin-Manson theory applies well to metal-based solders, it is unsure that it applies to polymer-based material such as those used in the IMUs. The great challenge relies on the vitreous transition (T_g) of the polymer and its effect on the materials' mechanical behavior as temperature rises. Bjorneklett [252], [253] presented a model for thermal fatigue based on Paris-Erdogan's law (crack propagation), while Su and Qu [254] applied a Coffin-Manson (strain-based) model to a measurement of conductivity by four-point bending fatigue test. Other sources related similar works for metallic solders with a similar method to understand the degradation of electronically conductive adhesive joints [255], [256]. The implications of viscoelasticity are essential for the proper elaboration of a Finite Element Model: the polymer behaves differently at the upper bound of the temperature cycles used for all testing in the present study (+190°C) than at the lower bound (-60°C). Several literature sources on epoxy and/or conductive adhesive materials characterization show that the storage modulus below T_g can drop by two orders of magnitude below the transition temperature [149], [257]–[260]. For instance, the high performance commercial conductive adhesive EPO-TEK H20S' datasheet indicated a vitreous transition temperature T_g at about 80°C. This adds a non-trivial consideration for building the current simulation. Viscoelastic models have to be used to treat the non-linearity of the thermomechanical response [261]. Provided that the exact formulation of the die attach material is unknown, a set of assumptions are made (Table 5.3).

Table 5.3: Assumptions in the FEA.

The die attach does not feature any initial internal stress due to gluing (fully relaxed), and the interface is considered as perfect.
COMSOL's internal physical data for an 85%wt silver loaded epoxy are used with manual corrections to consider the viscoelastic considerations.
At the low temperature bound (-60°C), the die attach material in glassy state is characterized by the CTE($T < T_g$) and the mechanical parameters from EPO-TEK H20S datasheet.
The viscoelastic behavior of the die attach between room temperature and the high temperature bound (+190°C) is implemented using a Generalized Maxwell model. The Prony series (G_i and τ_i coefficients) as well as the William-Landel-Ferry (WLF) coefficients, to cope with the thermal effects, are exploited from the work of Hamou <i>et al.</i> on a similar die attach material [261].

The viscoelastic behavior of an isotropic conductive adhesive (ICA) can be approximated by the Generalized Maxwell model [262]. The viscoelastic model adds a dampening element to the linear, spring constant-dependent representation of elastic materials. The material's response is, in this case, characterized by a series of spring-dash pots groups (Figure 5.8) described by their i -th shear coefficient G_i , alternatively compliance E_i and their time constants $\tau_i = \eta_i/E_i$ with η_i the viscosity. In linear elastics, a system can be simplified as a simple spring-like connector defined entirely by E_∞ , the constant compliance coefficient.

$$E(t) = \frac{\sigma(t)}{\varepsilon_0} = E_\infty + \sum_{i=1}^n E_i \exp\left(-\frac{t}{\tau_i}\right)$$

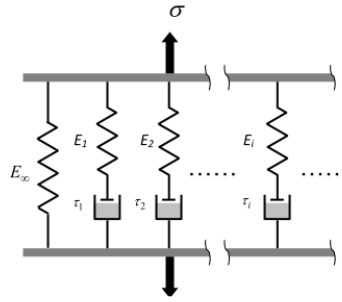


Figure 5.8: Spring-dash pots representation of a viscoelastic material in the Generalized Maxwell Model.

The equation for $E(t)$ is the relaxation modulus, and the series representation is called the "Prony series." This model permits to describe temperature effects thanks to the use of a *shift function*. The Prony series are adapted for different temperatures in this case. Assuming a first time-temperature $(t_0; T_0)$ and another set $(t_1; T_1)$, one has:

$$E(t_0^{(T_0)}) = E_\infty + \sum_{i=1}^n E_i \exp\left(-\frac{t_0^{(T_0)}}{\tau_i^{(T_0)}}\right)$$

$$E(t_0^{(T_1)}) = E_\infty + \sum_{i=1}^n E_i \exp\left(-\frac{t_1^{(T_1)}}{\tau_i^{(T_1)}}\right)$$

One can equalize these two equations and demonstrate that:

$$\tau_i^{(T_0)} = \frac{t_0^{(T_0)}}{t_1^{(T_1)}} \tau_i^{(T_1)}$$

If the fraction is substituted by a temperature-dependent parameter $A = A(T)$ and taking the logarithm, the expression transforms into:

$$\log(t_1^{(T_1)}) = \log(t_0^{(T_0)}) - \log(A)$$

This expression gives a linear relationship between the time unit t_0 at temperature T_0 and the necessary shift $\log(A)$ that it takes to express the time t_1 at temperature T_1 . This time-temperature equivalence principle permits to express the stress relation at any temperature by simply shifting the curve from a reference temperature. Therefore, for a successive set of temperature ranges, one can build a "master curve" by shifting and joining a succession of temperature-modulus curves into one. Such a demonstration is, for instance, as proposed by Liu *et al.* in [263]. Ultimately, the shift function can be related to a temperature-dependent relation, of which one of the most used is named the William-Landel-Ferry (WLF) function:

$$\log(A) = -\frac{C_1(T - T_{ref})}{C_2 + (T - T_{ref})}$$

With T_{ref} is a reference temperature and C_1 , and C_2 are dimensionless constants. These properties are generalized characterized by rheological experiments, such as the Dynamic Mechanical Analysis (not covered in the present work), such as mentioned in the work of Springer and Bosco [264].

These considerations are necessary to elaborate a thermomechanical model in COMSOL. The software features a viscoelasticity module that requires, in the case of a Generalized Maxwell Model, to provide as inputs the Prony series and WLF coefficients as substitutive and temperature-dependent materials properties of the die attach. In the present case, the 85%wt Ag-filled epoxy's default properties were redefined using the data from [261], as shown in Table 5.4.

Table 5.4: Viscoelastic properties of the die attach isotropic conductive adhesive.

Thermal				Prony series	Shear modulus G_i [Pa]	Relaxation time τ_i [s]
Vitreous transition	T_g	[°C]	90			
Thermal conductivity	k	[W·m ⁻¹ ·K ⁻¹]	14.2-12.4 [‡]	2	8.92	0.01584
Mechanical				3	53.33	0.6288
Bulk modulus	E	[MPa]	4487	4	57.37	12.54284
Shear modulus	G	[MPa]	11.67	5	65.88	198.6798
Poisson's ratio	ν	[-]	0.33	6	390.57	3082.669
Viscoelastic				7	622.762	30321.4
William-Landel-Ferry function coefficients	T_{WLF}	[K]	303	8	542.15	171099.1
	$C_{1,WLF}$	[-]	28.56	9	120.67	883451.5
	$C_{2,WLF}$	[K]	778.84	10	136.15	$3.13 \cdot 10^6$
				11	73.35	$9.95 \cdot 10^6$

(‡) COMSOL's temperature-dependent definition of k between 213 and 463K.

With this new definition, COMSOL is adapted to better simulate the die's behavior over the considered range of temperature, from -60°C to +190°C. The vitreous temperature being included, at 90°C, within this range means that the die attach's thermomechanical behavior strongly varies below, during, and above this threshold.

5.2.3 Two-dimensional partial model

To understand the evolution at the die attach's level over a full thermal shock cycle, a two-dimensional model, representative of the middle section of the package-die attach-die sandwich is obtained from a cross-section of the general 3D model to observe the effect of the input parameters (including the materials parameters defined previously). One important consideration presence of a thin layer of material sandwiched between to more rigid bodies. In COMSOL, specific mechanical considerations are to be considered:

- The die attach's 20 μm thickness is thin with respect to the package's and die's.
- With the addition of thermal stresses, the classical 2D *plane strain/stress* simplification is not as straightforward as in the purely mechanical stresses case.
- Formally, a 2D *plane strain* treatment can be applied to a beam that is infinitely long on both sides of its cross-section and constrained at infinity. *Plane strain* required the assumption that expansion in $Z = 0$.
- A thermal stress build-up occurs due to non-diagonal elements of the rigidity tensor which, for an isotropic material, means than Poisson's ratio $\nu > 0$.
- In this thermomechanical study, the part is not constrained in Z which means that expansion in Z from the die attach's perspective is free. It is consistent to the fact that the silicon die is not constrained on the top of itself: expansion in $Z \neq 0$ and the stress $\sigma_{zz} = 0$.
- *Plane stress* is therefore applied to the die attach in the model.

Additionally, *roller* is defined as boundary condition for the package's lower side. This permits a free expansion of the package's material in the in-plane (X - Z) directions while still being constrained in the Y direction. A fixed constrain is set at the lower-right summit for better stability during solving, while a symmetry condition ensuring the model's continuity on the right side (Figure 5.9).

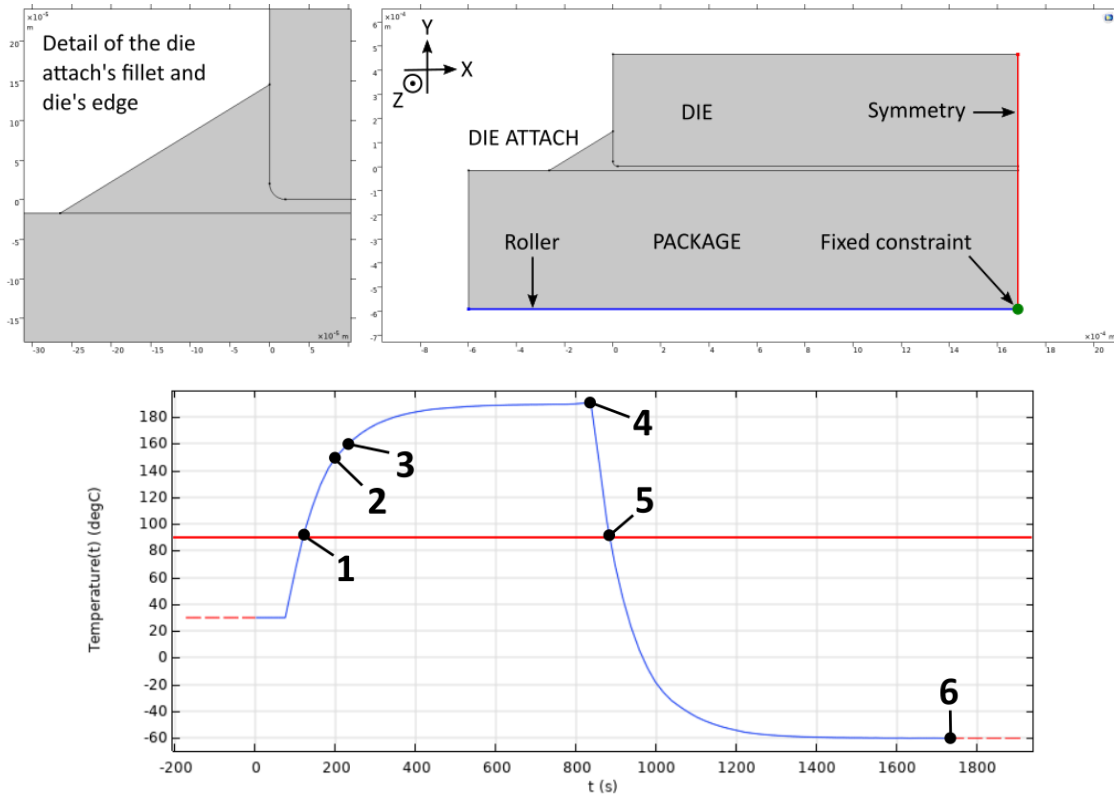


Figure 5.9: (top) Two-dimensional model of the package-die attach-die stack with locations of boundary conditions. (bottom) Temperature profile used in the 2D model and the analysis points. The horizontal line at 90°C corresponds to T_g .

Six snapshots at successive time-temperature couples along the thermal shock plot (Figure 5.9) were extracted to predict the thermally-induced von Mises stress and displacement field. Figure 5.11 presents the stress and displacement fields in the 2D model. Figure 5.12 presents zoomed-in views of the die attach region from the displacement plot. The color code is changed to better render the zero-displacement regions from the non-zero ones.

The von Mises analysis shows that stress is building up at the die's edge next to the fillet's edge. The die's edge acts as stress concentrator in this region, which then propagates to the entire stack as temperature changes. From a stressless situation at room temperature, the stress is increasing up to about 65 MPa at 94°C (slightly above T_g) in the dies in the vicinity of the edge. As temperature increases further on, a visible relaxation of the stress is predicted by the model, stalling at low values when the maximum temperature (190°C) is reached. When cooling occurs, stress appears back as contraction of the constituent takes place. At -60°C, stress levels reach amplitudes beyond 100 MPa (maximum: 336 MPa at the die's edge) in a large part of the elements. The visible bulge at the fillet is due to the mesh's definition and the 70 times exaggeration factor set in COMSOL's graphics.

On the other hand, displacement in the die attach evolves significantly as temperature increases, with a change of sign in its amplitude along the horizontal axis: in the hot regime, there is an inversion between the zone close to the fillet and the center of the die. The displacement field's amplitude reaches a maximum of +24.6% and a minimum of -14.5% at 148°C. In Figure 5.12, the main directions of the displacement field, probed at the boundaries between elements, feature a diverging behavior. Dissimilar displacement of the package (bottom) and the silicon die (top) is likely to be the cause, as suggested by the graphical representations. This divergence in displacement field is likely to generate shear in the die attach.

At -60°C, large variations of stress are visible between both sides (top and bottom) of the die attach. Therefore, the model predicts the apparitions of alternating stress and strain as cycling continues. This observation, combined to the optical views of the degraded adhesive such as in Figure 4.22 (Section 4.3.1.3), suggests that not only materials degradation is taking place as the thermal shocks progress, but also a probable plastic damage accumulation at the die attach level that is caused by a cyclic stretch/unstretch phenomenon at the interface. Additionally, this 2D model can predict why cracking preferentially occur at the die's edge initially, such as the needle shaped cracks seen in Figure 4.23 (Section 4.3.1.3).

Finally, the 2D model permits to extract the predicted value for the τ_{xy} element of the Cauchy-Green strain tensor, which relates to the non-diagonal shear element of the initial state of the material. Four plots have been compiled in Figure 5.10: they report the amplitude of strain at four locations in the die attach. At the edge, the Cauchy-Green strain reaches 5.6% at 835 seconds in the thermal shock (see Figure 5.9) and decreases to non-zero levels as temperature decreases to 60°C. At 900 seconds (below T_g) and further on, the strain amplitude stabilizes. Geographically, strain diminishes as the probe is far from the edge. This observation that shear occurs mostly in the regions far from the bulk of the package-die attach-die stack. Therefore, the single mechanical factors are not enough to explain the globular degradation: another phenomenon is taking place, supposedly materials degradation (shrinkage, outgassing).

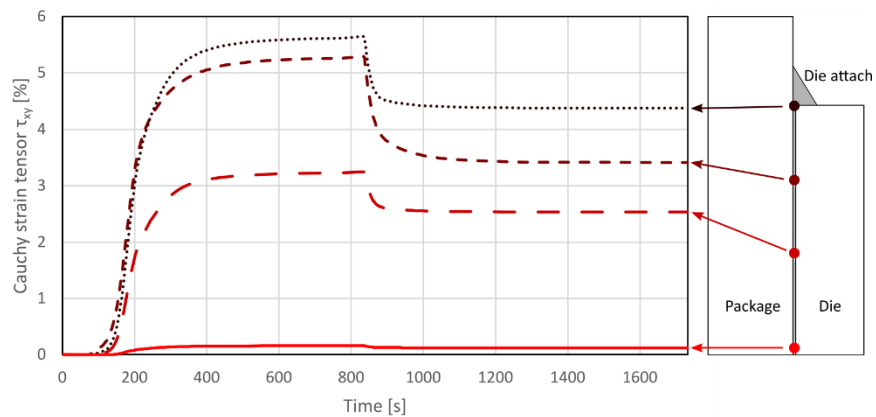


Figure 5.10: Cauchy-Green strain tensor element τ_{xy} depicting shear at four locations in the die attach (neutral line).

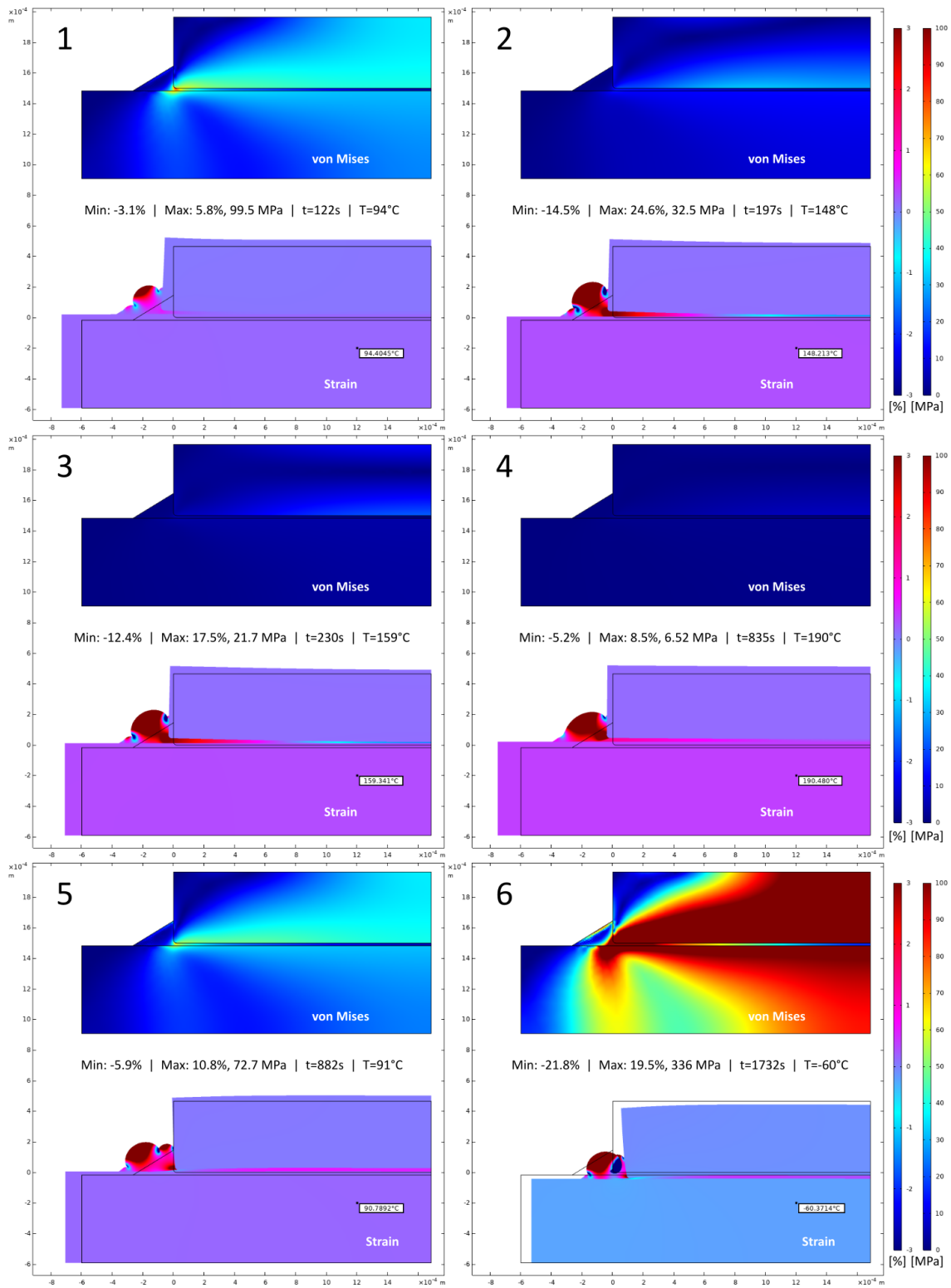


Figure 5.11: 2D heat maps representing the von Mises stress and volumetric strain in the package-die attach-die stack for several time-temperature values over one thermal shock. Minimum strain and maximum strain and von Mises stress are shown.

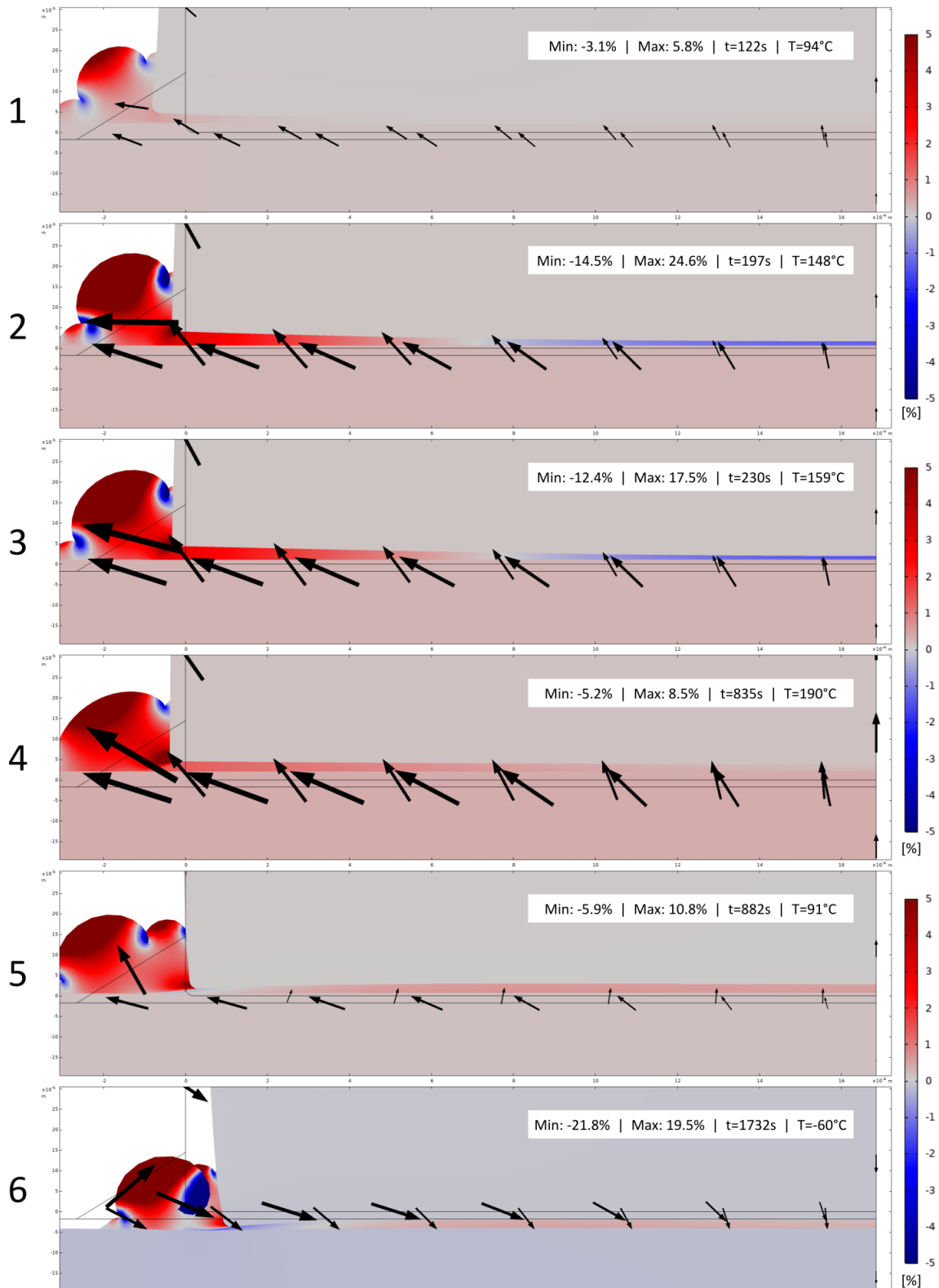


Figure 5.12: Close-up view of the die attach region to identify the displacement field at regions' boundaries and volumetric strain represented with a symmetrical color range. The time range corresponds to a single thermal shock.

5.2.4 3D numerical results

The learnings of the 2D model gave insights in a plane stress approximation, which does not consider boundary effects far from the center of the die. A 3D model is therefore built to cope with this aspect, and to verify if the model's behavior is the same in all four quadrants that a die is counting. Moreover, the inter-die space is of interest since fillets are joining. The important role of the fillet has been highlighted previously, and the conjunction between the two dies is of interest.

In this paragraph, the die and package are hidden in the 3D model. Only the die attach's volume is kept for clarity. The thermomechanical model is built to obtain the stress-strain figures in the die attach domain. Depictions of the stress and strain distribution are shown in Figure 5.13, which groups several views at selected temperatures.

At -60°C (cold model), a stationary model is elaborated to reduce computing time. It returns a maximum von Mises stress of 79.5 MPa with shear stresses (τ_{xy} , τ_{xz} , τ_{yz}) between 25 and 34 MPa both in tension and compression, which diverges sensibly from the 2D model. Using a stationary model was assumed to be consistent with the nearly linear behavior of polymers at low temperature, far from the vitreous transition point [265]. Doing so, the computation time is reduced to the portion of the cycle from the reference temperature T_{WLF} to $T_{max} = +190^{\circ}\text{C}$. Strain levels are ranging between -2.77% and -0.04% , which are in the ballpark of the displacement amplitudes found before.

In the hot model, a time-dependent study is defined with the reference temperature at 30°C and a thermal shock to $+190^{\circ}\text{C}$ using experimental data. The stress and strain values are reported in Figure 5.14 for several indicators: the maximum von Mises stress in the volume and maximum tensorial values of the shear stress.

The maximum measured stress values increase with the temperature and progressively relax past $T_g = 90^{\circ}\text{C}$ [261] with a slight lag. Graphical views of the stress and strain in the FE die attach domain are presented. Overall, the maximum

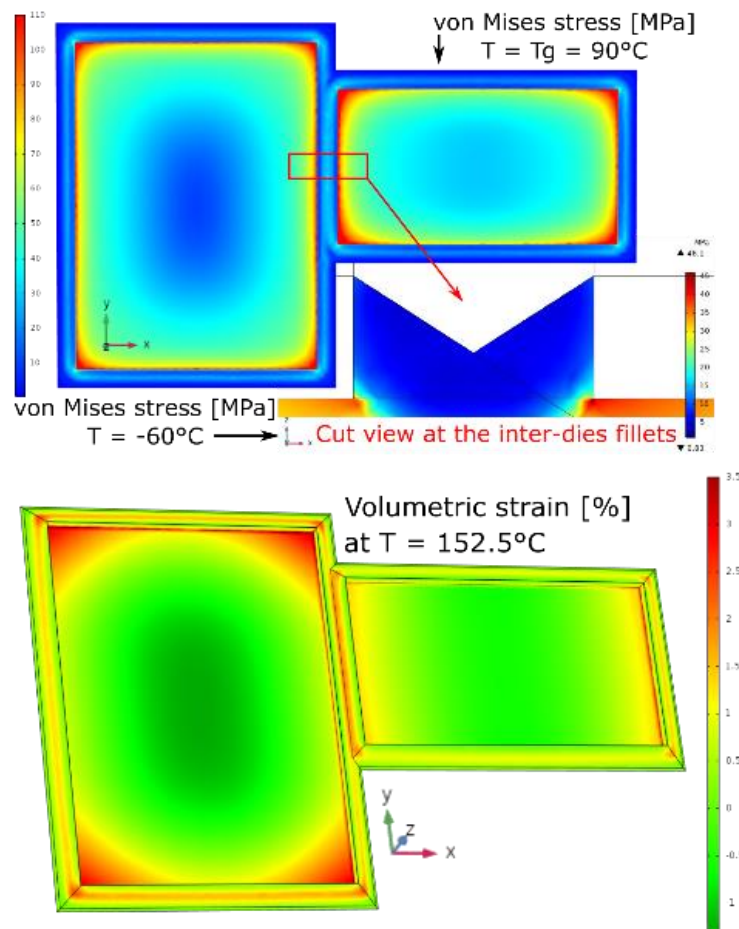


Figure 5.13: (left) von Mises stress heat map of the die attach domain. (right) strain plots with exaggerated deformation factor.

stress levels are observed at singularities (vertices or edges of the dies in the die attach) but more generally in a peripheral rim by the adhesive's fillet and corners. As shown in the 2D model, stress levels in the die attach drop as it is predicted far from the edges. Stress levels at the edges are in the range of 70-100 MPa can be observed, as highlighted graphically in Figure 5.14. Strain follows the same trend and can locally evolve to above 7%. Considering the viscoelastic properties of the conductive adhesive, such levels were expected. It is to be noted that the silicon die's contribution to the volumetric strain is insignificant. In EPO-TEK's datasheet, the shear strength is indicated to be 8.55 MPa (lap shear measurement) or 12.26 MPa (die shear).

On the other hand, Perichaud [149] reported tensile stress values between 20 and 60 MPa within the temperature range of 20 to 90°C, depending on the adhesive's formulation. Given the present computed stress, it is therefore probable that plastic strain accumulates in the die attach as the temperature cycles progress. Microcracks initiating at the fillet and the adhesive inter-dies gap have been observed by radiographic inspection during thermal tests. With a hypothetical damage accumulation at the die attach level, the FEA can foresee possible crack initiation at stress concentration sites, later propagating to the rest of the adhesive bulk. The damage accumulates progressively over the thermal shocks and weakens the bond. Finally, vibration testing leads to failure that would not otherwise have occurred (or only over large time durations).

To conclude, values the amplitudes found in the 3D model lack of directionality but are nevertheless providing an additional dimension in the thermomechanical analysis. It can also indicate that the behavior predicted by the 2D model might apply in the 3D case. Interestingly, the inter-die fillet does not seem to yield more stress, as suggested by the low stress levels in Figure 5.13. The Finite Element Model also shows the effect of dissimilar coefficients of thermal expansion (CTE) between the silicon chips, the die attach conductive adhesive, and the device's ceramic substrates. This makes the system vulnerable to thermally induced strain. More importantly, the fillet's importance uncovers new questions regarding design choices. Overall, the accumulated strain is expected to initiate and promote cracks in the die attach, leading to failure.

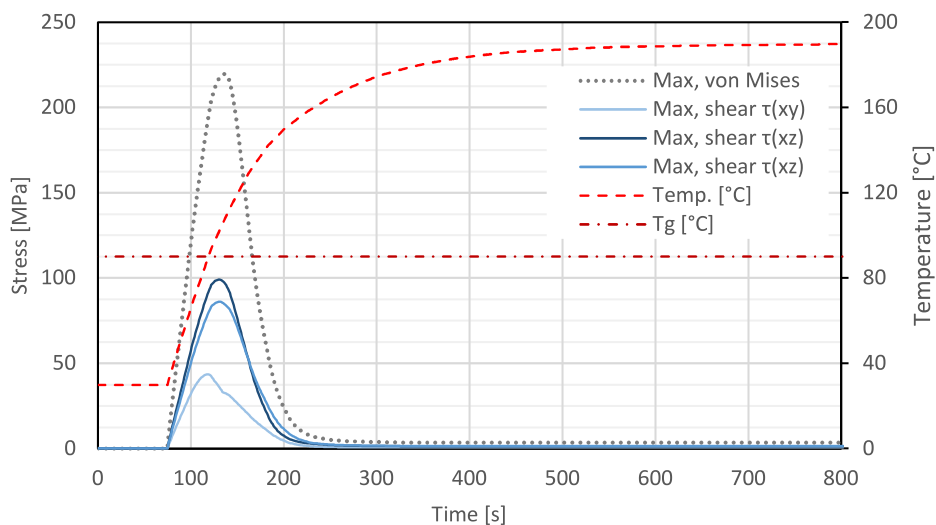


Figure 5.14: Relaxation of the thermally induced stress past T_g . Compressive shear stress – of similar amplitude – is not displayed for clarity.

Chapter 6 Discussions and conclusions

The present research addresses the need of a better definition of reliability testing procedures dedicated to MEMS devices for space application, by proposing an approach to accumulative multi-steps testing. The procedures are based on combinations of thermal and vibration loads in sequential and alternating manner. Reliability testing, as performed nowadays on MEMS devices, is mostly based on legacy standards that were historically developed for microcircuits or hybrids. To assess the lifetime under a given environment, test conditions specified in current methods miss to be representative or conclusive enough in the case of highly reliable components. Also, the selected commercial IMUs were sourced from the automotive field, which demonstrated excellent reliability figures under the mentioned environments.

6.1 General discussion

The experimental testing showed that single-parameter test conditions, based on methods from the MIL-STD-883K standards, are insufficient to lead to any significant degradation or failure in the robust DUTs. While being a good sign for the end application and user, such testing misses to provide insightful information other than a “pass” sign. The IMUs used as the focus of this first investigation did not exhibit failure as per the defined failure criteria, even at loads levels that were far greater than the maximum datasheet values. As reminder, the test conditions for both temperature cycles and thermal shocks were fixed between -60°C and $+190^{\circ}\text{C}$, while the datasheet values specified a maximum operation range of -40°C to $+110^{\circ}\text{C}$. A distinction is made upfront between the temperature cycles (low thermal gradient) and thermal shocks (high gradient), which gave raise to fundamental differences in the devices’ response to degradation due to different cumulative soak times. On the mechanical side, the tested vibration intensity of 50g is nearly ten times greater than the 15g safing full range of the datasheet. Most notably, the devices are immune to vibration, even at such levels. The statistical treatment used for representing the data, based on box-and-whiskers, demonstrated the very low variability induced on the measurement of gravity over vibration testing.

Using this knowledge as a basis, the test plan was adapted to submit the devices to accumulative testing. A dedicated visual method to represent the testing phases was developed and box-plot statistical data consolidated the meaningfulness of the observations. One highlight was the strong distinction to be made between temperature cycling and thermal shocks testing. A preconditioning based on temperature cycling damaged the devices in a significantly worse manner than a same number of thermal shocks would have ever done. The advanced weakening of the die attach adhesive, an isotropic conductive adhesive constituted of a silver-loaded epoxy matrix, could not handle the subsequent vibration, and failed rapidly (<333 sweeps), in comparison to other series of devices that have experienced thousands thereof. Through the failure of all devices of the sample group, a Weibull probability plot has been constructed and gave as parameters $\gamma = 133.78$ (shape) and $\alpha = 1.38$ (shape), the latter providing a statistical demonstration of the continuous degradation process induces by vibration testing after 220 temperature cycles.

On the other hand, for a same number of thermal shocks performed as preconditioning, devices withstood without effort the load sequence. This permitted the increasing accumulation of alternative thermal shocks and vibration steps, ending after 7 steps without complete functional failure (up to 2500 thermal cycles and 2880 vibration sweeps). Even in well-known and accepted specifications such as ESCC 2269000, thermal tests, typically defined for flip-chip circuit components with non-hermetic packages, are defined with 1500 cycles for the test program – a number lower than those used here. However, the robust devices, while returning readable signals by the readout socket, failed at fitting within the predefined failure criteria bounds of 2%. The box-and-whiskers treatment of the data showed a steady, negative degradation of the failure criteria as testing alternates between thermal and mechanical tests. Detailed analysis demonstrates the predominant effect of thermal shocks steps over vibration. While this observation corroborates the fact that thermally-activated phenomena dominate over mechanical, one could have expected a inversion of the roles as the die attach degrades. This has not been the case: in all series with extensive thermal testing, the deviation characterizing the drift of the measurement of the averaged gravity value were mostly caused by thermal shocks. Even though deviations as high as 8% were recorded (in absolute value), devices remained

functional, demonstrating accelerometer and gyroscope readouts devoid of errors. The relatively narrow amplitude changes of the 25% and 75% quantiles in the box-and-whiskers plots demonstrated a uniform aging throughout the testing, testifying of a reproducible method even on a restricted sampling size (maximum 13 devices by series). This opens interesting perspectives for reliability testing rationalization, both in terms of resources and test multiplicity.

The accumulative testing method also highlighted the distinction between effects of temperature cycles (long soak time at temperature extremes) compared thermal shocks (short soak time). This observation suggests that the decisive factor leading to devices' degradation is not preponderantly the temperature delta, but rather the exposure duration in the upper and lower bounds. While such an outcome can be explained by Arrhenius-type thermally activated phenomena, it is not straightforward. Effect of temperature (or changes thereof) was at the root cause of the die attach degradation, consisting of a combined effect of weakening (mechanical loss) and delamination (contact surface loss). This observation was further corroborated by FEM, which confirmed that the devices experience temperature changes that are equivalent to the imposed environmental conditions. The temperature dataset is then used as input for the viscoelastic study that demonstrate the variation of the stress and strain in the die attach, as the materials experiences changes in its properties due to the transition through the vitreous temperature T_g . The mechanical relaxation at $T > T_g$ has been highlighted thanks to the application of the Generalized Maxwell Model. The determined stress and strain loads are on par to previous knowledge on the resistance of isotropic conductive adhesives used in MEMS technology, which tends to indicate that stress concentration sites, especially at the fillet, will naturally lead to local cracking over the thermal cycling procedure. Overall, while the model can surely be improved, it permitted to back up the observation and quantitative analyses performed during the test campaigns. The die attach being a robust but heat-sensitive polymer-based material, its degradation directly (catastrophic detachment) or indirectly (deviation of the MEMS metrics) affects the devices' performances over time. These learnings could be useful for design choices when it comes to MEMS packaging technology.

Use of CT-scan and radiographic inspection tools were essential in the understanding of the root cause to the failure of the catastrophically damaged devices. It however did not permit to ensure that observed deviations were caused by thermal effects, since large drifts in the Y-axis measurement were in several cases not accompanied (at least at the same time) by a drift of the X-axis. This phenomenon remained unexplained, though hypothesis emanating from electronic effects in ASIC, anisotropic material effects or diverse dynamic response of the devices to the environments might explain it.

HRXRD results allowed for accurate strain evaluation in the gyroscope. The analysis revealed the presence of stress approaching 100 MPa at the interface between the die's two half covers. As such, it did not allow to assess the state of the MEMS microstructures', since X-rays can only interact with matter over a depth of a hundred nanometers. However, this shows the importance of the analysis of mesoscale samples, ranging from tens of micrometers to few millimeters, to which silicon microstructures belong. This result is at least an order of magnitude lower than the expected stress in the case of bulk silicon. As the physical models of failures used for microscopic (atomistic) and for macroscopic (bulk) scales are fundamentally different, HRXRD helps to the understanding of the lattice defect and residual stress build-up.

Sequential testing has rarely been studied in reliability testing. Results of this research, though based on investigating only two test conditions, shone a light on new developments that are yet possible to extract more valuable information while combining two tests into one plan. Thorough statistical treatment of the data permitted the identification of the main tendencies influencing the X- and Y-axis. It has been seen that a Weibull of data, using the aggregated number of cycles can possibly represent the failure probability with verified goodness-of-fit. Moreover, statistical analysis of die shear forces provided a clear graphical view of the detrimental effects of both vibration and thermal shocks (the latter being predominant) on the die attach's strength evolution. Also, a good fit of an exponential model could be elaborated, providing with an equation an estimation of the die attach's shear resistance as a function of the number of thermal cycles. Such a fit was however not possible with vibration – the influence thereof not being sufficient to enable the determination of a trend. On the other hand, wire bonds pull tests did not display any clear trends with respect to the position in the vibration-thermal test space. The accumulative test campaigns, though being focused on only two test parameters, provided with vast knowledge on the behavior of commercial inertial measurement units. The accumulation of an alternation loads demonstrated that, while the focus shall be set on the thermal effects influencing parameters and constitutive elements, that degradation phenomena could occur with test conditions that would not lead to failure in a standalone fashion. Keeping in mind that these conclusions are valid for

the defined test criteria bounds, this paves the way for new reliability testing assessments methods dedicated to robust MEMS-based devices, possibly with a greater variety of test conditions.

6.2 Synthesis of the research

Overall, the tested IMUs have proven their exceptional resilience to aging under temperature and vibration conditions well above their specification and purpose. Most certainly, tight processes and quality controls take place during manufacturing, that led to low variability of the resulting degradation observations. This opens new horizons and understandings for safe and trustful use in inhospitable environment such as space, where the obstacles to wider use are either focused on inherent capabilities or conservative decisional environment. Synergies between the space and the automotive fields can be envisioned considering the developments reported in this dissertation. This conclusion on accumulative testing might turn in valuable in future hypothetical space mission, but it applies also to ground-based application under extreme environments. One could imagine a spacecraft that capitalizes on its reusability for decreasing costs and resources waste. Embarked sensors would need, in sensitive subsystems such as propulsion or heat shield, be repetitively exposed to large temperature variations following or combined to vibrations. Premature thermal aging of adhesives or vital functions, let alone essential functions of the spacecraft, could fail due to the intense vibration of an atmospheric re-entry or another launch.

It is clear that reliability of MEMS is a challenging issue, as it is a cross-disciplinary subject combining multi-materials, electrical and mechanical aspects at once. The reliability issue of MEMS devices requires good understanding of failure mechanisms and remains a challenge on how to model it. Reflecting back at the results of this research and the pie chart figure presented in the literature review (Figure 1.5, page 29), the main failure mode has been determined to be the die attach. It corresponds to the 32% of the 79% package-related failures in MEMS. While the load cases are different (thermal shocks and vibration here, shocks and impacts in the reference), the campaign ends with MEMS devices still operating (though with deviations).

To conclude, one of the main questions addressed by the current study was to question the suitability of robust automotive MEMS for space application. While legacy reliability standards might still be up to date for conventional electronics, they barely yield to conclusions with the tested devices. In this regard, accumulative testing has been shown to be a solution to obtaining valuable information from “two tests in one”, combining thermal and vibration stresses. It must be mentioned that combination with other factors, such as humidity or radiation, could potentially lead to other failure modes. As this concerns the fundamental physical understanding of the phenomena taking place, potential of evolutions in the way reliability testing is done nowadays are possible. By combining several parameters in a single test flow, an engineer could very well reduce the required time, sampling and analysis time needed to extract information from a reliability test of robust devices, that otherwise would not yield to any significant information for lifetime prediction or failure modes identification. In the silicon revolution, reliability is the hindering element preventing the full potential utilization of MEMS for space application. This research attempted to provide a cost-effective solution in reliability evaluation and better understanding of bi-parameter test influence on failure mechanism in robust automotive MEMS devices. In this sense, it could set the grounds for further in-depth definitions of end-of-life test procedures, that could possibly lead to new standards in the future.

6.3 Outlook

6.3.1 Recommended test sequence

This work aimed at generating knowledge that could be exploited to build a reliability assessment flows of a standard. To summarize what could be a recommended test sequence, a general graphical flow has been built based on the model of the evaluation test program of ESCC Basic Specification No. 2269000.

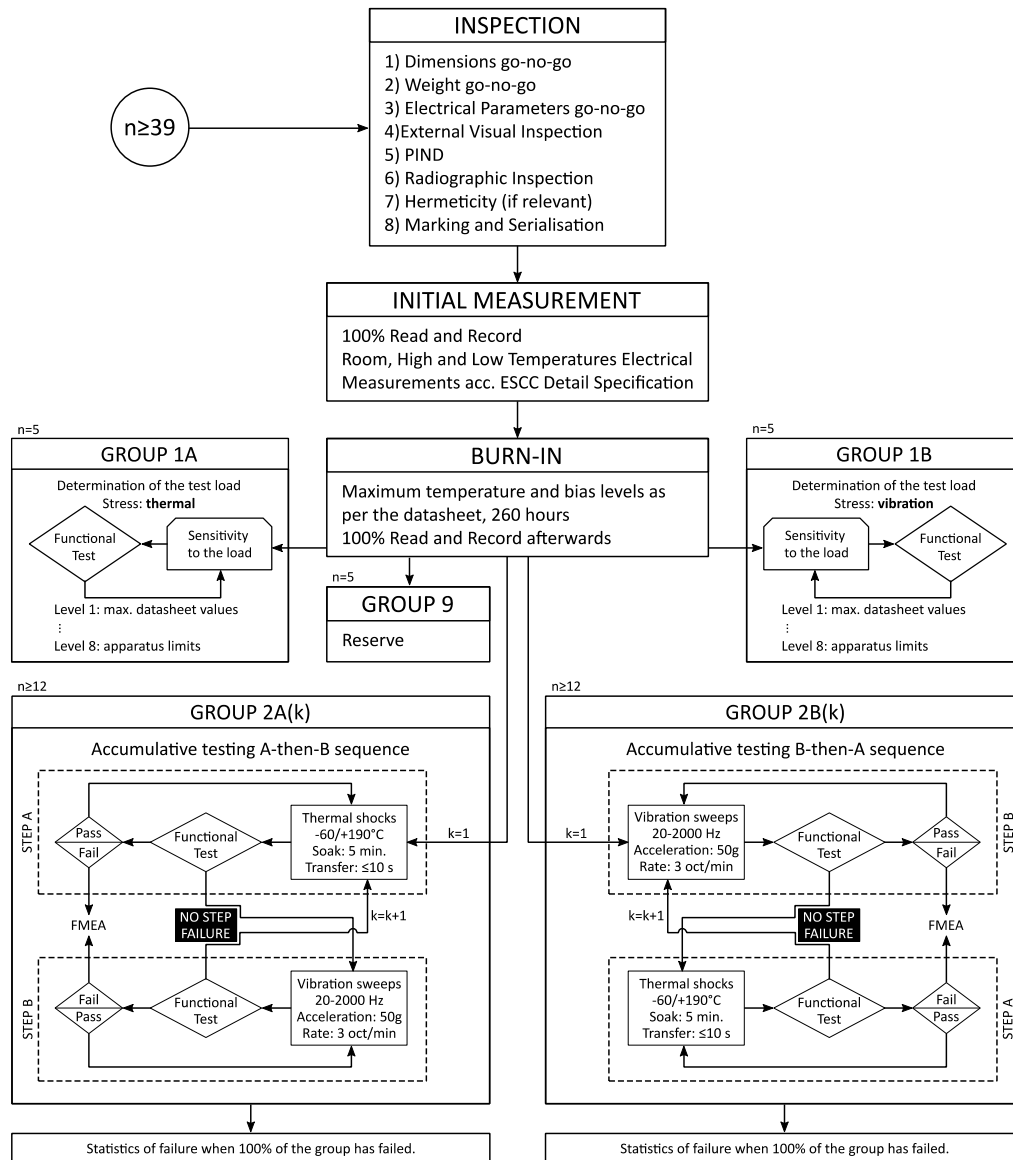


Figure 6.1: Tentative test program with an accumulative thermal and vibration test step.

6.3.2 Challenges ahead for a self-standing reliability test procedure for MEMS in space applications

The main limitation of this research is its focus on only one device (the IMU) and two environmental stresses: thermal shocks and vibration. Temperature cycling has also been covered but to a lesser extent. Of course, manufacturing and assembly techniques are similar throughout the current MEMS state-of-the-art, which suggests that the proposed methodology (and expected response to stresses) might be similar. However, space applications require specific needs, such as hermeticity, or the absence of polymer-based material (*i.e.* metallic die attach). The difficulty in accumulative testing is most likely to determine “*what is enough*” as test loads but also the number of cycles before switching of test nature.

Another possible issue lies in the definition of “*what is a failure*”, since it strongly depends on the operational requirements that concern the chosen devices. Here, either a 2% deviation or catastrophic failure were considered. But degradation could be used so that it avoids prolonging testing up to total failure, as suggested in Section 6.4.3. This would have even greater practical advantages, compared to an extensive test campaign that takes months to achieve. This is however to be compared to how reliability assessment is performed today: durations and sampling needs can surely be reduced thanks to an accumulative strategy. In terms of industrial time and resources, this perspective is definitely attractive.

6.4 Future works

This dissertation focused extensively on accumulative testing under two parameters: vibration and thermal shocks. Nevertheless, other parameters are of importance when dealing with reliability of components for space applications. Moreover, from the obtained results and observations, other analyses are of interest. Suggestions of further works in this field are presented in this paragraph.

6.4.1 Effect of preconditioning on lifetime

The test campaigns relied on identical conditions that were accumulated in a sequential way. However, the true effect of a unique preconditioning ("step 1") could constitute an investigation on its own. If the theory of thermally activated phenomena or step-stress theory (such as from the works of Nelson or Benavides [230], [233]) give tools to obtain lifetime curves from accelerated test, it is understood as arising from the application of a higher temperature compared to a datum. The following assumption could then be tested: if instead of temperature, one considered *temperature* cycles or thermal *shocks* as the accelerating factor, a similar time-temperature equivalence could be found. Graphically, this could be represented as following (Figure 6.2).

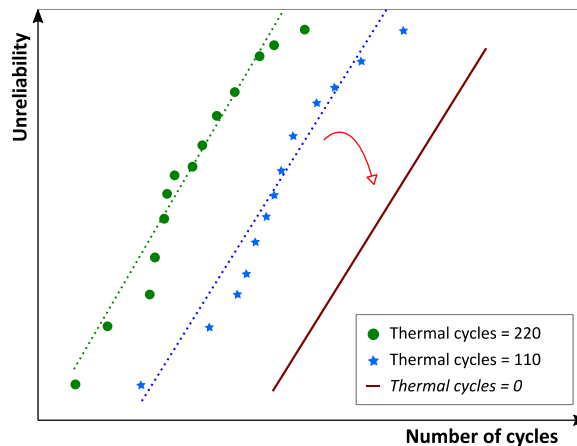


Figure 6.2: Depiction of the hypothesis to be confirmed by experiment of the effect of "preconditioning" (that is: number of thermal cycles prior to vibrations testing for example) to the lifetime of a set of devices.

The two dashed curves, the regression from the experiments, could help extrapolate a third hypothetical line that would permit to predict the lifetime of a batch of samples under no preconditioning – a simple vibration testing (which is experimentally laborious to obtain). In this sense, it could be possible to extrapolate the lifetime of a set of samples through the cumulative lifetime of load steps with increasing intensity (say: increasing ΔT , g ...). That is: the nature of a test a sample has been through does not modify the remaining lifetime of the sample. When jumping to a higher load (or in the present case: another nature of testing), only matters the "health points" already consumed by the samples for one level of load over their overall "health points" budget. In Arrhenius models for accelerating aging, the failure statistics of samples tested at different temperatures can lead to the determination of the acceleration parameter. Analogically, by using – not the temperature – but the preconditioning prior to testing (e.g. the number of thermal cycles undergone by the devices prior to vibration cycling) is intended to be used as the "acceleration variable" and lead to the lifetime prediction model.

6.4.2 Accumulative simultaneous testing

The entire campaign relies on accumulative sequential testing to draw conclusions on the reliability of robust MEMS devices. However, the real-life operational configurations of the environmental stresses are more likely to be simultaneous combinations of loads of different natures. Combined two or more tests conditions at the same time, say vibration, thermal and humidity, are expected to cause synergetic failure modes in devices. This aspect has however not been covered and would complement this research: viscoelastic effects due to a temperature higher than T_g would certainly induce a differentiated behavior of the die attach under vibration. This work could be continued by evaluation reliability under combined two or more tests conditions at the same time, as vibration, thermal and humidity, which might cause synergetic failure modes in devices.

The simultaneous testing consists in combining temperature cycles and vibration at the same time, as displayed in Figure 6.3. The same timing for vibration is used as described previously, while the temperature ramps are dictated by the used equipment.

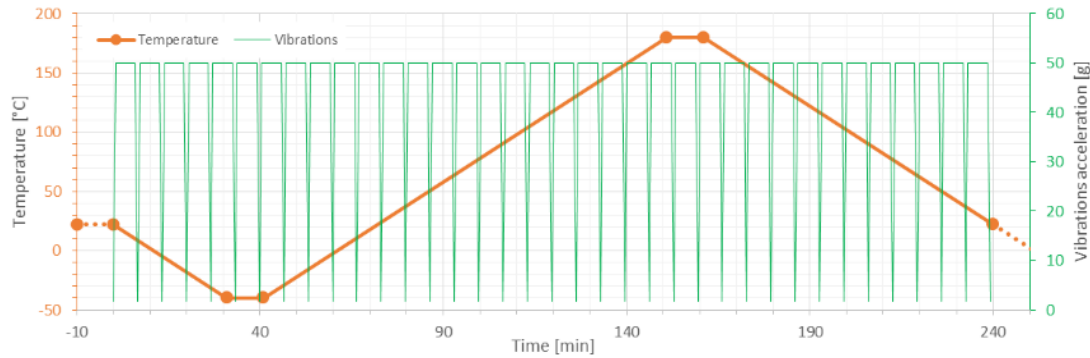


Figure 6.3: Accumulative simultaneous temperature and vibration testing.

While the accumulative sequential test flow considered the two stress natures one after the other, the present accumulative simultaneous method combined temperature cycles and vibration at the same time. This is graphically shown in Figure 6.4.

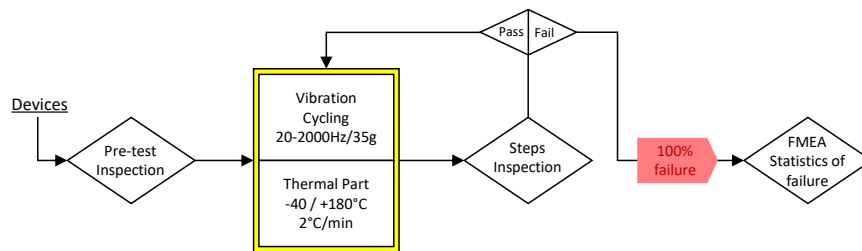


Figure 6.4: Accumulative concurrent testing.

6.4.3 DUTs functionality characterization

Another path of augmenting this research would be to also evaluate, individually, each device over the sequence of testing using the statistical evaluation of the gravity plateaus (see Section 3.2), measured during functional testing of the accelerometer. It has been observed that the accelerometers' signals respond to a normal law (Section 3.2.2), which can be fully characterized by its average (the actual gravity value used in the failure criteria in the devices' own arbitrary units) but also its standard deviation. The latter value would provide an addition information on the potential This would require a complete rework and refinement of the MATLAB script on the global data. Such a treatment would lead to new characterization methods, freed of the failure criteria as defined previously (Figure 6.5).

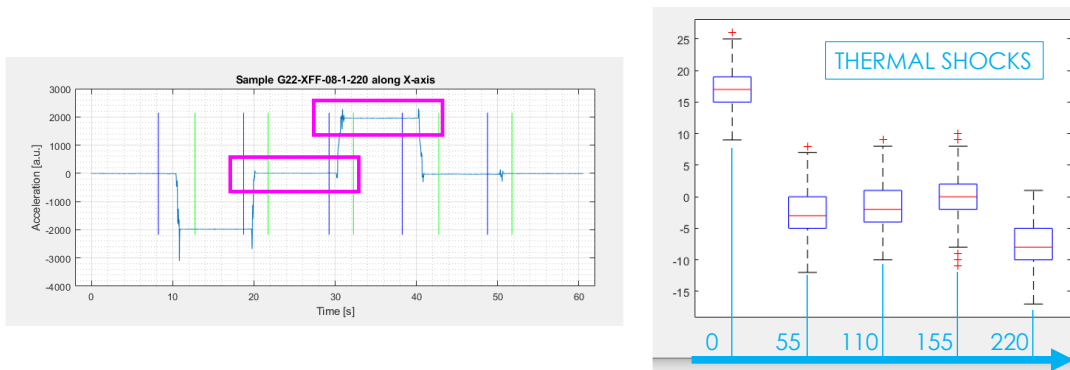


Figure 6.5: Illustration of a degradation-based data treatment from the accelerometers' signals. Computed from real experimental measurements.

6.4.4 Development of a mechanical model

Further investigations could be the mechanical-based model for the die attach. With the used testing (fixed temperature range, fixed vibration loads), the complete determination of thermal-based or mechanical-based aging models is not possible, since they require test plans designed with various ΔT or uniform T (or equivalent mechanical load parameters), to full assess the role of the temperature or vibration taken separately, for evaluation their correlations with the current results. For example, the Modified Coffin-Manson model applied to mechanical failures, materials fatigue or material deformations that takes as variable both the thermal range and the maximum temperature in the equation:

$$N_f = A \cdot f^{-\alpha} \cdot \Delta T^{-\beta} \cdot G(T_{max})$$

With N_f the number of cycles to failure, f the cycling frequency and ΔT the temperature range during a cycle. $G(T_{max})$ is an Arrhenius term evaluated at the maximum temperature of each cycle. This model has been successfully used to model crack growth in solders and other metals due to repeated temperature cycling¹⁵. It is, however, still unsure if sure a model applied to other materials than metals.

Another application, this time of classical, Coffin-Manson based fatigue [250], can treat of substantial differences in the coefficients of thermal expansion (CTE) between chip and laminated substrates, which make the assembly vulnerable to thermally induced strains and the resulting solder joint fatigue. In this paper, a Finite Element Model is proposed to back up experimental observations (Figure 6.6). These results together with the Coffin-Manson relation are used to predict the theoretical improvement in cycles to failure.

$$N_f = \left(\frac{A}{\Delta\gamma}\right)^m f^n e^{-\frac{\beta}{k_B T_{max}}}$$

N_f is the number of cycles to failures, A is a material constant, $\Delta\gamma$ is the cycling plastic shear strain, f is the cyclic frequency, T_{max} is the maximum temperature during the cycle, k_B is the Boltzmann's constant, n is an empirical constant and f may be thought of as an empirical "activation energy". The constant m is relating to the cycles-to-failure to the shear strain, can be found in the literature to vary from 1.89 to 2.5 for metals [251]. This equation gives the fatigue life of a conventional solder joint from the induced shear strain. The results suggest that to minimize fatigue failure, the CTE of an adhesive material should match that of solder material and its Young's Modulus should be as high as the adhesion strength of the underfill allows. Such a treatment could also benefit from the application of the design of experiment, a pre-test experimental matrices evaluation and refinement. As such, the 3D plots constructed in Section 4.3.4 and following could constitute an already interesting training field.

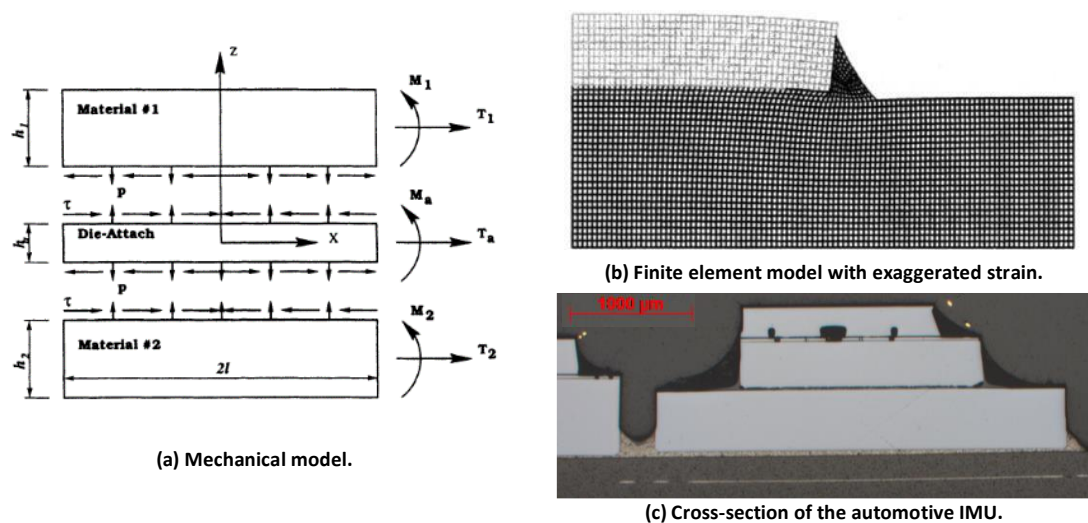


Figure 6.6: Mechanical model used for representing the die / die attach / package sandwich, used in FEM. Cross-section of a device used in the present study, with a similar sandwich indicated.

¹⁵ Source: NIST / SEMATECH / <https://www.itl.nist.gov/div898/handbook/apr/section1/apr153.htm>

6.4.5 Further die shear tests analysis

Regarding the die shear test results (and possibly the wire bonds pull results), analysis could go deeper by investigating individually, for each device, the force-displacement curve to extract the modulus of the materials under test. This would provide additional information on the die attach's properties after testing, which would be a valuable addition, for example, to a finite element model. An example of the force-displacement curve for a die shear test is given in Figure 6.7.

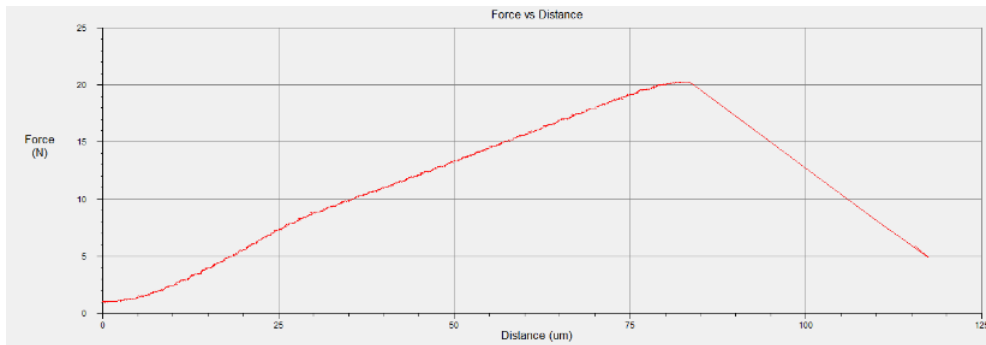


Figure 6.7: Force-displacement curve for a die shear test.

6.4.6 Refined 3D finite element models

On the numerical side, the Finite Element Analysis would benefit from further refinement, most notably (i) on the model's construction and (ii) the treatment of the viscoelastic study of the die attach. The first point refers to the complexity of the model: the abundance of imbricated geometries adds a toll on computation time. A reduced geometrical model, with symmetrical boundaries, would still be of good representativity in comparison with the entire model (Figure 6.8). On the viscoelastic study, the cold temperature simulation assumed a perfectly elastic behavior of the die attach, which enabled a stationary treatment. Using the reduced model, computation time would be greatly diminished, thus enabling to run the thermomechanical resolution over greater temperature fluctuations. Improvements and deeper tuning of the thermomechanical parameters would also bring more information to better fit the experimental data. Additionally, the effect of vibration on artificially diminished material inputs would represent a valuable information.

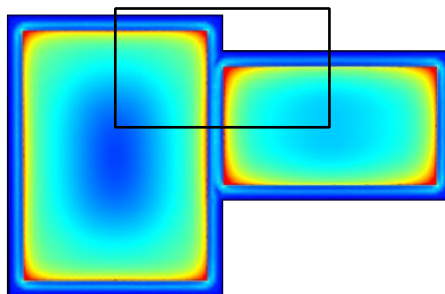


Figure 6.8: FEM stress heat map of the die attach. The square indicated a region of the volume where symmetrical boundary conditions could be applied and still constitute it a representative model.

References

- [1] H. R. Shea, 'Highlights in Microtechnology - MEMS for Space', presented at the 2014 Highlights in Microtechnology – Summer School, 2014. [Online]. Available: <https://pdfs.semanticscholar.org/30f9/ae7d1827f2dc8744241a3f925355c009ba92.pdf>
- [2] M. Noca *et al.*, 'Lessons Learned from the First Swiss Pico-Satellite: SwissCube', *Small Satellite Conference*, Aug. 2009, [Online]. Available: <https://digitalcommons.usu.edu/smallsat/2009/all2009/84>
- [3] M. Douglass, 'DMD reliability: a MEMS success story', in *Reliability, Testing, and Characterization of MEMS/MOEMS II*, Jan. 2003, vol. 4980, pp. 1–11. doi: 10.1117/12.478212.
- [4] E. Gaumont, A. Wolter, H. Schenk, G. Georgelin, and M. Schmoger, 'Mechanical and electrical failures and reliability of Micro Scanning Mirrors', in *Proceedings of the 9th International Symposium on the Physical and Failure Analysis of Integrated Circuits (Cat. No.02TH8614)*, Jul. 2002, pp. 212–217. doi: 10.1109/IPFA.2002.1025665.
- [5] M. N. Armenise, 'MEMS Gyroscopes', in *Advances in Gyroscope Technologies*, M. N. Armenise, C. Ciminelli, F. Dell'Olio, and V. M. N. Passaro, Eds. Berlin, Heidelberg: Springer, 2011, pp. 83–102. doi: 10.1007/978-3-642-15494-2_6.
- [6] R. S. Payne, S. Sherman, S. Lewis, and R. T. Howe, 'Surface micromachining: from vision to reality to vision [accelerometer]', in *Proceedings ISSCC '95 - International Solid-State Circuits Conference*, Feb. 1995, pp. 164–165. doi: 10.1109/ISSCC.1995.535506.
- [7] J. Bryzek, K. Petersen, L. Christel, and F. Pourahmadi, 'New Technologies for Silicon Accelerometers Enable Automotive Applications', SAE International, Warrendale, PA, SAE Technical Paper 920474, Feb. 1992. doi: 10.4271/920474.
- [8] Y. J. Chen, 'Advantages of MEMS and its Distinct New Applications', *Advanced Materials Research*, 2013. /AMR.813.205 (accessed Jun. 29, 2020).
- [9] A. Uhler, 'Electrolytic Shaping of Germanium and Silicon', *Bell System Technical Journal*, vol. 35, no. 2, pp. 333–347, 1956, doi: 10.1002/j.1538-7305.1956.tb02385.x.
- [10] H. Robbins and B. Schwartz, 'Chemical Etching of Silicon: II. The System HF, HNO₃, H₂O, and HC₂H₃O₂', *J. Electrochem. Soc.*, vol. 107, no. 2, p. 108, Feb. 1960, doi: 10.1149/1.2427617.
- [11] H. C. Nathanson and R. A. Wickstrom, 'A resonant-gate silicon surface transistor with high-q band-pass properties', *Appl. Phys. Lett.*, vol. 7, no. 4, pp. 84–86, Aug. 1965, doi: 10.1063/1.1754323.
- [12] R. Osiander, M. A. G. Darrin, J. L. Champion, M. A. G. Darrin, and J. L. Champion, 'Chapter 15: Reliability Practices for Design and Application of Space-Based MEMS', in *MEMS and Microstructures in Aerospace Applications*, CRC Press, 2018, p. 327. doi: 10.1201/9781420027747.
- [13] J. N. Burghartz, 'Marvels in MEMS Evolution and Development—Silicon as a Micromechanical Material has been Driving More-than-Moore', in *IEEE Technical Briefs*, 2020, vol. 27. Accessed: Aug. 17, 2020. [Online]. Available: <http://www.ieee.org/ns/periodicals/EDS/EDS-JANUARY-2020-HTML-v1/InnerFiles/Land-Page.html>
- [14] W. H. Ko, 'Trends and frontiers of MEMS', *Sensors and Actuators A: Physical*, vol. 136, no. 1, pp. 62–67, May 2007, doi: 10.1016/j.sna.2007.02.001.
- [15] J.-M. Stauffer, B. Dutoit, and B. Arbab, 'Standard MEMS sensor technologies for harsh environment', pp. 91–96, Jan. 2006, doi: 10.1049/ic:20060450.
- [16] J.-M. Stauffer, 'Current Capabilities of MEMS Capacitive Accelerometers in a Harsh Environment', *IEEE Aerospace and Electronic Systems Magazine*, vol. 21, no. 11, pp. 29–32, Nov. 2006, doi: 10.1109/MAES.2006.284356.
- [17] F. Rudolf, S. Gonseth, R. Brisson, and P. Krebs, 'New generation of high performance/high reliability MEMS accelerometers for harsh environment', in *2014 IEEE/ION Position, Location and Navigation Symposium - PLANS 2014*, May 2014, pp. 7–11. doi: 10.1109/PLANS.2014.6851350.
- [18] C. Patel and P. McCluskey, 'Performance of MEMS Vibratory Gyroscopes in Harsh Environments', p. 10, 2012.
- [19] P. Lall, A. S. Abrol, L. Simpson, and J. Glover, 'A study on damage progression in MEMS based Silicon oscillators subjected to high-g harsh environments', in *2016 15th IEEE Intersociety Conference on Thermal and Thermomechanical Phenomena in Electronic Systems (ITherm)*, May 2016, pp. 546–559. doi: 10.1109/ITHERM.2016.7517596.
- [20] T. Bifano, 'MEMS deformable mirrors', *Nature Photonics*, vol. 5, no. 1, Art. no. 1, Jan. 2011, doi: 10.1038/nphoton.2010.297.
- [21] S. A. Tadigadapa and N. Najafi, 'Developments in Microelectromechanical Systems (MEMS): A Manufacturing Perspective', *J. Manuf. Sci. Eng.*, vol. 125, no. 4, pp. 816–823, Nov. 2003, doi: 10.1115/1.1617286.

- [22] R. Osiander, M. A. G. Darrin, and J. Champion, *MEMS and Microstructures in aerospace applications*. Boca Raton: Taylor & Francis, 2006.
- [23] M. Kahrizi, *Micromachining Techniques for Fabrication of Micro and Nano Structures*. BoD – Books on Demand, 2012.
- [24] M. K. Mishra, V. Dubey, P. M. Mishra, and I. Khan, 'MEMS Technology: A Review', *Journal of Engineering Research and Reports*, pp. 1–24, Feb. 2019, doi: 10.9734/jerr/2019/v4i116891.
- [25] T. G. Brown and B. S. Davis, 'Dynamic high-g loading of MEMS sensors: ground and flight testing', in *Materials and Device Characterization in Micromachining*, Sep. 1998, vol. 3512, pp. 228–235. doi: 10.1117/12.324064.
- [26] T. G. Brown, 'Harsh military environments and microelectromechanical (MEMS) devices', in *2003 IEEE SENSORS*, Oct. 2003, vol. 2, pp. 753–760 Vol.2. doi: 10.1109/ICSENS.2003.1279042.
- [27] J. Karppinen, J. Li, J. Pakarinen, T. T. Mattila, and M. Paulasto-Kröckel, 'Shock impact reliability characterization of a handheld product in accelerated tests and use environment', *Microelectronics Reliability*, vol. 52, no. 1, pp. 190–198, Jan. 2012, doi: 10.1016/j.microrel.2011.09.001.
- [28] J. Meng *et al.*, 'Drop qualification of MEMS components in handheld electronics at extremely high accelerations', in *13th InterSociety Conference on Thermal and Thermomechanical Phenomena in Electronic Systems*, May 2012, pp. 1020–1027. doi: 10.1109/ITHERM.2012.6231537.
- [29] J. W. Kim, H. W. Park, M. K. Choi, W. K. Jeung, and J. W. Lee, 'Drop impact reliability of MEMS inertial sensors with membrane suspensions for mobile phones', in *2012 IEEE 62nd Electronic Components and Technology Conference*, May 2012, pp. 344–349. doi: 10.1109/ECTC.2012.6248853.
- [30] D. S. Eddy and D. R. Sparks, 'Application of MEMS Technology in Automotive Sensors and Actuators', *PROCEEDINGS OF THE IEEE*, vol. 86, no. 8, p. 9, 1998.
- [31] Y. Liu and B. Sun, 'Remaining useful life prediction of MEMS sensors used in automotive under random vibration loading', in *2013 Proceedings Annual Reliability and Maintainability Symposium (RAMS)*, Jan. 2013, pp. 1–6. doi: 10.1109/RAMS.2013.6517655.
- [32] C. Acar, A. R. Schofield, A. A. Trusov, L. E. Costlow, and A. M. Shkel, 'Environmentally Robust MEMS Vibratory Gyroscopes for Automotive Applications', *IEEE Sensors Journal*, vol. 9, no. 12, pp. 1895–1906, Dec. 2009, doi: 10.1109/JSEN.2009.2026466.
- [33] J. Makkonen, M. Broas, J. Li, J. Hokka, T. T. Mattila, and M. Paulasto-Kröckel, 'Reliability assessment of MEMS devices — A case study of a 3 axis gyroscope', in *2012 4th Electronic System-Integration Technology Conference*, Sep. 2012, pp. 1–8. doi: 10.1109/ESTC.2012.6542060.
- [34] M. Ciappa, F. Carbognani, and W. Fichtner, 'Lifetime prediction and design of reliability tests for high-power devices in automotive applications', *IEEE Transactions on Device and Materials Reliability*, vol. 3, no. 4, pp. 191–196, Dec. 2003, doi: 10.1109/TDMR.2003.818148.
- [35] J. C. McNulty, 'A perspective on the reliability of MEMS-based components for telecommunications', in *Reliability, Packaging, Testing, and Characterization of MEMS/MOEMS VII*, Feb. 2008, vol. 6884, p. 68840B. doi: 10.1117/12.773640.
- [36] I. De Wolf, P. Czarnecki, J. De Coster, O. V. Pedreira, X. Rottenberg, and S. Sangameswaran, 'Reliability of RF MEMS', in *Handbook of Mems for Wireless and Mobile Applications*, Elsevier, 2013, pp. 291–342. doi: 10.1533/9780857098610.1.291.
- [37] J. Li *et al.*, 'Reliability assessment of a MEMS microphone under shock impact loading', in *2013 14th International Conference on Thermal, Mechanical and Multi-Physics Simulation and Experiments in Microelectronics and Microsystems (EuroSimE)*, Apr. 2013, pp. 1–6. doi: 10.1109/EuroSimE.2013.6529899.
- [38] J. Hokka *et al.*, 'Methods for reliability assessment of MEMS devices — Case studies of a MEMS microphone and a 3-axis MEMS gyroscope', in *2012 IEEE 62nd Electronic Components and Technology Conference*, May 2012, pp. 62–69. doi: 10.1109/ECTC.2012.6248807.
- [39] O. Tabata and T. Tsuchiya, *Reliability of MEMS: Testing of Materials and Devices*. John Wiley & Sons, 2013.
- [40] R. Müller-Fiedler and V. Knoblauch, 'Reliability aspects of microsensors and micromechatronic actuators for automotive applications', *Microelectronics Reliability*, vol. 43, no. 7, pp. 1085–1097, Jul. 2003, doi: 10.1016/S0026-2714(03)00118-5.
- [41] S.-C. (Scott) Chang, 'MEMS in Automobiles', in *Microsystems and Nanotechnology*, Z. Zhou, Z. Wang, and L. Lin, Eds. Berlin, Heidelberg: Springer, 2012, pp. 721–757. doi: 10.1007/978-3-642-18293-8_19.
- [42] S. Tadigadapa and N. Najafi, 'Reliability of micro-electro-mechanical systems (MEMS)', in *Reliability, Testing, and Characterization of MEMS/MOEMS*, Oct. 2001, vol. 4558, pp. 197–205. doi: 10.1117/12.443002.
- [43] Federal Aviation Administration, 'The Annual Compendium of Commercial Space Transportation: 2018', 2018. [Online]. Available: https://www.faa.gov/about/office_org/headquarters_offices/ast/media/2018_ast_compendium.pdf
- [44] I. Walther *et al.*, 'Development of a miniature bioreactor for continuous culture in a space laboratory', *Journal of Biotechnology*, vol. 38, no. 1, pp. 21–32, Nov. 1994, doi: 10.1016/0168-1656(94)90144-9.
- [45] S. Janson, H. Helvajian, S. Amimoto, G. Smit, D. Mayer, and S. Feuerstein, 'Microtechnology for space systems', in *1998 IEEE Aerospace Conference Proceedings (Cat. No.98TH8339)*, Mar. 1998, vol. 1, pp. 409–418 vol.1. doi: 10.1109/AERO.1998.686938.
- [46] L. M. Miller, 'MEMS for space applications', in *Design, Test, and Microfabrication of MEMS and MOEMS*, Mar. 1999, vol. 3680, pp. 2–11. doi: 10.1117/12.341193.

- [47] R. Ramesham, 'Environmental testing of COTS components for space applications', in *Reliability, Packaging, Testing, and Characterization of MEMS/MOEMS and Nanodevices VIII*, Feb. 2009, vol. 7206, p. 72060H. doi: 10.1117/12.813408.
- [48] N. F. de Rooij *et al.*, 'MEMS for space', in *TRANSDUCERS 2009 - 2009 International Solid-State Sensors, Actuators and Microsystems Conference*, Denver, CO, USA, Jun. 2009, pp. 17–24. doi: 10.1109/SENSOR.2009.5285575.
- [49] H. R. Shea, 'MEMS for pico- to micro-satellites', in *MOEMS and Miniaturized Systems VIII*, Feb. 2009, vol. 7208, p. 72080M. doi: 10.1117/12.810997.
- [50] R. Thirsk, A. Kuipers, C. Mukai, and D. Williams, 'The space-flight environment: the International Space Station and beyond', *CMAJ*, vol. 180, no. 12, pp. 1216–1220, Jun. 2009, doi: 10.1503/cmaj.081125.
- [51] A. K. T. Sharma, 'Evaluation of Thermo-Mechanical Stability of COTS Dual-Axis MEMS Accelerometers for Space Applications', Jan. 01, 2000. Accessed: May 14, 2019. [Online]. Available: <https://ntrs.nasa.gov/search.jsp?R=20000097389>
- [52] R. Ghaffarian, D. G. Sutton, P. Chaffee, N. Marquez, A. K. Sharma, and A. Teverovsky, 'Thermal and Mechanical Reliability of Five COTS MEMS Accelerometers', p. 8, 2002.
- [53] X. Lafontan *et al.*, 'The advent of MEMS in space', *Microelectronics Reliability*, vol. 43, no. 7, pp. 1061–1083, Jul. 2003, doi: 10.1016/S0026-2714(03)00120-3.
- [54] F. Pressecq, X. Lafontan, G. Perez, and J.-P. Fortea, 'CNES reliability approach for the qualification of MEMS for space', in *Reliability, Testing, and Characterization of MEMS/MOEMS*, Oct. 2001, vol. 4558, pp. 89–96. doi: 10.1117/12.442990.
- [55] F. Pressecq, P. Schmitt, D. Veyrie, Q. Duong, X. Lafontan, and D. Lellouchi, 'MEMS Reliability: From Experimental Results to the Understanding of Physical Phenomena', in *CANEUS 2004 Conference on Micro-Nano-Technologies*, American Institute of Aeronautics and Astronautics, 2004. doi: 10.2514/6.2004-6744.
- [56] S. Dussy, D. Durrant, A. Moy, N. Perriault, and B. Celerier, 'MEMS Gyros for Space Applications - Overview of European Activities', presented at the AIAA Guidance, Navigation, and Control Conference and Exhibit, San Francisco, California, Aug. 2005. doi: 10.2514/6.2005-6466.
- [57] M. Nikulainen and P. Armbruster, 'Usage of Commercial Off-the-Shelf EEE Components in European Space Programs', presented at the ESCCON 2019, 2019. [Online]. Available: <https://escies.org/download/webDocumentFile?id=67090>
- [58] S. Kayali, 'Utilization of COTS Electronics in Space Application, Reliability Challenges and Reality', *6th International CMSE Conference*, p. 10, Feb. 2002.
- [59] X. J. Jiang *et al.*, 'Suitability analysis of commercial off-the-shelf components for space application', *Proceedings of the Institution of Mechanical Engineers, Part G: Journal of Aerospace Engineering*, vol. 220, no. 5, pp. 357–364, May 2006, doi: 10.1243/09544100JAERO99.
- [60] R. Ramesham, R. Ghaffarian, and N. P. Kim, 'Reliability issues of COTS MEMS for aerospace applications', in *MEMS Reliability for Critical and Space Applications*, Aug. 1999, vol. 3880, pp. 83–88. doi: 10.1117/12.359357.
- [61] P. Schmitt *et al.*, 'Reliability issues of an accelerometer under environmental stresses', in *Reliability, Testing, and Characterization of MEMS/MOEMS III*, Dec. 2003, vol. 5343, pp. 22–30. doi: 10.1117/12.524575.
- [62] H. R. Shea, 'Reliability of MEMS for space applications', Jan. 2006, vol. 6111, p. 61110A. doi: 10.1117/12.651008.
- [63] R. Ramesham and R. Ghaffarian, 'Commercial-Off-The-Shelf Microelectromechanical Systems', p. 10, 2000.
- [64] P. Schmitt *et al.*, 'Impact of the space environmental conditions on the reliability of a MEMS COTS based system', *Microelectronics Reliability*, vol. 44, no. 9, pp. 1739–1744, Sep. 2004, doi: 10.1016/j.microrel.2004.07.109.
- [65] I. Marozau *et al.*, 'Reliability assessment and failure mode analysis of MEMS accelerometers for space applications', *Microelectronics Reliability*, vol. 88–90, pp. 846–854, Sep. 2018, doi: 10.1016/j.microrel.2018.07.118.
- [66] D. Crowe and A. Feinberg, 'Concepts in Accelerated testing', in *Design for Reliability*, CRC Press, 2017.
- [67] V. T. Srikar, S. M. Spearing, and J. Williams, 'YIELD AND RELIABILITY OF MEMS', p. 26, Apr. 2003.
- [68] M. R. Douglass, 'MEMS reliability: coming of age', in *Reliability, Packaging, Testing, and Characterization of MEMS/MOEMS VII*, Feb. 2008, vol. 6884, p. 688402. doi: 10.1117/12.791010.
- [69] D. M. Tanner, 'MEMS reliability: Where are we now?', *Microelectronics Reliability*, vol. 49, no. 9–11, pp. 937–940, Sep. 2009, doi: 10.1016/j.microrel.2009.06.014.
- [70] A. Arab and Q. Feng, 'Reliability research on micro- and nano-electromechanical systems: a review', *Int J Adv Manuf Technol*, vol. 74, no. 9, pp. 1679–1690, Oct. 2014, doi: 10.1007/s00170-014-6095-x.
- [71] Y. Huang, A. S. S. Vasani, R. Doraiswami, M. Osterman, and M. Pecht, 'MEMS Reliability Review', *IEEE Transactions on Device and Materials Reliability*, vol. 12, no. 2, pp. 482–493, Jun. 2012, doi: 10.1109/TDMR.2012.2191291.
- [72] P. Rafiee, G. Khatibi, M. Zehetbauer, G. Khatibi, and M. Zehetbauer, 'A review of the most important failure, reliability and nonlinearity aspects in the development of microelectromechanical systems (MEMS)', *Microelectronics International*, vol. 34, no. 1, pp. 9–21, Jan. 2017, doi: 10.1108/MI-03-2015-0026.

- [73] L. Skogström, J. Li, T. T. Mattila, and V. Vuorinen, 'Chapter 44 - MEMS reliability', in *Handbook of Silicon Based MEMS Materials and Technologies (Third Edition)*, M. Tilli, M. Paulasto-Krockel, M. Petzold, H. Theuss, T. Motooka, and V. Lindroos, Eds. Elsevier, 2020, pp. 851–876. doi: 10.1016/B978-0-12-817786-0.00044-X.
- [74] Y.-C. Su, J. Kim, Y.-T. Cheng, M. Chiao, and L. Lin, 'Packaging and Reliability Issues in Micro/Nano Systems', in *Springer Handbook of Nanotechnology*, B. Bhushan, Ed. Berlin, Heidelberg: Springer, 2017, pp. 1505–1539. doi: 10.1007/978-3-662-54357-3_43.
- [75] B. Stark, 'MEMS Reliability Assurance Guidelines for Space Applications', Jan. 1999. Accessed: Jan. 14, 2020. [Online]. Available: <https://ntrs.nasa.gov/search.jsp?R=20000047448>
- [76] D. M. Tanner *et al.*, 'MEMS Reliability: Infrastructure, Test Structures, Experiments, and Failure Modes', Sandia National Labs., Albuquerque, NM (US); Sandia National Labs., Livermore, CA (US), SAND2000-0091, Jan. 2000. doi: 10.2172/750344.
- [77] F. Pascual, W. Meeker, and L. Escobar, 'Accelerated Life Test Models and Data Analysis', 2006, pp. 397–426. doi: 10.1007/978-1-84628-288-1_22.
- [78] A. Thura, V. N. Goroshko, B. N. Simonov, and S. P. Timoshenkov, 'Accelerated life time estimation of the MEMS devices in the thermal influence', in *2018 IEEE Conference of Russian Young Researchers in Electrical and Electronic Engineering (EIConRus)*, Jan. 2018, pp. 1590–1594. doi: 10.1109/EIConRus.2018.8317404.
- [79] H. Caruso and A. Dasgupta, 'A fundamental overview of accelerated-testing analytic models', in *Annual Reliability and Maintainability Symposium. 1998 Proceedings. International Symposium on Product Quality and Integrity*, Jan. 1998, pp. 389–393. doi: 10.1109/RAMS.1998.653809.
- [80] C. Fung, 'Industry study on issues of MEMS reliability and accelerated lifetime testing', in *2005 IEEE International Reliability Physics Symposium, 2005. Proceedings. 43rd Annual.*, Apr. 2005, pp. 312–316. doi: 10.1109/RELPHY.2005.1493104.
- [81] S. Łuczak, M. Zams, and K. Bagiński, 'Selected Aging Effects in Triaxial MEMS Accelerometers', *Journal of Sensors*, 2019. <https://www.hindawi.com/journals/js/2019/5184907/> (accessed Apr. 14, 2020).
- [82] D. M. Tanner *et al.*, 'Accelerating aging failures in MEMS devices', in *2005 IEEE International Reliability Physics Symposium, 2005. Proceedings. 43rd Annual.*, Apr. 2005, pp. 317–324. doi: 10.1109/RELPHY.2005.1493105.
- [83] D. J. Fonseca and M. Sequera, 'On MEMS Reliability and Failure Mechanisms', vol. 2011, no. International Journal of Quality, Statistics, and Reliability, Jan. 2011, doi: 10.1155/2011/820243.
- [84] I. Marozau, 'Technical Memorandum for ESA RFQ 3-13923, "MEMS-Real" Project, Test programme for reliability assessment of MEMS products', 2016.
- [85] A. Castillejo, D. Veychard, S. Mir, J. M. Karam, and B. Courtois, 'Failure mechanisms and fault classes for CMOS-compatible microelectromechanical systems', in *Proceedings International Test Conference 1998 (IEEE Cat. No.98CH36270)*, Washington, DC, USA, 1998, pp. 541–550. doi: 10.1109/TEST.1998.743197.
- [86] J. A. Walraven, 'Failure mechanisms in MEMS', in *International Test Conference, 2003. Proceedings. ITC 2003.*, Sep. 2003, vol. 1, pp. 828–833. doi: 10.1109/TEST.2003.1270915.
- [87] W. Merlijn van Spengen, 'MEMS reliability from a failure mechanisms perspective', *Microelectronics Reliability*, vol. 43, no. 7, pp. 1049–1060, Jul. 2003, doi: 10.1016/S0026-2714(03)00119-7.
- [88] Y. Li and Z. Jiang, 'An Overview of Reliability and Failure Mode Analysis of Microelectromechanical Systems (MEMS)', in *Handbook of Performability Engineering*, K. B. Misra, Ed. London: Springer, 2008, pp. 953–966. doi: 10.1007/978-1-84800-131-2_58.
- [89] J. Iannacci, 'Reliability of MEMS: A perspective on failure mechanisms, improvement solutions and best practices at development level', *Displays*, vol. 37, pp. 62–71, Apr. 2015, doi: 10.1016/j.displa.2014.08.003.
- [90] S. B. Brown, W. van Arsdell, and C. L. Muhlstein, 'Materials reliability in MEMS devices', in *Proceedings of International Solid State Sensors and Actuators Conference (Transducers '97)*, Jun. 1997, vol. 1, pp. 591–593 vol.1. doi: 10.1109/SENSOR.1997.613720.
- [91] A. L. Hartzell, M. G. da Silva, and H. R. Shea, *MEMS Reliability*. Springer Science & Business Media, 2010.
- [92] W. M. van Spengen, R. Modliński, R. Puers, and A. Jourdain, 'Failure Mechanisms in MEMS/NEMS Devices', in *Springer Handbook of Nanotechnology*, B. Bhushan, Ed. Berlin, Heidelberg: Springer, 2017, pp. 1437–1457. doi: 10.1007/978-3-662-54357-3_40.
- [93] K. F. Man, 'MEMS reliability for space applications by elimination of potential failure modes through testing and analysis', in *MEMS Reliability for Critical and Space Applications*, Aug. 1999, vol. 3880, pp. 120–129. doi: 10.1117/12.359361.
- [94] A. R. Maligno, D. Whalley, and V. V. Silberschmidt, 'Interfacial failure under thermal fatigue loading in multilayered MEMS structures', *IOP Conf. Ser.: Mater. Sci. Eng.*, vol. 10, p. 012087, Jun. 2010, doi: 10.1088/1757-899X/10/1/012087.
- [95] A. R. Maligno, D. C. Whalley, and V. V. Silberschmidt, 'Thermal fatigue life estimation and delamination mechanics studies of multilayered MEMS structures', *Microelectronics Reliability*, vol. 52, no. 8, pp. 1665–1678, Aug. 2012, doi: 10.1016/j.microrel.2012.03.023.
- [96] J. Zekry, B. Vandevelde, S. Bouwstra, R. Puers, C. Van Hoof, and H. A. C. Tilmans, 'Thermomechanical design and modeling of porous alumina-based thin film packages for MEMS', in *2010 11th International Thermal, Mechanical Multi-Physics Simulation, and Experiments in Microelectronics and Microsystems (EuroSimE)*, Apr. 2010, pp. 1–7. doi: 10.1109/ESIME.2010.5464584.

- [97] J. Puigcorbé, A. Vilà, and J. R. Morante, 'Thermal fatigue modeling of micromachined gas sensors', *Sensors and Actuators B: Chemical*, vol. 95, no. 1, pp. 275–281, Oct. 2003, doi: 10.1016/S0925-4005(03)00538-0.
- [98] K. Meyyappan, P. McCluskey, and Liang Yu Chen, 'Thermo-mechanical analysis of MEMS pressure sensor die-attach for high temperature applications', in *2004 IEEE Aerospace Conference Proceedings (IEEE Cat. No.04TH8720)*, Mar. 2004, vol. 4, pp. 2556-2561 Vol.4. doi: 10.1109/AERO.2004.1368049.
- [99] R. H. Krondorfer and Y. K. Kim, 'Packaging Effect on MEMS Pressure Sensor Performance', *IEEE Transactions on Components and Packaging Technologies*, vol. 30, no. 2, pp. 285–293, Jun. 2007, doi: 10.1109/TCAPT.2007.898360.
- [100] B. Charlot, S. Mir, F. Parrain, and B. Courtois, 'Electrically induced stimuli for MEMS self-test', in *Proceedings 19th IEEE VLSI Test Symposium. VTS 2001*, Apr. 2001, pp. 210–215. doi: 10.1109/VTS.2001.923441.
- [101] T. Kose, K. Azgin, and T. Akin, 'Temperature compensation of a capacitive MEMS accelerometer by using a MEMS oscillator', in *2016 IEEE International Symposium on Inertial Sensors and Systems*, Feb. 2016, pp. 33–36. doi: 10.1109/ISISS.2016.7435538.
- [102] P.-S. Huang, T.-L. Ren, Q.-W. Lou, J.-S. Liu, L.-T. Liu, and Z.-J. Li, 'Design of a Triaxial Piezoelectric Accelerometer', *Integrated Ferroelectrics*, vol. 56, no. 1, pp. 1115–1122, Jun. 2003, doi: 10.1080/10584580390259722.
- [103] Y. Xu, S. Wang, Y. Wang, Q. Shi, and X. Ji, 'A Monolithic Triaxial Micromachined Silicon Capacitive Gyroscope', in *2006 1st IEEE International Conference on Nano/Micro Engineered and Molecular Systems*, Jan. 2006, pp. 213–217. doi: 10.1109/NEMS.2006.334689.
- [104] G. Liu, F. Yang, X. Bao, and T. Jiang, 'Robust Optimization of a MEMS Accelerometer Considering Temperature Variations', *Sensors*, vol. 15, no. 3, Art. no. 3, Mar. 2015, doi: 10.3390/s150306342.
- [105] Y. Yin, Z. Fang, Y. Liu, and F. Han, 'Temperature-Insensitive Structure Design of Micromachined Resonant Accelerometers', *Sensors*, vol. 19, no. 7, Art. no. 7, Jan. 2019, doi: 10.3390/s19071544.
- [106] W. Mei, Q. Hu, C. Xing, N. Li, and Y. Xu, 'Simulation Analysis on Thermal Drift of MEMS Sandwich Accelerometer', in *2018 19th International Conference on Electronic Packaging Technology (ICEPT)*, Aug. 2018, pp. 740–744. doi: 10.1109/ICEPT.2018.8480829.
- [107] J. Meng, S. T. Douglas, and A. Dasgupta, 'MEMS Packaging Reliability in Board-Level Drop Tests Under Severe Shock and Impact Loading Conditions—Part I: Experiment', *IEEE Transactions on Components, Packaging and Manufacturing Technology*, vol. 6, no. 11, pp. 1595–1603, Nov. 2016, doi: 10.1109/TCPM.2016.2611646.
- [108] U. Wagner *et al.*, 'Mechanical Reliability of MEMS-structures under shock load', *Microelectronics Reliability*, vol. 41, no. 9, pp. 1657–1662, Sep. 2001, doi: 10.1016/S0026-2714(01)00173-1.
- [109] D. M. Tanner *et al.*, 'MEMS reliability in shock environments', in *2000 IEEE International Reliability Physics Symposium Proceedings. 38th Annual (Cat. No.00CH37059)*, Apr. 2000, pp. 129–138. doi: 10.1109/RELPHY.2000.843903.
- [110] J. Li, M. Broas, J. Makkonen, T. T. Mattila, J. Hokka, and M. Paulasto-Kröckel, 'Shock Impact Reliability and Failure Analysis of a Three-Axis MEMS Gyroscope', *Journal of Microelectromechanical Systems*, vol. 23, no. 2, pp. 347–355, Apr. 2014, doi: 10.1109/JMEMS.2013.2273802.
- [111] I. Yunis, 'The Standard Deviation of Launch Vehicle Environments', presented at the 46th AIAA/ASME/ASCE/AHS/ASC Structures, Structural Dynamics and Materials Conference, Austin, Texas, Apr. 2005. doi: 10.2514/6.2005-1937.
- [112] J. Wijker, *Spacecraft Structures*. Berlin, Heidelberg: Springer Berlin Heidelberg, 2008. doi: 10.1007/978-3-540-75553-1.
- [113] A. Beliveau, G. T. Spencer, K. A. Thomas, and S. L. Roberson, 'Evaluation of MEMS capacitive accelerometers', *IEEE Design Test of Computers*, vol. 16, no. 4, pp. 48–56, Oct. 1999, doi: 10.1109/54.808209.
- [114] D. M. Tanner *et al.*, 'MEMS reliability in a vibration environment', in *2000 IEEE International Reliability Physics Symposium Proceedings. 38th Annual (Cat. No.00CH37059)*, Apr. 2000, pp. 139–145. doi: 10.1109/RELPHY.2000.843904.
- [115] K. M. Delak, P. Bova, A. L. Hartzell, and D. J. Woodilla, 'Analysis of manufacturing-scale MEMS reliability testing', in *MEMS Reliability for Critical and Space Applications*, Aug. 1999, vol. 3880, pp. 165–174. doi: 10.1117/12.359367.
- [116] M. Bazu, L. Galateanu, V. E. Ilian, J. Loicq, S. Habraken, and J.-P. Colette, 'Reliability Accelerated Testing of MEMS Accelerometers', in *2007 International Semiconductor Conference*, Oct. 2007, vol. 1, pp. 103–106. doi: 10.1109/SMICND.2007.4519657.
- [117] S. Barthe, G. Cros, L. Lopez, S. Dussy, and L. Marchand, 'The study of MEMS failure mechanisms and Reliability / Qualification testing methods', p. 32, 2005.
- [118] G. De Pasquale and A. Somà, 'Reliability Testing Procedure for MEMS IMUs Applied to Vibrating Environments', *Sensors*, vol. 10, no. 1, pp. 456–474, Jan. 2010, doi: 10.3390/s100100456.
- [119] P. Lall, A. Abrol, and D. Locker, 'Effects of Sustained Exposure to Temperature and Humidity on the Reliability and Performance of MEMS Microphone', presented at the ASME 2017 International Technical Conference and Exhibition on Packaging and Integration of Electronic and Photonic Microsystems collocated with the ASME 2017 Conference on Information Storage and Processing Systems, Oct. 2017. doi: 10.1115/IPACK2017-74252.

- [120] D. B. Heinz, V. A. Hong, Y. Yang, C. Ahn, and T. W. Kenny, 'High-G (>20,000g) inertial shock survivability of epitaxially encapsulated silicon MEMS devices', in *2017 IEEE 30th International Conference on Micro Electro Mechanical Systems (MEMS)*, Jan. 2017, pp. 1122–1125. doi: 10.1109/MEMSYS.2017.7863611.
- [121] P. Lall, A. Abrol, D. Locker, and B. Hughes, 'Damage Evolution in MEMS Pressure Sensors during High Temperature Operating Life and Prolonged Storage at Sub-Zero Temperature', in *2018 17th IEEE Intersociety Conference on Thermal and Thermomechanical Phenomena in Electronic Systems (ITherm)*, May 2018, pp. 1050–1061. doi: 10.1109/ITHERM.2018.8419575.
- [122] J. Hokka, T. T. Mattila, J. Li, J. Teeri, and Jorma. K. Kivilahti, 'A novel impact test system for more efficient reliability testing', *Microelectronics Reliability*, vol. 50, no. 8, pp. 1125–1133, Aug. 2010, doi: 10.1016/j.microrel.2010.04.015.
- [123] P. Lall *et al.*, 'Modeling and reliability characterization of area-array electronics subjected to high-g mechanical shock up to 50,000g', in *2012 IEEE 62nd Electronic Components and Technology Conference*, May 2012, pp. 1194–1204. doi: 10.1109/ECTC.2012.6248988.
- [124] J. Li, M. Broas, J. Raami, T. T. Mattila, and M. Paulasto-Kröckel, 'Reliability assessment of a MEMS microphone under mixed flowing gas environment and shock impact loading', *Microelectronics Reliability*, vol. 54, no. 6, pp. 1228–1234, Jun. 2014, doi: 10.1016/j.microrel.2014.01.003.
- [125] J. Kimberley, I. Chasiotis, and J. Lambros, 'Failure of microelectromechanical systems subjected to impulse loads', *International Journal of Solids and Structures*, vol. 45, no. 2, pp. 497–512, Jan. 2008, doi: 10.1016/j.ijsolstr.2007.08.004.
- [126] V. T. Srikar and S. D. Senturia, 'The reliability of microelectromechanical systems (MEMS) in shock environments', *Journal of Microelectromechanical Systems*, vol. 11, no. 3, pp. 206–214, Jun. 2002, doi: 10.1109/JMEMS.2002.1007399.
- [127] M. A. Duesterhaus, V. I. Bateman, D. A. Hoke, and S. N. Laboratories, 'Shock Testing of MEMS Devices', p. 6, 2004.
- [128] S. Sundaram *et al.*, 'Vibration and shock reliability of MEMS: modeling and experimental validation', *J. Micro-mech. Microeng.*, vol. 21, no. 4, p. 045022, Mar. 2011, doi: 10.1088/0960-1317/21/4/045022.
- [129] M. I. Younis, 'Mechanical Shock in MEMS', in *MEMS Linear and Nonlinear Statics and Dynamics*, M. I. Younis, Ed. Boston, MA: Springer US, 2011, pp. 401–442. doi: 10.1007/978-1-4419-6020-7_8.
- [130] Xu-Wen Fang, Qing-An Huang, and Jie-Ying Tang, 'Modeling of MEMS reliability in shock environments', in *Proceedings. 7th International Conference on Solid-State and Integrated Circuits Technology, 2004.*, Oct. 2004, vol. 2, pp. 860–863 vol.2. doi: 10.1109/ICSICT.2004.1436643.
- [131] T. Hauck, Gary Li, A. McNeill, H. Knoll, M. Ebert, and J. Bagdahn, 'Drop Simulation and Stress Analysis of MEMS Devices', in *EuroSime 2006 - 7th International Conference on Thermal, Mechanical and Multiphysics Simulation and Experiments in Micro-Electronics and Micro-Systems*, Apr. 2006, pp. 1–5. doi: 10.1109/ES-IME.2006.1643999.
- [132] J. Meng *et al.*, 'Testing and multi-scale modeling of drop and impact loading of complex MEMS microphone assemblies', in *2012 13th International Thermal, Mechanical and Multi-Physics Simulation and Experiments in Microelectronics and Microsystems*, Apr. 2012, p. 1/8-8/8. doi: 10.1109/ESimE.2012.6191726.
- [133] S. Kurth, A. Shaporin, K. Hiller, C. Kaufmann, and T. Gessner, 'Reliability of MEMS devices in shock and vibration overload situations', in *Reliability, Packaging, Testing, and Characterization of MEMS/MOEMS VII*, Feb. 2008, vol. 6884, p. 688409. doi: 10.1117/12.763617.
- [134] P. Schmitt *et al.*, 'Space Microsystems and Reliability: The Contribution of Behavioral Modeling', presented at the CANEUS 2004 Conference on Micro-Nano-Technologies, Monterey, California, Nov. 2004. doi: 10.2514/6.2004-6723.
- [135] P. Lall, N. Kothari, and J. Glover, 'Mechanical Shock Reliability Analysis and Multiphysics Modeling of MEMS Accelerometers in Harsh Environments', presented at the ASME 2015 International Technical Conference and Exhibition on Packaging and Integration of Electronic and Photonic Microsystems collocated with the ASME 2015 13th International Conference on Nanochannels, Microchannels, and Minichannels, Nov. 2015. doi: 10.1115/IPACK2015-48457.
- [136] C. Yang, B. Zhang, D. Chen, and L. Lin, 'Drop-shock dynamic analysis of MEMS/package system', in *2010 IEEE 23rd International Conference on Micro Electro Mechanical Systems (MEMS)*, Jan. 2010, pp. 520–523. doi: 10.1109/MEMSYS.2010.5442450.
- [137] H. Jeong, K. Yamanaka, Y. Goto, T. Aono, and M. Hayashi, 'Three-axis MEMS inertial sensor for automobile applications', in *2011 IEEE SENSORS*, Oct. 2011, pp. 444–447. doi: 10.1109/ICSENS.2011.6126909.
- [138] Y. A. Nekrasov, S. V. Pavlova, and N. V. Moiseev, 'MEMS gyro vibration immunity and its measurement with TIRA shaker', in *2015 IEEE International Instrumentation and Measurement Technology Conference (I2MTC) Proceedings*, May 2015, pp. 1763–1768. doi: 10.1109/I2MTC.2015.7151547.
- [139] D. Capriglione *et al.*, 'Development of a test plan and a testbed for performance analysis of MEMS-based IMUs under vibration conditions', *Measurement*, vol. 158, p. 107734, Jul. 2020, doi: 10.1016/j.measurement.2020.107734.
- [140] P. Lall, D. R. Panchagade, P. Choudhary, S. Gupte, and J. C. Suhling, 'Failure-Envelope Approach to Modeling Shock and Vibration Survivability of Electronic and MEMS Packaging', *IEEE Transactions on Components and Packaging Technologies*, vol. 31, no. 1, pp. 104–113, Mar. 2008, doi: 10.1109/TCAPT.2008.916804.

- [141] Yue Liu, Bo Sun, and Qiang Feng, 'Package reliability of mems sensors used in automotive under random vibration', *Chemical Engineering Transactions*, vol. 33, pp. 481–486, Jul. 2013, doi: 10.3303/CET1333081.
- [142] K.-H. Glassmeier, H. Boehnhardt, D. Koschny, E. Kührt, and I. Richter, 'The Rosetta Mission: Flying Towards the Origin of the Solar System', *Space Sci Rev*, vol. 128, no. 1–4, pp. 1–21, May 2007, doi: 10.1007/s11214-006-9140-8.
- [143] J. P. Gardner *et al.*, 'The James Webb Space Telescope', *Space Sci Rev*, vol. 123, no. 4, pp. 485–606, Nov. 2006, doi: 10.1007/s11214-006-8315-7.
- [144] R. Ghaffarian and N. P. Kim, 'Reliability and failure analyses of thermally cycled ball grid array assemblies', *IEEE Transactions on Components and Packaging Technologies*, vol. 23, no. 3, pp. 528–534, Sep. 2000, doi: 10.1109/6144.868853.
- [145] J. B. Nysaether, Z. Lai, and J. Liu, 'Thermal cycling lifetime of flip chip on board circuits with solder bumps and isotropically conductive adhesive joints', *IEEE Transactions on Advanced Packaging*, vol. 23, no. 4, pp. 743–749, Nov. 2000, doi: 10.1109/6040.883767.
- [146] P. Lall, R. Vaidya, V. More, K. Goebel, and J. Suhling, 'Assessment of residual damage in leadfree electronics subjected to multiple thermal environments of thermal aging and thermal cycling', in *2010 Proceedings 60th Electronic Components and Technology Conference (ECTC)*, Jun. 2010, pp. 206–218. doi: 10.1109/ECTC.2010.5490907.
- [147] G. Gan *et al.*, 'Influence of thermal shock cycles on Sn-37Pb solder bumps', *Soldering & Surface Mount Tech*, vol. 31, no. 2, pp. 85–92, Feb. 2019, doi: 10.1108/SSMT-08-2018-0026.
- [148] M. Bouarroudj, Z. Khatir, and S. Lefebvre, 'Temperature levels effects on the thermomechanical behaviour of solder attach during thermal cycling of power electronic modules', in *2008 IEEE Power Electronics Specialists Conference*, Jun. 2008, pp. 2435–2440. doi: 10.1109/PESC.2008.4592306.
- [149] M. G. Perichaud, J. Y. Deletage, D. Carboni, H. Fremont, Y. Danto, and C. Faure, 'Thermomechanical behaviour of adhesive jointed SMT components', in *Proceedings of 3rd International Conference on Adhesive Joining and Coating Technology in Electronics Manufacturing 1998 (Cat. No.98EX180)*, Sep. 1998, pp. 55–61. doi: 10.1109/ADHES.1998.742003.
- [150] W.-S. Kwon, M.-J. Yim, K.-W. Paik, S.-J. Ham, and S.-B. Lee, 'Thermal Cycling Reliability and Delamination of Anisotropic Conductive Adhesives Flip Chip on Organic Substrates With Emphasis on the Thermal Deformation', *Journal of Electronic Packaging*, vol. 127, no. 2, p. 86, 2005, doi: 10.1115/1.1846062.
- [151] P. O. Quintero and F. P. McCluskey, 'Temperature Cycling Reliability of High-Temperature Lead-Free Die-Attach Technologies', *IEEE Transactions on Device and Materials Reliability*, vol. 11, no. 4, pp. 531–539, Dec. 2011, doi: 10.1109/TDMR.2011.2140114.
- [152] P. Quintero, P. McCluskey, and B. Koene, 'Thermomechanical reliability of a silver nano-colloid die attach for high temperature applications', *Microelectronics Reliability*, vol. 54, no. 1, pp. 220–225, Jan. 2014, doi: 10.1016/j.microrel.2013.08.002.
- [153] S. Moreau, T. Lequeu, and R. Jérisian, 'Comparative study of thermal cycling and thermal shocks tests on electronic components reliability', *Microelectronics Reliability*, vol. 44, no. 9–11, pp. 1343–1347, 2004.
- [154] J. W. C. de Vries, M. Y. Jansen, and W. D. van Driel, 'On the difference between thermal cycling and thermal shock testing for board level reliability of soldered interconnections', *Microelectronics Reliability*, vol. 47, no. 2, pp. 444–449, Feb. 2007, doi: 10.1016/j.microrel.2006.05.009.
- [155] D. Lellouchi *et al.*, 'Environmental Chamber for Temperature and Pressure Investigations on MEMS Devices', Aug. 2008, pp. 275–279. doi: 10.1115/CANEUS2006-11026.
- [156] E. Lemoine and P. Blondy, 'Reliability Assessment Methodologies for RF-MEMS', *9th ESA Round Table on MNT*, Jun. 2014.
- [157] R. Houlihan, R. Duane, C. Ryan, C. O'Mahony, and Z. Olszewski, 'Mechanical and Dielectric Reliability of an RF MEMS Capacitive Switch', *8th ESA Round-Table on MNT for Space Applications*, p. 24, Oct. 2012.
- [158] J. Dhennin, D. Lellouchi, and F. Presseccq, 'How to evaluate the reliability of MEMS devices without standards', in *2015 Symposium on Design, Test, Integration and Packaging of MEMS/MOEMS (DTIP)*, Apr. 2015, pp. 1–3. doi: 10.1109/DTIP.2015.7161015.
- [159] A. L. Hartzell, M. G. da Silva, and H. R. Shea, 'Testing and Standards for Qualification', in *MEMS Reliability*, A. L. Hartzell, M. G. da Silva, and H. R. Shea, Eds. Boston, MA: Springer US, 2011, pp. 215–252. doi: 10.1007/978-1-4419-6018-4_6.
- [160] J. Rigo, D. Tourtelier, and F. Davenel, 'Ensemble de recommandations pour migrer de la MIL-HDBK-217 vers FIDES', presented at the Congrès Lambda Mu 19 de Maîtrise des Risques et Sûreté de Fonctionnement, Dijon, 21-23 Octobre 2014, Jan. 2015. doi: 10.4267/2042/56138.
- [161] E. de Francesco, R. de Francesco, and E. Petritoli, 'Obsolescence of the MIL-HDBK-217: A critical review', Jun. 2017, pp. 282–286. doi: 10.1109/MetroAeroSpace.2017.7999581.
- [162] C. Hillman, 'The End is Near for MIL-HDBK-217 and Other Outdated Handbooks', *designnews.com*, Jul. 09, 2018. <https://www.designnews.com/electronics-test/end-near-mil-hdbk-217-and-other-outdated-handbooks> (accessed Aug. 19, 2020).
- [163] R. Ramesham and R. Ghaffarian, 'Interconnection and Packaging Issues of Microelectromechanical Systems (MEMS) and COTS MEMS', p. 14, 2000.

- [164] J. L. Zunino and D. Skelton, 'Department of Defense need for a micro-electromechanical systems (MEMS) reliability assessment program', in *Reliability, Packaging, Testing, and Characterization of MEMS/MOEMS IV*, Jan. 2005, vol. 5716, pp. 122–130. doi: 10.1117/12.602257.
- [165] A. Olney, 'Evolving MEMS qualification requirements', in *2010 IEEE International Reliability Physics Symposium*, May 2010, pp. 224–230. doi: 10.1109/IRPS.2010.5488824.
- [166] Lusospace, 'Challenges ahead of a MEMS Qualification Standard Methodology', *8th ESA Round-Table on MNT for Space Applications*, p. 24, Oct. 2012.
- [167] A. Neels et al., 'The HTA Reliability Platform', *8th ESA Round-Table on MNT for Space Applications*, p. 26, Oct. 2012.
- [168] J. Valldorf and W. Gessner, Eds., 'New MEMS Timing References for Automotive Applications', in *Advanced Microsystems for Automotive Applications 2007*, Berlin: Springer, 2007, p. 279.
- [169] N. Sinnadurai, 'Plastic packages survive where hermetic packages fail', *Microelectronics Reliability*, vol. 36, no. 7, pp. 1001–1018, Jul. 1996, doi: 10.1016/0026-2714(96)00065-0.
- [170] R. Gubser, 'Reliability and Quality Assessment (Stability and Packages)', in *Piezoelectric MEMS Resonators*, H. Bhugra and G. Piazza, Eds. Cham: Springer International Publishing, 2017, pp. 299–310. doi: 10.1007/978-3-319-28688-4_13.
- [171] M. Bazu, L. Galateanu, and V. Ilian, 'About using combined stresses for reliability testing of microsystems', in *2009 International Semiconductor Conference*, Oct. 2009, vol. 1, pp. 233–236. doi: 10.1109/SMICND.2009.5336561.
- [172] A. Margomenos and L. P. B. Katehi, 'Fabrication and accelerated hermeticity testing of an on-wafer package for RF MEMS', *IEEE Transactions on Microwave Theory and Techniques*, vol. 52, no. 6, pp. 1626–1636, Jun. 2004, doi: 10.1109/TMTT.2004.828467.
- [173] W.-T. Hsu, 'Low Cost Packages for MEMS Oscillators', in *2007 32nd IEEE/CPMT International Electronic Manufacturing Technology Symposium*, Oct. 2007, pp. 273–277. doi: 10.1109/IEMT.2007.4417076.
- [174] J. S. Lee et al., 'A Cost-Effective MEMS Cavity Packaging Technology for Mass Production', *IEEE Transactions on Advanced Packaging*, vol. 32, no. 2, pp. 453–460, May 2009, doi: 10.1109/TADVP.2009.2014121.
- [175] G. Wu et al., 'Robust Packaging For MEMS Sensors Using Plastic Moulding', in *2018 IEEE 20th Electronics Packaging Technology Conference (EPTC)*, Dec. 2018, pp. 916–919. doi: 10.1109/EPTC.2018.8654385.
- [176] G. Wu et al., 'Development of Six-Degree-of-Freedom Inertial Sensors With an 8-in Advanced MEMS Fabrication Platform', *IEEE Transactions on Industrial Electronics*, vol. 66, no. 5, pp. 3835–3842, May 2019, doi: 10.1109/TIE.2018.2851946.
- [177] A. Bensoussan, 'M-STORM reliability model applied to DSM technologies', in *2016 IEEE Nanotechnology Materials and Devices Conference (NMDC)*, Oct. 2016, pp. 1–2. doi: 10.1109/NMDC.2016.7777115.
- [178] P. Lall, A. S. Abrol, J. Suhling, L. Simpson, J. Glover, and D. Locker, 'Effect of simultaneous high temperature and vibration on MEMS based vibratory gyroscope', in *2017 16th IEEE Intersociety Conference on Thermal and Thermomechanical Phenomena in Electronic Systems (ITherm)*, May 2017, pp. 1214–1228. doi: 10.1109/ITHERM.2017.7992624.
- [179] P. Lall, A. S. Abrol, L. Simpson, and J. Glover, 'Reliability of MEMS devices under multiple environments', in *Fourteenth Intersociety Conference on Thermal and Thermomechanical Phenomena in Electronic Systems (ITherm)*, May 2014, pp. 1313–1321. doi: 10.1109/ITHERM.2014.6892432.
- [180] Z. Szucs, G. Nagy, S. Hodossy, M. Rencz, and A. Poppe, 'Vibration combined high Temperature Cycle Tests for capacitive MEMS accelerometers', in *2007 13th International Workshop on Thermal Investigation of ICs and Systems (THERMINIC)*, Sep. 2007, pp. 215–219. doi: 10.1109/THERMINIC.2007.4451781.
- [181] P. Lall, A. Abrol, L. Simpson, and J. Glover, 'Survivability of MEMS Accelerometer Under Sequential Thermal and High-G Mechanical Shock Environments', Jul. 2015, p. V003T07A013. doi: 10.1115/IPACK2015-48790.
- [182] T. Mai, 'Technology Readiness Level', NASA, May 06, 2015. http://www.nasa.gov/directorates/heo/scan/engineering/technology/txt_accordion1.html (accessed Jan. 22, 2021).
- [183] S. Gonseth, F. Rudolf (Colibrys), and D. Durrant (SEA), *High Performance Open Loop Accelerometer for Space Applications*. 8th ESA Round Table on Micro and Nano Technologies for Space Applications, 2012.
- [184] C. R. Francis, 'CryoSat Mission and Data Description', European Space Agency, CS-RP-ESA-SY-0059, Jan. 2007. Accessed: Sep. 14, 2020. [Online]. Available: <https://earth.esa.int/web/guest/-/cryosat-mission-and-data-description-4472>
- [185] S. Dussy, 'ESA preparing "sugar-cube" gyro sensors for future missions', 2009. http://www.esa.int/Enabling_Support/Space_Engineering_Technology/ESA_preparing_sugar-cube_gyro_sensors_for_future_missions (accessed Sep. 14, 2020).
- [186] M. Hartree, 'The Qualification and Market Entry of the SiREUS MEMS Coarse Rate Sensor for Space Mission Applications', presented at the 7th ESA Round Table on MNT for Space Applications, 7th ESA Round Table on MNT for Space Applications, 2010.
- [187] S. Kowaltschek, 'Lessons learnt from the SiREUS MEMS detector evaluation', presented at the 6th ESA Workshop on Avionics, Data, Control and Software Systems - ADCSS2012, 2012.
- [188] R. Durrant, S. Dussy, H. Crowle, and J. Robertson, 'SiREUS: Status of the European MEMS Rate Sensor', in *AIAA Guidance, Navigation and Control Conference and Exhibit*, American Institute of Aeronautics and Astronautics, 2012. doi: 10.2514/6.2008-6992.

- [189] R. Durrant, S. Dussy, B. Shackleton, and A. Malvern, 'MEMS Rate Sensor in Space Becomes a Reality', in *AIAA Guidance, Navigation and Control Conference and Exhibit*, American Institute of Aeronautics and Astronautics, 2012. doi: 10.2514/6.2007-6547.
- [190] B. Olivier, 'The SiREUS MEMS rate sensor program', 2008.
- [191] M. Nese and B. E. Seeberg, 'Silicon MEMS Pressure Sensors for Aerospace Applications', Aug. 2008, pp. 195–198. doi: 10.1115/CANEUS2006-11044.
- [192] Y. Zhang, R. Howver, B. Gogoi, and N. Yazdi, 'A high-sensitive ultra-thin MEMS capacitive pressure sensor', in *2011 16th International Solid-State Sensors, Actuators and Microsystems Conference*, Jun. 2011, pp. 112–115. doi: 10.1109/TRANSDUCERS.2011.5969151.
- [193] S. Sangameswaran *et al.*, 'ESD reliability issues in microelectromechanical systems (MEMS): A case study on micromirrors', in *EOS/ESD 2008 - 2008 30th Electrical Overstress/Electrostatic Discharge Symposium*, Sep. 2008, pp. 249–257.
- [194] K. D. Fourspring, Z. Ninkov, B. C. Fodness, M. Robberto, S. Heap, and A. G. Kim, 'Proton radiation testing of digital micromirror devices for space applications', *OE*, vol. 52, no. 9, p. 091807, May 2013, doi: 10.1117/1.OE.52.9.091807.
- [195] B.-W. Yoo *et al.*, 'MEMS micromirror characterization in space environments', *Opt. Express*, *OE*, vol. 17, no. 5, pp. 3370–3380, Mar. 2009, doi: 10.1364/OE.17.003370.
- [196] S. Hernandez, M. Zahir, F. Filhol, and L. Marchand, 'MOEMS for space application: the European Space Agency strategy for photonics components', in *MOEMS and Miniaturized Systems IX*, Feb. 2010, vol. 7594, p. 75940S. doi: 10.1117/12.855592.
- [197] F. Zamkotsian *et al.*, 'Micromirror arrays designed and tested for space instrumentation', in *2010 International Conference on Optical MEMS and Nanophotonics*, Aug. 2010, pp. 195–196. doi: 10.1109/OMEMS.2010.5672119.
- [198] F. Zamkotsian *et al.*, 'Successful evaluation for space applications of the 2048x1080 DMD', in *Emerging Digital Micromirror Device Based Systems and Applications III*, Feb. 2011, vol. 7932, p. 79320A. doi: 10.1117/12.876872.
- [199] F. Zamkotsian *et al.*, 'Space evaluation of a MOEMs device for space instrumentation', in *International Conference on Space Optics — ICSO 2010*, Nov. 2010, vol. 10565, p. 1056521. doi: 10.1117/12.2309205.
- [200] J. J. Yao *et al.*, 'Microelectromechanical system radio frequency switches in a picosatellite mission', *Smart Mater. Struct.*, vol. 10, no. 6, pp. 1196–1203, Nov. 2001, doi: 10.1088/0964-1726/10/6/308.
- [201] J. J. Yao, 'RF MEMS from a device perspective', *J. Micromech. Microeng.*, vol. 10, no. 4, pp. R9–R38, Oct. 2000, doi: 10.1088/0960-1317/10/4/201.
- [202] G. E. Ponchak, R. N. Simons, and M. Scardelletti, 'Microelectromechanical switches for phased array antennas', in *IEEE Antennas and Propagation Society International Symposium. Transmitting Waves of Progress to the Next Millennium. 2000 Digest. Held in conjunction with: USNC/URSI National Radio Science Meeting (C, Jul. 2000*, vol. 4, pp. 2230–2233 vol.4. doi: 10.1109/APS.2000.874937.
- [203] A. I. Zaghloul, O. Kilic, L. Q. Sun, E. C. Kohls, M. E. Zaghloul, and R. W. Kreutel, 'MEMS-based modular phased array for low earth orbiting satellite terminals', in *IEEE International Symposium on Phased Array Systems and Technology, 2003.*, Oct. 2003, pp. 500–505. doi: 10.1109/PAST.2003.1257032.
- [204] G. M. Rebeiz, Guan-Leng Tan, and J. S. Hayden, 'RF MEMS phase shifters: design and applications', *IEEE Microwave Magazine*, vol. 3, no. 2, pp. 72–81, Jun. 2002, doi: 10.1109/MMW.2002.1004054.
- [205] G. M. Rebeiz and J. B. Muldavin, 'RF MEMS switches and switch circuits', *IEEE Microwave Magazine*, vol. 2, no. 4, pp. 59–71, Dec. 2001, doi: 10.1109/6668.969936.
- [206] G. M. Rebeiz, 'RF MEMS switches: status of the technology', in *TRANSDUCERS '03. 12th International Conference on Solid-State Sensors, Actuators and Microsystems. Digest of Technical Papers (Cat. No.03TH8664)*, Jun. 2003, vol. 2, pp. 1726–1729 vol.2. doi: 10.1109/SENSOR.2003.1217118.
- [207] H. Saari, J. Antila, C. Holmlund, R. Mannila, J. Mäkyinen, and K. Viherkanto, *Fabry-Perot Interferometer Hyperspectral Imaging Technology Transfer to Space Applications*. 8th ESA Round Table on Micro and Nano Technologies for Space Applications, 2012.
- [208] S. S. D. HAMAMATSU PHOTONICS K.K., *MEMS-FTIR: Compact NIR spectrometer with a built-in fingertip size MEMS-FTIR engine*. 1126-1 Ichino-cho, Higashi-ku, Hamamatsu City, 435-8558 Japan, 2014.
- [209] K. Yu, N. Park, and L. Daesung, *Chip-scale High-speed Fourier-transform Spectrometer Based on a Combination of a Michelson and a Fabry-Perot Interferometer*. 2006, p. 415. doi: 10.1109/ICSENS.2007.355493.
- [210] A. Kestilä *et al.*, 'Aalto-1 nanosatellite - technical description and mission objectives', *Geoscientific Instrumentation, Methods and Data Systems Discussions*, vol. 2, pp. 925–951, Nov. 2012, doi: 10.5194/gid-2-925-2012.
- [211] J. Antila *et al.*, 'MEMS and piezo actuator-based Fabry-Perot interferometer technologies and applications at VTT', in *Next-Generation Spectroscopic Technologies III*, Apr. 2010, vol. 7680, p. 76800U. doi: 10.1117/12.850164.
- [212] S. Karlen, J. Gobet, T. Overstolz, J. Haesler, and S. Lecomte, 'Lifetime assessment of RbN₃-filled MEMS atomic vapor cells with Al₂O₃ coating', *Opt. Express*, *OE*, vol. 25, no. 3, pp. 2187–2194, Feb. 2017, doi: 10.1364/OE.25.002187.

- [213] S. Karlen, J. Gobet, T. Overstolz, J. Haesler, and S. Lecomte, 'Quantitative Micro-Raman Spectroscopy for Partial Pressure Measurement in Small Volumes', *Appl Spectrosc*, vol. 71, no. 12, pp. 2707–2713, Dec. 2017, doi: 10.1177/0003702817724410.
- [214] J. Kitching, 'Chip-Scale Atomic Clocks at NIST', p. 9, 2005.
- [215] G. Langfelder, C. Buffa, A. Frangi, A. Tocchio, E. Lasalandra, and A. Longoni, 'Z-Axis Magnetometers for MEMS Inertial Measurement Units Using an Industrial Process', *IEEE Transactions on Industrial Electronics*, vol. 60, no. 9, pp. 3983–3990, Sep. 2013, doi: 10.1109/TIE.2012.2210958.
- [216] M. J. Thompson and D. A. Horsley, 'Resonant MEMS magnetometer with capacitive read-out', in *2009 IEEE SENSORS*, Oct. 2009, pp. 992–995. doi: 10.1109/ICSENS.2009.5398216.
- [217] M. Díaz-Michelena, 'Small Magnetic Sensors for Space Applications', *Sensors*, vol. 9, no. 4, Art. no. 4, Apr. 2009, doi: 10.3390/s90402271.
- [218] S. J. Kapurch, *NASA Systems Engineering Handbook*. DIANE Publishing, 2010.
- [219] O. L. A. de Weck, *Fundamentals in Systems Engineering*. EPFL – MIT, 2015.
- [220] T. Kollias, *MEMS Capacitive Accelerometers for Future Launchers*. Theon Sensors, MEMS Business Unit, 2010.
- [221] Jérémie Bouchaud and Henning Wicht, 'RF MEMS: status of the industry and application roadmap', *Frequenz*, vol. 59, no. 1–2, pp. 24–26, Feb. 2005, doi: 10.1515/FREQ.2005.59.1-2.24.
- [222] S. Pranonsatit and S. Lucyszyn, 'RF-MEMS activities in Europe', in *Microwave Workshops and Exhibition (MWE 2005) Digest, Yokohama, Japan*, 2005, pp. 111–122.
- [223] C. Nicollier, 'Space Mission Design and Operations, Section 3.1: Orbital mechanics I, Dynamics of spaceflight, the concept of gravitational well, orbital motion, Kepler's laws, the case of circular orbits, Spring Semester course 2015 (EPFL)', Swiss Institute of Technology in Lausanne, Mar. 16, 2015.
- [224] J. Brugger and M. Gijs, 'Micro and Nanofabrication (MEMS) - Doctoral course, EPFL', Fall 2020.
- [225] D. J. Smith, 'Chapter 2 - Understanding Terms and Jargon', in *Reliability, Maintainability and Risk (Ninth Edition)*, D. J. Smith, Ed. Butterworth-Heinemann, 2017, pp. 15–30. doi: 10.1016/B978-0-08-102010-4.00002-9.
- [226] T. Bandi, 'Reliability Aspects of Microelectromechanical Systems for Space Applications', *Infoscience*, 2014. <https://infoscience.epfl.ch/record/202165> (accessed Jan. 15, 2020).
- [227] S. Shokrollahi, F. Adel, and H. Ahmadian, 'An investigation into the accelerometer mounting effects on signal transmissibility in modal measurements', *Scientia Iranica*, vol. 24, Aug. 2017, doi: 10.24200/sci.2017.4244.
- [228] *Handbook of Silicon Based MEMS Materials and Technologies*. Elsevier, 2015. doi: 10.1016/C2013-0-19270-7.
- [229] S. NIST, '1.3.6.6.8. Weibull Distribution', in *Engineering Statistics Handbook*, Accessed: Jan. 02, 2021. [Online]. Available: <https://www.itl.nist.gov/div898/handbook/eda/section3/eda3668.htm>
- [230] W. Nelson, 'Accelerated Life Testing - Step-Stress Models and Data Analyses', *IEEE Transactions on Reliability*, vol. R-29, no. 2, pp. 103–108, Jun. 1980, doi: 10.1109/TR.1980.5220742.
- [231] W. B. Nelson, *Applied Life Data Analysis*. John Wiley & Sons, 2005.
- [232] W. B. Nelson, *Accelerated Testing: Statistical Models, Test Plans, and Data Analysis*. John Wiley & Sons, 2009.
- [233] E. M. Benavides, 'Reliability Model for Step-Stress and Variable-Stress Situations', *IEEE Transactions on Reliability*, vol. 60, no. 1, pp. 219–233, Mar. 2011, doi: 10.1109/TR.2010.2085574.
- [234] H. Lilliefors, 'On the Kolmogorov-Smirnov Test for Normality with Mean and Variance Unknown', 1967, doi: 10.1080/01621459.1967.10482916.
- [235] A. R. Knudson *et al.*, 'The effects of radiation on MEMS accelerometers', *IEEE Transactions on Nuclear Science*, vol. 43, no. 6, pp. 3122–3126, Dec. 1996, doi: 10.1109/23.556914.
- [236] H. R. Shea, 'Effects of radiation on MEMS', in *Reliability, Packaging, Testing, and Characterization of MEMS/MOEMS and Nanodevices X*, Feb. 2011, vol. 7928, p. 79280E. doi: 10.1117/12.876968.
- [237] F. Sarvar, D. A. Hutt, and D. C. Whalley, 'Application of adhesives in MEMS and MOEMS assembly: a review', in *2nd International IEEE Conference on Polymers and Adhesives in Microelectronics and Photonics. POLYTRONIC 2002. Conference Proceedings (Cat. No.02EX599)*, Jun. 2002, pp. 22–28. doi: 10.1109/POLYTR.2002.1020178.
- [238] B. J. Kim and E. Meng, 'Review of polymer MEMS micromachining', *J. Micromech. Microeng.*, vol. 26, no. 1, p. 013001, Nov. 2015, doi: 10.1088/0960-1317/26/1/013001.
- [239] C. H. Li and C. K. Lee, 'Minimum cross entropy thresholding', *Pattern Recognition*, vol. 26, no. 4, pp. 617–625, Apr. 1993, doi: 10.1016/0031-3203(93)90115-D.
- [240] C. H. Li and P. K. S. Tam, 'An iterative algorithm for minimum cross entropy thresholding', *Pattern Recognition Letters*, vol. 19, no. 8, pp. 771–776, Jun. 1998, doi: 10.1016/S0167-8655(98)00057-9.
- [241] M. Sezgin and B. Sankur, 'Survey over image thresholding techniques and quantitative performance evaluation', *Journal of Electronic imaging*, vol. 13, no. 1, pp. 146–166, 2004.
- [242] T. Bandi, H. Shea, and A. Neels, 'Mechanical properties of MEMS materials: reliability investigations by mechanical- and HRXRD-characterization related to environmental testing', in *Sensors for Extreme Harsh Environments*, Jun. 2014, vol. 9113, p. 911309. doi: 10.1117/12.2050617.
- [243] A. Schifferle, A. Dommann, and A. Neels, 'In situ MEMS testing: correlation of high-resolution X-ray diffraction with mechanical experiments and finite element analysis', *Science and Technology of Advanced Materials*, vol. 18, no. 1, pp. 219–230, Dec. 2017, doi: 10.1080/14686996.2017.1282800.
- [244] A. Vailionis, 'High-Resolution XRD - Stanford University', Stanford University.

- [245] M. A. Hopcroft, W. D. Nix, and T. W. Kenny, 'What is the Young's Modulus of Silicon?', *J. Microelectromech. Syst.*, vol. 19, no. 2, pp. 229–238, Apr. 2010, doi: 10.1109/JMEMS.2009.2039697.
- [246] M. A. R. Tahir, S. A. R. Bukhari, and M. M. Saleem, 'Reliability based Design of MEMS Accelerometer Considering Residual Stress and Temperature Variations', in *2020 IEEE 23rd International Multitopic Conference (INMIC)*, Nov. 2020, pp. 1–6. doi: 10.1109/INMIC50486.2020.9318187.
- [247] H. Nguyen *et al.*, 'Temperature dependence of mechanical properties of isotropic conductive adhesive filled with metal coated polymer spheres', in *2011 IEEE 61st Electronic Components and Technology Conference (ECTC)*, May 2011, pp. 639–644. doi: 10.1109/ECTC.2011.5898580.
- [248] H. Nguyen, E. Andreassen, H. Kristiansen, and K. E. Aasmundtveit, 'Die Shear Testing of a Novel Isotropic Conductive Adhesive—Epoxy Filled With Metal-Coated Polymer Spheres', *IEEE Transactions on Components, Packaging and Manufacturing Technology*, vol. 3, no. 7, pp. 1084–1093, Jul. 2013, doi: 10.1109/TCPMT.2013.2259166.
- [249] M. Auchlin, I. Marozau, D. Z. Bayat, L. Marchand, V. Gass, and O. Sereda, 'Can automotive MEMS be reliably used in space applications? An assessment method under sequential bi-parameter testing', *Microelectronics Reliability*, vol. 114, p. 113913, Nov. 2020, doi: 10.1016/j.microrel.2020.113913.
- [250] V. Gektin, A. Bar-Cohen, and S. Witzman, 'Coffin-Manson based fatigue analysis of underfilled DCAs', *IEEE Transactions on Components, Packaging, and Manufacturing Technology: Part A*, vol. 21, no. 4, pp. 577–584, Dec. 1998, doi: 10.1109/95.740050.
- [251] T.-H. Ju, W. Lin, Y. C. Lee, and J. J. Liu, 'Effects of Ceramic Ball-Grid-Array Package's Manufacturing Variations on Solder Joint Reliability', *Journal of Electronic Packaging*, vol. 116, no. 4, pp. 242–248, Dec. 1994, doi: 10.1115/1.2905694.
- [252] T. Tuhus and A. Bjornekleit, 'Thermal cycling reliability of die bonding adhesives', in *31st Annual Proceedings Reliability Physics 1993*, Mar. 1993, pp. 204–208. doi: 10.1109/RELPHY.1993.283323.
- [253] A. Bjornekleit, T. Tuhus, and H. Kristiansen, 'A model for thermal fatigue of large area adhesive joints between materials with dissimilar thermal expansion', in *Proceedings of 1994 IEEE/CHMT 10th Semiconductor Thermal Measurement and Management Symposium (SEMI-THERM)*, Feb. 1994, pp. 138–141. doi: 10.1109/STHERM.1994.288983.
- [254] B. Su and J. Qu, 'Fatigue Behavior of Electrically Conductive Adhesives', *Journal of Adhesion Science and Technology*, vol. 22, no. 8–9, pp. 927–946, Jan. 2008, doi: 10.1163/156856108X305516.
- [255] R. R. Gomatam and E. Sancaktar, 'Dynamic fatigue and failure behavior of silver-filled electronically conductive adhesive joints at ambient environmental conditions', *Journal of Adhesion Science and Technology*, vol. 18, no. 7, pp. 731–750, Jan. 2004, doi: 10.1163/156856104840291.
- [256] R. R. Gomatam and E. Sancaktar, 'A comprehensive fatigue life predictive model for electronically conductive adhesive joints under constant-cycle loading', *Journal of Adhesion Science and Technology*, vol. 20, no. 1, pp. 87–104, Jan. 2006, doi: 10.1163/156856106775212413.
- [257] S. Deng, M. Hou, and L. Ye, 'Temperature-dependent elastic moduli of epoxies measured by DMA and their correlations to mechanical testing data', *Polymer Testing*, vol. 26, no. 6, pp. 803–813, Sep. 2007, doi: 10.1016/j.polymertesting.2007.05.003.
- [258] S. Pandini and A. Pegoretti, 'Time, temperature, and strain effects on viscoelastic Poisson's ratio of epoxy resins', *Polymer Engineering & Science*, vol. 48, no. 7, pp. 1434–1441, 2008, doi: 10.1002/pen.21060.
- [259] J. Feng and Z. Guo, 'Temperature-frequency-dependent mechanical properties model of epoxy resin and its composites', *Composites Part B: Engineering*, vol. 85, pp. 161–169, Feb. 2016, doi: 10.1016/j.compositesb.2015.09.040.
- [260] I. Maus *et al.*, 'Characterization of epoxy based highly filled die attach materials in microelectronics', in *2017 18th International Conference on Thermal, Mechanical and Multi-Physics Simulation and Experiments in Microelectronics and Microsystems (EuroSimE)*, Apr. 2017, pp. 1–7. doi: 10.1109/EuroSimE.2017.7926237.
- [261] R. F. Hamou *et al.*, 'Numerical investigation of ceramic package/ interposer interconnects using isotropic conductive adhesive', in *2015 16th International Conference on Thermal, Mechanical and Multi-Physics Simulation and Experiments in Microelectronics and Microsystems*, Apr. 2015, pp. 1–5. doi: 10.1109/EuroSimE.2015.7103144.
- [262] S. Park, D. Liu, Y. Kim, H. Lee, and S. Zhang, 'Stress evolution in an encapsulated MEMS package due to viscoelasticity of packaging materials', in *2012 IEEE 62nd Electronic Components and Technology Conference*, May 2012, pp. 70–75. doi: 10.1109/ECTC.2012.6248808.
- [263] R. Liu, H. Lee, S. Park, and X. Xue, 'Shrinkage of Post-Cure Die Attach Adhesives During Isothermal Storage', in *Volume 3: Advanced Fabrication and Manufacturing; Emerging Technology Frontiers; Energy, Health and Water- Applications of Nano-, Micro- and Mini-Scale Devices; MEMS and NEMS; Technology Update Talks; Thermal Management Using Micro Channels, Jets, Sprays*, San Francisco, California, USA, Jul. 2015, p. V003T07A005. doi: 10.1115/IPACK2015-48086.
- [264] M. Springer and N. Bosco, 'Linear viscoelastic characterization of electrically conductive adhesives used as interconnect in photovoltaic modules', *Progress in Photovoltaics: Research and Applications*, vol. 28, no. 7, pp. 659–681, Jul. 2020, doi: 10.1002/pip.3257.

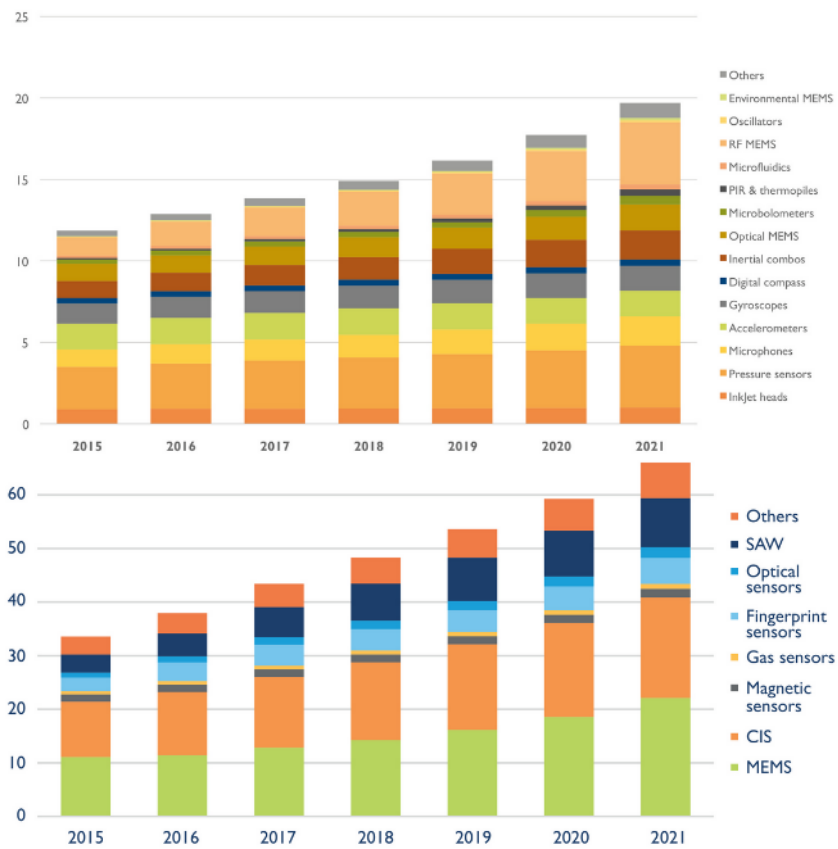
References

- [265] T. Fałat, J. Felba, A. Wymysłowski, K. M. B. Jansen, and J. Nakka, 'Viscoelastic Characterization of Polymer Matrix of Thermally Conductive Adhesives', *ESTC 2006 - 1st Electronics Systemintegration Technology Conference*, vol. 2, Jan. 2006, doi: 10.1109/ESTC.2006.280099.

Appendix

A. MEMS market overview

In terms of devices, the market is segmented into several main equivalently represented devices, as hinted in the bar charts below.

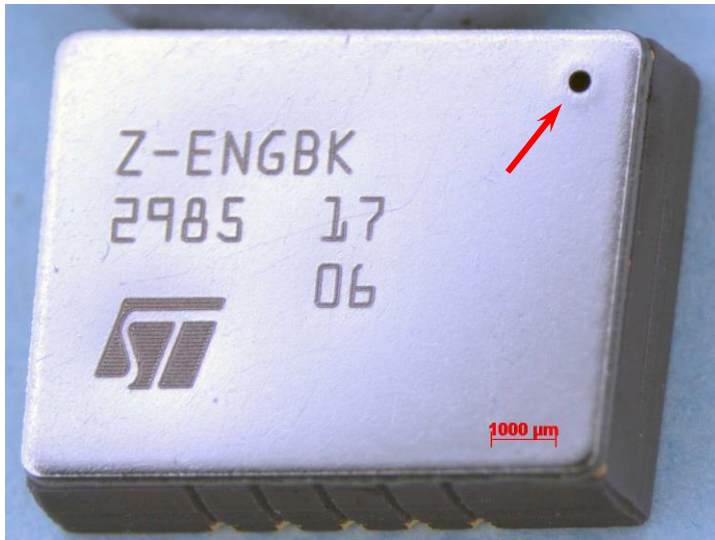


MEMS and sensors revenue market and forecast in billions of US dollars. Source: Status of the MEMS Industry 2016 (upper) and 2017 (lower), courtesy of Yole Development. Legends: PIR (Pyroelectric passive Infrared sensors), SAW (Surface Acoustic Wave sensor), CIS (CMOS Image Sensor).

B. Full results of the construction analysis

❖ Visual and radiographic inspections

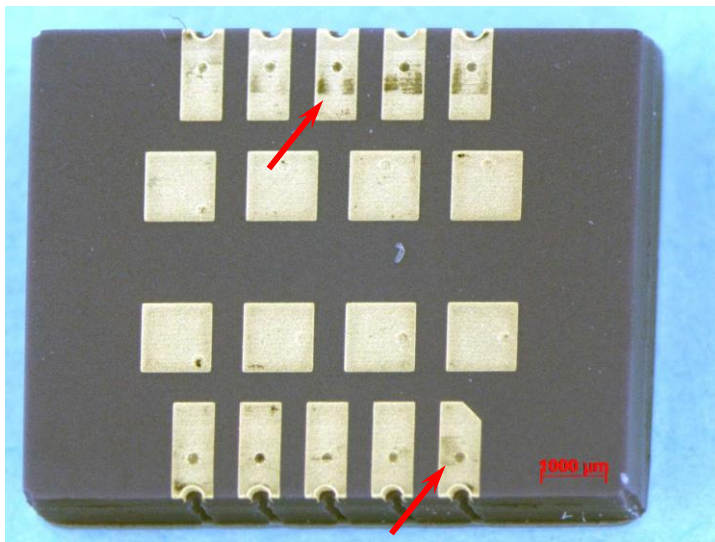
The detailed observations and commentaries about the construction analysis are presented in this Section. Those results were part of a technical report that was produced to the manufacturer and relies on well-established procedures used at the European Space Agency. The format of presentation and the tonality of the commentaries reflects therefore this aspect.



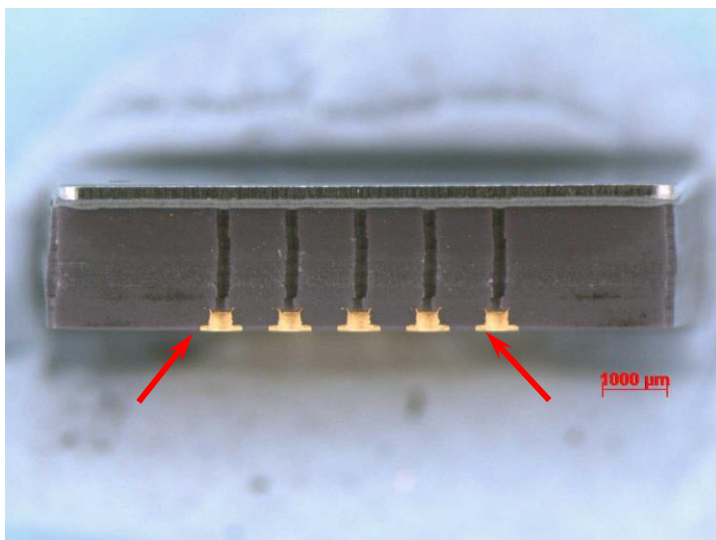
Typical top view of the component, as received. The laser-engraved marking is visible, including ST's logo on the bottom left corner. There is no manufacturer serial number. The 5 parts submitted to this analysis were serialized by position as follows:

- G11-FFF-01
- G11-FFF-02
- G11-FFF-03
- G11-FFF-04
- G11-FFF-05

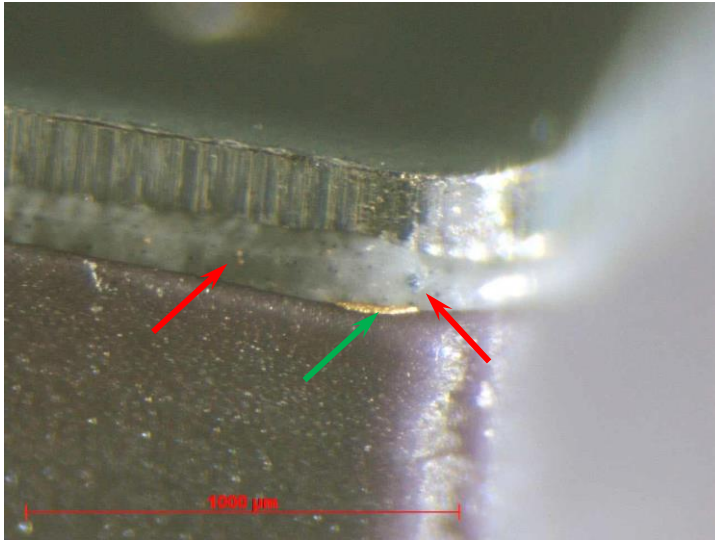
The image shows component G11-FFF-03. The red arrow points to the vent on the top right-hand corner. The component has therefore a non-hermetic package.



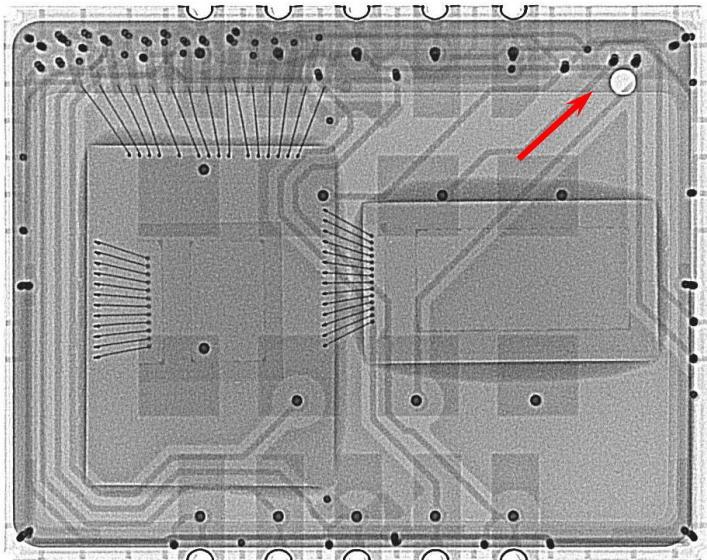
Bottom view of the component G11-FFF-03. The 18 electrical contacts are levelled with the ceramic package. The component's contacts show some traces (see red arrows) that indicate that the component had been inserted in a socket adapter before being delivered.



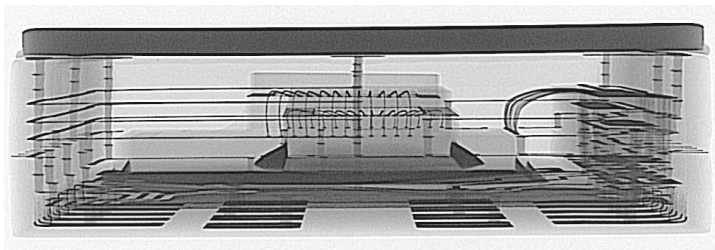
Side view of the component G11-FFF-03. The wettable flanks (castellations) are metallized on the bottom side of the component (see red arrows).



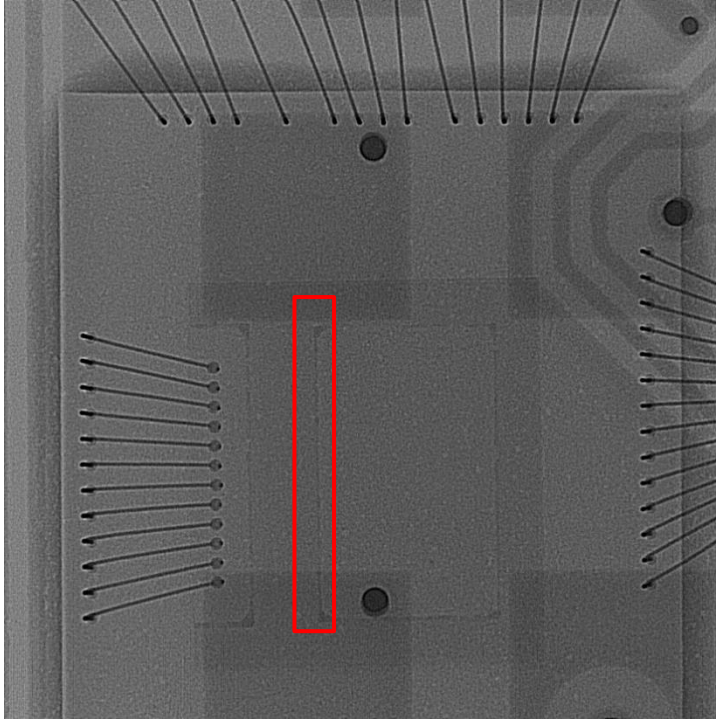
Detail view of the lid, the glue and the ceramic package on the component G11-FFF-03. The adhesive includes traces of metallic filler (see red arrows). The green arrow points to one of the metallic contacts embedded in the ceramic of the package.



General top view of the G11-FFF-03 component. The top left corner shows the orifice corresponding to the vent on the lid (see red arrow). The picture depicts well-separated wires and metallic tracks running in the ceramic package. The rectangular 0-level package on the right side of the image is a 1D gyroscope. The left side of the image shows the ASIC die at the bottom and the 0-level package of the 2D-accelerometer on top of it.

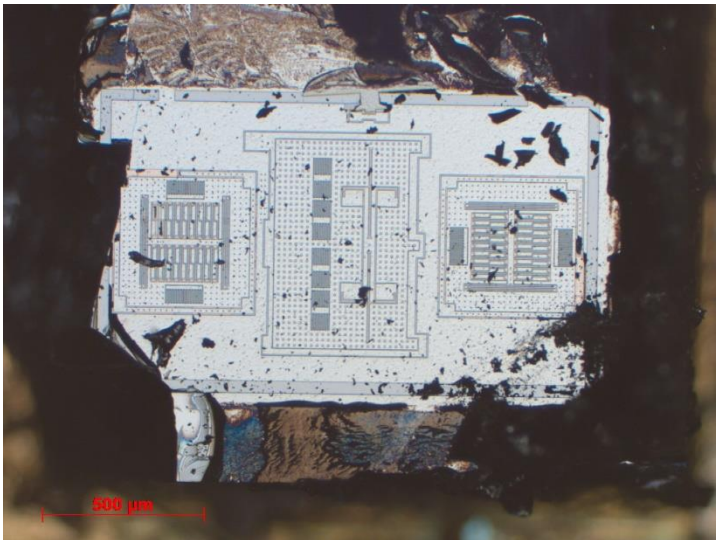


Side view of the G11-FFF-03, showing the wires and the lid clearance.

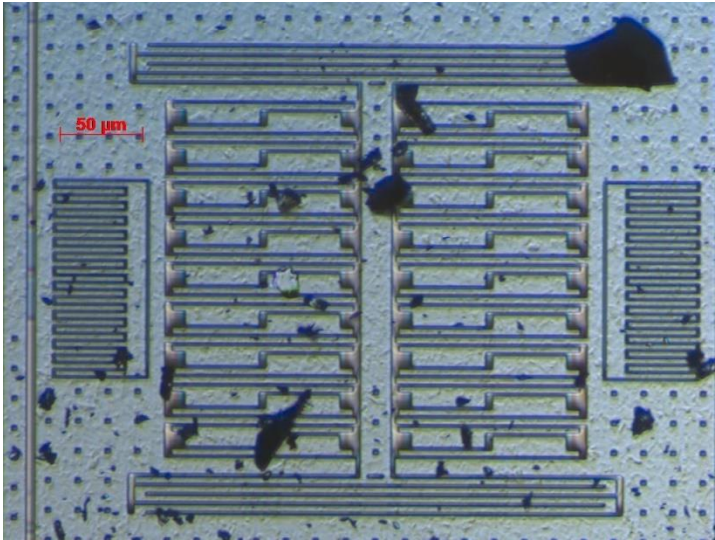


Close-up view of the 2D accelerometer 0-level package in part G11-FFF-03, showing a slight overflow of the solder within the accelerometer's 0-level package's cap and the underlying silicon (see red rectangle). This is visible in the cross-section performed later and is generally visible on all the samples.

Additionally to the previous observations, a sample has been further destructively analysed in order to reveal the MEMS structures of the sensors. The pictures are displayed hereafter, first for the accelerometer.



Open view of the accelerometer die. Debris from the destructive manipulation are visible. The X and Y accelerometers are visible on the left and right side of the central structure.

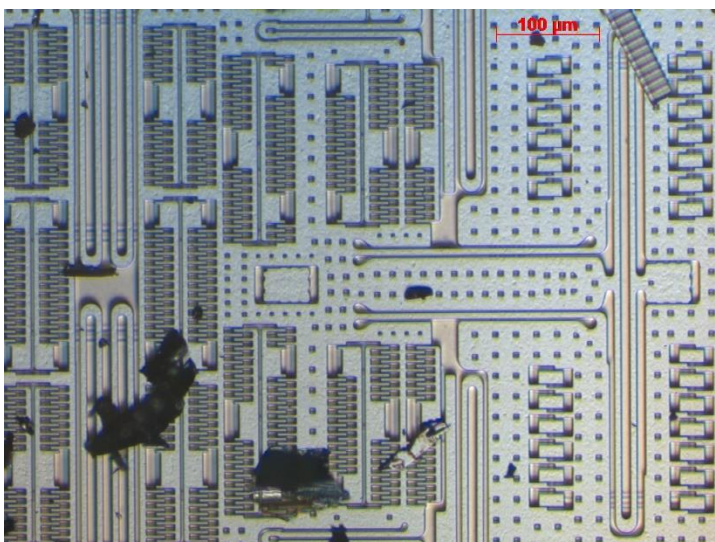


The peculiarly shaped comb drives of the accelerometer.

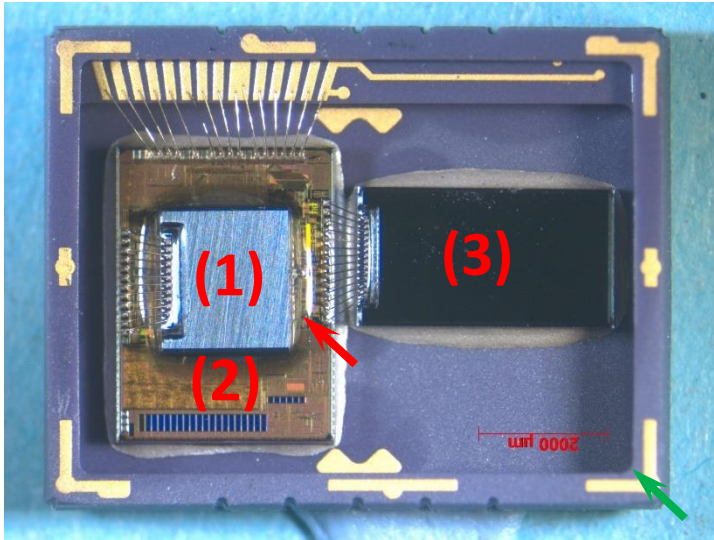
The gyroscope has also been opened destructively and the pictures are recorded without disrupting further the sensing elements, leaving therefore the debris visible.



The gyroscope die features a higher level of complexity in the etched silicon sensor.



Close-up view of the gyroscope die. The darker parts are debris originating from the opening manipulation.



General top view of the G11-FFF-02 component as de-capped. The three internal components are identified as follows:

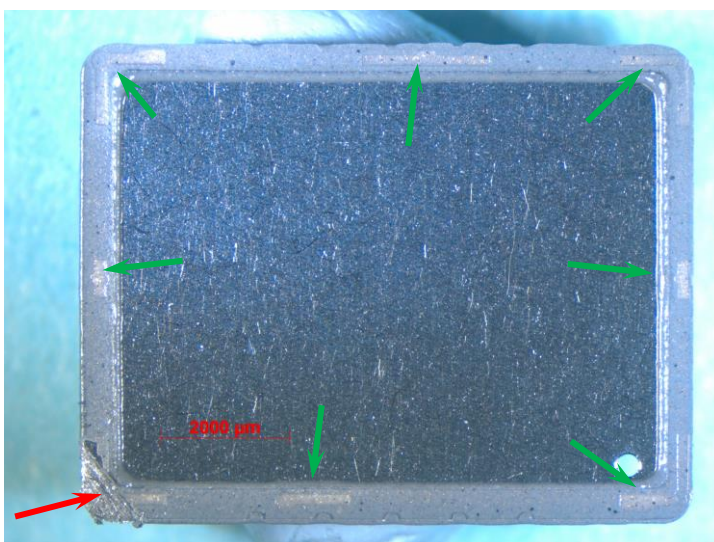
1. Accelerometer
2. ASIC
3. Gyroscope

A gel covers the top part of the (2) ASIC (with presence of meniscuses at the edge of the (1) accelerometer die, see the red arrow), the bond pads and the wire bonds themselves. It is present on all samples. It is applied to supposedly protect against oxidation, and possibly to damp vibrations and shocks and insure electrical insulation.

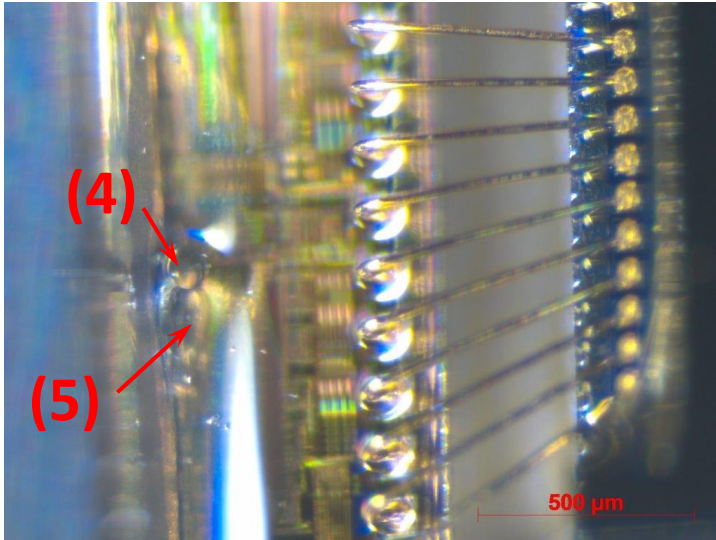
The green arrow points to one of the metallic contacts embedded in the ceramic of the package, visible also before de-capping the part.



The gel covering the bond pads, creating a meniscus, is highlighted by the lighting employed.

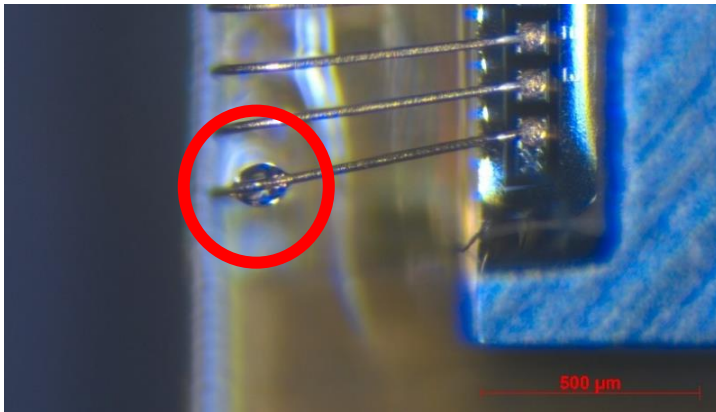


Backside view of the metallic lid of the component G11-FFF-02 ceramic package. The component was de-capped by inserting a surgical blade under the lid (see red arrow) and exerting a force out of the plane. The vent hole is visible at the bottom right corner of the figure. Traces of the golden tracks at the ceramic package are visible as well on the edges (see green arrows).

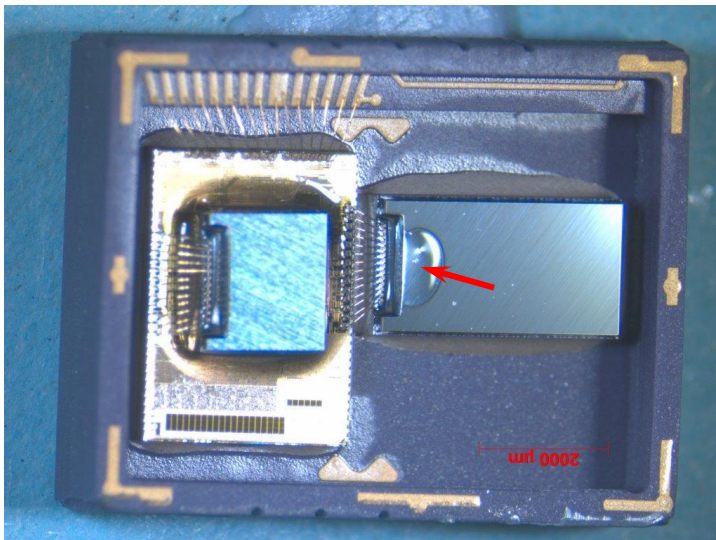


Samples G11-FFF-01, G11-FFF-02, G11-FFF-04 and G11-FFF-05 displayed the presence of one or several bubbles underneath the gel, particularly in the corner formed by two perpendicular surfaces such as the ASIC and the accelerometer dies (shown in the detail view of G11-FFF-02 here).

- 4. Hole
- 5. Bubble

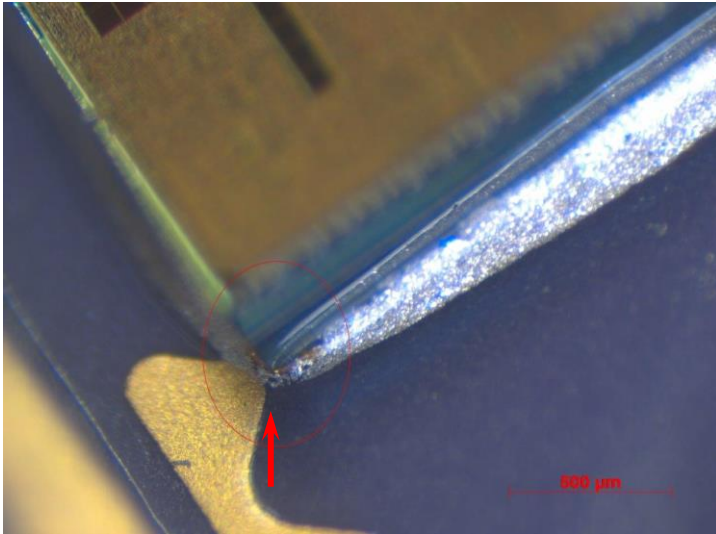


The figure shows a droplet of gel that is attached to the wire bond in G11-FFF-05. It is to be noted that this has been observed at the same location (left side of the accelerometer) on all of the 5 samples. This might increase the weight of the wire as well as causing a bigger amplitude of the movement of the wire during shock or vibration test.

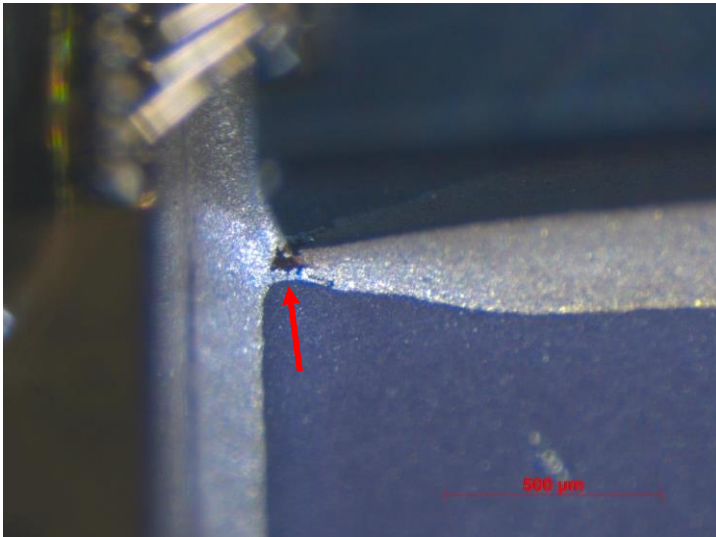


Sample G11-FFF-04 shows the presence of a relatively large droplet of gel on top of the gyroscope (see red arrow).

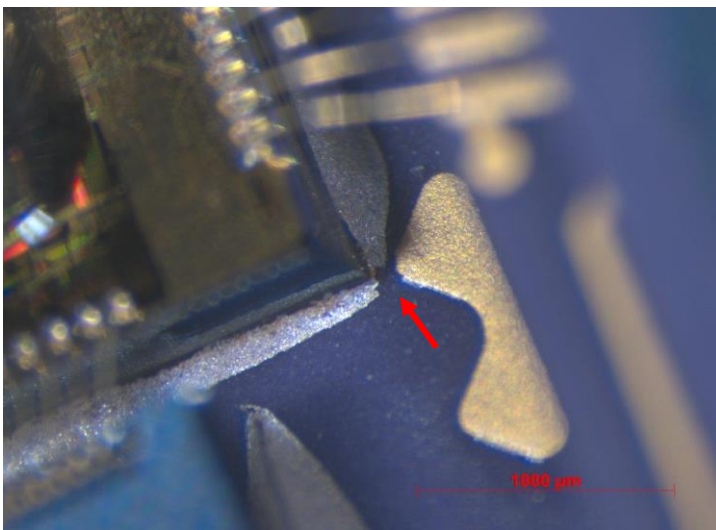
A separation of the two phases of the 0-level package adhesive (die attach) was observed in 4 of the 5 parts submitted to this CA (G11-FFF-01, G11-FFF-03, G11-FFF-04 and G11-FFF-05). All the parts successfully passed the die shear test which suggests that this feature does not represent an issue in terms of structural integrity.



Detailed view of one of the corners of the ASIC die of part G11-FFF-03. The figure illustrates a separation of the two phases of the adhesive (see red arrow).



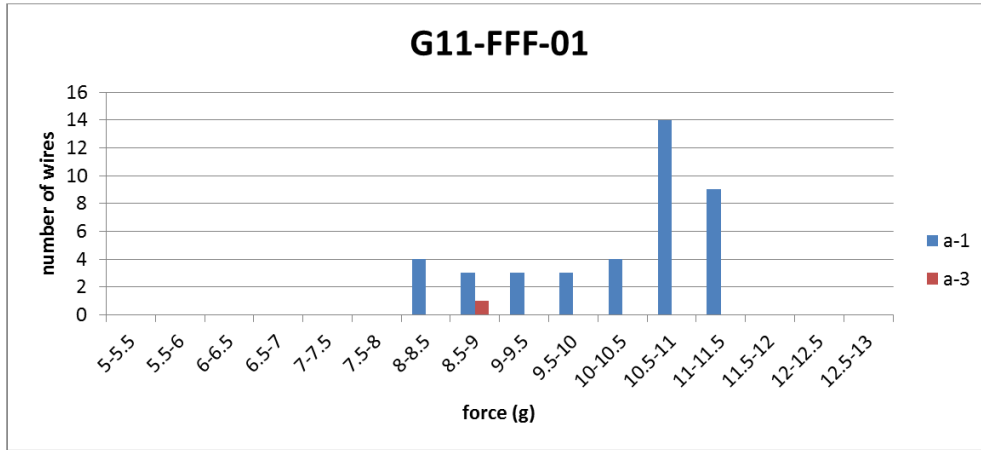
Detailed view of one corner of the accelerometer 0-level package of part G11-FFF-04. The separation of the two phases of the adhesive is visible (see red arrow).



The figure illustrates the separation of the two phases of the die adhesive along the side of the ASIC die (see red arrows) in the G11-FFF-05 component.

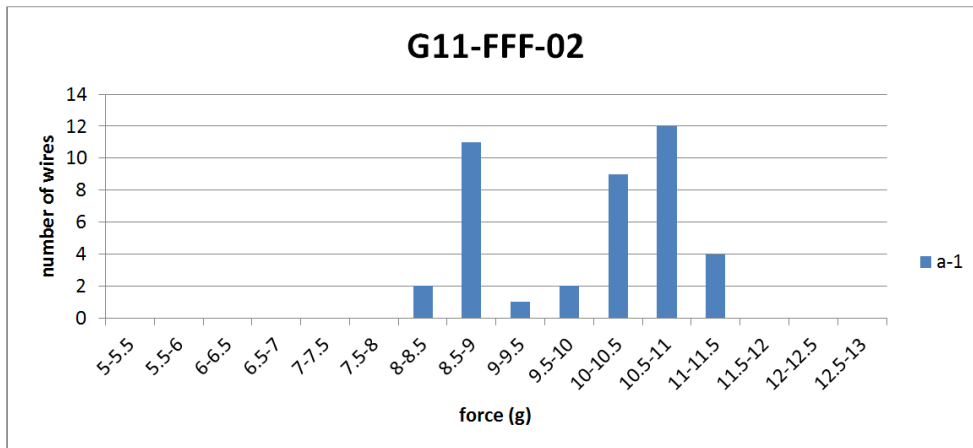
❖ Wire bond test

The details of the wire bond tests performed on the 5 samples submitted to the construction analysis are given in the following graphs. The failure modes for the wire bonds were classified as per the standard MIL-STD-883K, test method 2011.9 for wire bonds testing.

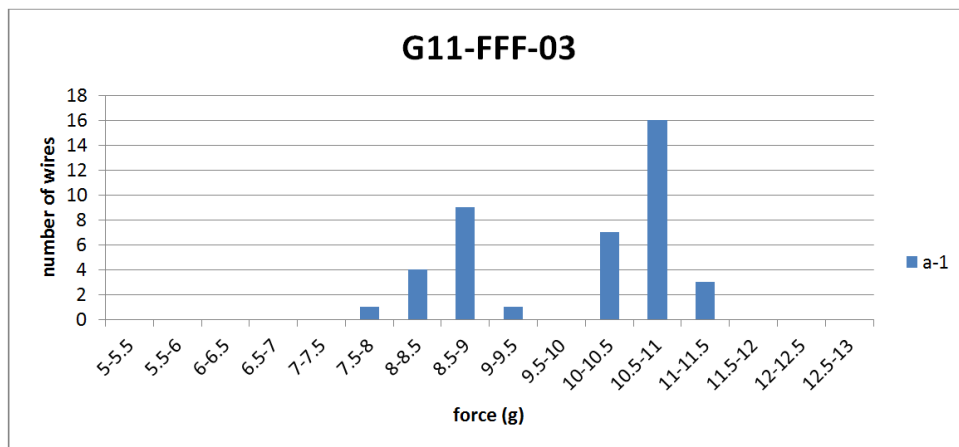


a-1: wire break at neckdown point (die side)

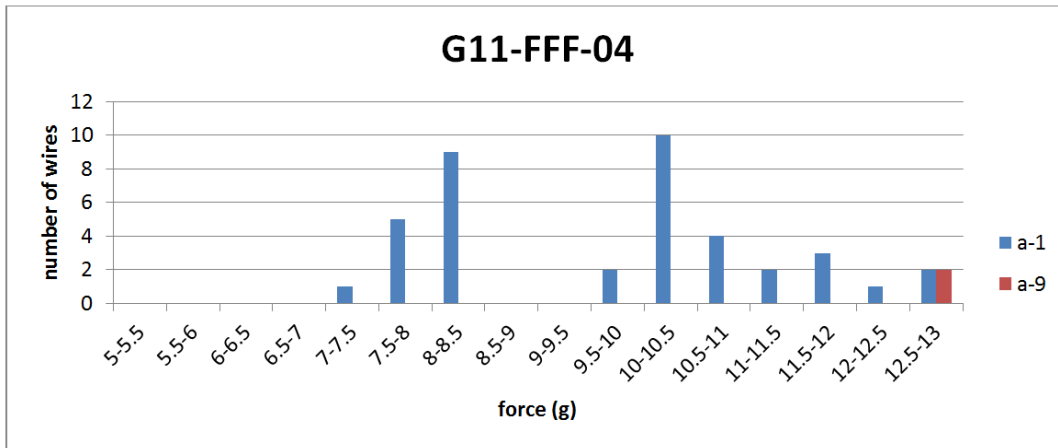
a-3: Failure in bond (interface between wire and metallization) at die.



a-1: wire break at neckdown point (die side)

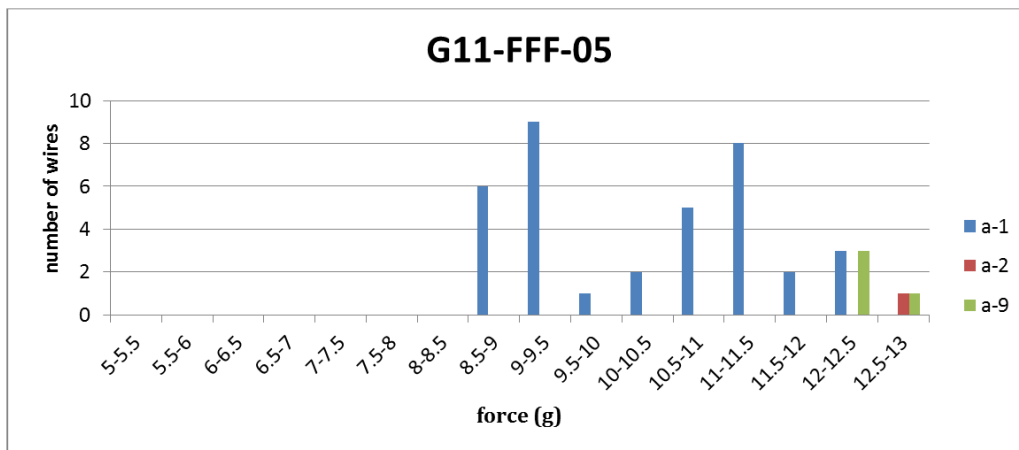


a-1: wire break at neckdown point (die side)



a-1: wire break at neckdown point (die side)

a-9: wire break at neckdown point (opposite side to a-1)



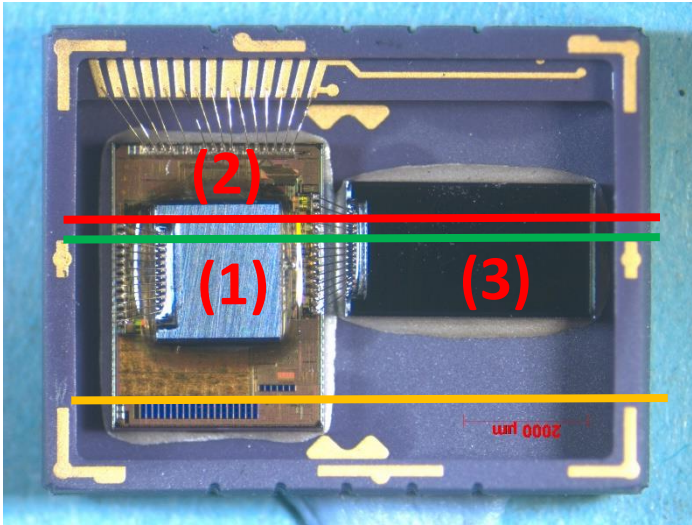
a-1: wire break at neckdown point (die side)

a-2: wire break at point other than neckdown

a-9: wire break at neckdown point (opposite side to a-1)

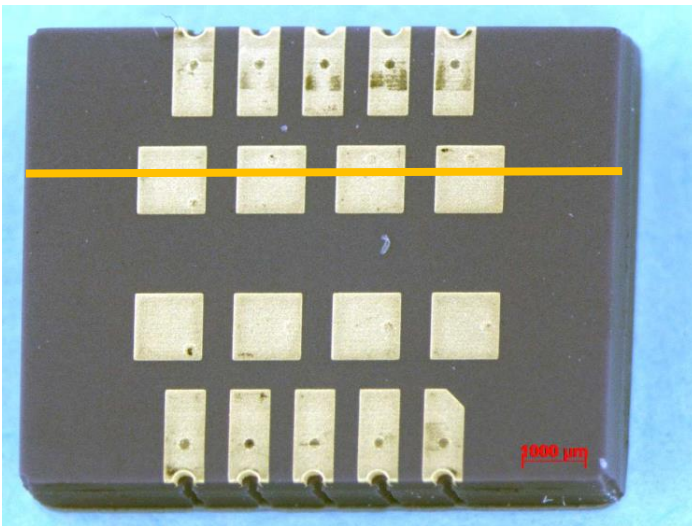
❖ Cross-Sections and SEM imaging

The sample G11-FFF-05 was potted in resin after bond strength test, to perform three cross-Sections. The gel was not removed for this operation. The first one is indicated by the red line. Then, the sample was ground further and polished at the plane shown by the green line. Finally, observation of the external contact pads was performed at the orange line.



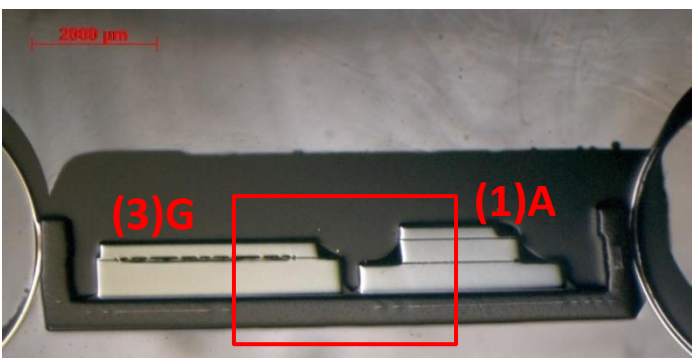
Position of the Sections performed, indicated by the red line (first Section) and by the green line (second Section). The third section is indicated by the orange line.

1. Accelerometer
2. ASIC
3. Gyroscope

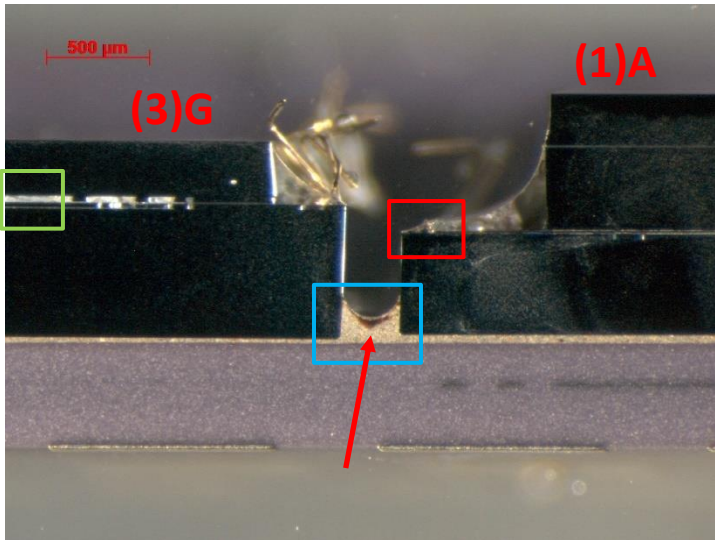


Flip view of the device. The third section (orange line) with respect to the contact pads.

The next figures are depicting the cross-Sections at the level of the red line.

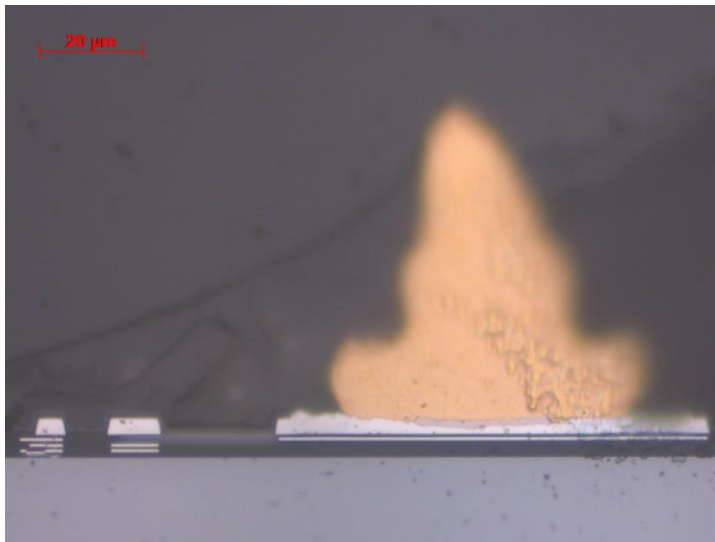


General view of the cross-Section. The gyroscope is on the left hand side of the figure. The ASIC and the accelerometer are on the right side of the figure.

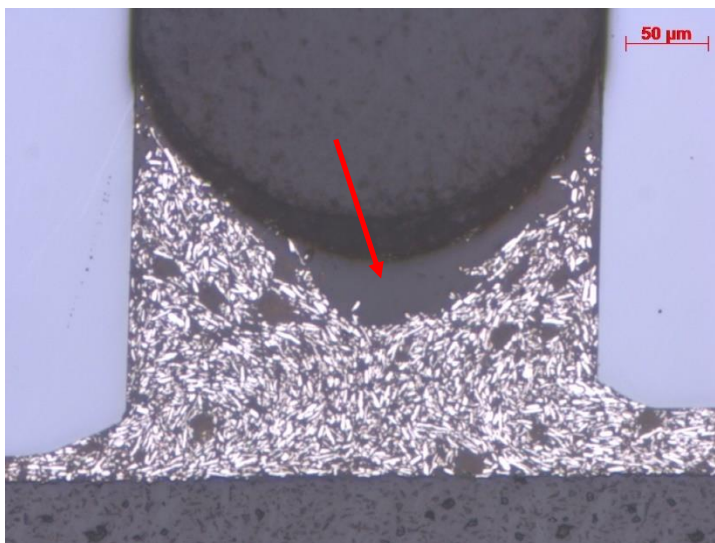


Zoomed view of the red rectangle of the figure above. Detail view of the gap between the gyroscope 0-level package (on the left), and the ASIC with the accelerometer on top (on the right). The silver-filled adhesive (see red arrow) produces a meniscus.

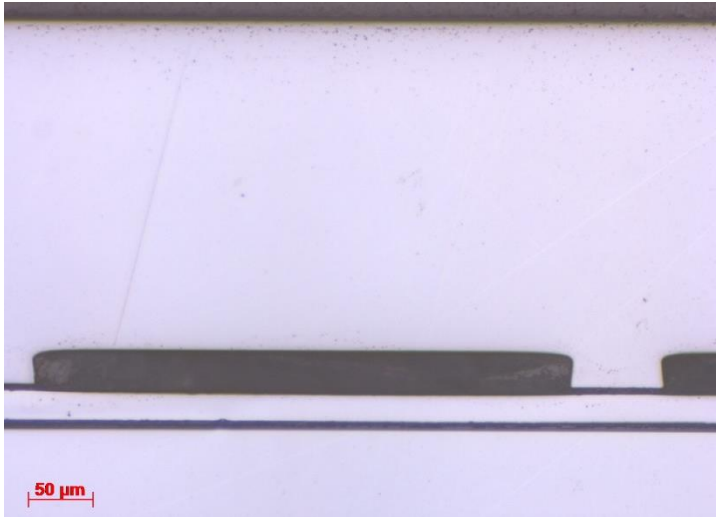
- (1) Accelerometer
- (3) Gyroscope



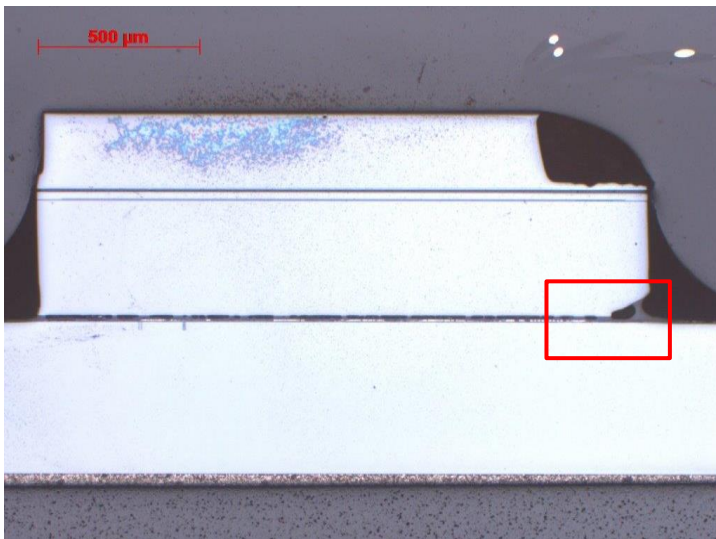
Close-up view of the bonding pad enclosed in the red rectangle above. The bond pad is on top of the ASIC die.



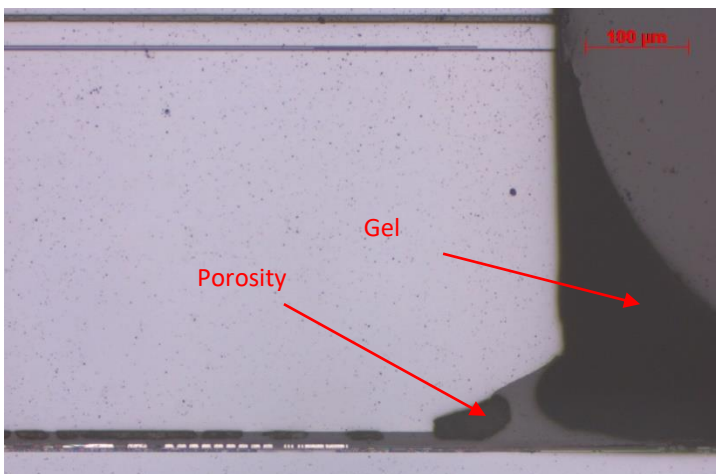
Close-up view of the adhesive, as indicated by the red arrow and blue rectangle. The red arrow indicates a separation of the two phases of the adhesive, as already detected during the Internal Visual Inspection.



Close-up view of the gyroscope cavity, as illustrated in the cross-section above by the green rectangle.

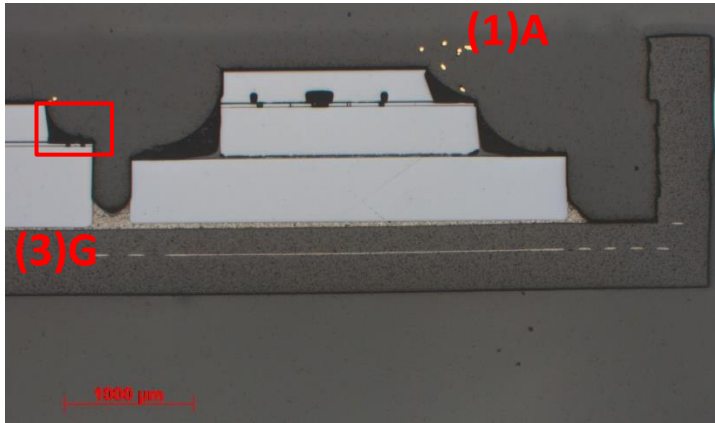


Detail view of the accelerometer 0-level package on top of the ASIC die.

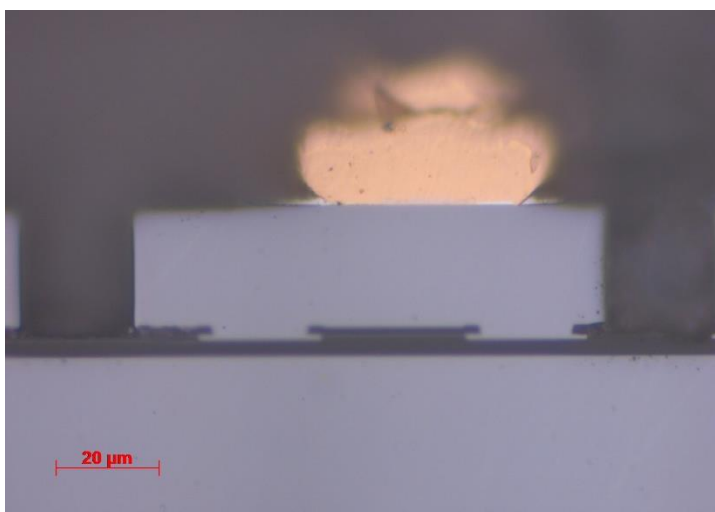


Close-up view of the red square shown above. The figure illustrates a porosity in 0-level package's adhesive, which could potentially lead to crack initiation and propagation due to thermal or vibrations fatigue.

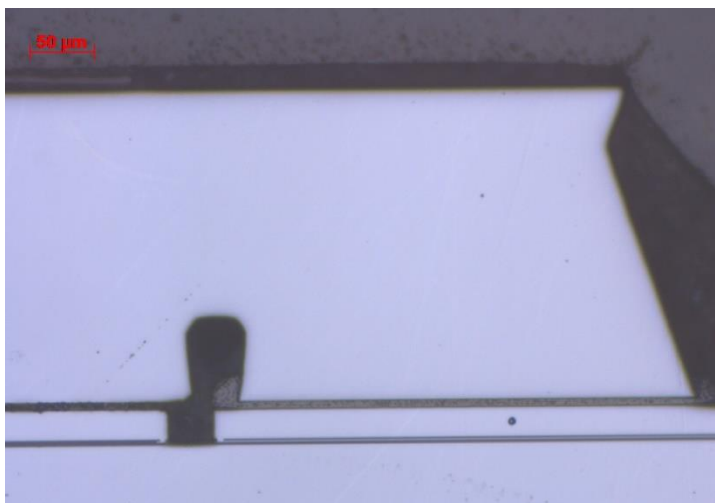
A second grinding/polishing sequence to reach the second cavity (accelerometer) was performed, until the green line on the picture of the outer view of the device.



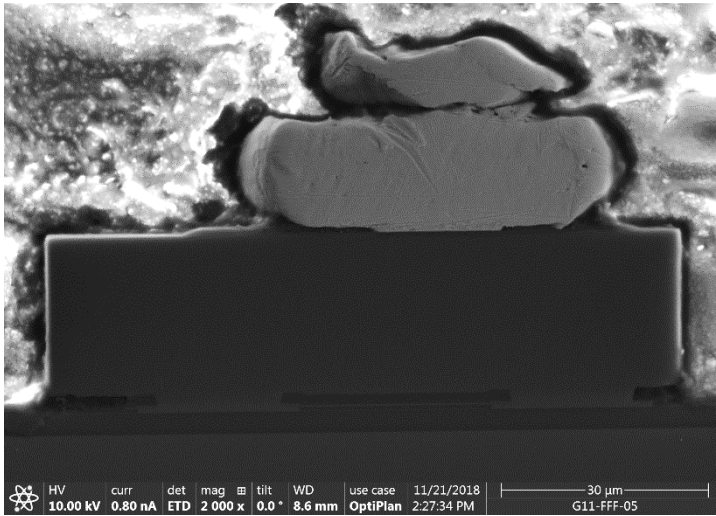
New cross-section view showing the accelerometer's cavity.



Contact pad with aluminum metalization, and Au ball bond. This contact pad is enclosed by the red square shown above, on top of the gyroscope.

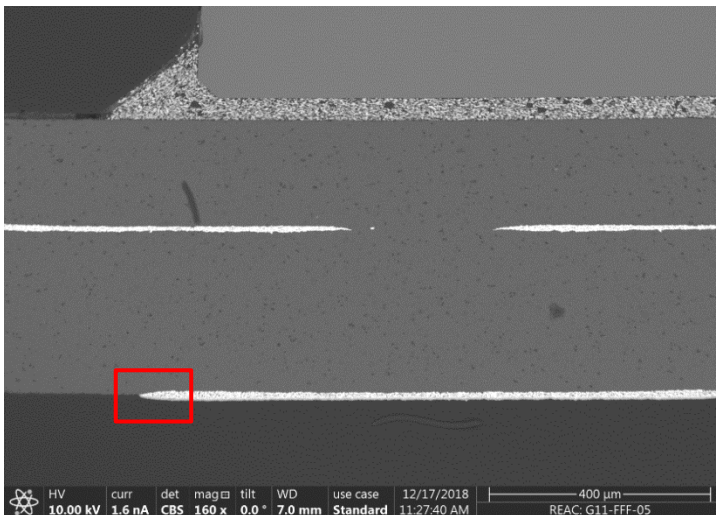


Solder of the cap over the accelerometer die.



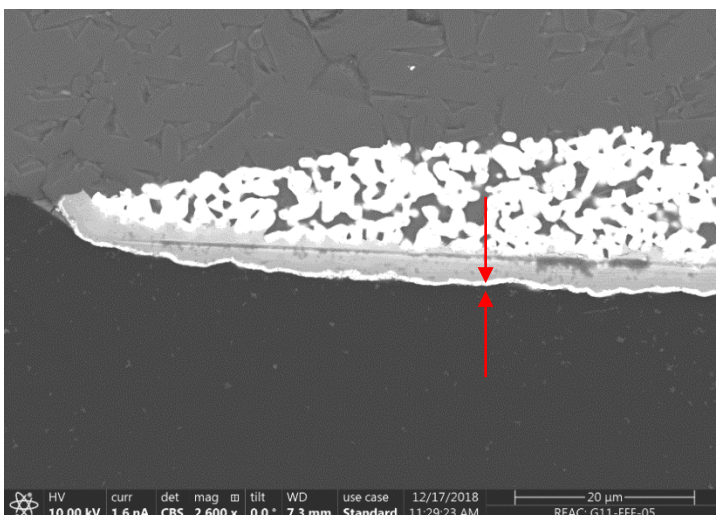
SEM view of the bond pad.

The external contact pads are observed in the next couple of figures.



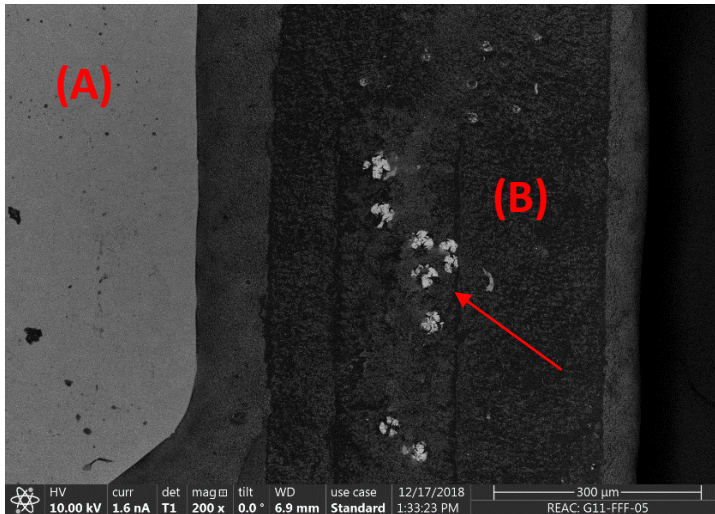
New cross-section view showing the edge of the ASIC, and the embedded tracks of the package as well as external contacts (see red square).

Third grinding/polishing sequence to reach the package contacts, until the orange line in the introductory figure for cross-Sections.



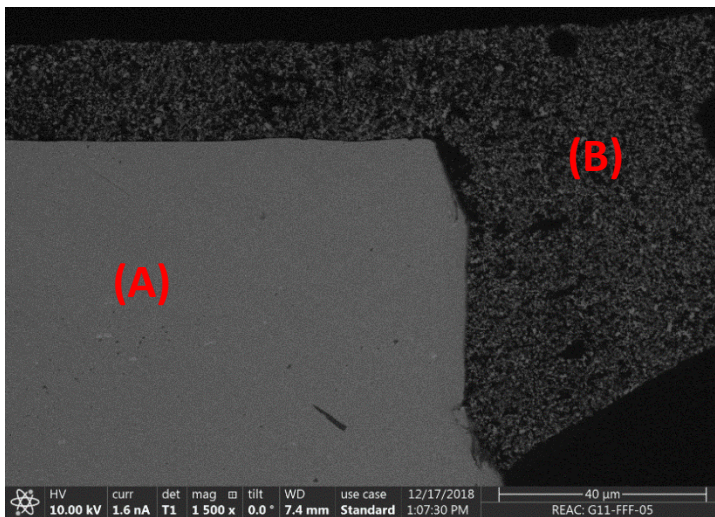
Detail from of the package external contacts (red rectangle). The tungsten, sintered onto the ceramic of the package, is covered with a nickel layer, coated with gold (between red arrows).

The package's lid has also been prepared for SEM imaging and chemical analysis. The following figures depict the close-up views in bird's eye view as well as in cross-Section.



Detail of the bottom side of the lid. (A) indicates the lid base material (stainless steel) and (B) the bonding adhesive to the ceramic package.

The red arrow indicates gold left-overs from the contact pads that have come loose from the ceramic package upon mechanical opening.



Cross-section of the edge of the metallic lid. (A) stainless steel base material and (B) the glass frit adhesive.

C. MATLAB script for functional characterization

```

%%%%%%%%%%%%%%%%%%%%%%%%%%%%%%%%%%%%%%%%%%%%%%%%%%%%%%%%%%%%%%%%%%%%%%%%
ANALYSER ST MICROELECTRONICS COMBOGZAXY
%
% Written by Maxime Auchlin
% March 2018, ESTEC, Noordwijk (NL)
% 2017-2021, CSEM, Neuchatel (CH)
%%%%%%%%%%%%%%%%%%%%%%%%%%%%%%%%%%%%%%%%%%%%%%%%%%%%%%%%%%%%%%%%%%%%%%%%

% This program extracts the raw data from the accelerometers and the
% gyroscope of the sensor and does the following operations:
% - Display the sequence of gravity testing
% - Compute the measured values of the gravity

%Clear the field
close all
clearvars
delete 'K-summary.txt'

%Display individual figure OFF (0) and ON (1)
dispfig=1;
labelAbscissa=('Vibration sweeps 20-2000-20Hz@50g [-]');

%%%%%%%%%%%%%%%%%%%%%%%%%%%%%%%%%%%%%%%%%%%%%%%%%%%%%%%%%%%%%%%%%%%%%%%%
raw_files_unsrtd=dir('*.txt');
numberOfTests=length(raw_files_unsrtd);
%%%%%%%%%%%%%%%%%%%%%%%%%%%%%%%%%%%%%%%%%%%%%%%%%%%%%%%%%%%%%%%%%%%%%%%%
%Problem with the above: order of fields in raw_files is not good. So we
%need to rearrange following file names.
%https://blogs.mathworks.com/pick/2010/09/17/sorting-structure-arrays-based-on-fields/

%Create a vector containing the load levels, orn the x-axis of the 3 final
%plots.
abscissa=zeros(1,numberOfTests);
abscissa_digit=zeros(1,numberOfTests);

%I am replacing one unused field (datenum) with scalars by the step number
%coming from the filename

for z=1:1:numberOfTests
    [~,pickSampleName,ext]=fileparts(raw_files_unsrtd(z).name);
    [sampleGroup,sampleSequence,sampleNumber,sampleIndex,sampleLoad]=...
        strread(pickSampleName,'%s %s %s %s %s','delimiter','-');
    abscissa_digit(z)=str2num(sampleLoad{1});

    raw_files_unsrtd(z).datenum=abscissa_digit(z);
end

genericSampleName_cell=[sampleGroup sampleSequence sampleNumber sampleIndex];
genericSampleName={genericSampleName_cell{1} '-' genericSampleName_cell{2}...
    '-' genericSampleName_cell{3} '-' genericSampleName_cell{4}};

Afields = fieldnames(raw_files_unsrtd);
Acell = struct2cell(raw_files_unsrtd);
sz = size(Acell);
% Convert to a matrix
Acell = reshape(Acell, sz(1), []); % Px(MxN)
% Make each field a column
Acell = Acell'; % (MxN)xP
% Sort by fifth field "datenum"
Acell = sortrows(Acell, 6);
% Put back into original cell array format
Acell = reshape(Acell', sz);
% Convert to Struct
raw_files = cell2struct(Acell, Afields, 1);

%Abscissa values

abscissa=sort(abscissa_digit,'ascend');

%Definition of finite difference parameters
segmentSize=300; %Number of point in a segment (difference element)
expectedNumberOfPlateau=6; %How the measurement is made and how many plateaus AT MINIMUM are in meas-
urements
testTime=70; %[s]
toleranceStd=1.5; %Multiplier of std defines the thresholds or setting to zero or not values of
GRAVITY. Helps removing hitches and noise. To be varied around 1.

indicationPlateau=0; %To display light-blue lines on graphs. On=1, Off=0.

acq=200; %[Hz] acquisition frequency
delay=1.5; %[s] delay before averaging

%Get he +g and -g values

```

```

oneG=1;
twoG=2;
nbAxis=2;

%Outputs
gZero1=zeros(nbAxis,1);
gZeroY2=zeros(nbAxis,1);
gZeroX3=zeros(nbAxis,1);
gZeroY4=zeros(nbAxis,1);
gZeroX5=zeros(nbAxis,1);
gZero6=zeros(nbAxis,1);
stdGZero1=zeros(nbAxis,1);
stdGZeroY2=zeros(nbAxis,1);
stdGZeroX3=zeros(nbAxis,1);
stdGZeroY4=zeros(nbAxis,1);
stdGZeroX5=zeros(nbAxis,1);
stdGZero6=zeros(nbAxis,1);
gZero16=zeros(nbAxis,1);
gZeroStd16=zeros(nbAxis,1);
gZeroCalc=zeros(nbAxis,1);

gMIN=zeros(nbAxis,1);
stdGMIN=zeros(nbAxis,1);

gMAX=zeros(nbAxis,1);
stdGMAX=zeros(nbAxis,1);

deltaTot=zeros(nbAxis,1);
gPlusToBaseline=zeros(nbAxis,1);
gMinusToBaseline=zeros(nbAxis,1);

vectorSampleNames=cell(numberOfTests,1);
vectorSampleNames{numberOfTests,1} = [];

OUTPUTS = cell(numberOfTests,1);
OUTPUTS{numberOfTests,1} = [];

%Display figure or not
if dispfig == 0
    set(0,'DefaultFigureVisible','off');
end

%Added for v4 - plot of the gyro
GYRG=cell(numberOfTests,1);
TIMG=cell(numberOfTests,1);
%

for f=1:1:numberOfTests
    fileName=raw_files(f).name;
    [~,currentSampleName,ext]=fileparts(fileName);
    groupName=currentSampleName(1:10);

    matrixOfK=zeros(nbAxis,expectedNumberOfPlateau);
    matrixOfStd=zeros(nbAxis,expectedNumberOfPlateau);

    RAWFILE=fopen(fileName,'r');
    %Read Logbook file with number, direction and file name
    %https://ch.mathworks.com/matlabcentral/answers/134953-how-do-i-determine-the-number-of-header-
    lines-in-a-text-document
    RAWDATA = textscan(RAWFILE, '%f %f %f %f %f %f ','delimiter','\n');

    %We remove the last line to avoid problem of uncomplete last line of
    %the text file
    R1=length(RAWDATA{1,1});
    R6=length(RAWDATA{1,6});

    if R1~=R6
        discrepancy=0;
        for r=2:1:length(RAWDATA)
            if length(RAWDATA{1,1})~=length(RAWDATA{1,r})
                discrepancy=discrepancy+1;
            end
        end

        for p=1:1:(length(RAWDATA)-discrepancy)
            RAWDATA{1,p}(length(RAWDATA{1,p}))=[];
        end
    end

    %Assign variables

    sizeDATA=size(RAWDATA);
    dRows=sizeDATA(1); dColumns=sizeDATA(2);

    TIME=(RAWDATA{1}-min(RAWDATA{1}))/1000^2;
    TEMP=RAWDATA{2};
    ACCX=RAWDATA{3};
    ACCY=0*ACCX;

```

```

ACCX=RAWDATA{4};
GYRX=RAWDATA{5};
GYRZ=RAWDATA{6};

%Update v4
GYRG{f}=GYRZ;
TIMG{f}=TIME;
%

%%First row of figures - Plot of figures

figure('units','normalized','outerposition',[0 0 1 1]); %Full screen figure
%set(gcf,'Visible','on');

%% Plot of the first line of figures

subplot(3,2,1); %subplot(3,3,1) <- old
plot(1)
plot(TIME,ACCX);
maxOfGraph=max(TIME)-mod(max(TIME),2)+2;
xlim([-2 maxOfGraph]);
hold on

grid on
grid minor
title(['Sample ' currentSampleName ' along X-axis'])
xlabel('Time [s]')
ylabel('Acceleration [a.u.]')

% subplot(3,3,2) %First subplot in 2x1 grid
% plot(1)
% plot(TIME,ACCY);
% maxOfGraph=max(TIME)-mod(max(TIME),2)+2;
% xlim([-2 maxOfGraph]);
% hold on
%
% grid on
% grid minor
% title(['Sample ' sampleName ' along Y-axis'])
% xlabel('Time [s]')
% ylabel('Acceleration x 9.81 [m/s^2]')

subplot(3,2,2) %subplot(3,3,2) %First subplot in 2x1 grid
plot(1)
plot(TIME,AC CZ);
maxOfGraph=max(TIME)-mod(max(TIME),2)+2;
xlim([-2 maxOfGraph]);
hold on

grid on
grid minor
title(['Sample ' currentSampleName ' along Y-axis'])
xlabel('Time [s]')
ylabel('Acceleration [a.u.]')

%% Second row of figures - DELTA

nbRows=length(TIME);
DELTA=zeros(nbRows,1);

for axis=1:nbAxis

    if axis==1
        GRAVITY=ACCX;
        naming='\Delta_X=(a_i-a_{i+1})';
    elseif axis==2
        GRAVITY=AC CZ;
        naming='\Delta_Z=(a_i-a_{i+1})'; %'\Delta_Y=(a_i-a_{i+1})';
    else
        GRAVITY=AC CZ;
        naming='\Delta_Z=(a_i-a_{i+1})';
    end

    for z=1:nbRows %Compute DELTA(Z)
        if isequal(z,nbRows)
            DELTA(z)=0;
        else
            DELTA(z)=GRAVITY(z+1)-GRAVITY(z);
        end
    end

    posLine2=axis+2;

    subplot(3,2,posLine2)
    plot(TIME,DELTA,'r')
    grid on
    grid minor

```



```

xlabel('Time [s]')
xlim([-2 maxOfGraph])
ylabel(naming)
hold on

posStd=std(DELTA);
negStd=-posStd;

plot([0 nbRows],[posStd posStd], '-.k');
hold on
plot([0 nbRows],[negStd negStd], '-.k');
hold on

DELTA_ZERO=DELTA;

for i=1:size(DELTA)
    if norm(DELTA(i)) < (std(DELTA)*toleranceStd)
        DELTA_ZERO(i)=0;
    end
end

moreThanTestTime=find(TIME>testTime);
DELTA_ZERO(moreThanTestTime)=0;

%p=plot(TIME,DELTA_ZERO,'k');
%set(p,'color',[0.5 0.5 0.5])

%Average on segments of DELTA_ZERO to smoothen the function

rest=mod(length(DELTA_ZERO),segmentSize);
bulk=length(DELTA_ZERO)-rest;
segmentNumber=bulk/segmentSize;
DELTA_MEAN=zeros(1,segmentNumber);
TIME_MEAN=zeros(1,segmentNumber);
STAMP=zeros(1,segmentNumber);

for s=1:segmentNumber
    if s==1
        span=1:(s*segmentSize);
    elseif s<segmentNumber
        span=((s-1)*segmentSize+1):(s*segmentSize);
    else
        span=((s-1)*segmentSize+1):length(DELTA_ZERO);
    end
    stamp=round(median(span));
    DELTA_MEAN(s)=mean(DELTA_ZERO(span)); %last segment adds up the rest of the vector in order to
avoid effect of ending noise in the measurement
    if DELTA_MEAN(s)~=0
        DELTA_MEAN(s)=posStd;
    end
    TIME_MEAN(s)=TIME(stamp); %median(TIME(((s-1)*segmentSize+1):length(DELTA_ZERO)));
end

%Remove zero values from pre-set STAMP vector. Since STAMP can at
%maximum have segmentNumber components, we set it from
%segmentNumber and then remove unecessary stuff.

%     STAMP(STAMP==0)=[];

%     for d=1:length(DELTA_MEAN)
%         if DELTA_MEAN(d)~=0
%             DELTA_MEAN(d)=posStd;
%         end
%     end

plot(TIME_MEAN,DELTA_MEAN,'k');

%Vector DELTA_MEAN has a given number of elements, and we need to
%parametrize it over the time span of the dataset. DELTA_MEAN(1) =
%t=0 and DELTA_MEAN(n) = t=TIME(last)

%%

%% Third row NEW METHOD - ALL values below stdev are set to zero. Plateau
%determined from the zero values at +/- 2 seconds

posLine3=axis+4;

subplot(3,2,5)% subplot(3,3,posLine3)

[AX,YT,YG]=plotyy(TIME,TEMP,TIME,GYRZ,'plot');
set(YT,'Color','m')
set(YG,'Color','b')
set(AX,{ 'ycolor' }, { 'm'; 'b' })

```



```

indexFlag=1;

for k=1:expectedNumberOfPlateau
    if k==1
        boundLeft=min(TIME);
        boundRight=flagLeft(indexFlag)-delay;
    elseif (k>1) && (k<expectedNumberOfPlateau)
        boundLeft=flagRight(indexFlag)+delay;
        boundRight=flagLeft(indexFlag+1)-delay;
        indexFlag=indexFlag+1;
    else
        boundLeft=flagRight(indexFlag)+delay;
        boundRight=max(TIME);
    end

    %PlateauIndices=find(TIME>=boundLeft & TIME<boundRight);

    findInTIME=find(TIME>=boundLeft & TIME<(boundRight));
    matrixOfK(axis,k)=mean(GRAVITY(findInTIME));
    matrixOfStd(axis,k)=std(GRAVITY(findInTIME));

%
%
%     if (axis==2) && (k==1)
%         return
%     end

    if indicationPlateau==1
        subplot(3,3,axis)
        plot([TIME(1) TIME(length(TIME))],[matrixOfK(axis,k) matrixOfK(axis,k)],'c')
        hold on
    end
end

axisNamingVector={'ACCX';'ACCY'};

%As there is no Z axis anymore:
%matrixOfK(3,:)=[]

%Table of K's
defTable=uitable('Data', matrixOfK, 'ColumnName', namingK, 'rowName', axisNamingVector,
'ColumnWidth', {70});

pos = get(subplot(3,2,6),'position');
delete(subplot(3,2,6))
set(defTable,'units','normalized')
set(defTable,'position',pos)

%
%     %Table of STDs
%     defTable=uitable('Data', matrixOfStd, 'ColumnName', namingStd, 'rowName', axisNamingVector,
'ColumnWidth', {70});
%
%     pos = get(subplot(3,3,9),'position');
%     delete(subplot(3,3,9));
%     set(defTable,'units','normalized');
%     set(defTable,'position',pos);

%Create the file

%     [finalFile,errmsg]=fopen('K-summary.txt','w');
%     fprintf(finalFile, 'Hereafter are the values for: CAMPAIGN %s\r\n',campaignNumber);
%     fprintf(finalFile, '#\t Sample \t K0 \t K0_stdev \t K1 \t K1_stdev \t K0_dev \t K1_dev \r\n');
%
%     for d=1:numberOfTests
%         fprintf(finalFile, '%s\t %s\t %f\t %f\t %f\t %f\t %f\t %f\t \r\n',...
%             numberStorage{d}, string(fileNoExt{d}), K0(d), K0_stdev(d), K1(d), K1_stdev(d), K0_dev(d),
%             K1_dev(d));
%     end

currentK=matrixOfK(axis,1:(length(matrixOfK)));
currentStd=matrixOfStd(axis,1:(length(matrixOfK)));
gMAX(axis)=max(currentK); %Where is the max value (e.g. +g)
gMIN(axis)=min(currentK); %Where is the min value (e.g. -g)

%% Moved piece of code from above

subplot(3,2,posLine2-2)
for i=1:length(flagRight)
    tRight=flagRight(i)+delay;
    plot([tRight tRight],[1.1*gMIN(axis) 1.1*gMAX(axis)],'-g');
    hold on
end
for i=1:length(flagLeft)
    tLeft=flagLeft(i)-delay;
    plot([tLeft tLeft],[1.1*gMIN(axis) 1.1*gMAX(axis)],'-b');
    hold on

```

```

end

subplot(3,2,posLine2)
for i=1:length(flagRight)
    tRight=flagRight(i)+delay;
    plot([tRight tRight],[gMIN(axis) gMAX(axis)],'-g');
    ylim([10*negStd 10*posStd]);
    hold on
end
for i=1:length(flagLeft)
    tLeft=flagLeft(i)-delay;
    plot([tLeft tLeft],[gMIN(axis) gMAX(axis)],'-b');
    ylim([10*negStd 10*posStd]);
    hold on
end

%%%

indexPlus=find(currentK==gMAX(axis)); %Position index of +g
indexMinus=find(currentK==gMIN(axis)); %Position index of -g

stdGMAX(axis)=currentStd(indexPlus);
stdGMIN(axis)=currentStd(indexMinus);

%We look for all of the zero-g plateaus and fill the special values
if axis==1
    gZeroX3(axis)=currentK(3);
    stdGZeroX3(axis)=currentStd(3);
    gZeroX5(axis)=currentK(5);
    stdGZeroX5(axis)=currentStd(5);

    gZeroY2(axis)=NaN;
    stdGZeroY2(axis)=NaN;
    gZeroY4(axis)=NaN;
    stdGZeroY4(axis)=NaN;
elseif axis==2
    gZeroY2(axis)=currentK(2);
    stdGZeroY2(axis)=currentStd(2);
    gZeroY4(axis)=currentK(4);
    stdGZeroY4(axis)=currentStd(4);

    gZeroX3(axis)=NaN;
    stdGZeroX3(axis)=NaN;
    gZeroX5(axis)=NaN;
    stdGZeroX5(axis)=NaN;
else
    error('Cannot extract zero-g values for the 4 intermediate plateau!');
end

%Fill the rest of zero values
gZero1(axis)=currentK(1);
gZero6(axis)=currentK(length(currentK));

stdGZero1(axis)=currentStd(1);
stdGZero6(axis)=currentStd(6);

%ONLY on the FIRST and the LAST value, for when the sensor is flat
%on the table (i.e. when Z points upward).

lastPlateauIndex=length(currentK);
gZero16(axis)=(currentK(1)+currentK(lastPlateauIndex))/2;
gZeroStd16(axis)=abs(currentK(1)-currentK(lastPlateauIndex))/2; %Useful to assess if the sensor
is consistent (i.e. Z accelerometer gives 0 where tilted over X and Y)

gPlusToBaseline(axis)=abs(gZero16(axis)-gMAX(axis)); %Value of +g with respect to the baseline
gMinusToBaseline(axis)=-(gZero16(axis)-gMIN(axis)); %Value of -g with respect to the baseline

deltaTot(axis)=abs(gMAX(axis)-gMIN(axis)); %Total 2g delta between -g and +g
gZeroCalc(axis)=gMAX(axis)-deltaTot(axis)/2; %Value of 0g computed from +g and -g of raw results

end

%Now we have to build a matrix of results for all files
%The following variables are to be saved into the file

matrixOfOutputs=[gZero1,gZeroY2,gZeroX3,gZeroY4,gZeroX5,gZero6,... %0g
    stdGZero1,stdGZeroY2,stdGZeroX3,stdGZeroY4,stdGZeroX5,stdGZero6,... %0g
    gZero16,gZeroStd16,gZeroCalc,... %0g
    gMIN,stdGMIN,... %-g
    gMAX,stdGMAX,... %+g
    deltaTot]; %2g

OUTPUTS{f}=matrixOfOutputs;

vectorSampleNames{f}=currentSampleName;

%One also has to save the name of the

```



```

computedPos1g_X(u)=OUTPUTS{u}(1,18)/conversionRate_X;
computedPos1g_Y(u)=OUTPUTS{u}(2,18)/conversionRate_Y;

computedNeg1g_X(u)=OUTPUTS{u}(1,16)/conversionRate_X;
computedNeg1g_Y(u)=OUTPUTS{u}(2,16)/conversionRate_Y;

%Loop for graph 2

D1_X(u)=(computed2g_X(u)-computed2g_X(1))/computed2g_X(1)*100;
D1_Y(u)=(computed2g_Y(u)-computed2g_Y(1))/computed2g_Y(1)*100;

Dpos_X(u)=(computedPos1g_X(u)-computedPos1g_X(1))/computedPos1g_X(1)*100;
Dpos_Y(u)=(computedPos1g_Y(u)-computedPos1g_Y(1))/computedPos1g_Y(1)*100;

Dneg_X(u)=(computedNeg1g_X(u)-computedNeg1g_X(1))/computedNeg1g_X(1)*100;
Dneg_Y(u)=(computedNeg1g_Y(u)-computedNeg1g_Y(1))/computedNeg1g_Y(1)*100;

%Loop for graph 3

K0_X(u)=(OUTPUTS{u}(1,18)+OUTPUTS{u}(1,16))/2;
K0_Y(u)=(OUTPUTS{u}(2,18)+OUTPUTS{u}(2,16))/2;

K1_X(u)=(OUTPUTS{u}(1,18)-OUTPUTS{u}(1,16))/2;
K1_Y(u)=(OUTPUTS{u}(2,18)-OUTPUTS{u}(2,16))/2;

if u>1
    D2_X(u)=(K0_X(u)-K0_X(1))/K1_X(u-1)*100;
    D2_Y(u)=(K0_Y(u)-K0_Y(1))/K1_Y(u-1)*100;
end
end

if dispfig == 0
    set(0,'DefaultFigureVisible','on');
end

%Graph 1 - Absolute values of normalized g

h=figure;
plot(abcissa,computed2g_X,'b:o');
hold on
plot(abcissa,computedPos1g_X,':s','Color',[0,0.6,0.9]);
hold on
plot(abcissa,computedNeg1g_X,':d','Color',[0,0.8,0.9]);
grid on
%grid minor
xlabel(labelAbscissa,'Interpreter','latex');
xlim([-2 max(abcissa)+2])
ylabel('Normalized value of g [-]','Interpreter','latex');
ylim([-1.2 2.2])
title(['Device ' genericSampleName ' (X-axis)'],'Interpreter','latex');
legend({'Computed 2g','Computed +g','Computed -g'],'Location','west','Interpreter','latex');

a = get(gca,'XTickLabel');
set(gca,'XTickLabel',a,'FontName','CMU Serif');
b = get(gca,'YTickLabel');
set(gca,'YTickLabel',b,'FontName','CMU Serif');

set(h,'Units','Inches');
pos = get(h,'Position');
set(h,'PaperPositionMode','Auto','PaperUnits','Inches','PaperSize',[pos(3), pos(4)])
print(h,'plot1_X','-dpdf','-r0');

h=figure;
plot(abcissa,computed2g_Y,'b:o');
hold on
plot(abcissa,computedPos1g_Y,':s','Color',[0,0.6,0.9]);
hold on
plot(abcissa,computedNeg1g_Y,':d','Color',[0,0.8,0.9]);
grid on
%grid minor
xlabel(labelAbscissa,'Interpreter','latex')
xlim([-2 max(abcissa)+2])
ylabel('Normalized value of g [-]','Interpreter','latex')
ylim([-1.2 2.2])
title(['Device ' genericSampleName ' (Y-axis)'],'Interpreter','latex');
legend({'Computed 2g','Computed +g','Computed -g'],'Location','west','Interpreter','latex')

a = get(gca,'XTickLabel');
set(gca,'XTickLabel',a,'FontName','CMU Serif');
b = get(gca,'YTickLabel');
set(gca,'YTickLabel',b,'FontName','CMU Serif');

set(h,'Units','Inches');
pos = get(h,'Position');

```

```

set(h,'PaperPositionMode','Auto','PaperUnits','Inches','PaperSize',[pos(3), pos(4)])
print(h,'plot1_Y','-dpdf','-r0');

%Graph n^2 - Deviation on g

h=figure;
plot(abscissa,D1_X,'k:o');
hold on
plot(abscissa,Dpos_X,'b:s');
hold on
plot(abscissa,Dneg_X,'c:d');
grid on
%grid minor
xlabel(labelAbscissa,'Interpreter','latex')
xlim([-2 max(abscissa)+2])
ylabel('Deviation on g [\%'],'Interpreter','latex')
ylim([-5.9 5.9])
title(['Device ' genericSampleName ' (X-axis)'],'Interpreter','latex');
legend({'Criterion $D_1\$ (variation on computed 2g)','Variation on +1g',...
'Variation on -1g'},'Location','southwest','Interpreter','latex');

a = get(gca,'XTickLabel');
set(gca,'XTickLabel',a,'FontName','CMU Serif');
b = get(gca,'YTickLabel');
set(gca,'YTickLabel',b,'FontName','CMU Serif');

set(h,'Units','Inches');
pos = get(h,'Position');
set(h,'PaperPositionMode','Auto','PaperUnits','Inches','PaperSize',[pos(3), pos(4)])
print(h,'plot2_X','-dpdf','-r0');

h=figure;
plot(abscissa,D1_Y,'k:o');
hold on
plot(abscissa,Dpos_Y,'b:s');
hold on
plot(abscissa,Dneg_Y,'c:d');
grid on
%grid minor
xlabel(labelAbscissa,'Interpreter','latex')
xlim([-2 max(abscissa)+2])
ylabel('Deviation on g [\%'],'Interpreter','latex')
ylim([-5.9 5.9])
title(['Device ' genericSampleName ' (Y-axis)'],'Interpreter','latex');
legend({'Criterion $D_1\$ (variation on computed 2g)','Variation on +1g',...
'Variation on -1g'},'Location','southwest','Interpreter','latex');

a = get(gca,'XTickLabel');
set(gca,'XTickLabel',a,'FontName','CMU Serif');
b = get(gca,'YTickLabel');
set(gca,'YTickLabel',b,'FontName','CMU Serif');

set(h,'Units','Inches');
pos = get(h,'Position');
set(h,'PaperPositionMode','Auto','PaperUnits','Inches','PaperSize',[pos(3), pos(4)])
print(h,'plot2_Y','-dpdf','-r0');

%Graph number 3 - Failure criteria

h=figure;
plot(abscissa,D1_X,':o','Color',[0,0,0]);
hold on
plot(abscissa,D2_X,':*','Color',[0,0.8,0.4]);
grid on
%grid minor
xlabel(labelAbscissa,'Interpreter','latex')
xlim([-2 max(abscissa)+2])
ylabel('Failure criteria [\%'],'Interpreter','latex')
ylim([-5.9 5.9])
title(['Device ' genericSampleName ' (X-axis)'],'Interpreter','latex');
legend({'Criterion $D_1\$','Criterion $D_2\$'},...
'Location','southwest','Interpreter','latex');

a = get(gca,'XTickLabel');
set(gca,'XTickLabel',a,'FontName','CMU Serif');
b = get(gca,'YTickLabel');
set(gca,'YTickLabel',b,'FontName','CMU Serif');

set(h,'Units','Inches');
pos = get(h,'Position');
set(h,'PaperPositionMode','Auto','PaperUnits','Inches','PaperSize',[pos(3), pos(4)])
print(h,'plot3_X','-dpdf','-r0');

```

```

h=figure;
plot(abcissa,D1_Y,':o','Color',[0,0,0]);
hold on
plot(abcissa,D2_Y,':*','Color',[0,0.8,0.4]);
grid on
%grid minor
xlabel(labelAbscissa,'Interpreter','latex')
xlim([-2 max(abcissa)+2])
ylabel('Failure criteria [\%]','Interpreter','latex')
ylim([-5.9 5.9])
title(['Device ' genericSampleName ' (Y-axis)'],'Interpreter','latex');
legend({'Criterion $D_1$', 'Criterion $D_2$'},...
'Location','southwest','Interpreter','latex');

a = get(gca,'XTickLabel');
set(gca,'XTickLabel',a,'FontName','CMU Serif');
b = get(gca,'YTickLabel');
set(gca,'YTickLabel',b,'FontName','CMU Serif');

set(h,'Units','Inches');
pos = get(h,'Position');
set(h,'PaperPositionMode','Auto','PaperUnits','Inches','PaperSize',[pos(3), pos(4)])
print(h,'plot3_Y','-dpdf','-r0');

%%%%
% Plot of the gyro values

h=figure('units','normalized','outerposition',[0 0 1 1]);
offset=0;

for f=1:1:numberOfTests
    plot(TIMG(f),GYRG(f)+offset,'-','Color',[.9,.6,.2]);
    hold on
    offset=offset+10^4;
end

grid on
%grid minor
xlabel('Time [s]','Interpreter','latex')
xlim([-4 64])
ylim([-1e4 max(GYRG(f))+offset])
ylabel('Gyroscope signals [a.u.]','Interpreter','latex')

title(['Device ' genericSampleName ' (gyro)'],'Interpreter','latex');
legendCell = cellstr(num2str(abcissa,'%-d'));

legend(flip(legendCell),'Location','southeast','Interpreter','latex');

a = get(gca,'XTickLabel');
set(gca,'XTickLabel',a,'FontName','CMU Serif');
b = get(gca,'YTickLabel');
set(gca,'YTickLabel',b,'FontName','CMU Serif');

set(h,'Units','Inches');
pos = get(h,'Position');
set(h,'PaperPositionMode','Auto','PaperUnits','Inches','PaperSize',[pos(3), pos(4)])

print(h,'plot4_GYR','-dpdf','-r0');

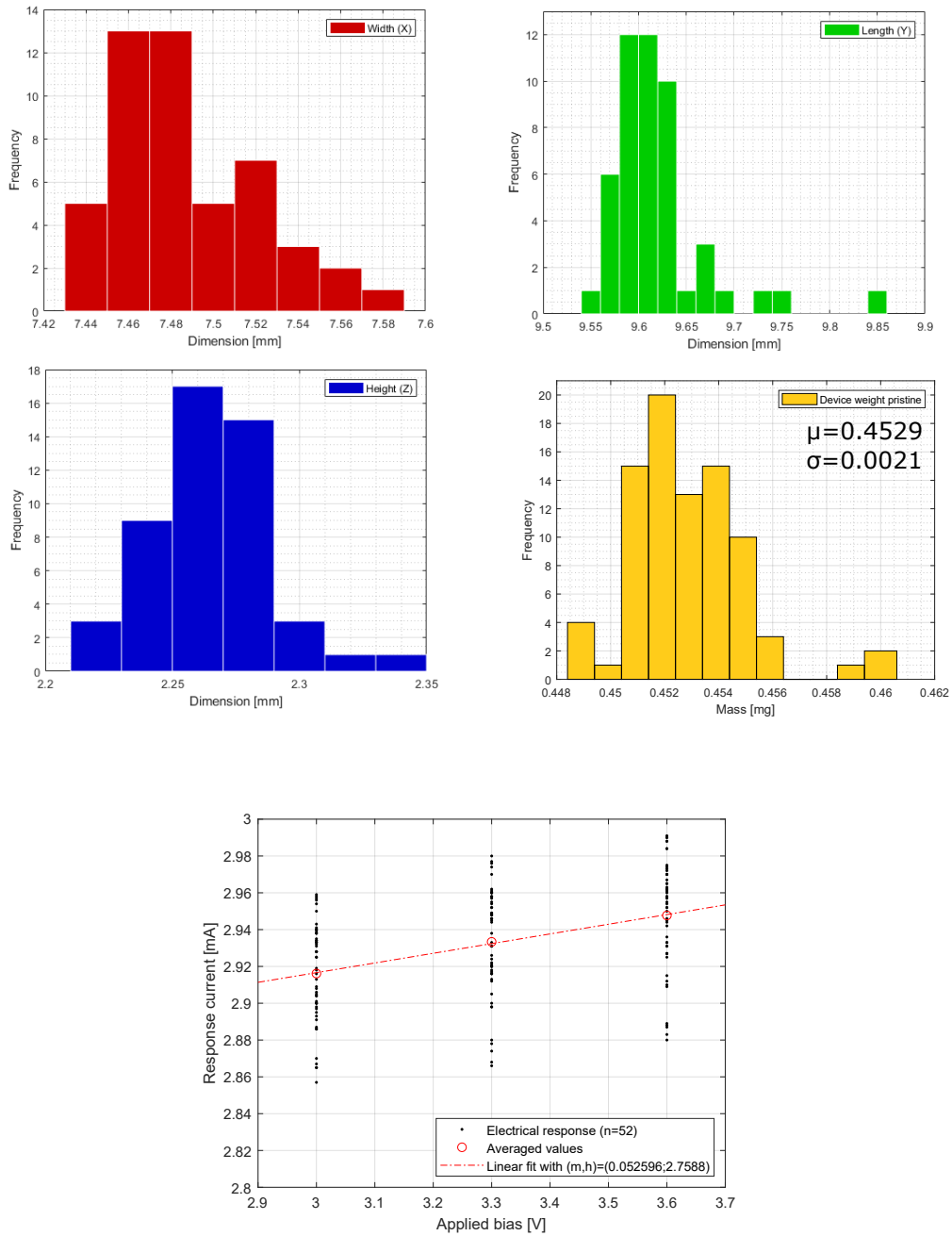
```


D. Initial devices screening

An initial screening of the devices is done to collect their physical and electrical characteristics. In particular, the electrical values are measured for all samples before and after the burn-in procedure, which are detailed in Section 3.2.

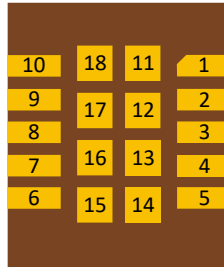
❖ Physical and electrical characterization

The pristine samples, as received by the manufacturer, are firstly attributed a codename. A selection of samples sees their dimensions, mass and electrical response measured each time a lot is constituted for the next step (burn-in). This data is used for comparison with degraded devices after testing.

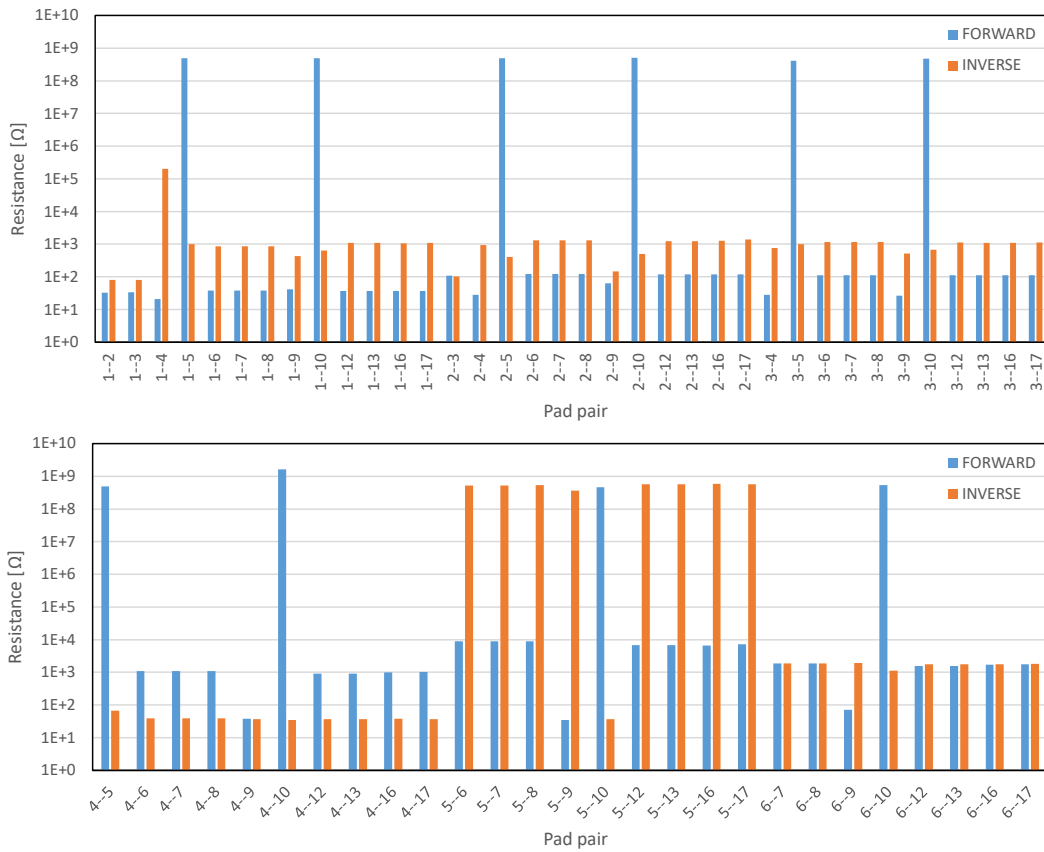


❖ Pin-to-pin insulation

The pin-to-pin insulation is a simple method to check for any shorts or discrepancies in the devices' contact pads. The numbering of the bond pads is reported in the next figure, and the values of the resistance between pads in the bar charts hereafters.



The pin-to-pin measurement was done by use of a Keithley 2400 Sourcemeter. The values of the resistance have been measured for both forward and inverse biases at voltage of 3.0 V (nominal operational value).



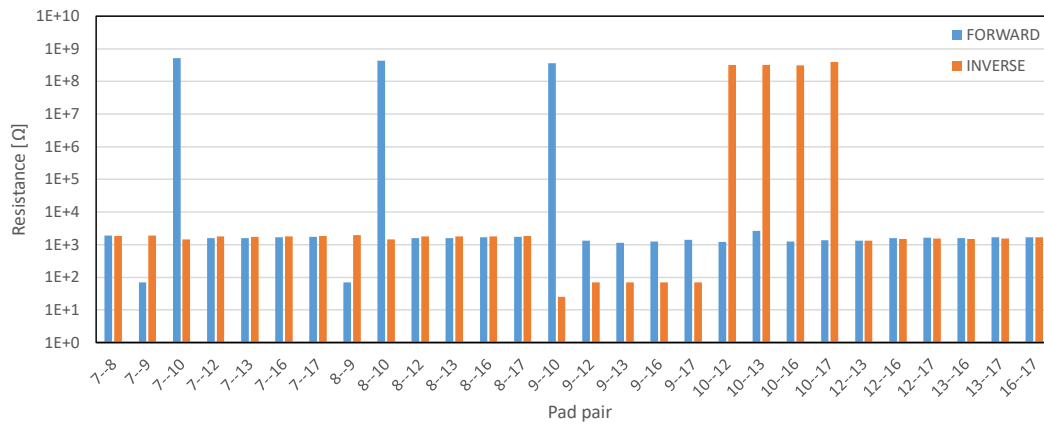
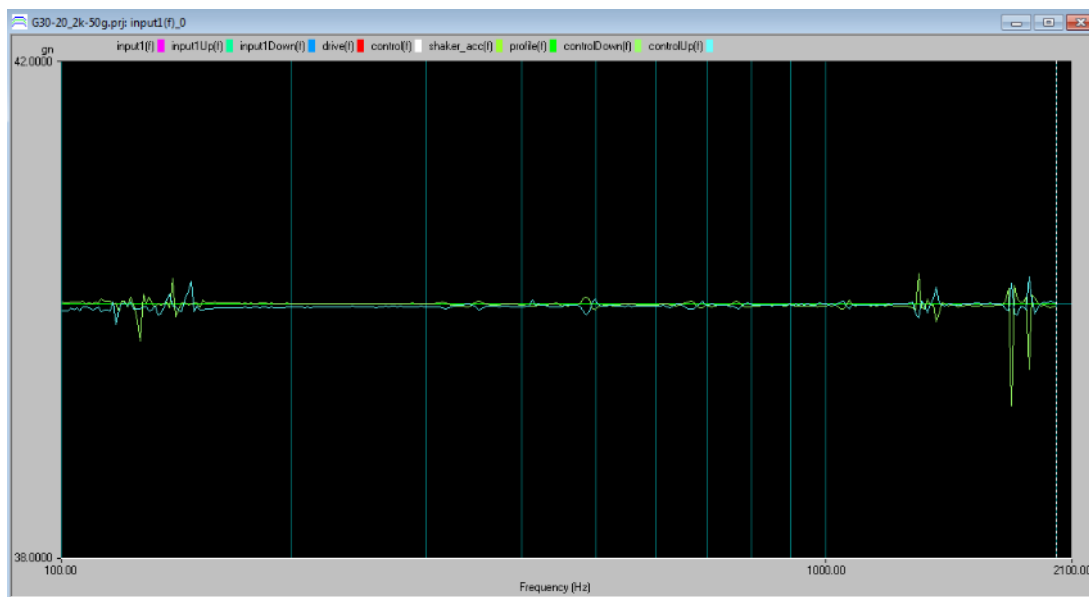


Figure 1.1: Pin-to-pin insulation.

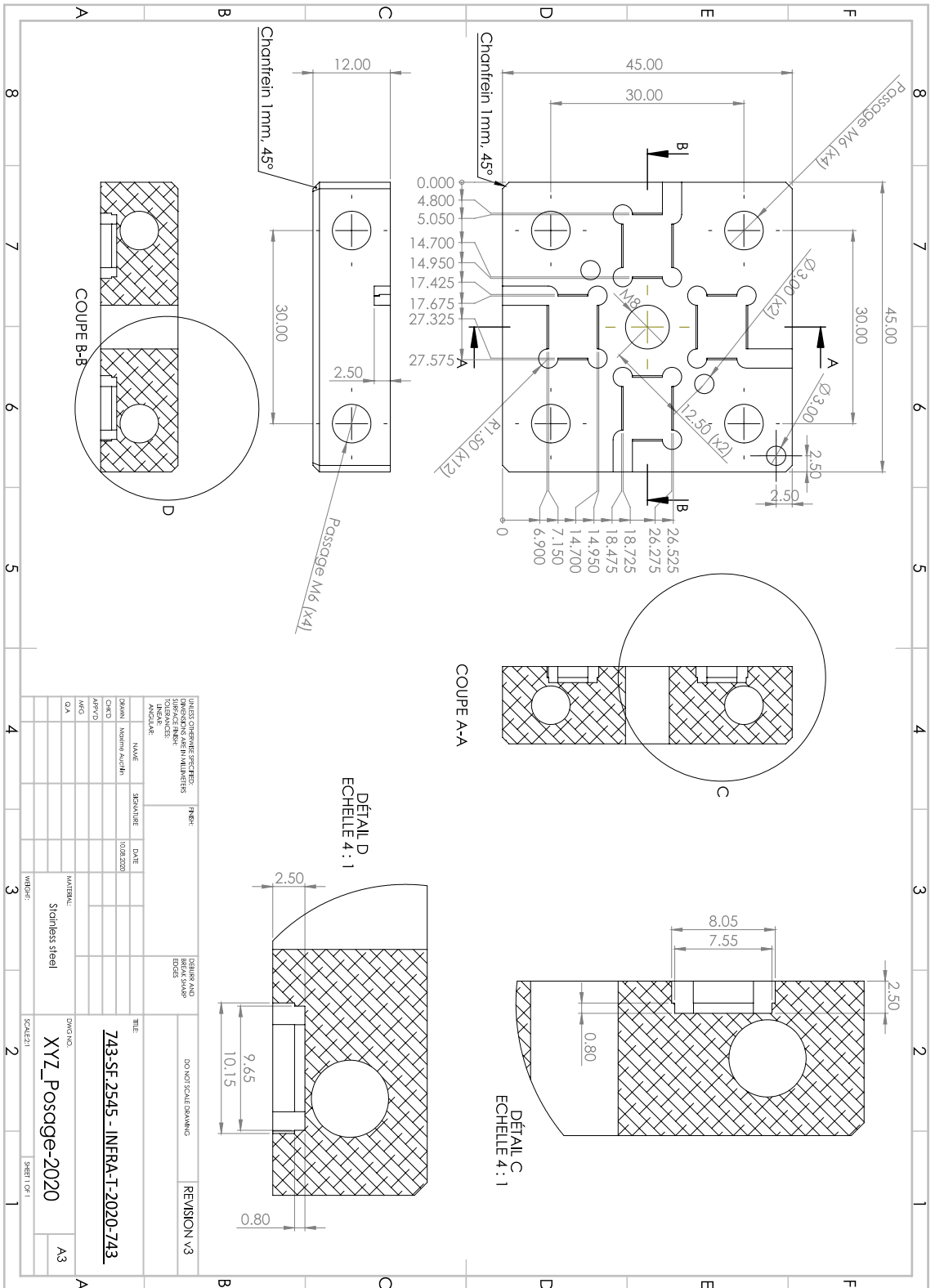
Since the pads group 4, 9, 14-18 are all grounded, some pairs were ignored for the pin-to-pin insulation.

E. Parasitic resonance measurement and vibration sample holder

Detail of a vibration full sweep (20-2,000-20 Hz) at 40g showing only minor parasitic vibration modes.

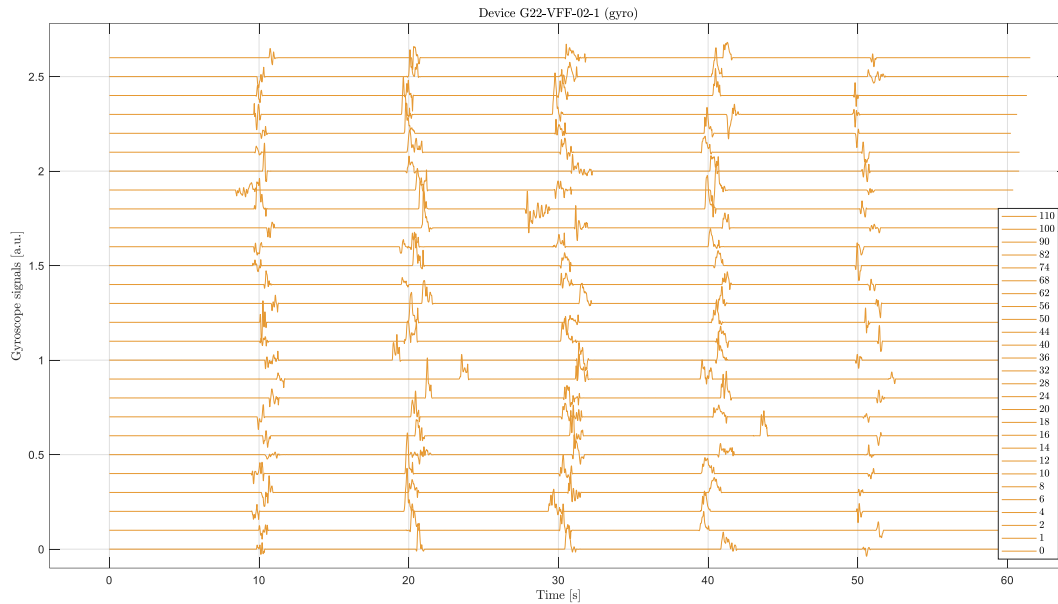


The full technical plan for the sample is provided on the next page.



F. Gyroscope readouts recording example

Example of the gyroscope's signals recording during a functional test. Changes of positions are visible by the spikes of the signal.



G. ImageJ bandpass and contrast macro

This routine has been use in ImageJ for setting a threshold function on the die attach CT scan to extract the relative surface area fraction of delamination adhesive.

```
run("Invert")

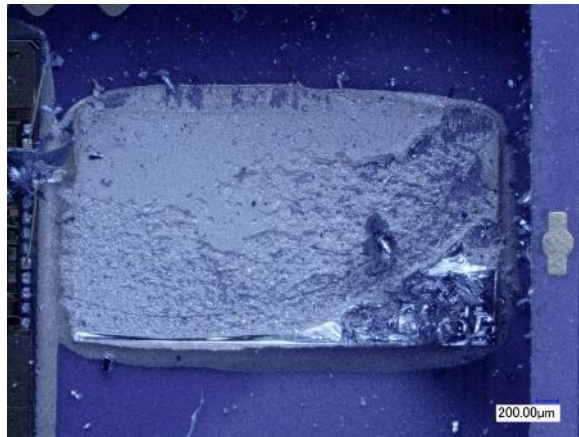
//convert to 32 bit image
//manually by: Image->Type->32 bit
run("32-bit");
//Apply bandpass Filter:
//Manually by: Process->FFT->Bandpass Filter...
run("Bandpass Filter...", "filter_large=75 filter_small=0 suppress=None tolerance=0");
//Enhance Contrast
run("Enhance Contrast", "saturated=0.35");

setAutoThreshold("Default");
//run("Threshold...");
setAutoThreshold("Li");
//setThreshold(0, 214);
setOption("BlackBackground", false);
run("Convert to Mask");
```

H. Die attach tomography and post-die shear imaging

❖ G21-CVF group

The following gyroscope fractured at the level of the silicon bulk when performing the die shear test. The resistance of the adhesive is therefore greater than the 447 MPa found for this case. In general, samples from the G21-CVF did not detach and either fractured or exploded under the applied load.

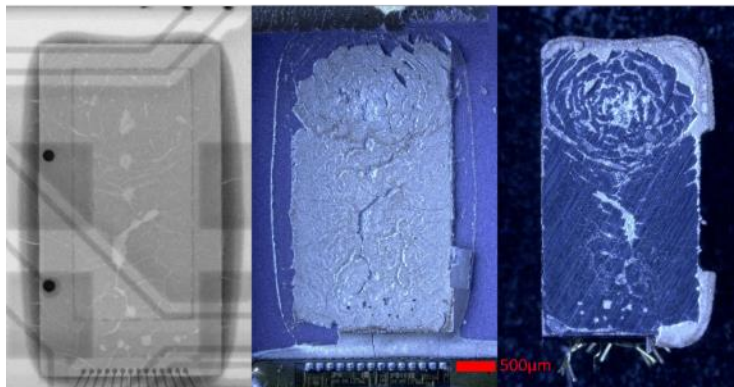


Device number 204 fractured before delaminating.

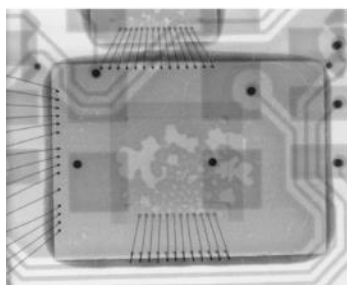
❖ G22-XVX group

The degradation of the die attach can be better understood with the observation of the post-die shear adhesive interface, and the residual material on the backside of the gyroscope's die. Additionally, the delamination can take several forms: either a large patch of adhesive fails in the center (as seen in the dedicated Section 4.3.1), either the development of globular failure of the adhesive occurs.

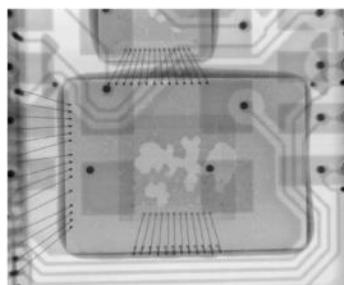
G22-XVX-06-1000



G22-XVX-01-1000



G22-XVX-04-1000

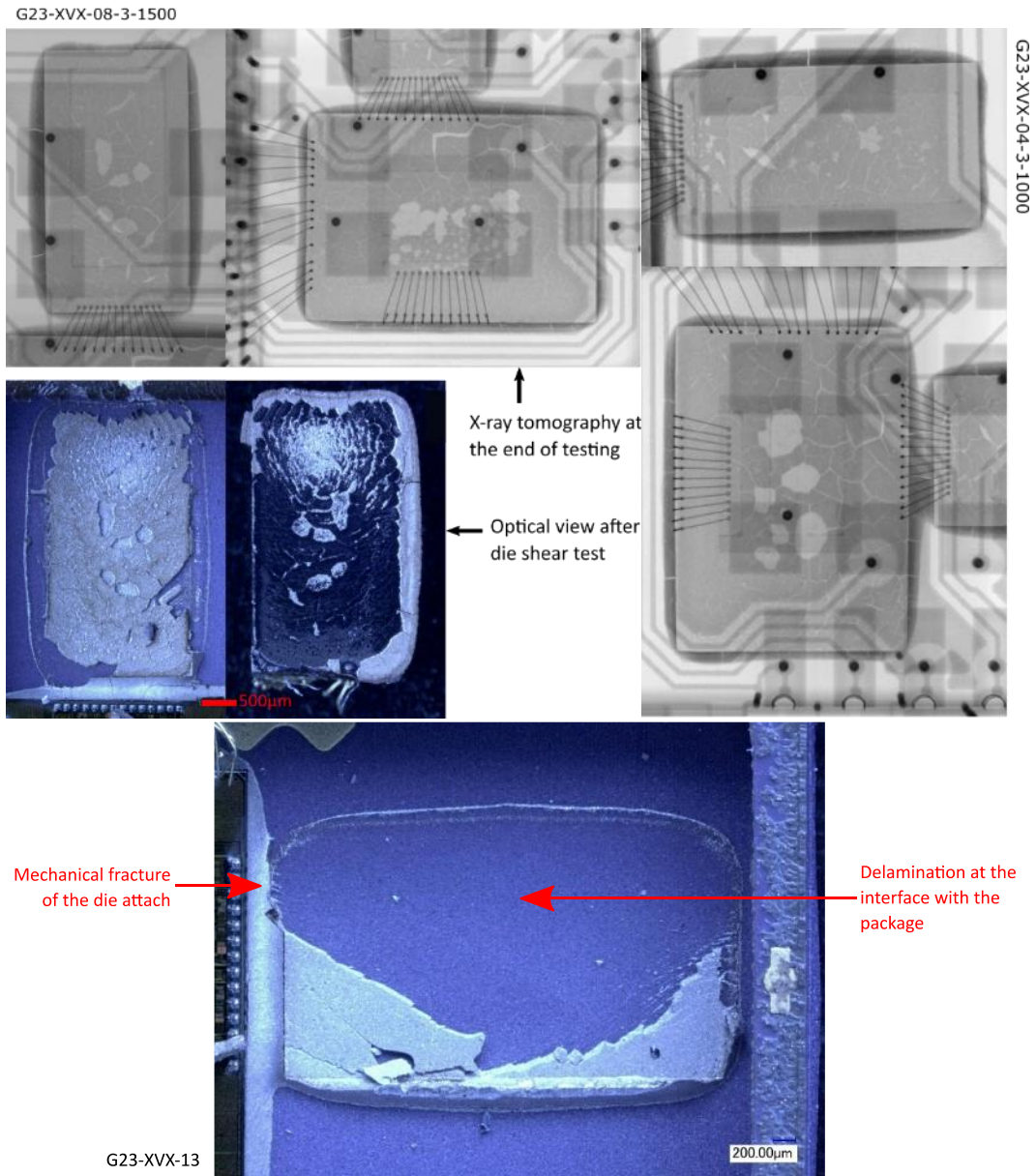


Upper view: view of the degradation die attach after shear test. The clearer shapes viewed in X-rays tomography indicated delamination or shrinkage of the adhesive at this location.

Lower view: the die attach's delamination can take several forms.

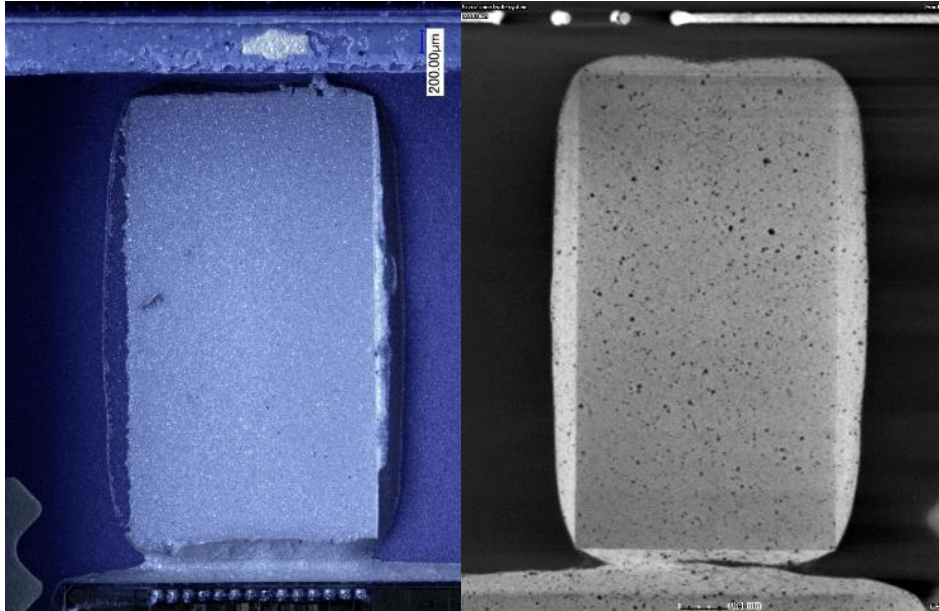
❖ G23-XVX group

A similar treatment made on the G23 group enables to visualize in optical view the observations made in tomography. The delamination holes are indeed areas of the absence of adhesive, should that be due to shrinkage, failure or loss of mass. On the contrary, a device that has been prematurely removed from the series, G23-XVX-13, demonstrates that the failure of the die attach occurs at the adhesive-package interface.



❖ Control group

Finally, a group of control has been tested for a point of comparison. While most of the devices displayed brutal fractures of the dies upon shearing, one test produced a clean detachment of the die from the package and a clear look at the high-quality interface at the die attach level. Light porosity is present but is not visible on the image. A CT-scan of a pristine sample permitted to observe the porosity.



I. Details of the post-campaign bond pull test.

❖ Accelerometer die and ASIC connections

This series of measurement constituted of a total of 252 pull tests of the connection between the accelerometer and the ASIC dies. The trend lines' equations are indicated with R^2 number. A counter-intuitive increasing trend is observed, though the uncertainty is of the range of the measured pull forces.

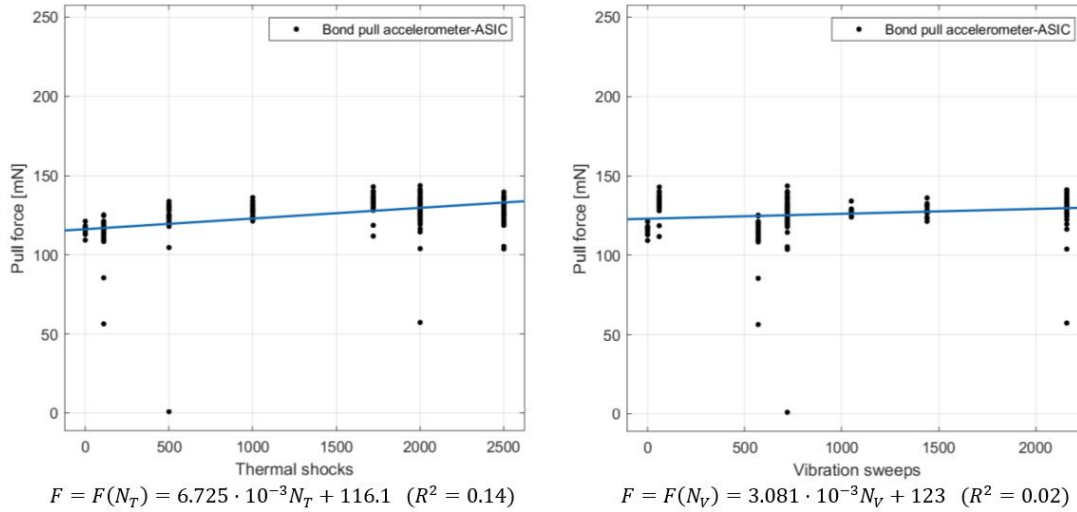


Figure 1.2: Pull test for the wire bonds connecting the accelerometer to the ASIC.

❖ Gyroscope die and ASIC connections

The following two graphs gather 294 pull tests of the bonds linking the gyroscope to the ASIC. A decreasing trend is visible, though the large scattering of the data does not permit to bring any conclusion.

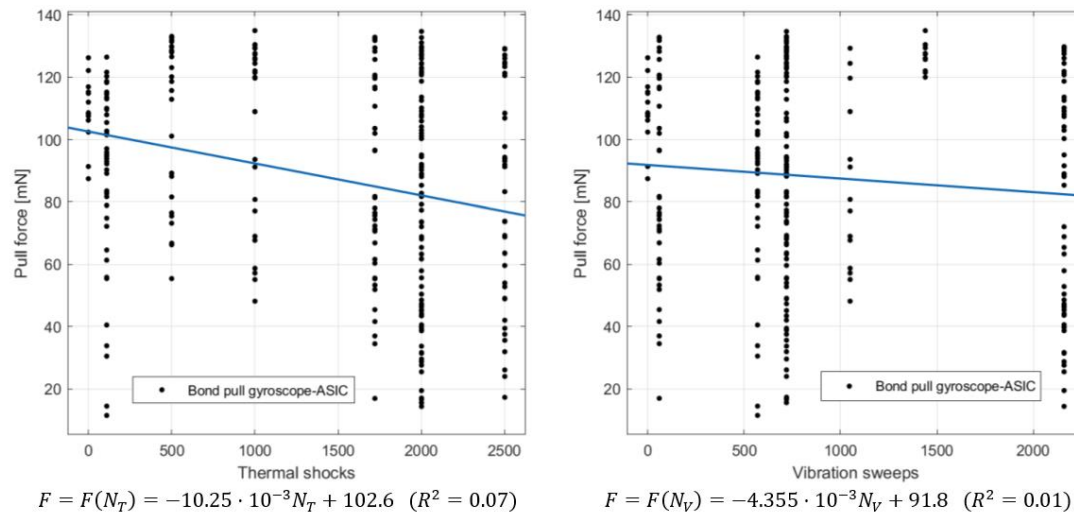


Figure 1.3: Pull test for the wire bonds connecting the gyroscope to the ASIC.

❖ Wire bonds between the ASIC and the package

Finally, the same outcome appears from the ASIC-package 315 pull tests.

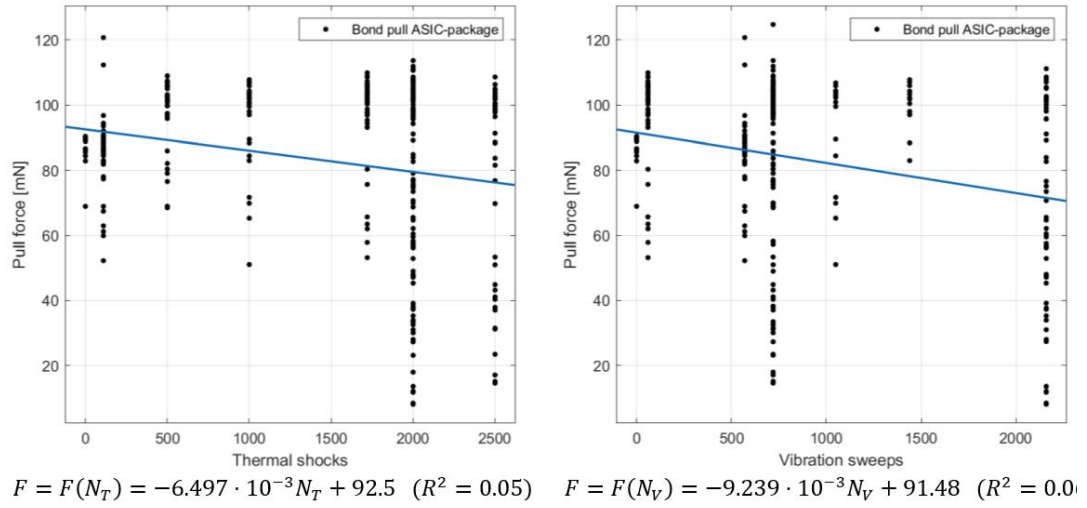


Figure 1.4: Pull test for the wire bonds connecting the ASIC to the package.

Curriculum Vitae



Personal information

First name, surname	Maxime Auchlin
Date of birth	August 29 th , 1992
Nationalities	Swiss, European

Contact information

Email	maxime.auchlin@alumni.epfl.ch
LinkedIn	https://www.linkedin.com/in/maxime-auchlin-05756668/

Languages

French	Mother tongue
English	Professional working proficiency
German, Russian	Limited conversational proficiency

Education

High school	Matura with major in biology and chemistry
September 2007 to July 2010	Lycée Denis-de-Rougemont in Neuchâtel, Switzerland
University	Materials science and engineering. Minor in space technologies.
September 2010 to October 2016	Swiss Institute of Technology in Lausanne (EPFL), Switzerland
Master thesis exchange	Special program student at the Smart Materials & Structures Lab
March to September 2016	University of Houston, Texas, USA
Graduate school	Ph.D. student at the Electrical Engineering Doctoral School
March 2017 to February 2021	Space Innovation (formerly: Swiss Space Center), EPFL

Employment history

Summer 2012	Trainee in materials science, metallurgy
	Lamineries Matthey SA, La Neuveville, Switzerland
February 2014 to August 2014	Engineering Intern (R&D in metallurgy)
	Novelis Switzerland SA, Sierre, Switzerland
Summer 2015	Summer intern
	Usine Métallurgiques de Vallorbe, Vallorbe Switzerland

Academic positions

September 2013 to January 2014	Experiments assistant
	Laboratory of Construction Materials at EPFL, Lausanne, Switzerland
December 2016 to February 2017	Research position
	Swiss Space Center, EPFL, Lausanne, Switzerland
February 2018 to April 2018	NPI (Networking/Partnership Initiative) student
June 2018 to August 2019	ESTEC, European Space Agency, Noordwijk, The Netherlands

Publications & awards

29th European Symposium on Reliability of Electron Devices, Failure Physics and Analysis, ESREF 2018	I. Marozau, M. Auchlin, V. Pejchal, F. Souchon, D. Vogel, M. Lahti, N. Saillen, O. Sereda, <i>Reliability assessment and failure mode analysis of MEMS accelerometers for space applications</i> in <i>Microelectronics Reliability</i> , Volumes 88–90, 2018, Pages 846-854, ISSN 0026-2714, https://doi.org/10.1016/j.microrel.2018.07.118 .
31st European Symposium on Reliability of Electron Devices, Failure Physics and Analysis, ESREF 2020 <u>Best Paper Award</u>	M. Auchlin, I. Marozau, D. Z. Bayat, L. Marchand, V. Gass, O. Sereda, <i>Can automotive MEMS be reliably used in space applications? An assessment method under sequential bi-parameter testing</i> , <i>Microelectronics Reliability</i> , Volume 114, 2020, 113913, ISSN 0026-2714, https://doi.org/10.1016/j.microrel.2020.113913
International Conference on Solid State Sensors and Actuators (TRANSDUCERS)	S. Lani, O. Chandran, M. Auchlin, I. Marozau and B. Dunan, "3d Printing on MEMS: Integration of 3d Shock Stopper on a Micro Mirror," 2019 20th International Conference on Solid-State Sensors, Actuators and Microsystems & Eurosensors XXXIII (TRANSDUCERS & EUROSENSORS XXXIII), 2019, pp. 113-116, doi: 10.1109/TRANSDUCERS.2019.8808274.
COMSOL Technical Papers and Presentations	D. Z. Bayat, M. Auchlin, O. Sereda, M. M. Dadras, <i>Investigation of environmental variations on the performance of a cascade impactor</i> , https://www.comsol.ch/paper/investigation-of-environmental-variations-on-the-performance-of-a-cascade-impact-95791

Achievements and trainings

- Participant to the 2015 Space Development: Theory and Practice summer school at the Bauman Moscow State Technical University, Moscow, Russia
 - Certificate of participation to the continuing education on "Radiation environment and its effects in EEE components and hardness assurance for space applications" (Swiss Space Center & CERN, Switzerland, 2017)
 - Elected deputy in the local parliament, legislature 2017-2021, Canton of Neuchâtel, Switzerland
 - Certificate of participation to ESA Academy's Product Assurance and Safety Training Course 2018
 - Certificate of participation to EPFL's continuing education program: Fundamentals of Systems Engineering (organized for RUAG Space, 2019)
-